Piezoelectric MEMS for Energy Conversion in Biomedical Devices

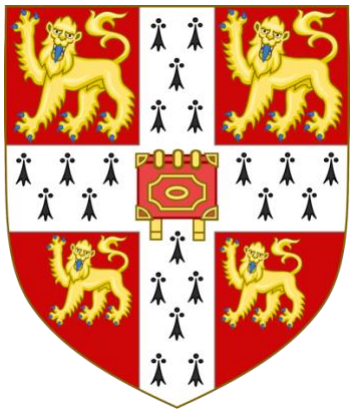

Teng Zhang

Supervisor: Prof. Ashwin A. Seshia

Department of Engineering,
University of Cambridge

This thesis is submitted for the degree of

Doctor of Philosophy

Queens' College October 2024

Declaration

This thesis is the result of my own work and includes nothing which is the outcome of work done in collaboration except as declared in the preface and specified in the text. It is not substantially the same as any work that has already been submitted, or, is being concurrently submitted, for any degree, diploma or other qualification at the University of Cambridge or any other University or similar institution except as declared in the preface and specified in the text. It does not exceed the prescribed word limit for the relevant Degree Committee.

Teng Zhang

October 2024

Piezoelectric MEMS for Energy Conversion in Biomedical Devices

Teng Zhang

Next-generation implantable medical devices are increasingly dependent on the development of sustainable and safe power sources that eliminate the need for bulky battery packs, as well as efficient and miniaturized sensing mechanisms capable of monitoring multiple physical vital signs with low power consumption. In this context, micro-electromechanical systems (MEMS) has emerged as a promising technology, attracting significant attention for their potential in various industries and applications under stringent operational requirements. This thesis explores MEMS technology, focusing on innovative methods for energy harvesting and vital signs monitoring using miniaturized, micromachined piezoelectric transducers. Specifically, the study designs transducers targeting two primary energy sources: internal mechanical movements of body organs and a safe, reliable ultrasound power source.

The first half of this work introduces a frequency comb-vibrational energy harvester, designed and characterized to function under a broadband and random vibration source. The frequency comb phenomenon is traditionally studied in the optical domain for applications in timing and spectroscopy. In this thesis, an application to vibration energy harvesting utilizing a MEMS transducer is studied leveraging its effective signal mixing and mode coupling capabilities when driven off-resonance within a specific range. This thesis marks the first instance of operating a frequency comb harvester with a broadband vibrational signal, mimicking real-world application conditions, and resulting in significant improvements in energy output and performance. Testing across multiple conditions, the study analyzes the dependency of the harvester's performance on various driving conditions, including frequency and signal amplitude. Notably, when operated in frequency comb mode with a single-frequency signal, the device achieved a total output power of 14.74 μW under 0.07 g acceleration, a marked enhancement from the 4.03 μW generated in non-comb mode at the same acceleration level.

The latter half of the thesis examines piezoelectric micromachined ultrasonic transducers (PMUTs) to tackle the challenges of energy generation and sensing in biomedical devices via ultrasound sources. An equivalent circuit method with defined lumped parameters was developed to understand the performance metrics of PMUTs. Leveraging insights from these figures of merit, two multi-channel PMUTs prototypes were firstly designed and fabricated in both circular and square configurations, capable of operating across multiple resonant modes simultaneously. An innovative dual-frequency channel concept was tested between two PMUT arrays, assigning the low-frequency mode to wireless power transfer and the high-frequency mode to data telemetry within a single device framework. Experimental tests on a silicone biomimicking phantom demonstrated that the circular PMUT prototype achieved a power output of 411.3 nW and a data transmission rate of 50 kbps with a bit error rate (BER) of 1.7×10^{-2}. In contrast, the square PMUT prototype delivered a power output of 202.4 nW and a data rate of 10 kbps with a BER of 8.1×10^{-4}. Prompted by the limitations observed in these initial prototypes, subsequent developments focused on numerically analyzing the mechanical responses of various mode combinations, which led to targeted optimizations in the electrode configuration and an increase in operating frequencies aimed at boosting overall device performance. The optimized multi-channel PMUTs featured customized electrode designs and increased operating frequencies, achieving a marked improvement in system capabilities. Notably, these enhancements led to an increase in the data transfer rate to 945 kbps and enhanced the power output to 504.3 nW, achieving 22.7% boost in power output compared to the initial prototype.

Lastly, aiming to exploit the multi-frequency capabilities with a different approach, a high-density PMUTs array with varied on-chip transducer dimensions and frequencies is designed to improve the transmitting and receiving sensitivity across an expanded bandwidth. This multi-frequency PMUTs array is tested for its ability to sense the dynamic motion of a blood vessel model with a wall thickness of 0.75 mm and temperature of blood-mimicking fluid, achieving a sensitivity of 9.7° phase shift per degree Celsius within a temperature range of 35°C to 45°C. Further testing of its broadened bandwidth and improved sensitivity includes efficiently capturing the emitted ultrasound signals from photoacoustic imaging applications. Tests on imaging phantoms with target dimensions ranging from 0.3 mm to 0.7 mm allow the PMUTs to characterize the corresponding frequency response and reconstruct images with comparable resolution and quality by integrating multiple transducer designs on the same chip.

Acknowledgements

I would like to first express my deepest gratitude to my advisor, Prof. Ashwin Seshia, for providing the perfect balance of guidance and independence throughout my research journey. Your supervision, mentoring, and support enabled me to navigate the challenges of my doctoral work with confidence.

I am also immensely thankful for the wisdom, experience, and patience of my fellow group members and collaborators: Dr. Sijun Du, Shenglin Hou, Dr. Madan Parajuli, Dr. Hamad Raheem, and Dr. Xiaolong Wen (alphabetically by last name). Your readiness to assist and share your insights has been invaluable from the start of my doctoral research, and I look forward to continuing to learn from each of you.

A special thanks goes to my family, whose unwavering support and encouragement have been my foundation throughout this journey. To my parents, Haijun and Haihong, thank you for your unconditional love and support. You are everything for whom I am today. To my brother, Andrew, for imparting the values of responsibility, sharing, and love. To my furry companion, Duffy, for your trust, loyalty, and limitless affection. Most importantly, to my wife, Siyu, your support and understanding have carried me to this point. Thank you for being there for me across the distances—from Beijing to Boston, from New York to Cambridge. The memories we made in La Foce will stay with us forever. I would not be the person I am today without all of you. Thank you, and I love you all eternally.

This marks the start of a new journey—always learning, always exploring.

Table of Contents

List of Figures . . . . . **IX**

List of Tables . . . . . **XIX**

List of Abbreviations . . . . . **XX**

List of Symbols . . . . . **XXII**

1. Introduction **1**

1.1 Vibrational Energy Harvester 3

1.2 Micromachined Ultrasonic Transducer 12

1.3 Conclusion 17

2. Theory and Methods **19**

2.1 Piezoelectricity 21

2.2 Electric Domain and Power Management 24

2.3 Analysis and Characterization Methods 26

2.3.1 Lumped Model 26

2.3.2 Distributed Parameter Electromechanically Coupled Analysis 28

2.3.3 Rayleigh-Ritz Method 31

2.3.4 Finite Element Analysis (FEA) 32

3. Nonlinear Vibrational Energy Harvester **36**

3.1 Mode coupling and Parametric Resonance 37

3.2 Frequency Comb Harvester 42

3.2.1 Concept 43

3.2.2 Modeling and Device Design 47

3.2.3 Experimental Characterization 49

3.2.4 Conclusion 55

4. Piezoelectric Micromachined Ultrasonic Transducers 56

4.1 State of the Art: Micromachined Ultrasonic Transducers 56

4.2 Piezoelectric Micromachined Ultrasonic Transducers 58

4.3 Numerical Analysis: Equivalent Circuit Method 61

5. Multi-Channel Piezoelectric Micromachined Ultrasonic Transducers **72**

5.1 Device Design 73
5.2 Dual-Channel PMUTs Operation 77
5.3 Acoustic Coupling and Remote Excitation 81
5.3.1 Crosstalk Characterization 81
5.3.2 Remote Excitation 85
5.3.3 Conclusion 88
5.4 Crosstalk and On-chip Filter 89
5.4.1 Experimental Setup 89
5.4.2 Communication with On-chip Filtering 94
5.4.3 Conclusion 96
5.5 Dual-Function Wireless Power Transfer and Data Telemetry 96
5.5.1 Dual-Function Characterization 97
5.5.2 Conclusion 101
5.6 Electrode Optimization 102
5.6.1 Device Design 103
5.6.2 Device Characterization 108
5.6.3 Wireless Power Transfer and Data Telemetry 110
5.6.4 Conclusion 111
5.7 Conclusion 112

6. Multi-Frequency PMUT Array 114
6.1 Device Design 114
6.2 Concurrent Pulse-Echo and Through-Transmission Ultrasound Tracking 116
6.2.1 Multi-Frequency Blood Vessel Motion and Temperature Measurement 118
6.2.2 Results and Discussion 121
6.3 Multi-Frequency PMUT for Photoacoustic Imaging 124
6.3.1 Device Design and Frequency Response 126
6.3.2 Experimental Setup 127
6.3.3 Photoacoustic Imaging 128
6.4 Conclusion 133

7. Conclusion 135
7.1 Future Work. 137
7.1.1 Frequency Comb Energy Harvester 137
7.1.2 Multi-Channel PMUT. 138

7.1.3 Multi-Frequency PMUT Array 139
Appendix A: Contribution of the Author 141
References 143

List of Figures

Figure 1. A: Overview of modern implantable medical devices, including various types such as brain-computer interfaces, cochlear implants, pacemakers, and neuromodulation devices. B: Illustration of the CardioMEMS HF System, a vascular pressure monitoring device developed by Abbott Inc., showing its design and operational principle. C: Power consumption ranges of critical medical devices, highlighting that most devices operate primarily within the micro-watt (μW) to milli-watt (mW) range.

Figure 2. Growing research interests in energy harvesting field of study over recent decades. Among them, it highlights the rapidly increasing focus on piezoelectric energy harvesters, demonstrating a faster growth rate in its research interest compared to electrostatic and electromagnetic energy harvesters.

Figure 3. A (1)-(2): A PZT-conformal piezoelectric energy harvester designed to harness energy from muscle contractions during heartbeats, shown in experimental setup on a bovine heart. (3) Voltage output of the harvester attached to a bovine heart, demonstrating a peak voltage of up to 1 V. B (1)-(2) Schematic and operation of an alternative energy harvester that generates power by inducing mechanical stress from heart muscle movements. (3) Power output of the harvester, reaching up to 33 μW when optimized with an impedance-matched load. C (1)-(2): A spiral energy harvester integrated with a pacemaker lead, designed to convert kinetic energy from heart movements into electrical power. (3): Voltage output observed when the spiral harvester is attached to the pacemaker lead.

Figure 4. A-C: Frequency spectrum of acceleration signals from heartbeats, measured across different studies, showing a broadband and noisy frequency distribution below 100 Hz. .

Figure 5. A (1) Cantilever energy harvester design incorporating a large proof mass to lower the resonance frequent to 28-29 Hz; (2)-(3): The power output and frequency response of harvester under varying acceleration. B (1)-(3): Folded energy harvester design with a double piezoelectric layer configuration, aimed at enhancing power output at low frequencies. C (1)-(3): Buckled clamped-clamped beam energy harvester, demonstrating the impact of varying buckling levels on reducing the resonant frequency

Figure 6. A: (1) Vibrational energy harvester utilizing a clamped-clamped beam structure; (2) The jump-down phenomenon resulting from Duffing nonlinearity, which enhances the bandwidth of the harvester. B: (1) Bistable energy harvester featuring buckling induced by pre-stress between different material layers during fabrication; (2) Oscillation behavior of the central proof mass, illustrating intrawell oscillation before (left) and interwell oscillation after (middle and right) crossing the bistability threshold.

Figure 7. A (1)-(2) Illustration of a clamped-clamped beam harvester demonstrating coupled second and third modal frequencies and auto-parametric resonance; (3) Time-domain representation of auto-parametric resonance, observed around 250 seconds, showing energy transfer from the third mode to the second mode. B. (1)-(3) Schematic and simulation of a coupled cantilever harvester exhibiting mechanical responses due to two-mode auto-parametric resonance; (4) Combined time- and frequency-domain responses, highlighting the simultaneous excitation of two modes under a single-frequency drive.

Figure 8. A: Overview of wireless power telemetry and power transfer topologies, highlighting essential functions and components. B: Comparative analysis of ultrasound, inductive, and capacitive power transfer methods, focusing on penetration depth, device size, and link efficiency. C: A miniaturized, FDA-approved cardiac pacemaker powered by ultrasound, demonstrating a 70% reduction in size compared to conventional designs. D: (1) Schematic of an ultrasound-based system for neural recording modulation. (2)-(3) Illustration of simultaneous data communication using a backscattering and pulse-echo mechanism.

Figure 9. A: A 1261-PMUTs array design features enhanced bandwidth performance. B: PMUT array utilizing advanced ScAlN material, designed for optimized electromechanical efficiency

and improved acoustic characteristics. C: Broadband PMUT configuration employing induced mode overlap to achieve extended bandwidth.

Figure 10. Design considerations and flowcharts for MEMS energy transducers.

Figure 11. A: The polling direction in a crystal material, showing 33- and 31- modes in B (bottom) and B(up) respectively, which refer to electric charges induced parallel and perpendicular to the applied strain direction, respectively. These modes are pivotal in selecting materials for specific applications due to their differing efficiencies.

Figure 12. Cross sectional view of PiezoMUMPs fabricated device.

Figure 13. A: A standard full-bridge rectifier with shaded area indicating power loss during transduction. B: A SSHI circuit with synchronized inductors controlled by an analog gate and reduced shaded area showing efficiency improvement.

Figure 14. Lumped model of a piezoelectric energy harvester with (left) uncoupled and (right) electromechanically coupled responses.

Figure 15. A: FEA simulation results of a clamped-clamped structure with stress distribution and deflection profile. B: A clamped-clamped energy harvester was designed and fabricated based on insights from COMSOL simulation results.

Figure 16. A: Deflection profile of a circular PMUT at its fundamental mode. B: Acoustic pressure field and C: Sound pressure level around PMUT. D: Frequency spectrum of the proposed PMUT with fundamental mode's resonant frequency at 100 kHz. E: Deflection profile at the center of circular PMUT driven electrically at its fundamental mode. F: Voltage response from a PMUT receiver separated 1 cm away from a TX in air.

Figure 17. A: Parameter plane for Mathieu equation. Shaded (unstable) region marks the parametric resonance. B: Effect of viscous damping on threshold of parametric resonance. C: Auto-parametric and energy exchange between two modes without damping (Left) and with damping (Right).

Figure 18. A: Cross-section view of a circular piezoelectric energy harvester with dual-ring electrode and central proof mass. B: Picture of the fabricated MEMS energy harvester. C: Mode profile of the energy harvester at its fundamental mode under FEA simulation. D: Mode profile of the energy harvester at a higher mode 2 under FEA simulation. E: Resonant frequencies of designed circular VEH across various eigenmodes.

Figure 19. A: Time-domain response of VEH prototype from two points of interest at center of two ring electrodes. B: Frequency spectrum demonstrates multiple modes being excited with a single-frequency signal at mode 2 frequency.

Figure 20. A: Concept of resonant frequency tracking using phononic frequency combs: when a single sinusoidal drive is applied to a free-free resonator, a series of equidistant spectral lines are generated through the process of phononic frequency comb generation. B: Emergence of phononic frequency combs in the strong coupling regime. Phononic frequency combs arise in the strong coupling regime through coherent energy transfer, as depicted by the modulation of amplitudes and phases of two coupled mechanical modes (mode I and II, shown by blue and red curves).

Figure 21. Existing observation on frequency and drive amplitude dependence on generation of frequency comb. A: Frequency spectrum with driving frequency threshold $\omega_{D,min}$ and $\omega_{D,max}$ in generation of frequency comb. B: Frequency comb appears when driving signal excites the system between linear and duffing nonlinear region given experimental results.

Figure 22. A: Photo of the packaged MEMS energy harvester. B: Cross-sectional view of fabricated FC harvester.

Figure 23. A-C: COMSOL simulated results of first three modes at 261.3 Hz, 422.7 Hz and 515.6 Hz respectively. The harvester is anchored by a central rectangular post from the bottom.

Figure 24. A: Block diagram of experimental setup for vibrational energy harvester. B: Experimental setup installed in the lab.

Figure 25. A: Frequency sweep around the comb mode under low acceleration shows a linear response. B: A frequency sweep under moderate acceleration levels shows evidence of Duffing nonlinearity. C: Increasing the driving acceleration until internal resonance occurs. D: Further increase of the driving levels results in the emergence of the frequency comb.

Figure 26. A: Intermodulation involving three distinct signals from the comb mode, coupled mode, and drive signal. B: Depiction of the comb regime and corresponding detuning level $\delta_{detuning}$.

Figure 27. A: Spectrum indicating internal resonance and mode coupling when driving with a single tone signal at 578.4Hz. B: Spectrum characterizing frequency combs when driving with a single tone signal at 588.4Hz and 10Hz detuning level.

Figure 28. A: Band-limited noise spectrum (with inset showing the corresponding time-domain) of the electrical signal used to drive the shaker. B: Output spectrum of the frequency comb driven by noise with the response spanning multiple octaves.

Figure 29. A: traditional composite PMN/PT or PZT bulky US transducer. B: capacitive micromachined ultrasonic transducer requiring a high DC bias voltage on top of AC drive signal. C: piezoelectric micromachined ultrasonic transducer requiring only AC driving signal on electrodes across piezoelectric layer.

Figure 30. A: COMSOL simulated mode shape for (0,1), (0,2) and (0,3) modes. B: Deflection profile of numerical analysis results.

Figure 31. A: Normalized deflection profile of a circular PMUT at fundamental mode. B: Radial, tangential and total stress under fundamental mode. The electrode aims to match a critical radius at $\sqrt{2}/2$ when total stress equals flip the polarity.

Figure 32. A: Mason's equivalent circuit diagram representation in the electrical, mechanical, and acoustic domains. B: Butterworth–Van dyke (BVD) equivalent circuit converted in mechanical domain only, when the PMUT is employed as transmitter. C: BVD equivalent circuit in electrical domain only, when the PMUT is employed as receiver.

Figure 33. Dimensionless resistance r_a (A) and reactance x_a (B)components of the radiation impedance for the rigid piston mode.

Figure 34. Equivalent circuit of three symmetric modes operating simultaneously.

Figure 35. Top and cross-sectional views of circular (A) and square (B) PMUTs, alongside fabricated arrays of circular (C) and square (D) PMUTs.

Figure 36. A: DHM recorded vibration profile of the circular PMUT. B: Frequency sweep of COMSOL simulations and experimental results for single and dual-electrode PMUTs, showing sensitivity balance improvement at 101 kHz and 828 kHz modes.

Figure 37. A: DHM recorded vibration profile of a square PMUT. B: Comparison of frequency response between COMSOL simulations for a single electrode design and experimental data from a fabricated PMUT with dual electrodes, illustrating the enhanced sensitivity achieved with the dual electrode configuration.

Figure 38. Open-circuit voltage recorded at the receiver at fundamental mod as a function of separation distance between the transmitter and receiver.

Figure 39. A: Illustration of dual-channel operation with TX and RX chips separated 1.5 cm in air. B: Experimental setup of a PMUT TX and a RX in air. B: A bio-mimicking phantom is inserted between the TX and RX chips.

Figure 40. A: DHM recorded deflection profile of a circular PMUT TX in dual-channel operation (left). The summed drive signal (black), time-domain deflection responses at center X (green) and annular ring Y (red). B: DHM recorded deflection profile of a square PMUT TX in dual-channel operation (left). The summed drive signal (black), time-domain deflection responses at center Z (blue) and side W (orange).

Figure 41. Sources of crosstalk between adjacent PMUTs. A: Acoustic crosstalk depicted as coupling between adjacent PMUTs across various media or interfaces. B: Electrical crosstalk shown through the interaction of electrodes from two neighboring PMUTs. C: Predominant acoustic crosstalk in PMUTs, primarily propagated through the SOI wafer.

Figure 42. A: Frequency mismatch of two adjacent PMUTs under 3Vpk-to-pk drive. B: Electrical response from coupled PMUT 1 when increasing drive voltage on PMUT 2 under frequencies f_1, f_2 and f_3.

Figure 43. Comparative analysis of optically recorded deflection amplitudes on PMUT 1 with phased driving on PMUT 2. A: The deflection amplitude reduction correlates with acoustic coupling designed for propagation through a solid-air interface. B: The same phenomenon is observed when acoustic coupling is designed for propagation through an SOI wafer, demonstrating more pronounced coupling. In both scenarios, the drive voltage (V pk-to-pk) on PMUT 2 increases incrementally from 2 V (top) to 10 V (middle), and finally to 20 V (bottom), illustrating the effect coupling levels on PMUT 1.

Figure 44. A-D: Measured frequency response and coupling level of direct-excited (black) and acoustically coupled (blue) PMUTs at (0,1), (0,2), (1,2) and (0,3) modes. Maximal deflection amplitude measured at center of PMUT using a DHM.

Figure 45. A: Deflection profile of the coupled PMUT. B: Waveform used to directly drive the actuated PMUT; Red channel 1 at 101 kHz; Green: channel 2 at 828 kHz; Blue: combined driving signal. C: Vibration amplitude of directly driven PMUT. D: Electric response of acoustically coupled PMUT shows the filtering effect with a signal at 101 kHz only.

Figure 46. A: Experimental setup for inducing dual-mode operation in the central pmut through remote excitation. B: Deflection profile of coupled secondary PMUT shows coupling of both (0,1) and (0,2) modes. C: Measured time-domain electrical response for the (0,1) mode. D: Measured time-domain electrical response for the (0,2) mode.

Figure 47. A: Fabricated array comprising multi-channel PMUT and filtering PMUT. B: Cross-sectional view of proposed PMUT design.

Figure 48. DHM recorded vibration profile and frequency sweep of multi-channel and filtering PMUT across fundamental and higher modes.

Figure 49. Illustration of multi-channel and filtering PMUT operation. In this study, channels 1 and 2 are focused and studied.

Figure 50. The DHM recorded vibration profile and waveform of drive signal. (Left): channel 1 at fundamental (1,1) mode. (Right): channel 2 at asymmetric (1,2) model. (Center): summed signal used for dual-channel mode.

Figure 51. A schematic of the on-chip PMUT filtering operation, with one of the output electrodes on the multi-channel PMUT connected to the filtering PMUT. The bottom left plot (red) shows the output electrical signal before filtering, while the right plot (green) presents the output electrical signal after filtering.

Figure 52. (Top): Randomly generated 8-bit binary data cycled for 3 times. (Middle): Electric signal from multi-channel PMUT RX. (Bottom): Electric signal after passing through the on-chip filtering PMUT.

Figure 53. Illustration of dual-function operation of multi-channel PMUT with one channel specified for WPT and another for COM.

Figure 54. The impact of drive amplitude ratio between WPT and COM channel of the circular PMUT on A: power transfer efficiency and B: data transfer fidelity as quantified by BER while maintaining the drive level on WPT channel.

Figure 55. Top: driving signal (blue) with binary data encoded at channel 2 and 1.7:1 drive amplitude ratio between COM(CH2) and WPT(CH1) channel. Middle: open-circuit voltage output from the annular electrode. Bottom: demodulated binary signal using an asynchronous ASK demodulator with envelope detection scheme.

Figure 56. A: The circular and square dual-channel PMUT prototypes. B: The electrode layout of circular and square prototypes targeting axisymmetric and asymmetric modes.

Figure 57: Normalized deflection profile of first 3 axisymmetric and 2 asymmetric modes.

Figure 58. A: Top electrode pattern with splitting electrode E_1 (yellow), and two annular ring electrode E_2 (gray) and E_3 (red). B: Cross-section view of proposed electrode-optimized PMUT. C: Normalized stress distribution of two targeting axisymmetric modes and one asymmetric mode.

Figure 59. Optical image of optimized multi-channel PMUT A: TX; and B: RX.

Figure 60. A: COMSOL simulated mode profile of a traditional single-electrode PMUT. B: Experimentally measured vibration profiles of an electrode optimized multi-channel PMUT for first 5 modes from 464 kHz to 4.3 MHz.

Figure 61. A: Experimental Setup for dual-function WPT and COM experiments on optimized multi-channel PMUT utilizing asymmetric (1,1) mode for WPT and axisymmetric (0,3) mode for COM. B: A summed signal to drive the PMUT TX with 1:1 amplitude ratio between WPT and COM channels. C: Electrical response from splitting electrode reflecting a dominant response from (1,1) mode WPT channel. D: Electrical response from annular electrode showing sharp ASK-modulated response from (0,3) mode COM channel.

Figure 62. Fabricated multi-frequency PMUTs array with different dimension as PMUT 1 (yellow), PMUT 2 (green), and PMUT 3(red).

Figure 63. Frequency response of PMUT 1(left), PMUT 2(middle), and PMUT 3(right) arrays coated and immersed in engineered liquid FC-70.

Figure 64. Working principle of the multi-frequency PMUTs array in simultaneous tracking pulse-echo and through-transmission ultrasound signals.

Figure 65. A: Experimental setup of temperature monitoring and blood vessel expansion tracking B: PMUT TX and RX arrangements for Pulse-Echo and Through-Transmission methods. C: Signal processing workflow for relative phase shift tracking and time-of-flight measurement.

Figure 66. A: The working principle of transmitting and echo measurements of upper and lower walls on the silicone tube. B: Recorded echo response of upper and lower walls when the pump is kept off and BMF static. C: Recorded echo response of upper and lower walls when the pump is turned on and BMF expanded the tube walls.

Figure 67. The relative phase shift measured between PMUT 1(blue) and PMUT2 (red), with a peak at signal from PMUT 1 marked in green line as reference mark to track the relative phase shift of two measurements A and B. C: The linear correlation between relative phase shift and temperature of BMF.

Figure 68. Workflow of photoacoustic imaging measurements with Galvo control module and signal processing unit.

Figure 69. Experiment setup for photoacoustic imaging with multi-frequency PMUTs array.

Figure 70. A, C, and E: PA signal recorded from PMUT 1, 2 and 3 in time domain. B, D, and F: Corresponding signal recorded in frequency domain.

Figure 71. A: Prepared phantom with pencil leads as imaging target at varying dimensions. Yellow arrow indicates the 1D A-line scan direction, and red box marks the 2D scan area. B-D: The frequency response of PA signal from imaging target at diameter of 0.7, 0.5 and 0.3 mm, highlighting the shift in central frequency associated with the reducing dimension of the target. The plotted results are recorded from PMUT 1.

Figure 72. A-C: The 1D A-line scanned PA results using PMUT 1, 2, and 3 respectively. D: The 1D scanned PA results using all PMUTs. E: 2D scanned image processed and reconstructed using all channels from multi-frequency PMUTs array.

Figure 73. A: Schematic of the proposed dual-mode ultrasound and photoacoustic system featuring a multi-channel PMUT array and laser diode array. B: Layered structure stacked on a flexible substrate, designed for wearable applications to enable continuous monitoring of a patient's biomarkers.

List of Tables

Table 1. Electromechanical and piezoelectric properties for popular piezoelectric materials.

Table 2. Mode-specific constants for first five modes of the circular PMUT clamped at edges.

Table 3. Effective area for first five symmetric modes of a circular PMUT.

Table 4. Equivalent circuit parameters obtained from exact solution for first 4 symmetric modes.

Table 5. Calculated phase delay for vibration inhibition.

Table 6. Zero-crossing mechanical stress radius and resonant frequency ratio for first 3 axisymmetric and 2 asymmetric modes of circular PMUTs.

Table 7. SBW comparison between dual-channel PMUT prototype and electrode optimized PMUT.

List of Abbreviations

MEMS	Micro-electromechanical systems
IoT	Internet of Things
VEH	Vibrational energy harvesters
CMOS	Complementary metal oxide semiconductor
AlN	Aluminum Nitride
NIR	Near-infrared
IME	Implantable medical device
IC	Integrated circuit
PMUT	Piezoelectric micromachined ultrasonic transducer
CMUT	Capacitive micromachined ultrasonic transducer
AC	Alternating current
IMD	Implantable medical device
FEA	Finite-element analysis
SOI	Silicon-on-insulator
FC	Frequency comb
RF	Radio Frequency
EM	Electromagnetic
Cr	Chromium
Al	Aluminum
DHM	Digital Holographic Microscope
TX	Transmitter
RX	Receiver
ASK	Amplitude-shift keying
COM	Communication
SNR	Signal-to-noise ratio
BER	Bit-error rate
TIA	Transimpedance amplifier

VGA	Voltage gain amplifier
BMF	Bio-mimicking fluid
PAI	Photoacoustic imaging
FWHM	Full width at half maximum
DAQ	Data acquisition

List of Symbols

A_{eff}	Effective area in acoustic domain in Mason's equivalent circuit
c	Damping coefficient
c_m	Speed of sound in medium
C_0	Shunt capacitance
D	Electric displacement field
E	Electric field
$f_r(t)$	The external forcing function for the r-th mode, representing applied forces
h	Thickness
I	Moment of inertia
I_m	Bessel functions of order m of the hyperbolic form
I_p	Mechanical strain by electrode
J_1	First order Bessel function
J_m	Bessel functions of order m of the first kind
k	Stiffness constant
K_1	First order Struve function
k	Wavenumber
m	Mass
M	Bending moment
q	Electric charge
Q	Quality factor
r_a	Dimensionless resistive of radiation impedance
s	Elastic compliance
S	Mechanical strain
T	Mechanical stress
U	Potential energy
Y	Young's Modulus
Z_a	Radiation impedance in acoustic domain in Mason's equivalent circuit

x	Displacement amplitude
ε	Material permittivity
d_{ij}	Piezoelectric charge constant
k_{ij}	Electromechanical coupling coefficient
g_{ij}	Piezoelectric voltage coefficient
ε_0	Relative permittivity
ω_N	Resonant frequency
ς_e	Mechanical ratio
ς_m	Electrical damping ratio
σ	Bending stress
$\omega(x,t)$	Displacement at position x and time t
$\phi_r(x)$	Eigenfunction associated with the r-th mode of vibration
$\eta_r(t)$	Modal mechanical response for the r-th mode
χ_r^s	A coupling term representing interaction between mechanical and electrical
δ	Detuning level for frequency comb
α	Coefficient of Quadratic Coupling between two designated modes
λ	Mode shape and frequency dependent parameter for PMUT
σ_r	Radial stress
σ_θ	Tangential stress
η	Transformer's turn in Mason's equivalent circuit
x_a	Dimensionless reactive of radiation impedance
ρ_m	Density of medium

Chapter 1

Introduction

Over recent decades, the development of implantable biomedical devices has increasingly focused on autonomous monitoring and support of organ functions. These advanced devices, as shown in Figure 1, are continuously researched to enhance miniaturization, biocompatibility, wireless functionality, and longevity. Despite these advancements, power limitations remain a significant bottleneck, particularly as the miniaturization of power sources has not kept pace with the reduction in size of sensing and treatment components. For instance, cardiac pacemakers, which are crucial for maintaining appropriate heart rates, have seen size reductions of over 40%. Yet, they still rely on primary batteries that occupy a substantial portion of the device's volume and require periodic surgical replacement—even when the patient is otherwise healthy and the device functions properly. This not only inconveniences patients but also increases the risk of surgical complications. Meanwhile in the semiconductor industry, MEMS (micro-electromechanical systems) has emerged as a transformative solution, finding applications not only in microsensors and resonators but also extending to personal electronics and the Internet of Things (IoT). Given their miniaturization capabilities, reliability, and low power consumption, MEMS technology has been increasingly incorporated into the healthcare sector, utilized in devices such as blood pressure sensors and emerging brain-computer interfaces. Although most implantable medical devices operate within the microwatt (μW) power range, MEMS energy transducers have shown potential in generating adequate power from both internal and external sources. This capability suggests a viable solution to the power constraints faced by small medical electronics. For example, Figure 1. B illustrates an FDA-approved passive artery pressure monitor (CardioMEMS), which delivers accurate pressure readings without requiring energy storage components.

This project aims to investigate sustainable power sources for healthcare environments, with a focus on piezoelectric MEMS energy conversion technologies that harness mechanical energy from both

ambient body movements at implant sites and external power sources. Mechanical energy, derived from natural activities such as blood flow, limb movements, and heartbeats, as well as external energy inputs such as ultrasound, provides a viable source of power for devices such as blood pressure sensors, limb neuroprostheses, and cardiac pacemakers. There have been pioneering efforts explored the potential of internal energy conversion using flexible or vibrational harvesters, but the variability in frequency, amplitude, and other dynamic characteristics of body movements presents significant challenges to the efficiency of energy conversion. These challenges are by narrow bandwidths that limit operational frequency ranges and the risks associated with high bias voltages necessary for effective energy conversion. Additionally, for those devices that require invasive methods for placement, the complexities of surgical implantation procedures pose additional operational challenges. Addressing these challenges, this research commences with an exploration of the nonlinear mechanisms in piezoelectric energy harvesters based on classical MEMS structures, such as cantilevers, clamped-clamped beams, and membranes. These investigations, conducted under laboratory conditions, have demonstrated that nonlinear mechanisms can enhance bandwidth response, validating the feasibility of generating microwatts of power by harnessing mechanical energy from noisy and intermittent ambient vibrations.

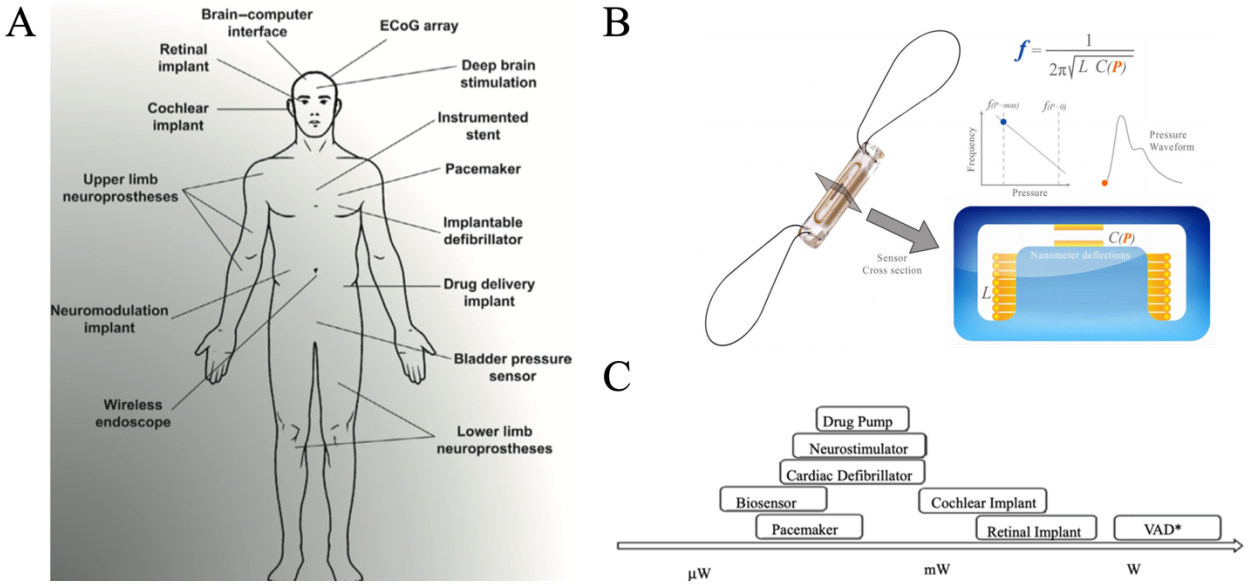

Figure 1. A: Overview of modern implantable medical devices, including various types such as brain-computer interfaces, cochlear implants, pacemakers, and neuromodulation devices. B: Illustration of the CardioMEMS HF System, a vascular pressure monitoring device developed by Abbott Inc., showing its design and operational principle. C: Power consumption ranges of critical medical devices,

highlighting that most devices operate primarily within the micro-watt (μW) to milli-watt (mW) range. © 2015 Elsevier B.V. Reprinted with permission from [1].

Despite MEMS harvester designs primarily targeting ambient energy sources characterized by broadband and low vibration frequencies, this project seeks to develop a comprehensive array of MEMS energy harvesting technologies that also explore extracorporeal energy sources for their long-term stability and safety. Furthermore, this research extends to developing high-frequency transducers targeting ultrasonic energy, a well-established and safe technology widely used in various medical applications including imaging and vital signs monitoring. Traditionally, ultrasound applications relied on bulky transducers operating at fixed frequencies. However, different ultrasound frequency bands offer unique advantages; for instance, lower frequencies typically provide deeper penetration due to reduced attenuation, while higher frequencies yield better resolution in imaging and communication. Leveraging MEMS technology and microfabrication capabilities, this study developed miniaturized micromachined ultrasonic transducers capable of operating across multiple frequencies simultaneously. This innovation not only enhances traditional energy harvesting capabilities but also enables new experimental setups for wireless power transfer, data telemetry, temperature monitoring, blood vessel expansion tracking, and photoacoustic imaging, significantly broadening the scope and application of energy conversion technologies in medical settings.

1.1 Vibrational Energy Harvester

In the realm of biomedical applications, internal energy harvesters are engineered to efficiently convert mechanical movement within human bodies into electrical power without compromising patient health. These devices employ Micro-Electro-Mechanical Systems (MEMS) transducers, categorized into four principal types based on operational principles: electrostatic, electromagnetic, triboelectric, and piezoelectric. Electrostatic transducers function using capacitor-like structures that generate charges from the relative motion between plates, allowing for adjustable power output and coupling efficiency through capacitance adjustment [2]. However, their dependency on an external power supply for capacitor polarization presents a significant drawback, particularly in the development of battery-less medical devices. Electromagnetic transducers operate based on Lenz's law, inducing electric currents through variations in external magnetic fields, yet they risk magnetic field interference, potentially affecting other biomedical devices. Triboelectric transducers leverage the triboelectric effect, where electrical charges are generated through contact and separation between

specific materials. The friction involved can cause wear and tear, diminishing the device's durability and efficacy in energy conversion—a limiting factor for their application in biomedical contexts. In contrast, piezoelectric transducers, generating electricity through mechanical stress applied to piezoelectric materials, do not require an external DC bias or magnetic field, making them highly suitable for energy harvesting applications. Recent research highlights the significant potential of piezoelectric harvesters for powering low-energy electronics, proving their capability and effectiveness in sustainable energy solutions within medical technology, as illustrated in Figure 2.

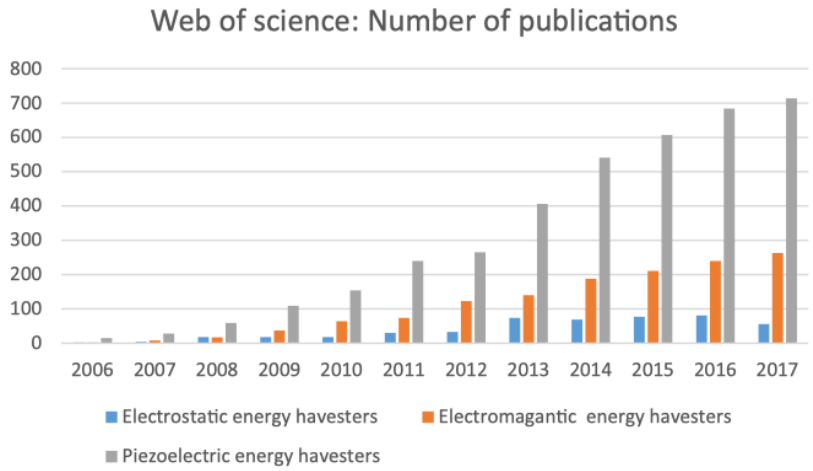

Figure 2. Growing research interests in energy harvesting field of study over recent decades. Among them, it highlights the rapidly increasing focus on piezoelectric energy harvesters, demonstrating a faster growth rate in its research interest compared to electrostatic and electromagnetic energy harvesters. © 2019 Elsevier B.V. Reprinted with permission from [3, 4].

The most effective method to induce large deformation in piezoelectric materials involves using flexible and stretchable structures that directly interact with kinetic energy sources like blood flow or muscle contractions. Dagdeviren et al. developed flexible energy harvesters for medical applications, employing conformable thin films encapsulating capacitor-type PZT ribbons within biocompatible coatings [5]. As illustrated in Figure 3. A, the PZT material is sandwiched between two electrodes, generating electric charges under periodic deformation. When applied to the outer surface of an animal heart, these muscle contractions and relaxations caused sufficient deformation to produce a power output of 0.18 $\mu W/cm^2$ per layer, and up to 1.2 $\mu W/cm^2$ with a five-layer stack, at a heart rate of approximately 1 Hz. This energy was effectively harnessed to power a cardiac pacemaker via a connected rectifier circuit. Similarly, Li et al. introduced a compressible piezoelectric energy harvester encapsulated within a capsular structure, as depicted in Figure 3. B [6]. This design utilized

two layers of PMN-PT piezoelectric materials, joined by a central PET sheet, allowing for bending under compression. Tested on the cardiac apex, where maximum single-axis deformation occurs, this device generated up to 33 μW power during cardiac cycles—sufficient to power a pacemaker without external batteries. Further exploring the potential of flexible designs, Dong et al. developed a stress-driven helical model using PVDF-TrFE, a polymer piezoelectric material shown in Figure 3. C [7]. This self-wrapping film was attached to the leads of implantable devices such as pacemakers or defibrillators, and its inherent elasticity enabled it to detect and convert heart motion into electric charges. By layering multiple strips of the active material, this harvester was capable of producing up to 2.1V, showcasing the practicality of such designs in medical applications.

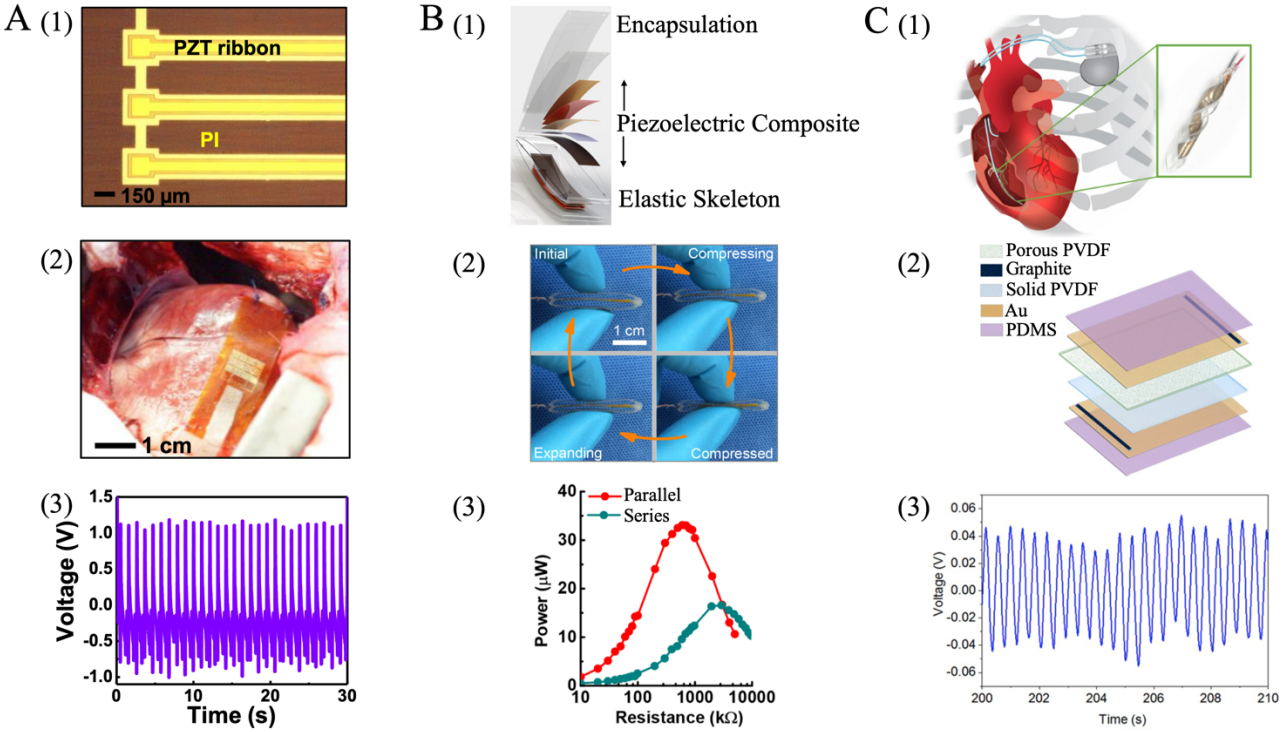

Figure 3. A (1)-(2): A PZT-conformal piezoelectric energy harvester designed to harness energy from muscle contractions during heartbeats, shown in experimental setup on a bovine heart; (3): Voltage output of the harvester attached to a bovine heart, demonstrating a peak voltage of up to 1 V. © 2014 National Academy of Sciences. Reprinted with permission from [5]. B (1)-(2): Schematic and operation of an alternative energy harvester that generates power by inducing mechanical stress from heart muscle movements; (3): Power output of the harvester, reaching up to 33 μW when optimized with an impedance-matched load. © 2019 American Chemical Society. Reprinted with permission from [6]. C (1)-(2): A spiral energy harvester integrated with a pacemaker lead, designed to convert kinetic energy from heart movements into electrical power; (3): Voltage output observed when the

spiral harvester is attached to the pacemaker lead. © 2019 John Wiley & Sons. Reprinted with permission from [7].

In addition to heart motion, there are some previous research studies investigating different energy sources across bodies. Those design utilizes flexible and stretchable structures to transform kinetic energy from organs or limb movements into electric power, for example bellow design for blood pressure and blood flow, wrapping-ring film for pulsation of ascending aorta, and PZT transducers for instrumented knee tibial tray and knee bearing [8-11]. However, despite its straightforward working principles, flexible energy harvesters have several limitations. For instance, implementing these harvesters, such as film on the heart or muscle surface, requires complex open-chest surgery and additional wires connecting harvester to the medical devices throughout the body. By doing so, it places patients' safety at risk and introduces uncertainties as to how the organ's normal activities are impacted. Given those physical limitations, researchers are now looking for alternative solutions to address energy conversion from those periodic and sustainable internal energy. Addressing these limitations, MEMS vibrational energy harvesters (VEH) is drawing increasing amount of attention as an off-grid energy solution targeting self-sustainable mechanic energy from ambient vibrations to electrical power for small biomedical implants. Comparing to flexible piezoelectric energy harvester, the VEH has its advantages in miniaturization, non-invasiveness, and excellent compatibility with CMOS (complementary metal oxide semiconductor) technology for ultimate system integration. For optimal power generation, a VEH needs to operate at its resonant frequency, at which the vibration amplitude is exponentially amplified. As shown in frequency spectrum in Figure 4, under biomedical applications where the frequency is much lower than typical for MEMS resonators, operation at frequencies < 100Hz is of interest.

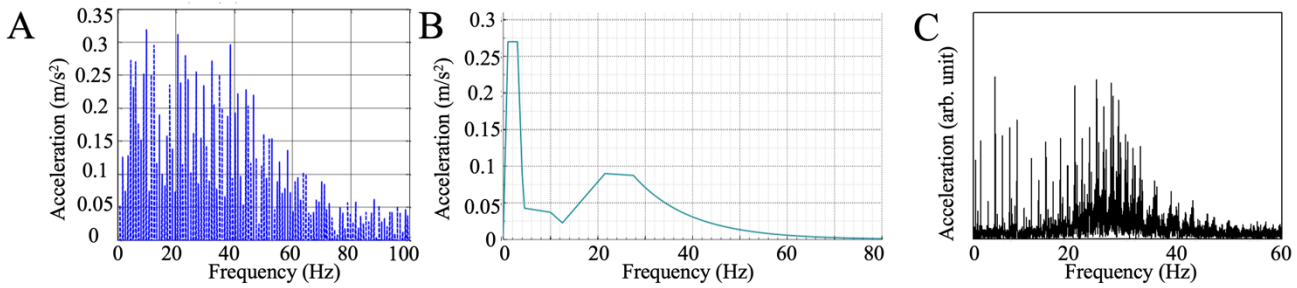

Figure 4. A-C: Frequency spectrum of acceleration signals from heartbeats, measured across different studies, showing a broadband and noisy frequency distribution below 100 Hz. A-B: © 2005 IEEE. Reprinted with permission from [12]. C: © 2018 SAGE Publications. Reprinted with permission from [13].

The resonant frequency equals the square root of effective stiffness over effective mass, meaning either reducing stiffness or improving effective mass could efficiently reduce the resonant frequency. Some previous researches have studied low-frequency harvesters from these two aspects. Jackson et al. conducted a research in using a cantilever structure with a proof mass to match its resonant frequency to the heartbeat [14]. The stiffness of a cantilever can be reduced through diminishing its thickness, and increasing the proof mass on the other hand can reduce the resonant frequency. The proposed structure comprises a cylinder cantilever beam with 450 nm AlN film on top of a 4.6 μm thick Si wafer, and total length is controlled within 8 mm long (tip to tip) and 4.8 mm wide (widest part). As shown in Figure 5. A, fabricated device has a resonant frequency at around 20-30 Hz and generated up to 3 μW peak power under 0.15g acceleration. While a modern leadless pacemaker consumes roughly 10 μW power, the proposed design validated the preliminary feasibility in extending the device's life span and significantly reduce the size of a battery. However, the device's narrow operational bandwidth and the physical bulk of the proof mass, which increases the risk of structural failure, highlight the need for designs that accommodate more dynamic operational conditions. Karami et al. took a step forward and designed a zigzag structure to further improve the output power based on cantilevers as shown in Figure 5. B [15]. The zigzag device is formed by 5 bimorph cantilevers, 2 cm long and 0.5 cm wide each, and each cantilever has two layers of PZT (0.19 mm thick) sandwiching a middle brass support layer (0.19 mm thick). Additionally, an 18.4 gr tungsten proof mass is included to further reduce the resonant frequency. By adjusting the number of cantilevers and size of each, the 1 cm^2 zigzag VEH achieves resonant frequency of 15.65 Hz and 63.34 Hz for its first and second modes. Under a normal heartbeat waveform, it could generate 13.15 μW average power, which is sufficient to maintain normal operation of a small cardiac device without needing a battery. Besides of adjusting dimensions, an alternative approach could also lead to resonant frequency reduction by applying axial force and buckled shape. A VEH prototype was proposed by Ansari et al. in Figure 5. C [13]. A bimorph beam of 2 cm by 0.25 cm with 5 gr platinum proof mass was clamped on both ends, and active PZT layers and brass substrate layer are 0.01 cm thick each. The in-plane axial force was then exerted from two clamped ends to induce buckling and in tun reduce effective stiffness, and its impact on resonant frequency is demonstrated in Figure 5. C(3). The analytical analysis revealed that a vertical buckling of 0.15 μm was sufficient to bring down the resonant frequency of the proposed clamped-clamped harvester to around 30 Hz. This adjustment in buckling significantly impacted the harvester's efficiency, yielding a power output of 10-15 μW, which could sustain the operation of implantable medical devices.

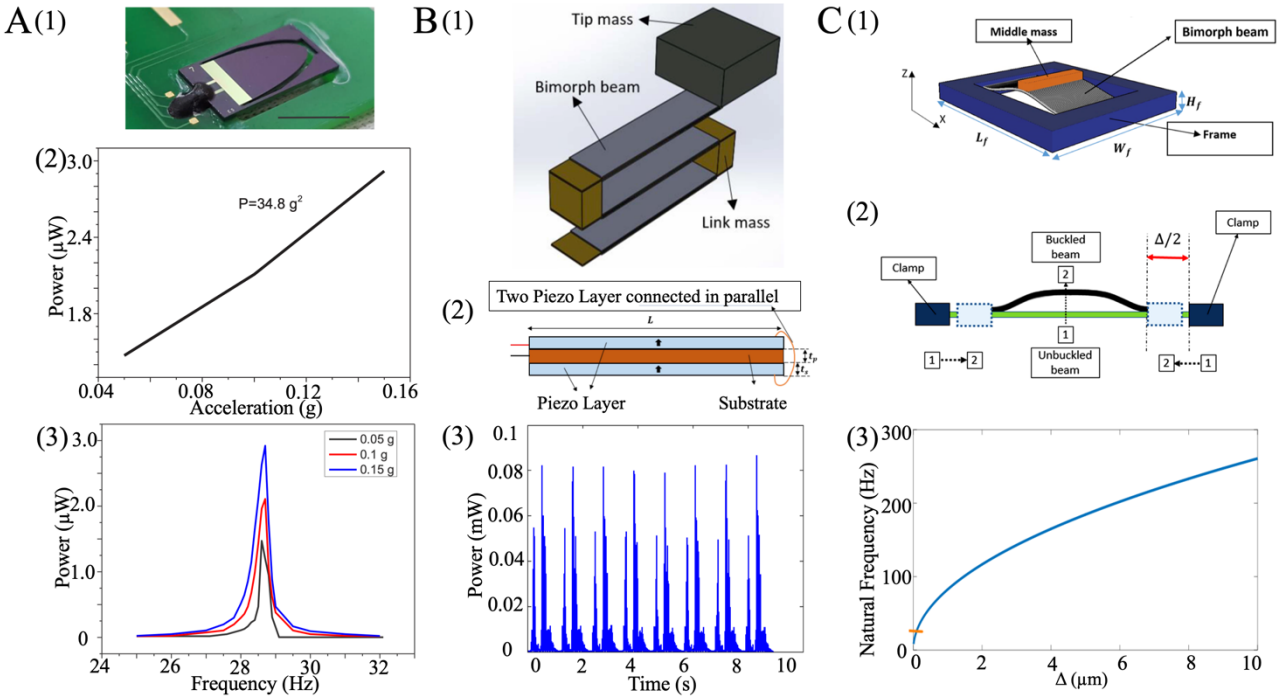

Figure 5. A (1): Cantilever energy harvester design incorporating a large proof mass to lower the resonant frequency to 28-29 Hz; (2)-(3): The power output and frequency response of harvester under varying acceleration. © 2018 SAGE Publications. Reprinted with permission from [13]. B (1)-(3): Folded energy harvester design with a double piezoelectric layer configuration, aimed at enhancing power output at low frequencies. © 2018 IEEE. Reprinted with permission from [14]. C (1)-(3): Buckled clamped-clamped beam energy harvester, demonstrating the impact of varying buckling levels on reducing the resonant frequency. © 2018 IOP Publishing. Reprinted with permission from [15].

While more and more smart structures are being proposed aimed at low-frequency operation, a critical issue is their adaptability for biomedical applications. The operational bandwidth of most vibrational energy harvesters (VEHs) spans only a few Hz. However, in a biomedical context, the central frequency of internal kinetic energy can vary significantly from one individual to another. For instance, heartbeat acceleration may differ by more than 30% between individuals and can shift substantially depending on various activities such as sitting, sleeping, or exercising. With such a narrow bandwidth, linear VEHs often operate off-resonance under these conditions, resulting in minimal power output. To address this, expanding a MEMS harvester's bandwidth typically involves introducing nonlinearity, achievable through both internal and external modifications. Certain structures, including clamped-clamped beams and membranes, inherently possess mechanical

nonlinearity. With precise excitation, they can exhibit a nonlinear Duffing response, which effectively broadens the bandwidth by bending the nonlinear resonant peak toward higher or lower frequencies. This phenomenon is illustrated in Figure 6. A, where the bandwidth expands significantly, creating additional usable regions as the harvester experiences jump-up or -down responses due to instability. For example, a clamped-clamped beam harvester operating in the Duffing nonlinear region demonstrates a power bandwidth that exceeds 50% of the arithmetic center frequency—marking a twofold improvement over the same device's 1% bandwidth when driven linearly [16]. To activate the Duffing nonlinearity, a specific amplitude threshold must be met, correlated with the system's linear stiffness divided by the square root of the quality factor [17]. The quality factor, inversely proportional to system damping, can be adjusted through methods such as vacuum packaging and material optimization. Nonetheless, typical nonlinear devices operate within the kHz range and necessitate high acceleration to trigger nonlinearity. This requirement poses a significant challenge for biomedical applications, where inherent vibrations are predominantly below 100 Hz, and the minimal acceleration amplitude can hardly reach the threshold necessary to induce nonlinearity.

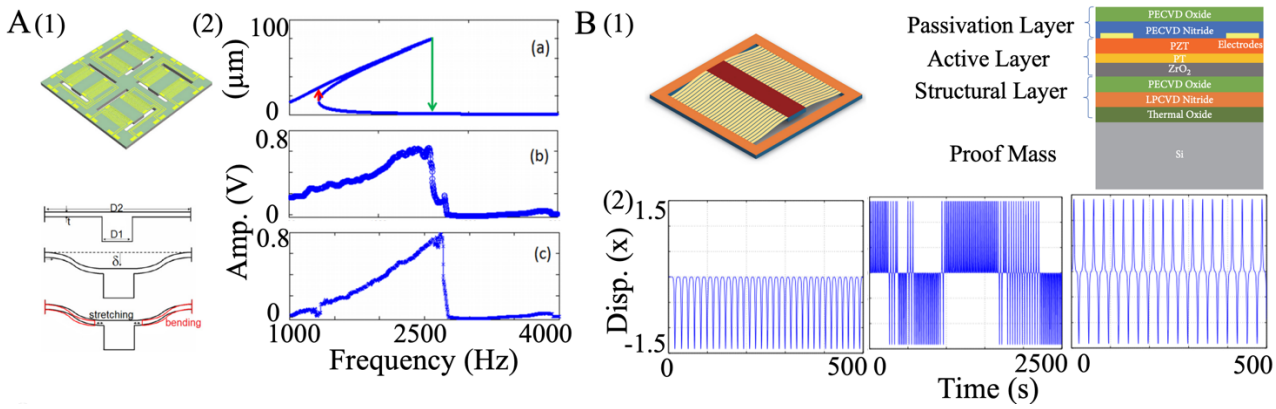

Figure 6. A: (1) Vibrational energy harvester utilizing a clamped-clamped beam structure; (2) The jump-down phenomenon resulting from Duffing nonlinearity, which enhances the bandwidth of the harvester. © 2011 American Institute of Physics. Reprinted with permission from [16]. B: (1) Bistable energy harvester featuring buckling induced by pre-stress between different material layers during fabrication; (2) Oscillation behavior of the central proof mass, illustrating intrawell oscillation before (left) and interwell oscillation after (middle and right) crossing the bistability threshold. © 2019 American Association for the Advancement of Science. Reprinted with permission from [18].

A multi-stable mechanism can enhance the oscillating displacement of a nonlinear harvester, activating its nonlinear behavior through external modification. A classical MEMS structure with a

monostable system typically has one stable equilibrium position at the minimum of a potential energy (U) curve, described by

$$U = \frac{1}{2}kx^2 \tag{1}$$

where k represents stiffness and x is the deflection. At this point, a device vibrates at its natural frequency, leading to significant displacement due to resonance. In contrast, a bistable oscillator features a double-well potential energy curve

$$U = \frac{1}{2}k_{linear}x^2 + \frac{1}{4}k_{nonlinear}x^4 \tag{2}$$

which results in two stable equilibria separated by an unstable equilibrium at the local maximum. Here, k_{linear} represents the stiffness in the linear term, quantifying the direct proportional response of the system to displacement. $k_{nonlinear}$, on the other hand, is the coefficient for the nonlinear stiffness term, which significantly influence the system's response under larger displacements, introducing additional stability points. Bistability can be induced by external forces, but common methods involving magnets are unsuitable for biomedical applications due to MRI compatibility issues. An alternative is targeted beam buckling to achieve bistability. Hajtati et al. explored this by using a buckled beam in a low-frequency and low-amplitude energy harvester in Figure 6. B [18]. They calculated that clamped-clamped beams buckle due to residual stresses from microfabrication. Post-buckling, the beam maintains two symmetric stable positions above and below its original horizontal orientation. Under minor acceleration, the harvester remains near one equilibrium (intrawell oscillations), limiting effective power output. However, sufficient kinetic energy allows it to oscillate between both stable positions, thus amplifying deflection and broadening bandwidth. Research on tuning nonlinear threshold amplitudes and multi-stability in MEMS oscillators is expanding, with new studies exploring dynamic magnification by adding degrees of freedom to nonlinear systems, particularly in low-frequency environments. All mechanical systems inherently possess multiple degrees of freedom or vibrational modes. With an appropriate design, leveraging nonlinear interactions and mode coupling can facilitate internal energy transfer from a lower to a higher mode, potentially enabling efficient energy harvesting from low-frequency and noisy excitations. This phenomenon, known as auto-parametric resonance or internal resonance, has been observed but remains underexplored in energy harvesting contexts [19].

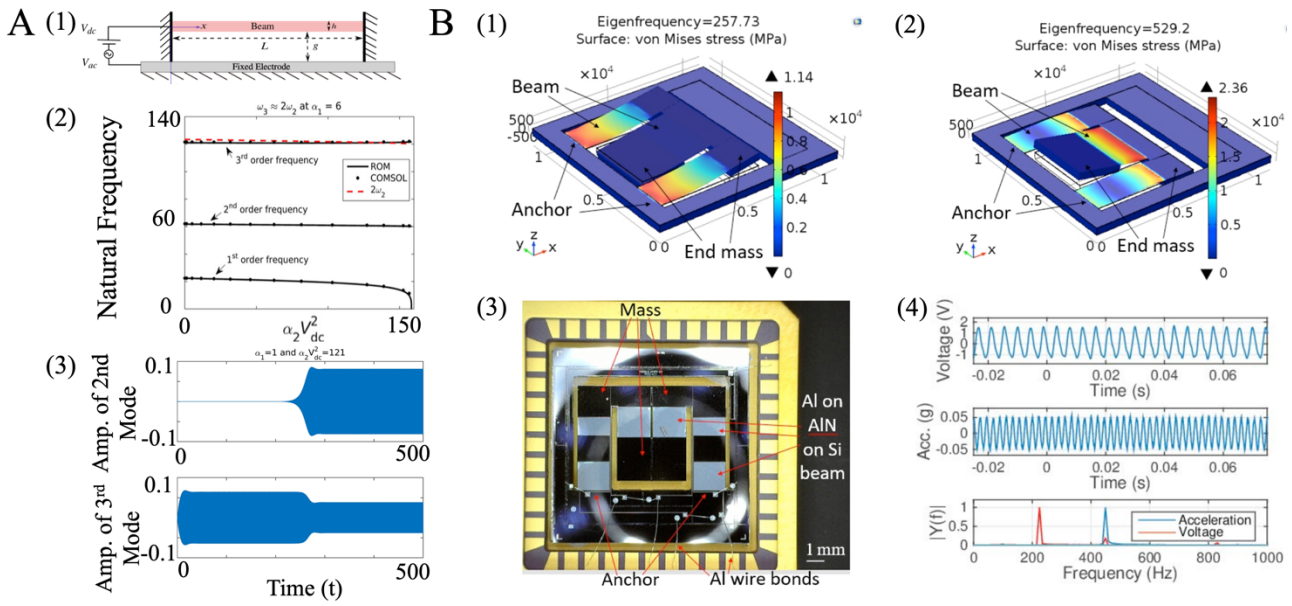

Figure 7. A (1)-(2): Illustration of a clamped-clamped beam harvester demonstrating coupled second and third modal frequencies and auto-parametric resonance; (3) Time-domain representation of auto-parametric resonance, observed around 250 seconds, showing energy transfer from the third mode to the second mode. © 2020 Springer Publishing. Reprinted with permission from [20]. B (1)-(3): Schematic and simulation of a coupled cantilever harvester exhibiting mechanical responses due to two-mode auto-parametric resonance; (4) Combined time- and frequency-domain responses, highlighting the simultaneous excitation of two modes under a single-frequency drive. © 2018 IEEE. Reprinted with permission from [21].

Kumar et al. investigated mode coupling and energy transfer in a clamped-clamped beam resonator exhibiting commensurate modal frequencies [20]. They noted nonlinear modal coupling when the second and third modes exhibited a modal frequency ratio of two. When the third mode of the clamped-clamped beam resonator was electrically driven, it accumulated energy until reaching a threshold where internal resonance triggered energy transfer to the second mode. As illustrated in Figure 7. A, at approximately 250 seconds, the energy began to transition from the third to the second mode, with both modes simultaneously excited. Building on these findings, Jia et al. from our research team applied this phenomenon to energy harvesting, designing a coupled vibrational energy harvester based on dual cantilever structures [21, 22]. This VEH exhibited two modal frequencies close to a 2:1 ratio, specifically 257 Hz and 529 Hz. During tests on a shaker set to 529 Hz, the output voltage predominantly concentrated around 257 Hz, demonstrating energy transfer through internal resonance. This nonlinear coupling mechanism facilitates energy transfer between multiple modes within a single

device, leading us to develop a scalable energy harvester inspired by the frequency comb concept, previously explored in MEMS resonators but not yet applied to energy harvesters. Utilizing nonlinear signal mixing across various modes, the frequency comb energy harvester is designed to efficiently capture energy from the broadband and noisy vibrational inputs typical in biomedical settings, addressing the common efficiency limitations of existing vibrational energy harvesters.

1.2 Micromachined Ultrasonic Transducer

Besides harvesting energy from internal organ and body movements, the conversion of energy from external power sources is increasingly recognized for its sustainability, stability, and long-term safety. Wireless telemetry and power transfer effectively utilizes remote energy sources to transmit power, deliver operational commands, and establish communication links, with controlled losses during propagation through tissue. Common energy sources for wireless telemetry include radio frequency (RF) electric fields, acoustic pressure waves, and near-infrared (NIR) light. NIR can transmit photovoltaic power through skin, and studies have successfully powered devices like cardiac pacemakers using this method [23, 24]. However, unlike RF and ultrasound, NIR cannot support data communication along with power transfer. Its efficacy may also vary based on skin tone, fat thickness, and any potential obstructions at the implant site. At present, inductive power transfer, using RF in the near-field region, is the predominant method for implantable medical electronics (IMEs). This technique requires an implanted receiver (coils) and an external transmitter, with power efficiency dependent on the electric field intensity and receiver design. Due to the high impedance of body tissues like fat and skin against the electric field, the intensity must be maintained within a safe threshold (10 mW/cm^2) to avoid mechanical damage and thermal injury. In brief, physics limits the efficiency of an RF receiver due to long wavelength of RF energy and high degree of energy absorption by tissue. In contrast, acoustic power transfer, particularly through ultrasound, has shown superior performance. Ultrasound enables deeper penetration and higher power efficiency with miniaturized transducers, significantly smaller than inductive coils [25, 26].

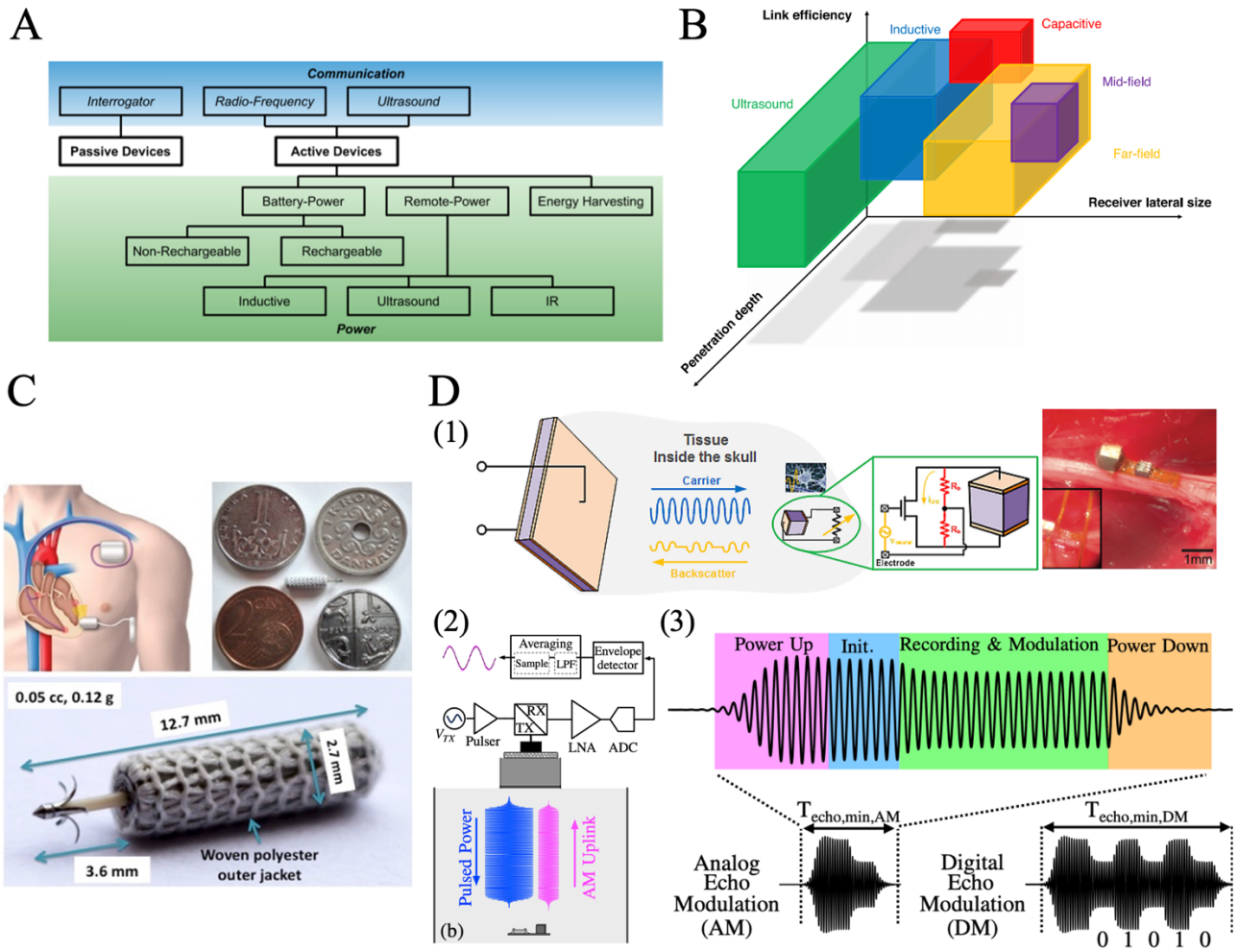

Figure 8. A: Overview of wireless power telemetry and power transfer topologies, highlighting essential functions and components. B: Comparative analysis of ultrasound, inductive, and capacitive power transfer methods, focusing on penetration depth, device size, and link efficiency. © 2020 IEEE. Reprinted with permission from [25]. C: A miniaturized, FDA-approved cardiac pacemaker powered by ultrasound, demonstrating a 70% reduction in size compared to conventional designs. © 2013 Oxford University Press. Reprinted with permission from [27]. D: (1) Schematic of an ultrasound-based system for neural recording modulation. (2)-(3) Illustration of simultaneous data communication using a backscattering and pulse-echo mechanism. © 2020 IEEE. Reprinted with permission from [28].

Because body tissues exhibit lower impedance against ultrasound waves compared to electromagnetic signals, a higher intensity threshold (720 mW/cm²) is allowed, making ultrasound a common and safe tool in medical imaging and treatment. A significant early application of ultrasound for wireless power transfer (WPT) was conducted by Auricchio et al., who implemented the first-in-man ultrasound-powered leadless pacemaker [27]. This pacemaker without any energy storage unit is

powered solely by piezoelectric transducers. Its volume of 0.05cc represents a 95% reduction compared to traditional leadless pacemakers, typically between 0.8-1cc. Subsequent clinical trials confirmed its long-term safety, leading to FDA approval in 2019. Another research in ultrasound power transfer took a step forward. Further research by Seo et al. advanced ultrasound power transfer by employing pulse-echo characteristics for simultaneous uplink data transmission [29]. Their harvester design included two electrodes sandwiching a bulk piezoelectric crystal with a thickness set to half the wavelength of the ultrasound signal, thus inducing maximal internal stress and optimizing energy transfer efficiency. The uplink communication protocol and feedback mechanism in the receiver modulates the vibration of the piezoelectric crystal, altering the reflected ultrasonic intensity, which is decoded using synchronized code multiplication and averaging. The dimensions of Seo et al.'s ultrasound transducer are notably compact, measuring 750 μm × 750 μm × 750 μm, with the entire device including IC components measuring 3800×8400 μm. At a 1.85 MHz operating frequency, the transducer produces a 0.12mW power output and transmits an effective 9 bits of data per echo.

Ultrasound WPT has demonstrated excellent power performance and communication capabilities. Future researches are necessary in improving its efficiency, long-term reliability, and compatibility with implantable medical electronics (IMEs). Despite the efficiency of ultrasound transducers with a piezoelectric block, their relatively large volume challenges integration into next-generation integrated circuits. The significant ongoing reduction in circuit dimensions and power requirements has led to focused research into onboard power sources, with CMOS (complementary metal oxide semiconductor) compatibility becoming a critical factor in evaluating the adaptability of electronic components. While power management and communication circuits can be fabricated using CMOS technology, the CMOS compatibility of ultrasound transducers increasingly influences the overall device's integrity, cost, and efficiency [30]. Traditional bulky PZT transducers contain lead, which restricts their use in CMOS facilities, posing significant limitations on biocompatibility, mass production, and reliability. At the same time, the development of PMUTs (piezoelectric micromachined ultrasonic transducers) have been rapid in recent years. PMUTs typically feature a piezoelectric membrane—circular, square, or rectangular—designed to resonate with the ultrasound source for maximum power efficiency. Low-temperature sputtered CMOS-compatible piezoelectric materials like AlN offer better acoustic coupling, reduced manufacturing costs, and lower power consumption. Some existing research by Lu et al. and Wang et al. on circular AlN PMUTs with diameters of 25 μm and 50 μm, resonating at frequencies of 25 MHz and 17.5 MHz respectively, has

highlighted their potential in biomedical imaging applications [31-33]. These PMUTs shown in Figure 9. A-B, tested as transmitters, exhibit impressive efficiencies and sensitivities. Lu et al.'s 7x7 array design achieved 0.7 kPa/V, and Wang et al.'s 1261-element phased array reached a sensitivity of 9 kPa/V at their fundamental resonant modes respectively.

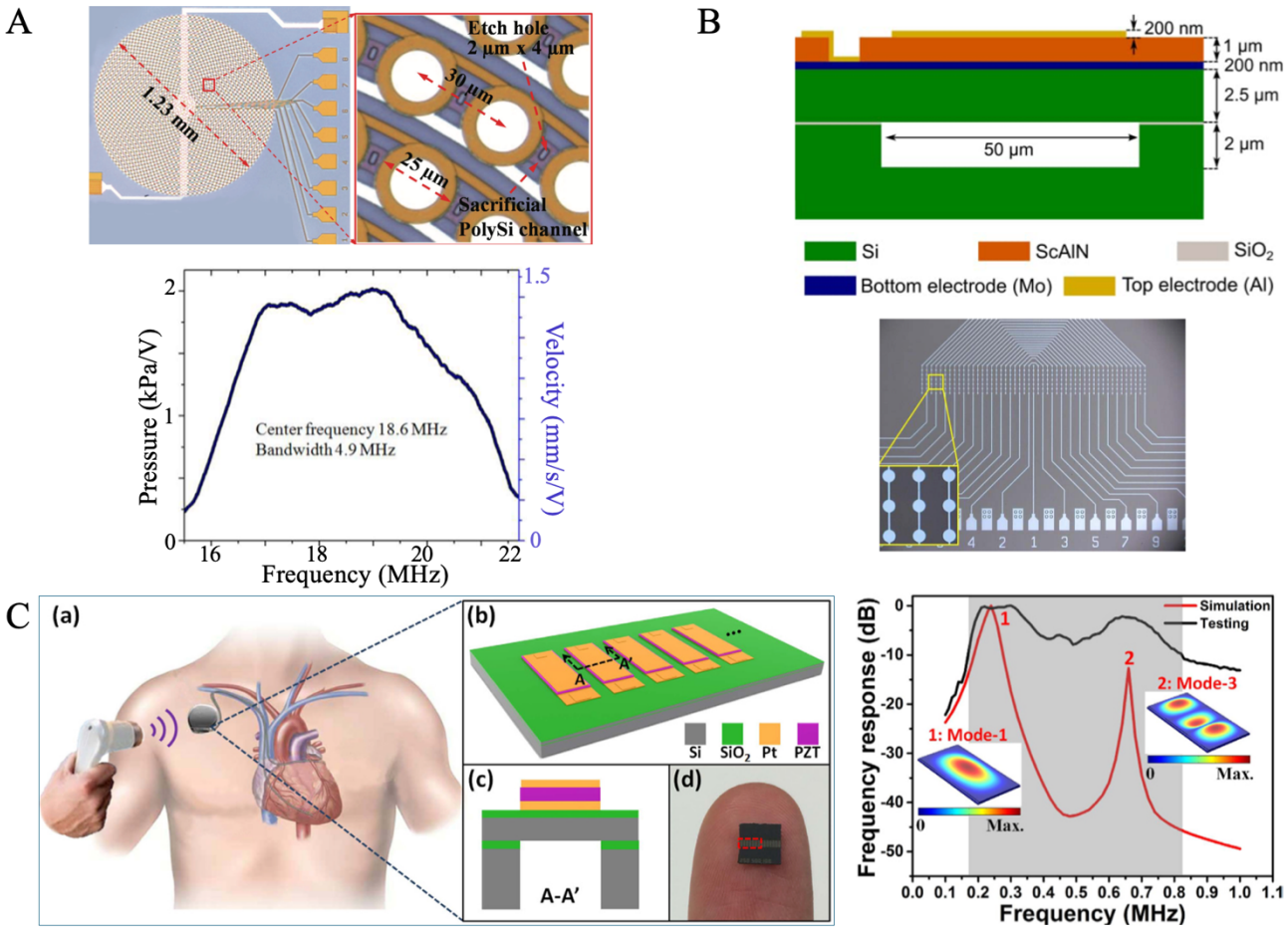

Figure 9. A: A 1261-PMUTs array design features enhanced bandwidth performance. © 2017 IEEE. Reprinted with permission from [32]. B: PMUT array utilizing advanced ScAlN material, designed for optimized electromechanical efficiency and improved acoustic characteristics. © 2015 IEEE. Reprinted with permission from [34]. C: Broadband PMUT configuration employing induced mode overlap to achieve extended bandwidth. © 2020 Nature Publishing Group. Reprinted with permission from [35].

While high-frequency ultrasound targets biomedical imaging for higher resolution, there're also attempts in reducing the ultrasound frequency to achieve less attenuation and deeper penetration for wireless power transfer application. Shi et al. developed a piezoelectric micromachined ultrasonic

transducer for medical implants that operates in the kHz range by tuning the resonant frequency of various modes [35]. This adjustment involved adjusting the length-to-width ratio of a rectangular membrane, as illustrated in Figure 9. C. The design overlaps the first and third modes on a membrane measuring 500 μm by 250 μm, substantially expanding the PMUT's bandwidth. This setup achieved a -6dB bandwidth of 73.7% at the first mode at 285kHz and 30.8% at the third mode at 650kHz. The -10dB bandwidth extended from 170kHz to 820kHz. When testing under aquatic environment at its first mode, the PMUT produced a power output of 3.75 μW/cm², roughly 90 nW under a 1mW/cm² ultrasound intensity—well below the FDA's safe limit of 720mW/cm². At an intensity of 700 mW/cm², the PMUT could deliver at least 59 μW, sufficient for powering most implantable medical devices. These encouraging outcomes illustrate the potential of PZT-based PMUTs, which hold potential for further enhancements in chip integrity and manufacturing efficiency by integrating CMOS-compatible materials. Although materials like AlN, ZnO, or PVDF polymers typically show lower coupling coefficients than PZT, they offer potential benefits in terms of acoustic coupling, reduced manufacturing costs, and lower energy consumption. To compensate for their generally lower coupling coefficients comparing to PZT, further research is required to explore improvements through advanced PMUT structure and electrode designs, along with acoustic and electrical impedance matching techniques, and more efficient power management integrated circuits (ICs) [36].

Additionally, existing research often involves balancing trade-offs by designing PMUTs to operate at fixed frequencies for specific applications, thereby limiting the exploration of ultrasound's full frequency spectrum where both low- and high-frequency ultrasound exhibit distinctive operational advantages. Meanwhile, the emerging interest in MEMS resonator research demonstrates the potential of micromachined devices to operate beyond their fundamental mode, thereby enhancing measurement accuracy and sensitivity. This capability is particularly promising for ultrasound applications, which could significantly improve PMUTs' performance across various applications. In this context, our study introduces a potential strategy for simultaneously activating a PMUT across multiple modes at diverse frequencies. By assigning specific measurement targets to designated resonant modes, it is possible to leverage both low- and high-frequency ultrasound within a single device, potentially enhancing overall system integrity and efficiency which is crucial for implantable medical electronics. The advances in MEMS technology and microfabrication capabilities are paving the way for the design of compact, multifunctional devices on a chip scale. By meticulously analyzing and simulating the mechanical and frequency responses of a miniaturized PMUT array, combined with the design of customized electrode patterns, we aim to develop an efficient transducer that

operates across various modes and frequencies simultaneously. This approach aims to extend application possibilities and achieve significant improvements in the utility and effectiveness of ultrasound-based systems.

1.3 Conclusion

This chapter provides an overview of existing research on MEMS transducers that target internal body movements and external energy sources. By evaluating these studies' innovations and limitations, this research seeks to overcome existing challenges and bridge the gap between the practical needs of applications and the development of new transducers with enhanced performance. Based on their unique operational principles and the specific energy sources they target, MEMS transducers investigated in this study are categorized into two primary types: vibrational energy harvesters and piezoelectric micromachined ultrasound transducers (PMUTs).

In Chapter 2, we explore the common numerical and analytical methods applied in studying these transducers, detailing the techniques used to assess their performance and functionality. Following this, Chapter 3 delves into the fundamental theories of nonlinear mechanisms and frequency comb phenomena. This section focuses on the critical relationships between energy conversion efficiency and external drive conditions. Drawing from these insights, a new energy harvesting prototype utilizing the frequency comb concept is introduced and tested in response to the challenge of achieving efficient energy capture from broadband and variable vibrational sources, particularly prevalent in biomedical applications. Chapter 4 expands on the fundamental theory and numerical analysis specific to PMUTs. This model is specifically designed to analyze the mechanical and acoustic performance of PMUTs operating under multiple resonant modes simultaneously, facilitating an optimized balance between structural design and performance metrics. Following this, Chapter 5 details the design of three multi-mode PMUT prototypes, followed by an evaluation of their mechanical and frequency responses. The potential of these prototypes is further examined through their application in dual-function wireless power transfer and data telemetry, demonstrating promising results in establishing a dual-frequency link between paired PMUT chips. In Chapter 6, a alternative design strategy for a multi-frequency PMUT array is presented and validated. This strategy involves a high-density PMUT array with transducers varying in design and operational frequencies, customized for simultaneous temperature monitoring, vessel motion tracking, and photoacoustic imaging. The successful application of this multi-frequency array not only underscores the feasibility

of improved bandwidth and sensitivity but also demonstrates enhanced performance in practical settings.

The final chapter, Chapter 7, summarizes the energy transducers developed throughout this research, emphasizing their unique design strategies and performance metrics. These innovative designs bridge the gap between theoretical energy conversion mechanisms and practical biomedical applications, setting the stage for future research aimed at enhancing the performance of piezoelectric energy transducers to better meet the specific needs of biomedical contexts.

Chapter 2

Theory and Methods

In this thesis, the piezoelectric effect is employed to transform mechanical stress into electrical charge. This process for energy-conversion devices described in this thesis can be schematically broken down into various phases of energy transformation, as illustrated in Figure 10 [37]. For example, in an energy harvester, the transducer converts ambient mechanical excitation (typically below 100 Hz), into periodic mechanical oscillations of the device. There is always some energy dissipation associated due to both internal and external sources. For example, external damping can arise due to fluid induced dissipation (for instance air drag) depending on the environment that the device is operated in. For ultrasonic transducers, oscillations in a micromachined membrane result from a coupled response to periodic acoustic pressure variations, with operational frequencies generally above 100 kHz. At such frequencies, acoustic impedance mismatches between the transducer and its surrounding medium can cause significant energy losses, necessitating careful design to minimize these losses. The next phase converts the induced mechanical vibrations in the transducers into an alternating current (AC) electrical signal via the piezoelectric effect. Designing highly efficient transducers at this stage is crucial; considerations include ensuring ambient frequency adaptability, material compatibility, and maximizing energy transformation efficiency. These design criteria are crucial for optimizing the effectiveness of both internal vibrational energy conversion and ultrasound power conversion mechanisms, ensuring optimal performance across a range of applications. The final phase occurs within the electrical domain, involving the implementation of a front-end interface that may include matching networks, rectifying circuits, and power management systems to regulate and manage the converted electrical power. In this project, we adopted a straightforward impedance-matching approach to evaluate the actual power conversion efficiency against an ideal load.

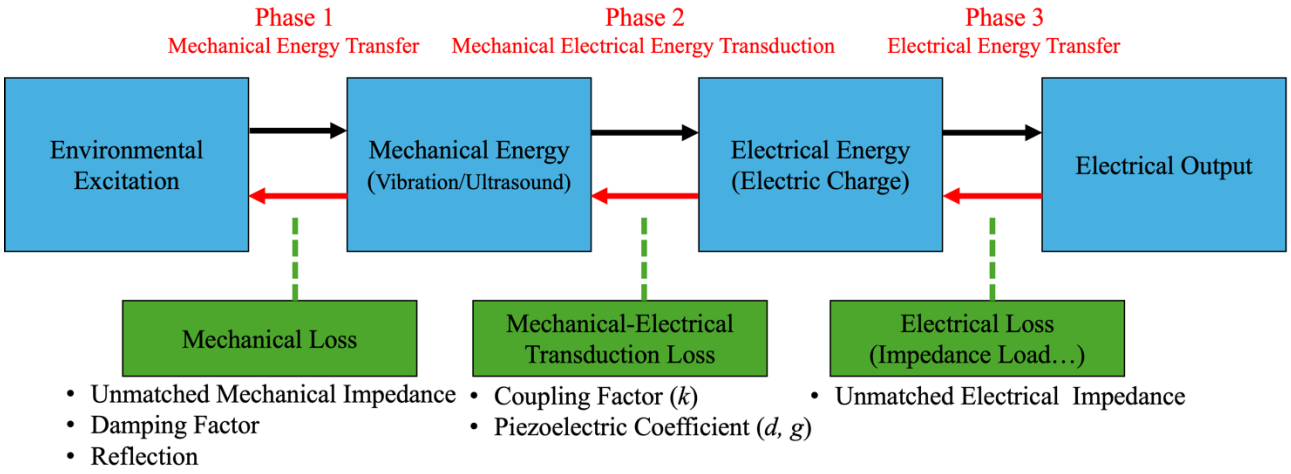

Figure 10. Design considerations and flowcharts for MEMS energy transducers.

This research primarily focuses on the first two phases, aiming to develop high-efficiency piezoelectric transducers that address existing limitations in both internal vibration energy harvesters and ultrasonic transducers. This targeted development is intended to advance the efficiency and application scope of these devices. In this chapter, we explore the fundamental working principles of piezoelectric transducers, emphasizing critical factors such as material selection, polarization direction, and operation mode. These factors play pivotal roles in determining the performance of piezoelectric vibrational energy harvesters (VEH) and micromachined ultrasound transducers (PMUT). The operation of these MEMS devices spans multiple domains: VEH operates within the electrical and mechanical domains, while PMUT interacts across the electrical, mechanical, and acoustic domains. To navigate the complexities and understand the structural merits essential for device design, three numerical analysis methods were examined: the lumped model, distributed parameter electromechanically coupled analysis, and the Rayleigh-Ritz method. Each method offers distinct advantages for understanding device mechanisms and estimating performance prior to the device design. Complementing these numerical methods, Finite Element Analysis (FEA) provides deeper insights through the simulation of various structural designs. FEA is particularly beneficial in this research for its ability to model complex geometries and materials, which allows for detailed stress and vibration analysis under real-world conditions. This approach enables precise predictions of device behavior under various operational conditions, thereby optimizing the design process. In this research, COMSOL Multiphysics software is utilized to simulate and analyze the performance of the proposed designs.

2.1 Piezoelectricity

The piezoelectric effect was first demonstrated by Pierre Curie and Jacques Curie in 1880. This phenomenon exhibits a unique coupling between mechanical stress and electric fields. In vibrational energy harvesters and PMUTs (Piezoelectric Micromachined Ultrasonic Transducers), when there is environmental excitation, the mechanical deformation induces stress across the piezoelectric material, generating an electric field due to the electromechanical coupling effect. This electric field, in turn, drives charge displacement and can be converted into usable electrical power via electrodes. The direct piezoelectric effect is mathematically represented by the constitutive equation:

$$\begin{bmatrix} S \\ D \end{bmatrix} = \begin{bmatrix} s^E & d^t \\ d & \varepsilon^T \end{bmatrix} \begin{bmatrix} T \\ E \end{bmatrix} \tag{3}$$

Here, S and T denote strain and stress, respectively—both described as second-order tensors that represent mechanical properties. D and E are the electric displacement and electric field in the electrical domain. The tensors s^E, representing elastic compliance at constant electric field, and ε^T, indicating permittivity at constant stress, depict how the piezoelectric material's mechanical and electrical properties interact under various conditions. d, the piezoelectric stress constant, transforms mechanical stress into electric displacement, while its transpose, d^t, links electric field changes to mechanical strain modifications. Rearranging the equations yields:

$$S = s^E T + d^t E \tag{4}$$

$$D = dT + \varepsilon^T E \tag{5}$$

Equation (1) indicates that strain in a piezoelectric material result from both the applied mechanical stress and the external electric field. Similarly, Equation (2) reveals that electric displacement is a product of both applied stress and ambient electric fields, showing how mechanical and electrical properties influence each other. To maximize transformation efficiency, piezoelectric materials have been extensively researched for high transformation efficiency. Two crucial parameters to evaluate a material's piezoelectric properties are the piezoelectric charge constant d_{ij} and electromechanical coupling coefficient k_{ij}.

$$d_{ij} = \frac{short\ circuit\ charge\ density}{applied\ mechanical\ stress}; C\ N^{-1}$$

$$k_{ij}{}^2 = \frac{Electrical\ Energy\ Stored}{Input\ Mechanical\ Energy} = \frac{d_{ij}{}^2 E}{\varepsilon^T};$$

Where d_{ij} represents the material's figure of merit and k_{ij} describes the energy conversion efficiency. The indices *i* and *j* correspond to the directions of induced polarization and stress, respectively, within the material's crystallographic system. The direction of d_{ij} indexes of constants in rectangular crystallographic system is given in Figure 11. A, showing the anisotropic nature of piezoelectric materials and their response to external forces. The principal properties along X, Y and Z axes are denoted as 1, 2 and 3 directions [38]. The poling process plays a vital role in maximizing these piezoelectric properties. During fabrication, a strong electric field is applied to the material at high temperatures to align the dipolar molecules along a preferred direction, typically the 3-axis. This alignment enhances the material's responsiveness to mechanical stresses, thereby facilitating the use of different operational modes. In the 31-mode, electric charges are induced perpendicular to the poling direction when subjected to mechanical stress, making it suitable for applications where stress is applied laterally. Conversely, in the 33-mode, charges are induced parallel to the poling direction, optimal for applications involving longitudinal stress. These modes are essential in selecting materials for specific applications due to their differing efficiencies in converting mechanical energy to electrical energy.

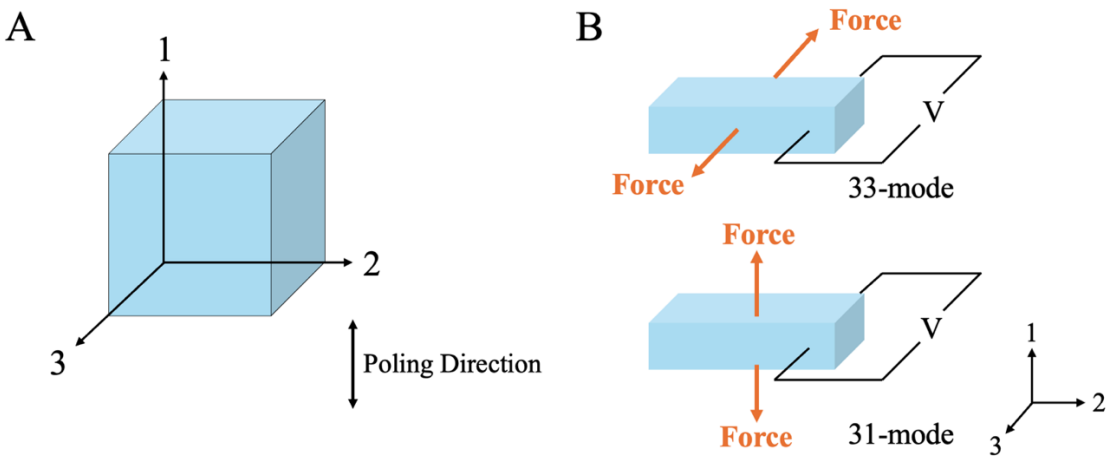

Figure 11. A: The poling direction in a crystal material, showing 33- and 31- modes in B (up) and B(bottom) respectively, which refer to electric charges induced parallel and perpendicular to the applied strain direction, respectively. These modes are pivotal in selecting materials for specific

applications due to their differing efficiencies. © 2019 De Gruyter. Reprinted with permission from [38].

Table 1. Electromechanical and piezoelectric properties for popular piezoelectric materials [16].

Property	PZT5H	PZT5A	$BaTiO_3$	PVDF	**AlN**
d_{33} (10^{-12} C/N)	593	374	149	33	5.5
d_{31} (10^{-12} C/N)	274	171	78	23	3
g_{33} (10^{-13} m/N)	19.7	24.8	14.1	330	69
g_{31} (10^{-13} m/N)	9.1	11.4	5	216	37.6
k_{33}	0.75	0.71	0.48	0.15	0.33
k_{31}	0.39	0.31	0.21	0.07	0.18
Relative Permittivity (ε_0)	3400	1700	1700	12	9

Although the 33-mode generally yields superior energy conversion efficiency, its application in thin-film microstructures can be challenging due to the complexities in microfabrication and the potential for high electrical resistance caused by small cross-sectional areas between electrodes. Importantly, while a material's intrinsic electromechanical coupling properties are essential, they contribute only a part of the overall power output. Several studies have demonstrated that considerations such as electrode configuration and structural design play a much more significant role in enhancing overall energy transduction efficiency [39]. Therefore, despite the higher theoretical efficiency of 33-mode, 31-mode is favored in practical applications due to its simpler electrode design and more accessible fabrication process.

For material choice, while piezoelectric ceramics such as lead zirconate titanate (PZT-5A and PZT-5H) offer high energy conversion efficiencies ($k_{31}^2 \simeq 20\%$), their compatibility with silicon substrates is limited. The ease of integrating piezoelectric materials into a fabrication sequence becomes crucial, especially as CMOS-compatible materials such as aluminum nitride (AlN), zinc oxide (ZnO), and polymers are increasingly favored for on-chip integration. Notably, PZT contains lead, which could pose toxicity risks in biomedical applications, making it less desirable. Consequently, AlN, with its relatively high coupling coefficient and accessible microfabrication profile, is selected for this project. The PiezoMUMPs process—a common micromachining fabrication technique for piezoelectric devices—will be used as the standard procedure for energy harvesters and PMUTs. The fabrication of MEMS transducers in this study utilizes the commercially available PiezoMUMPs process provided by MEMSCAP. This process involves depositing a thin film of AlN (0.5 μm) by reactive sputtering onto a Silicon on Insulator (SOI) device layer, available in thicknesses of 10 μm or 25 μm.

From top to bottom, the structural layer comprises the top metal electrode, AlN, doped silicon, insulation oxide layer, and silicon substrate.

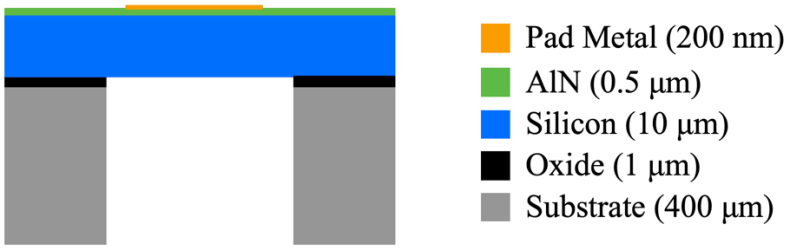

Figure 12. Cross sectional view of PiezoMUMPs fabricated device.

Figure 12 provides a cross-sectional view of a PiezoMUMPs fabricated device, detailing the layer arrangement from the top metal electrode down to the silicon substrate. The metal electrode layer, typically comprising 20 nm of chromium and either 1000 nm of aluminum or 500 nm of gold, covers the AlN piezoelectric layer. Beneath the AlN, doped silicon serves as the bottom electrode, with an additional metal pad often needed to extend electric charge movement into the circuit. The silicon oxide layer serves as an insulator connected to the bulk silicon substrate, which acts as an anchor. Depending on the design requirements, this substrate can be patterned as a suspending proof mass to adjust the resonant frequency.

2.2 Electric Domain and Power Management

Once the transducer harvested and transformed mechanical energy into electrical charge displacement, the last phase of energy conversion converts this to usable AC or DC power. In electronics, impedance matching is a practice in maximizing power transfer efficiency according to power-transfer theorem. It requires the impedance from the electrical load to be matched to the input source, or the piezoelectric transducer in our case. In this research, while standard impedance matching technique is utilized to evaluate the power performance of developed MEMS transducers, it's necessary to introduce and highlight the advanced power management techniques to further improve the power performance in electric domain. Due to electromechanical coupling between mechanical and electrical domains, the backward coupling from electric domain induces an anti-resonance at a characteristic frequency. A piezoelectric transducer holds minimum and maximum impedance at resonant and anti-resonant frequencies correspondingly. Even though total power from both frequencies are same, one can choose to achieve max current or max voltage at resonant and anti-resonant frequencies, which is important for certain applications such as PMUT power management

circuits where frequency selection is viable and impedance matching plays critical role. The ratio to link resonant frequency to anti-resonant frequency is k_e, which is defined as

$$k_e^2 = \frac{\omega_{ar}^2 - \omega_r^2}{\omega_{ar}^2} \approx \frac{{k_{ij}}^2}{1+{k_{ij}}^2} \text{ (neglecting inactive structural layer)} \quad (6)$$

Since most devices are powered by a DC source, the periodic AC voltage from transducers needs to be rectified before charging a capacitor or directly powering a medical device. In Figure 13. A shows a standard full-wave bridge rectifier circuit, at which four diodes are integrated to flip the sign of negative AC signal. In such a way, voltage across transducer V_{PZ} does not flow into output and charge capacitor C_s until it surpasses the sum of output capacitor voltage V_S and voltage drop of two diodes $2V_D$, and during that period (shaded area in Figure 13. A), more than half of energy might get lost.

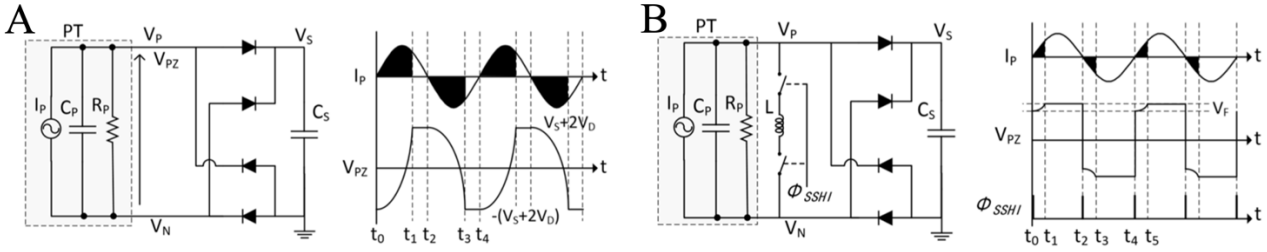

Figure 13. A: A standard full-bridge rectifier with shaded area indicating power loss during transduction. B: A SSHI circuit with synchronized inductors controlled by an analog gate and reduced shaded area showing efficiency improvement. © 2019 IEEE. Reprinted with permission from [36].

To improve power extraction efficiency, a nonlinear technique SSHI (synchronized switch harvesting on inductor) was developed by Guyomar et al. [12, 40]. An SSHI interface comprises parallelly connected inductors, which are controlled by analog switches based on synchronous pulse signal θ_{SSHI}. Thus, every time inductors connected as I_p changes polarity, the inductor creates a resonant RLC loop with transducer, allowing a natural inversion of voltage across electrode capacitor V_{PZ}. While this method significantly reduces wasted energy (shaded area in Figure 13. B) and enhances power efficiency, the physical size of the inductors required—typically in the millihenry range—presents considerable challenges for device miniaturization and integration within compact systems.

In contrast, the SSHC technique utilizes external capacitors to achieve similar voltage inversion but with a more compact and efficient design. Capacitors, unlike inductors, offer faster response times and require less physical space, making them more suitable for integration into

microelectromechanical systems. Moreover, capacitors do not suffer from the energy losses typically associated with the magnetic fields in inductors, leading to more efficient energy transfer and reduced power dissipation. By transferring charge from the transducer's internal capacitor and flipping its polarity upon activation by the synchronized signal, SSHC not only simplifies the circuit design but also enhances the overall efficiency and performance of the energy harvesting system. In this project, a straightforward impedance-matching approach is employed to assess the actual power conversion efficiency of our MEMS transducers against an ideal load.

2.3 Analysis and Characterization Methods

2.3.1 Lumped Model

To study frequency response of a MEMS transducer, a lumped model is frequently adopted. A lumped model starts with integrating and representing physical parameters of transducers in the form of a compact spring-mass-damper system. By studying the mechanical response of the lumped oscillation, we then can achieve the full picture of how transducer behaves in response to ambient excitation. For most situations, lumped analysis could accurately predict a system's mechanical response, significantly simplifying the analysis process while neglecting minor impact factors such as inactive component's structure layer. In Figure 14. A below shows a standard uncoupled spring-mass-damper system in pure mechanical domain, and in Figure 14. B, a spring-mass-damper system including the backward coupling from electrical domain.

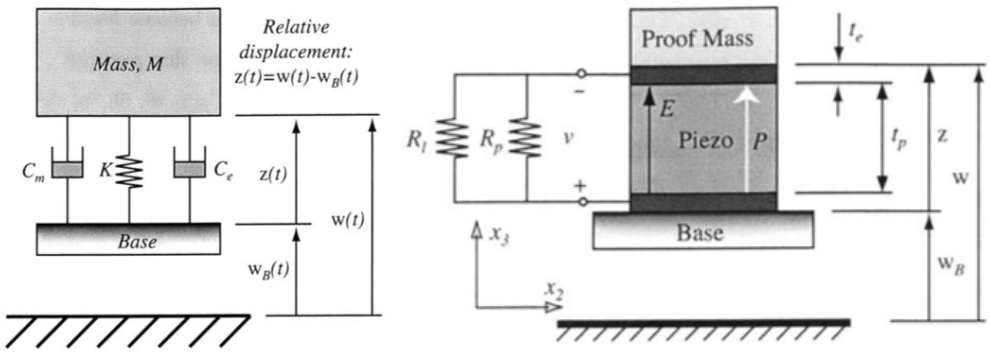

Figure 14. Lumped model of a piezoelectric energy harvester with (left) uncoupled and (right) electromechanically coupled responses. © 2005 MIT Library. Reprinted with permission from [41].

In the context of an internal vibrational energy harvester, the system is modeled as being base-excited by ambient vibrations, represented by $w_B(t)$. The governing equation of motion, as shown in Equation (3), is given by [42, 43]:

$$\ddot{z} + 2(\zeta_m + \zeta_e)\omega_N \dot{z} + \omega_N^2 z = -\ddot{w}_B \tag{7}$$

This equation describes the vibrational behavior of the system. The acceleration of a lumped mass M is represented by $\ddot{z}$, while velocity of the mass is represented by $\dot{z}$ and its displacement by z, which are influenced by the base excitation $w_B(t)$. The damping coefficients C_e (electrical) and C_m (mechanical) , which represent electrical and mechanical damping, respectively, are expressed as $C= 2M\omega_N \zeta$, where parameters ζ_m *and* ζ_e represent the mechanical and electrical damping ratios, respectively, quantifying the energy lost through internal mechanical friction and electrical resistance. This expression for damping coefficients highlights how the damping force is proportional to both the mass and the natural frequency of the system, with damping reducing the vibrational amplitude and dissipating energy. The term $\omega_N$is the natural frequency of the system, which depends on the system's stiffness and mass and indicates the frequency at which the system naturally oscillates when subjected to dynamic loads.

$$\omega_N = \sqrt{\frac{K}{M}} \tag{8}$$

Here, K is the effective stiffness of the system, and M is the lumped mass. To determine the amplitude of vibration, $|z|$, under base excitation, Equation (5) is derived:

$$|z| = \frac{M\ddot{w}_B}{K} \frac{1}{\sqrt{(1-\Omega^2)^2+[2(\zeta_m+\zeta_e)\Omega]^2}} \tag{9}$$

This expression gives the amplitude of vibration in response to the base acceleration $\ddot{w}_B$. The term $M\ddot{w}_B$ represents the excitation force imposed by the base. The dimensionless frequency ratio Ω is defined as the ratio of the excitation frequency ω to the system's natural frequency ω_N, i.e., $\Omega=\omega/\omega_N$. The available power $|P| = \frac{1}{2} C_e \dot{z}^2$ could be harvested without considering any loss then becomes:

$$|P_{out}| = \frac{M\zeta_e \Omega^2 \omega^4 w_B^2}{\omega_N[(1-\Omega^2)^2+(2\zeta_T\Omega)^2]} = \frac{M\zeta_e \Omega^2 \ddot{w}_B{}^2}{\omega_N[(1-\Omega^2)^2+(2\zeta_T\Omega)^2]} \tag{10}$$

As expected, the maximized power occurs when excitation frequency matches fundamental frequency as Ω approaches 1, and electrical damping ratio matches mechanical damping $\zeta_e=\zeta_m$. Then the output could be reduced to:

$$|P_{out}|_{opt} = \frac{\sqrt{M^3 \ddot{w}_B{}^2}}{16\zeta_m\sqrt{K}} \tag{11}$$

The electrical power can also be derived from lumped analysis. With the maximum displacement *z*, the device's deflection profile *w(x)* can be derived accordingly based on its geometry. The bending stress σ, generated charge q and power P in electrical domain are related to deflection w(x) as:

$$\sigma = -z\frac{d^2w(x)}{dx^2} \tag{12}$$

$$q = \sigma_{average} d_{31} A \tag{13}$$

$$P = V * I = \frac{qh_{piezo}}{\varepsilon A} \times \frac{dq}{dt} = \frac{q^2 h_{pc}\omega}{\varepsilon A} \tag{14}$$

$\sigma_{average}$ is the stress across electrode area A and ω is the angular oscillation frequency. Intuitively, given constant excitation acceleration and resonant frequency, the mechanical power is inversely proportional to mechanical damping ratio from Equation (10). Meanwhile, in electrical domain, the electrical power is mainly determined by thickness of active piezoelectric layer and generated charge. When designing a micro energy harvester under biomedical context, the ambient vibration frequency is generally less than 100 Hz with limited acceleration amplitude. Thus, it's critical to work on system damping reduction and frequency tuning in order to achieve higher energy output.

2.3.2 Distributed Parameter Electromechanically Coupled Analysis

Despite its simplicity, the lumped model has some limits. For example, it's best suited for uniform structures where homogeneous parameters can be accurately integrated into a spring-mass-damper system. However, for devices where the interaction between electrical and mechanical components is complex and spatially variable, the lumped model may not provide sufficient accuracy. In such cases, the distributed parameter method offers a more accurate solution for modeling deflection and strain pattern by a detailed simulation of electromechanical systems including the continuous distribution of parameters. This method is crucial for understanding how different parts of a device respond to electrical and mechanical inputs, proving invaluable for optimizing designs that feature

intricate interactions within the device. For instance, the Euler–Bernoulli beam model is proposed to describe the beam deflection characteristics under loading through an analytical approach. The analysis is built on the relationship among the bending moment (load), transverse displacement at given position, radius of curvature, and stress. The absolute displacement at any position *x* of a beam is described by a general equation [41, 44]:

$$-\frac{\partial^2 M(x,t)}{\partial x^2} + c_s I \frac{\partial^5 w_{rel}(x,t)}{\partial x^4 \partial t} + c_a \frac{\partial w_{rel}(x,t)}{\partial t} + m\frac{\partial^2 w_{rel}(x,t)}{\partial t^2} = -[m + M_s\delta(x-L)]\frac{\partial^2 w_b(x,t)}{\partial t^2} \quad (15)$$

Where, *M(x,t)* represents the bending moment at position *x* and time *t*, describing the internal forces within the beam that resist deformation. The term c_s is the damping coefficient, accounting for material damping effects, while *I*, the moment of inertia, is related to the beam's cross-sectional geometry. The relative displacement of the beam is denoted as $w_{rel}(x,t)$, indicating how the beam deforms over time and space. The coefficient c_a introduces viscous damping proportional to the velocity of the beam's deflection, and *m* is the mass per unit length, contributing to the beam's inertia. The Dirac delta function, *δ(x-L)* indicates a concentrated load or mass at the position *x=L*, where an additional force or mass M_s is applied. Finally, $w_b(x,t)$, represents external displacements or base motions applied to the beam, influencing its dynamic response. Altogether, this equation models the beam's vibrational behavior by balancing internal moments, damping effects, inertia, and external forces. Then bending moment is replaced with Equation (12) in terms of axial stress and design parameters such as thickness h_p of each piezoelectric layer, thickness h_s of each substrate layer, and width *b* of the structure.

$$M(x,t) = b\left(\int_{-\frac{h_p+h_s}{2}}^{-\frac{h_p}{2}} T_1^{\bar{p}} z\, dz + \int_{-\frac{h_s}{2}}^{\frac{h_s}{2}} T_1^{\bar{s}} z\, dz + \int_{\frac{h_s}{2}}^{\frac{h_p+h_s}{2}} T_1^{\bar{p}} z\, dz\right) \quad (16)$$

Stress T^p and T^s in each piezoelectric and substrate layer are linked to the axial strain by young's modules and piezoelectric effect matrix as in equation (13). Then in Euler-Bernoulli theory, strain can be derived from the radius of curvature and *z*, the distance from the neutral axis of the composite beam:

$$T_1^{\bar{s}} = Y_{\bar{s}} S_1^{\bar{s}}, \quad T_1^{\bar{p}} = \overline{c_{11}^E} S_1^{\bar{p}} - \overline{e_{31}} E_3 \quad (17)$$

Where axial strain S is given by

$$S_1(x,z,t) = -z\frac{\partial^2 w_{rel}(x,t)}{\partial x^2} \quad (18)$$

Finally, after substituting defined parameter back to the original governing equation (11), the governing equation of the beam can be expressed as:

$$YI\frac{\partial^4 w_{rel}(x,t)}{\partial x^4} + c_s I\frac{\partial^5 w_{rel}(x,t)}{\partial x^4 \partial t} + c_a\frac{\partial w_{rel}(x,t)}{\partial t} + m\frac{\partial^2 w_{rel}(x,t)}{\partial t^2} + \vartheta_v(t)\left[\frac{d\delta(x)}{dx} - \frac{d\delta(x-L)}{dx}\right] = -m\frac{\partial^2 w_b(x,t)}{\partial t^2} - c_a\frac{\partial w_b(x,t)}{\partial t} \quad (19)$$

In this expression, the term $\vartheta_v(t)$ introduces a backward coupling effect, which depends on the mode of the piezoelectric effect being utilized (e.g., 33 or 31 mode) as well as the configuration of the electrodes. The general solution for the beam displacement $w_{rel}(x,t)$ in modal response takes the form:

$$w_{rel}(x,t) = \sum_{r=1}^{\infty} \phi_r(x)\eta_r(t) \quad (20)$$

Here, ϕ_r and η_r represent the mass-normalized eigenfunctions and modal mechanical responses for the *r*-th mode, respectively. Their expressions depend on the specific design of the piezoelectric layers and electrodes. The eigenfunction $\phi_r(x)$ can be expressed as

$$\phi_r(x) = C_r\left[\cos\left(\frac{\lambda_r}{L}x\right) - \cosh\left(\frac{\lambda_r}{L}x\right) + \zeta_r\left(\sin\left(\frac{\lambda_r}{L}x\right) - \sinh\left(\frac{\lambda_r}{L}x\right)\right)\right] \quad (21)$$

The modal response $\eta_r^s(t)$ is governed by the following equation:

$$\frac{d^2\eta_r^s(t)}{dt^2} + 2\zeta_r\omega_r\frac{d\eta_r^s(t)}{dt} + \omega_r^2\eta_r^s(t) + \chi_r^s v_s(t) = f_r(t) \quad (22)$$

Both ϕ_r *and* η_r can be solved numerically based on the parameters of the transducer. Here χ_r^s quantifies the interaction between the mechanical mode and the electrical system through the piezoelectric effect, contributing to the overall electrical output as a function of mechanical deformation. Once the displacement function $w_{rel}(x,t)$ is known, the mechanical and electrical responses (such as voltage and power output) can be calculated. This method is employed in this study to simulate and analyze the mechanical response of a unimorph piezoelectric energy harvester, providing valuable insights for designing and optimizing electromechanical coupling efficiency and enhancing performance prior to device fabrication.

2.3.3 Rayleigh-Ritz Method

In the numerical analysis of vibrational energy harvester and micromachined ultrasonic transducers within this research, the Rayleigh-Ritz method is strategically utilized in conjunction with lumped models and equivalent circuit models to provide a comprehensive understanding of internal mechanical behaviors and optimize design parameters [45, 46]. This integrated approach is particularly crucial for addressing the complex dynamics involved in multiple mode interactions, which are often encountered in advanced MEMS transducers systems. The Rayleigh-Ritz method is important in connecting continuous system behaviors to their discrete mechanical and electrical counterparts through the application of energy principles. By employing Hamilton's principle, this method integrates kinetic energy and potential energy with the work done by external forces alongside electrical interactions, reducing the dimensionality of the problem and providing significant insights into the natural frequencies and mode shapes of the system. This integration is crucial for accurately representing the dynamics of piezoelectric systems where mechanical and electrical domains interact.

Central to the Rayleigh-Ritz method is its ability to express the dynamics of the system in matrix form, encompassing the mass distribution (Mass Matrix, M), which reflects the system's inertia. The Damping Matrix (C) captures the energy dissipation within the system due to internal friction or other resistive forces. The Stiffness Matrix (K) quantifies the system's resistance to deformation when subjected to mechanical loads. The Electromechanical Coupling Matrix (Θ) plays a crucial role by linking mechanical deformations to electrical outputs, a key characteristic in piezoelectric materials. Additionally, Capacitance (C_p) denotes the system's ability to store electrical energy, and the Forcing Vector (B_f) describes the external forces applied to the system. The method simplifies these complex interactions by using lumped parameter models, which assume that properties like mass and stiffness are concentrated at discrete points. This simplification aids in applying equivalent circuit models, translating the mechanical and acoustic behaviors of the system into electrical analogs. This translation is essential for applying lumped model and equivalent circuit analysis techniques to evaluate system behavior effectively. The governing equations, derived from this method, are as follows [47]:

$$M\ddot{r} + C\dot{r} + Kr - \Theta v = B_f \ddot{w}_B \tag{23}$$

$$\Theta^t \dot{r} + C_p \dot{v} + \frac{1}{R_l} v = 0 \tag{24}$$

where $\ddot{r}$ and $\dot{r}$ denote the system's acceleration and velocity, respectively, reflecting how the physical displacement r evolves over time. The voltage v across the piezoelectric material, influenced by mechanical deformations due to the electromechanical coupling, and the external dynamic loads $\ddot{w}_B$ from the forcing vector B_f , impact the mechanical state of the system. The load resistance R_l is integral in determining the electrical damping and energy dissipation. Equation (19) outlines the motion of the system, incorporating effects of mass, damping, and stiffness, and how these are influenced by the electromechanical coupling due to applied external dynamic loads. Equation (20) highlights the electrical behavior, linking mechanical movements to changes in electrical state, moderated by the capacitance and load resistance which are critical for the operation of piezoelectric devices. This matrix formulation is essential for the Rayleigh-Ritz method's integration with lumped parameter models, which simplifies the complex continuum problems into manageable segments by assuming that the properties like mass or stiffness are concentrated at discrete points. Such simplifications make it feasible to use equivalent circuit models, which further translate mechanical and acoustic behaviors into electrical analogs, thereby facilitating the use of standard circuit analysis techniques to study system behavior.

The combination of these methods enhances the capability to conduct detailed sensitivity analyses, which are essential for tuning the design to achieve optimal performance. This is especially beneficial in energy harvester design, where understanding the nuanced interactions between multiple vibrational modes can lead to substantial improvements in energy conversion efficiency. The combination of the Rayleigh-Ritz method with practical frameworks such as lumped models and equivalent circuit models enables the study to effectively address the complexities of designing devices that operate across a wide range of dynamic conditions. This comprehensive modeling approach enhances both theoretical understanding and practical applications of complex MEMS devices, ensuring that devices like PMUTs and energy harvesters achieve optimal performance.

2.3.4 Finite Element Analysis (FEA)

Numerical analysis is essential for predicting the frequency and mechanical responses of straightforward MEMS transducer structures. However, when developing complex transducers that incorporate intricate electrode layouts, anchor designs, and operate across multiple domains—electrical, mechanical, and acoustic—the analysis becomes significantly more complex. To address

these complexities more effectively and accurately, Finite Element Analysis (FEA) is employed as a crucial supplement to traditional numerical methods.

In this research, COMSOL software is utilized to examine both the mechanical and frequency responses of innovative energy harvesters and PMUTs. For instance, Figure 15. A presents an FEA model of a clamped-clamped beam, displaying its fundamental mode vibration profile. This model allows for the visualization of vibration shapes, natural frequencies, and bending stress distribution, highlighted by varying colors to indicate different intensities. These visual insights offer clear, intuitive insights into the behavior of the structures, thus facilitate a more intuitive approach to MEMS transducer design. Consequently, a clamped-clamped type energy harvester, featuring 19 segment electrodes on each side, was developed to exploit these advanced modeling capabilities.

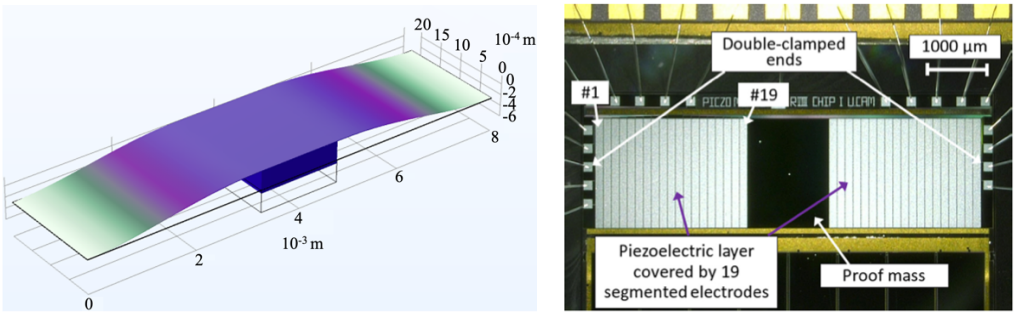

(A) (B)

Figure 15. A: FEA simulation results of a clamped-clamped structure with stress distribution and deflection profile. B: A clamped-clamped energy harvester was designed and fabricated based on insights from COMSOL simulation results.

Beyond standard applications like stress distribution, FEA analytical analysis is particularly advantageous in the design of PMUTs. COMSOL is employed to comprehensively simulate responses across electrical, mechanical, and acoustic domains. While numerical analysis is adept at predicting mechanical response of standard MEMS transducer, it faces challenges with acoustic responses due to increased complexity. In contrast, FEA emerges as a powerful tool, enabling precise predictions of acoustic attenuation and thorough analysis of key characteristics, such as Rayleigh length and focal points. These capabilities are crucial for exploring ultrasound-based applications including but not limited to wireless energy transfer. For instance, designing a high-power PMUT array must take consideration of the acoustic intensity safety level. According to FDA regulations, the maximum permissible ultrasound intensity is 94 mW/cm² for general use. The Mechanical Index

(MI)—a measure evaluating ultrasound power and its biological effects on human tissue—is calculated using the formula MI = P/√f, with a safe threshold of 1.9 as per FDA guidelines [48]. P is the peak rarefactional pressure produced by the ultrasound, measured in megapascals (MPa), and f is the ultrasound's frequency, measured in megahertz (MHz). In practical design and testing, a simple circular PMUT prototype was modeled and analyzed using COMSOL to fulfill these requirements. The frequency sweep validated its fundamental mode at 91 kHz, as detailed in Figure 16. D. As a transmitter, the PMUT was driven under a 10 V_{peak}- AC signal and its mechanical responses, including maximum deflection patterns and output acoustic pressure fields, were simulated in air and depicted in Figures 16. A-C. Conversely, when employed as a receiver, positioned 1 cm from the transmitter in air, its output voltage from a central electrode reached 75 mV, with results plotted in Figure 16. D.

These experimental findings are instrumental in advancing the design of innovative PMUTs. During the design phase, FEA is integrated with numerical analysis to finely tune the PMUT's sensitivity across both fundamental and higher operational modes. This strategic combination of analytical techniques optimizes the device's performance across diverse operational conditions, significantly enhancing its efficacy for real-world applications.

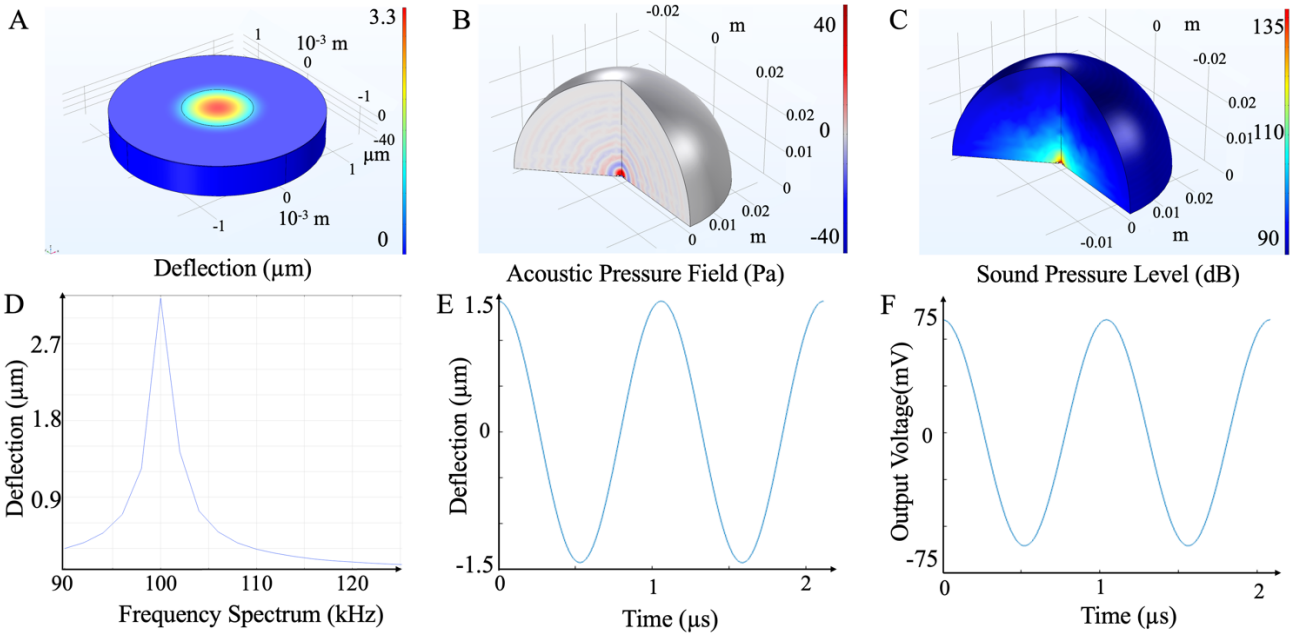

Figure 16. A: Deflection profile of a circular PMUT at its fundamental mode. B: Acoustic pressure field and C: Sound pressure level around PMUT. D: Frequency spectrum of the proposed PMUT with fundamental mode's resonant frequency at 100 kHz. E: Deflection profile at the center of circular

PMUT driven electrically at its fundamental mode. F: Voltage response from a PMUT receiver separated 1 cm away from a TX in air.

Chapter 3

Nonlinear Vibrational Energy Harvester

In Chapter 1, we reviewed the current advancements in energy harvesters for biomedical applications. These devices can be broadly categorized into two types based on their operating mechanisms: flexible energy harvesters that attach directly to organ surfaces to convert muscle or organ movements into electrical power, and vibrational energy harvesters that are mounted within an implantable medical device (IMD) to convert physiological vibrations, such as heartbeats and body movements, into electrical energy. Flexible energy harvesters, while not sensitive to frequency or environmental factors, face significant limitations due to the high-risk surgical procedures required for device attachment. Consequently, research has pivoted towards developing sustainable and highly efficient vibrational harvesters, which are embedded directly within IMDs, thereby avoiding the need for invasive surgeries and enhancing safety. However, these vibrational harvesters, designed to operate at their resonant frequencies, often face efficiency challenges due to the unpredictable and irregular nature of body movement vibrations. Traditional vibrational energy harvesters typically utilize a linear mechanical structure and operate at a fixed resonant mode to match their resonant frequency with that of ambient vibrations. This integration ensures safety but at the cost of efficiency; these harvesters typically suffer from limited operational bandwidth due to the inherent variability in body movement frequencies, confining them to resonate only at specific frequencies that match the ambient vibrations.

To overcome these performance limitations in unpredictable vibrational environments, our research introduces an innovative MEMS harvester employing an auto-parametric resonance scheme to establish mode coupling and trigger frequency comb. This design leverages the structural benefits of clamped-clamped beams and symmetric membrane structures, enabling precise frequency tuning and nonlinear mode coupling, which are crucial for this advanced resonance mechanism. This approach expands the operational bandwidth and enhancing energy harvesting efficiency beyond traditional

methods especially under noise-induced excitations. The harvester design requires only a single unidirectional mechanical vibration signal with minimal acceleration— as low as 0.07 g (0.69 m/s^2) —to initiate the frequency comb response. It operates on the principle of two-mode, three-wave mixing, which arises from nonlinear modal interactions inherent to the MEMS device. This capability significantly broadens the operational bandwidth, making the device more effective for vibration energy harvesting applications. By employing diverse mechanical driving conditions, both auto-parametric resonance and frequency comb phenomena are observed, allowing the device to function efficiently across a wide range of conditions.

3.1 Mode coupling and Parametric Resonance

When reviewing traditional vibrational energy harvesters, it is noted that most designs mainly capture energy at a fixed frequency, typically focusing on the fundamental vibrational mode or a single degree of freedom. This is largely due to the ambient low-frequency environments in which these harvesters operate, necessitating a compromise in energy transformation efficiency to align the fundamental resonant frequency ω_n, with the ambient frequency directly exciting the system. However, the performance and efficiency of these devices are often limited by their narrow operational bandwidth. This limitation becomes particularly important given the inherent variability in internal mechanical energy sources, such as organ and muscle movements, which exhibit broad bandwidths and time-varying characteristics. To overcome these challenges, our project explores a frequency comb concept expected to significantly enhance the efficiency of VEH in random and broadband vibrational environments. Unlike traditional designs that operate at a fixed frequency or resonant mode, the frequency comb energy harvester utilizes a mechanism known as parametric resonance, which integrates multiple vibrational modes. Parametric resonance not only enhances the range of working frequencies but also improves the efficiency of energy transformation. For example, a classic demonstration of parametric resonance is observed in the pendulum experiment, where a vertical harmonic oscillation at twice the resonant frequency induces horizontal resonance [49].

- **Direct excited resonance**: The energy input E_{input} is proportional to the amplitude A, which is a function of the square root of the stored energy E_{store}, described as $E_{input} \propto A \propto \sqrt{E_{store}}$
- **Parametric Resonance**: In this mode, the energy input is proportional to the square of the amplitude, directly proportional to the stored energy $E_{input} \propto A^2 \propto E_{store,}$ leading to more efficient energy storage and lower dissipation from damping.

Given constant input energy $E_{max} = \frac{1}{2}kx^2$ where k and x are equivalent spring constant and oscillation amplitude, parametric resonance demonstrates a superior capability to store and transform energy compared to direct excitation, leading to substantial improvements in energy transformation efficiency.

- **Parametric Resonance**

  $\Omega = \frac{2\omega_n}{n}$, where ω_n is the nth order resonant frequency, and n is a positive integer that denotes the order of resonance.

- **Auto-parametric Resonance or Internal Resonance**

  $\omega_i = n\omega_j$ or $\omega_i = a\omega_j + b\omega_k + \cdots$. Here, *n, a, b,* are positive integers that describe the order of nonlinearity in the system, while $\omega_{i,j,k}$ ... represent the resonant frequencies represent the resonant frequencies associated with the orders of resonance *i*, *j*, *k*…

For instance, the first order parametric resonance phenomenon can be activated externally away from natural frequencies at $\omega=2\omega_n+\epsilon$, where ϵ represents a small detuning factor. Unlike directly excited resonance, parametric resonance involves a homogeneous differential equation with periodically varying system parameters. A common approach to numerically study such mechanism is through Mathieu equation, which represents by a simple differential equation with periodic coefficients [50, 51].

$$\ddot{x} + (\delta + 2\varepsilon\cos(2t))x = 0 \tag{25}$$

δ and ε are related to the square of natural frequency and amplitude of the parametric excitation correspondingly. Using Floquet theory, the normal solution is

$$x(t) = e^{\gamma t}\theta(t) \tag{26}$$

where γ represents the characteristic exponent, and $\theta(t) = \theta(t + \pi)$. indicates that when the real part of γ is positive, the response is unbounded and unstable, suggesting parametric driving. This condition exponentially amplifies the oscillation amplitude until physical or nonlinearity constraints are reached. Conversely, when γ approaches zero or a negative value, the system stabilizes, and *x(t)* decays due to

external damping. A transition curve is plotted *in* δ-ε plane based on a Mathieu equation in Figure 17. A, showing the division and transition from stable(unshaded) into unstable(shaded) regime.

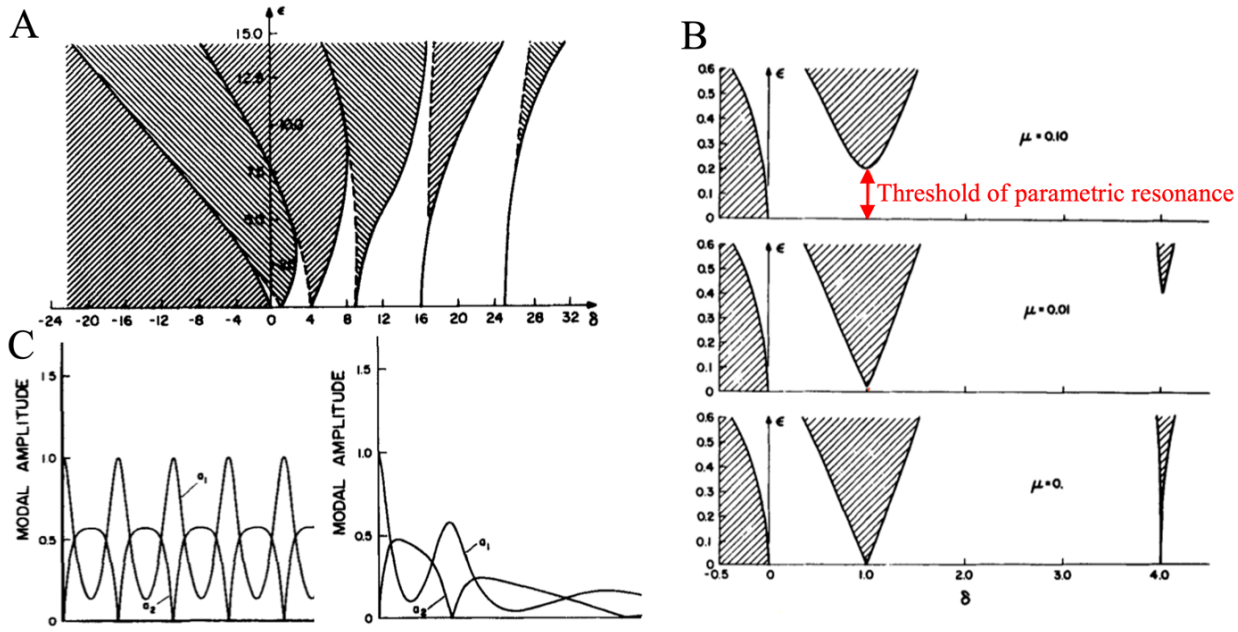

Figure 17. A: Parameter plane for Mathieu equation. Shaded (unstable) region marks the parametric resonance. B: Effect of viscous damping on threshold of parametric resonance. C: Auto-parametric and energy exchange between two modes without damping (Left) and with damping (Right). © 2024 John Wiley & Sons. Reprinted with permission from [52].

Parametric resonance in vibrational energy harvesters depends on several factors. First of all, the occurrence of parametric resonance is influenced by ε, a factor proportional to the excitation amplitude. Higher orders of parametric resonance require greater excitation levels to destabilize the system, enhancing energy harvesting efficiency. Additionally, the system's damping significantly affects the resonance threshold. Systems with minimal damping require lower excitation amplitudes to trigger parametric resonance, as detailed in Figure 17. B. These observations have guided the development of design guidelines aimed at reducing damping to improve operational efficiency. Parametric resonance inherently modulates system parameters at specific modes, enabling another mechanism known as auto-parametric resonance. This involves the coupling of multiple eigenmodes within the system, which becomes feasible when the frequency of two modes aligns closely or exactly, typically at an integer or near-integer ratio ($\omega_i = n\omega_j$), Once it occurs, the energy initially given to the directly driven mode transfers to the coupled mode, facilitating continuous energy exchange across the system, as shown in Figure 17. C. A case of auto-parametric excitation on membrane VEH was observed in the lab through a digital holographic microscope (DHM) and frequency response

analyzer. The DHM measures the deflection profile of the MEMS transducer by recording the interference pattern between a reference beam and the light reflected from the transducer. The core advantage of the DHM is its ability to capture optical phase information, which directly correlates to the path length differences between the two beams. When the MEMS transducer is driven and begins to deform or vibrate, these changes modulate the phase of the light waves reflecting from its surface. By capturing and analyzing the hologram, the DHM reconstructs a full-field image of the transducer's surface with high spatial resolution. The phase shift data extracted from this image provides a precise measurement of the surface deflection at each point, enabling detailed analysis of the transducer's behavior under different conditions.

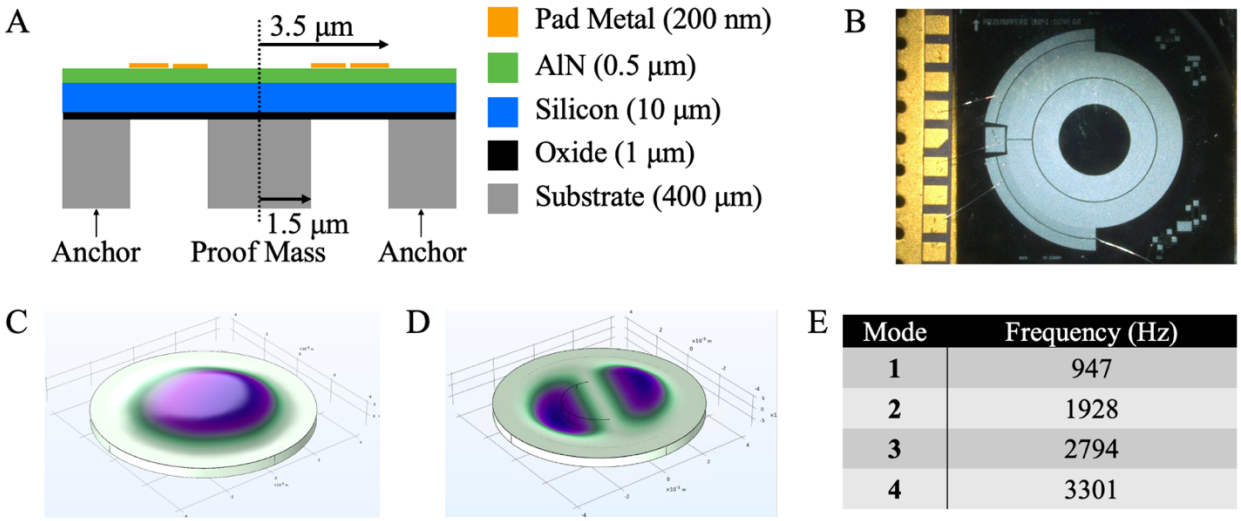

E

Mode	Frequency (Hz)
1	947
2	1928
3	2794
4	3301

Figure 18. A: Cross-section view of a circular piezoelectric energy harvester with dual-ring electrode and central proof mass. B: Picture of the fabricated MEMS energy harvester. C: Mode profile of the energy harvester at its fundamental mode under FEA simulation. D: Mode profile of the energy harvester at a higher mode 2 under FEA simulation. E: Resonant frequencies of designed circular VEH across various eigenmodes.

This prototype features a circular membrane structure constructed through the PiezoMUMPs process. It features a 3.5 µm radius with two ring-shaped electrodes surrounding a central proof mass with a radius of 1.5 µm. The device also incorporates a 0.5 µm thick aluminum nitride (AlN) piezoelectric layer atop a 10 µm silicon-on-insulator (SOI) wafer. DHM and frequency response analysis were employed to validate the operational modes of the device. The initial tests involved driving the device with an electrical signal from 500 Hz to 4000 Hz at the inner ring electrode and measuring the response from the outer ring electrode. The fundamental mode 1 was recorded at approximately 950

Hz, with additional higher order modes closely matching integer or near-integer multiples of this frequency, as detailed in Figure 18. E. These findings confirm that the symmetric configuration of the circular membrane structure promotes dense mode interactions and increases the likelihood of successfully exciting internal resonances, owing to the reliance on multiple modes and near-integer ratios between modal frequencies. These findings demonstrate that the symmetric configuration of the circular membrane structure enhances dense mode interactions and increases the probability of successfully exciting internal resonances, which necessitate multiple modes and near-integer ratios between modal frequencies.

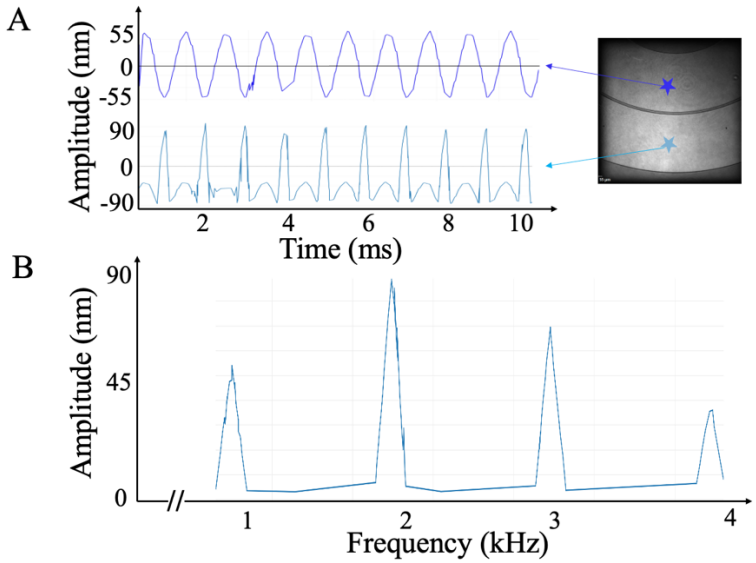

Figure 19. A: Time-domain response of VEH prototype from two points of interest at center of two ring electrodes. B: Frequency spectrum demonstrates multiple modes being excited with a single-frequency signal at mode 2 frequency.

To induce internal resonance, the second mode, which has a frequency approximately twice that of the fundamental mode, was specifically targeted. The harvester was driven with a 10 V AC signal at 1928 Hz (mode 2). During this process, deflection patterns of the membrane were closely monitored utilizing DHM at two points of interest marked in dark and light blue at the centers of two ring electrodes. The resulting time-domain response, depicted in Figure 19. A, displayed distinct deflection patterns indicative of multiple modes being excited simultaneously. Despite being driven explicitly at mode 2 (1928 Hz), the harvester demonstrated a flexural response comprising two distinctive frequencies: the fundamental mode 1 at 949 Hz and mode 2 at 1928 Hz. This simultaneous excitation of two modes under a single frequency drive illustrates the intricate mode interactions within the harvester's structure. Further analysis in the frequency domain, shown in Figure 19. B,

supported these findings by highlighting several peaks corresponding to the engagement of various modes. Notably, while the drive signal primarily exciting the harvester on mode 2, there was a notable mechanical response at mode 3, accompanied by strong peaks at modes 1 and 2. This analysis confirmed the simultaneous excitation of multiple modes, thereby affirming the internal resonance and effective nonlinear mode coupling within the harvester. Building on these insights, a frequency comb energy harvester was developed to leverage the nonlinear modes coupling between multiple modes. This design aims to enhance the energy harvester's overall bandwidth and energy conversion performance, optimizing the interactions between various operational modes to maximize energy efficiency and output.

3.2 Frequency Comb Harvester

Internal resonance triggers nonlinear mode coupling, enabling energy exchange between multiple modes within a device. This internal mode coupling facilitates intrinsic signal mixing and modulation, leading to several promising applications, such as frequency combs. A photonic frequency comb, characterized by equally spaced and phase-coherent discrete lines in the frequency domain, precisely defines the frequency spacing between combs and is used in high-accuracy physical measurements such as spectroscopy and molecular fingerprinting [53]. In the optical domain, frequency combs have numerous applications in metrology and precision time and frequency measurements. Recently, phononic frequency combs have been observed in the MEMS domain, mediated by nonlinear modal coupling in resonator devices [54-56]. Phononic frequency combs emerge in a strong coupling regime involving nonlinear resonances, where the amplitudes and phases of two coupled mechanical modes are modulated via coherent energy transfer. Ganesan et al. developed a micromechanical resonator that successfully triggered a phononic frequency comb via three-mode parametric three-wave mixing [57, 58]. Using an AlN-on-Si free-free beam structure, as shown in Figure 20. A, the frequency comb is formed through intrinsic coupling between the drive and resonant frequencies, resulting in a frequency comb with spacing corresponding to the separation between these frequencies. This observation provides a stable and precise approach for resonance tracking. Sun et al. conducted a detailed analysis on the generation and evolution mechanisms of phononic frequency combs in a nonlinear micromechanical resonator, focusing on coherent energy transfer between two mechanical modes [55]. Using a microelectromechanical disk resonator, as shown in Figure 20. B, they analytically studied the frequency comb characteristics, including spacing and the number of comb

teeth, by modeling the interaction of these coupled modes under specific driving conditions. A phenomenological model accurately predicted this evolution.

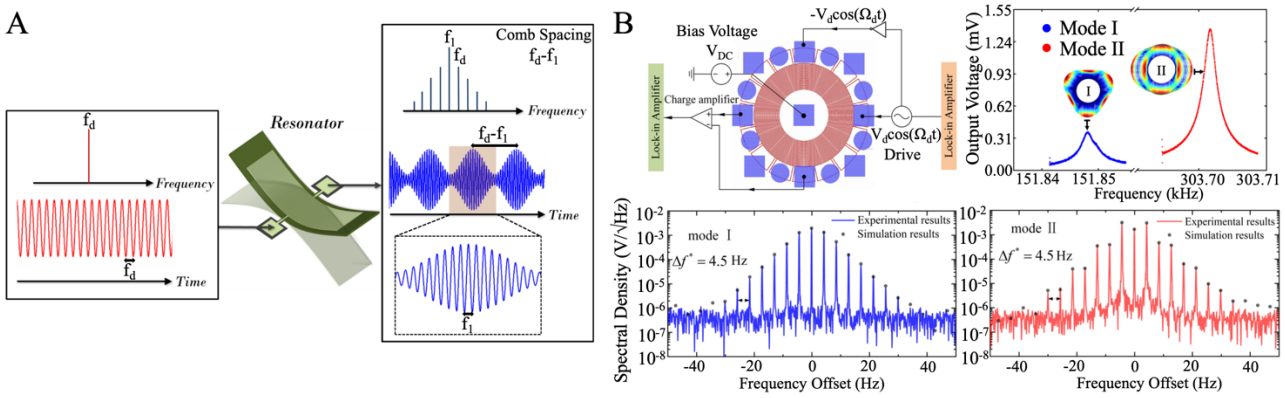

Figure 20. A: Concept of resonant frequency tracking using phononic frequency combs: when a single sinusoidal drive is applied to a free-free resonator, a series of equidistant spectral lines are generated through the process of phononic frequency comb generation. © 2023 American Physical Society. Reprinted with permission from [52]. B: Emergence of phononic frequency combs in the strong coupling regime. Phononic frequency combs arise in the strong coupling regime through coherent energy transfer, as depicted by the modulation of amplitudes and phases of two coupled mechanical modes (mode I and II, shown by blue and red curves). © 2019 Springer Publishing. Reprinted with permission from [57].

Most of these promising researches were conducted using electrically driven resonator devices, with the observation of frequency combs depending on several parameters, including the nature and strength of modal coupling, associated damping factors, and driving parameters. However, in the context of piezoelectric MEMS resonators, there has been limited study of frequency comb phenomena in mechanically driven systems. This research reports a distinctive frequency comb in a mechanically driven MEMS device and adopts the concept for energy harvesting applications.

3.2.1 Concept

The frequency comb (FC) phenomenon arises from intrinsic nonlinear coupling among different modes inherent within a device [59]. For successful implementation in an energy harvester, it is essential that the device supports mode coupling via internal resonance. This means the device must possess multiple modes that can interact, specifically at least two modes with integer or near-integer

frequency ratios. These modes are referred to as the comb mode and the coupled mode, each with distinct resonant frequencies

$$\omega_{coupled}=n\omega_{comb} \text{ or } \omega_{coupled}=\omega_{comb}/n \quad (27)$$

Where n is a positive integer. When a vibration source slightly detunes the MEMS harvester by a detuning factor δ from its primary mode $\omega_d \approx \omega_{comb} = \omega_{comb} + \delta$, the nearest fundamental mode, referred to as the comb mode, is first excited. As the excitation amplitude increases to a certain threshold, it triggers an internal resonance, channeling excess energy into another mode, termed the coupled mode. Further increasing the excitation leads to energy being cyclically transferred back to the comb mode via higher-order nonlinear interactions. This interplay establishes a continuous energy exchange between the comb and coupled modes, leading to a state of dynamic equilibrium. Once the excitation amplitude crosses a critical threshold, such modal interaction eventually builds up energy and results in mixing among driving signal, comb and coupled mode responses. With a relative phase difference between modal response and driving signal, the system transitions from a steady state into a complex, temporally oscillating state, characterized by periodic modulations visible as a series of equally spaced, phase-coherent spectral lines in the frequency domain, indicative of the frequency comb.

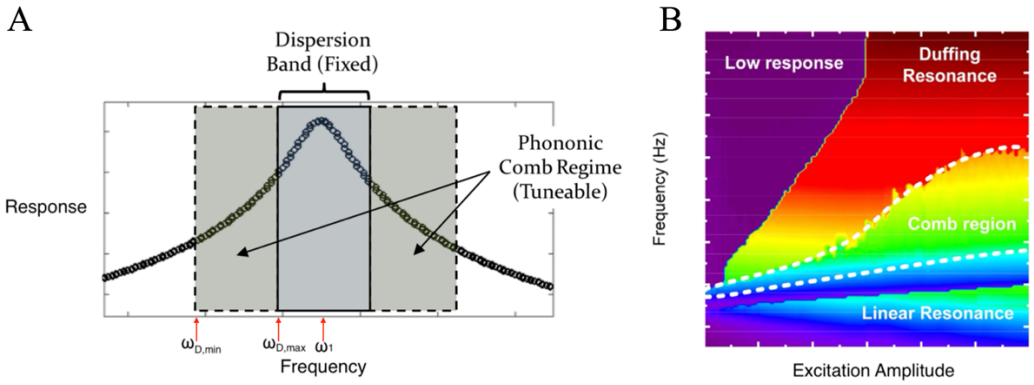

Figure 21. Existing observation on frequency and drive amplitude dependence on generation of frequency comb. A: Frequency spectrum with driving frequency threshold $\omega_{D,min}$ and $\omega_{D,max}$ in generation of frequency comb. © 2017 American Physical Society. Reprinted with permission from [54]. B: Frequency comb appears when driving signal excites the system between linear and Duffing nonlinear region given experimental results. © 2021 IEEE. Reprinted with permission from [59].

This phenomenon of frequency comb generation fundamentally results from the mixing of distinct signals due to inherent mode coupling activated by internal resonance. Two primary factors crucial for initiating the frequency comb are frequency detuning and the drive amplitude threshold. As shown

in Figure 21, existing research have observed the frequency dependency of driving on the generation of frequency comb. To be effective, the frequency detuning $\delta = |\omega_{\mathrm{comb}} - \omega_{\mathrm{D}}|$ must position the driving signal within a specific frequency band to slightly separate the driving frequency and comb mode frequency. A Fermi-Pasta-Ulam (FPU) framework can be employed to model the energy distribution among modes in a nonlinear system, illustrating that energy does not uniformly distribute across modes, a condition necessary for the persistent presence of a frequency comb [54, 60, 61]. The mathematical model for the mechanical behaviors of nonlinearly coupled modes can be complex, influenced by the mechanical structure and the degree of nonlinearity. To illustrate this concept, we utilize general governing equations of motion for a system with two second-order nonlinearly coupled modes:

$$\ddot{x_{comb}} + 2\zeta_{comb}\dot{x_{comb}} + {\omega_{comb}}^2 x_{comb} + \alpha_{coupled}{x_{comb}}^2 = ma\,cos(\omega_D t) \quad (28)$$

$$\ddot{x_{coupled}} + 2\zeta_{coupled}\dot{x_{coupled}} + {\omega_{coupled}}^2 x_{coupled} + \alpha_{comb-coupled}x_{comb}x_{coupled} = 0 \quad (29)$$

Here, x denotes displacement, while ω_{comb}, $\omega_{coupled}$, and ω_D represent the resonance and drive frequencies, with the relationship $\omega_{comb} \approx n\omega_{coupled}$, with n as an integer. The terms ζ and α signify the damping ratios and nonlinear coupling coefficients, respectively. This system is actuated by a vibration, characterized by acceleration a and the harvester's mass m. The coefficients $\alpha_{coupled}$ and $\alpha_{comb-coupled}$ are integral to the FPU framework. Furthermore, the Routh-Hurwitz criteria were applied to analyze system stability and predict the onset of sustained amplitude oscillations essential for frequency comb generation. This mathematical criterion evaluates the stability of the linearized system dynamics, requiring that all parts of the characteristic roots have negative real parts to ensure stability. Through this analysis, we can trace the transition of eigenmodes from stability to instability under specific driving conditions, understanding the thresholds where such instability leads to phononic frequency combs. Although this analysis explores only a limited aspect of dynamic behavior within these instability boundaries, it enhances our understanding of the frequency dependence of frequency combs. Later experimental results confirm the existence of specific drive frequencies that induce these instability boundaries, supporting desired resonance phenomena within the system. This understanding allows for controlled exploration of internal and auto-parametric resonances within the device. Derived from the Routh-Hurwitz criteria, the boundary condition for non-zero amplitude modulations is essential for the effective generation of frequency combs [54]. This leads to the conditions for generation of the frequency comb:

$$2\Delta_1\Delta_2 \leq -1(1 + {\Delta_1}^2 + 2\frac{\zeta_{coupled}}{\zeta_{comb}}) \quad (30)$$

Where:

$$\Delta_1 = \frac{\omega_D - \omega_{comb}}{\zeta_{comb}};\ \Delta_2 = \frac{\omega_D - 2\omega_{coupled}}{\zeta_{coupled}} \quad (31)$$

The generation of a frequency comb is intricately linked to the frequency and amplitude of the drive signal, which must be precisely controlled within a designated frequency band known as the comb regime. This band's boundaries and the spacing between the combs are defined by the systematic damping of the comb and coupled modes, reflected by their damping ratios or quality factors $Q = \frac{1}{2\zeta}$. To understand the frequency dependence and dynamic behavior of the system, we undertake an analytical derivation based on the governing Equations (25) and (26). This involves assuming a slowly varying envelope solution $x_j = (u_j e^{i\omega_D t} + {u_j}^* e^{-i\omega_D t})/2$ for the displacement variables, which simplifies into a set of first-order differential equations for the normalized amplitudes. These equations are then analyzed to identify stable and unstable regimes by studying stationary points, following methodologies similar to those described by Ganesan et al. [62]:

Frequency detuning: $\delta = |\omega_{\mathrm{comb}} - \omega_{\mathrm{D}}| \geq \delta_{threshold} = \frac{\omega_{\mathrm{comb}}}{\sqrt{2}Q_{\mathrm{comb}}Q_{\mathrm{coupled}}}$ (32)

Frequency comb drive range: $\omega_{\mathrm{D,max}} - \omega_{\mathrm{D,min}} = \left|\omega_{\mathrm{coupled}} - \frac{\omega_{\mathrm{comb}}}{2}\right| - (\frac{\sqrt{2}\omega_{\mathrm{comb}}}{\sqrt{Q_{\mathrm{comb}}Q_{\mathrm{coupled}}}})$ (33)

Frequency ratio: $\left|\omega_{\mathrm{coupled}} - \frac{\omega_{\mathrm{comb}}}{2}\right| \geq \frac{2\sqrt{2}\omega_{\mathrm{comb}}}{\sqrt{Q_{\mathrm{comb}}Q_{\mathrm{coupled}}}}$ (34)

Quality factor/damping: $Q_{\mathrm{coupled}} \geq \frac{2}{Q_{\mathrm{comb}}(1 - \frac{2\omega_{\mathrm{coupled}}}{\omega_{\mathrm{comb}}})^2}$ (35)

In practice, the quality factors, inversely related to the damping ratios for both the comb and coupled modes, play crucial roles in determining both the critical detuning level and the operational regime of the frequency comb. Reducing the damping in these modes can significantly decrease the required level of detuning. Besides, as specified by Equation (27), a crucial prerequisite for generating a frequency comb is the precise detuning of the excitation input. This detuning must exceed a threshold value either above or below the fundamental comb mode, $\omega_D = \omega_{comb} \pm \delta_{\mathrm{threshold}}$, while also remaining within the specific range outlined as $\omega_{D,max} - \omega_{D,min}$ in Equation (28). The production of a frequency comb is heavily influenced by these parameters, alongside the system's capacity to maintain a low damping factor. These critical factors are further affected by the physical properties of the

system, such as mechanical tolerances and environmental variations, which can alter the essential parameters that govern the behavior of the frequency comb. However, it is vital to recognize that these conclusions are drawn from analytical models that include several assumptions. As a result, different structural designs may demonstrate varying degrees of modal coupling and nonlinearity. Thus, in the practical design of a frequency comb energy harvester, the design must account for additional tolerances due to limitations in the model and tolerances in material properties and fabrication processes. Even minor discrepancies in structural configurations can lead to substantial deviations in mode frequencies and systematic damping.

3.2.2 Modeling and Device Design

Frequency combs can result from nonlinear mixing of signals comprising different frequencies. Such inherent signal mixing in driven mechanical systems can arise via nonlinear modal coupling [63, 64]. In this work frequency comb phenomena is observed in a MEMS structure describing 1:2 internal resonance [65, 66]. Based on its operating principles, a frequency comb necessitates two critical prerequisites. First, auto-parametric resonance is essential for achieving robust nonlinear modal coupling. As elaborated in the previous sections, this resonance condition demands that two or more modal frequencies be commensurable, or nearly so, with an integer ratio ($\omega_i \approx n\omega_j$). Consequently, the design of energy harvesters necessitates the selection of MEMS structures that support a high density of modes. Additionally, it is crucial to integrate structures that allow for flexible frequency tuning, thereby increasing the likelihood of triggering auto-parametric resonance. Consequently, the design of frequency comb harvesters involves not only the selection of MEMS structures that inherently possess a high density of modes but also the integration of structures that facilitate flexible frequency tuning, thus inducing higher chance to trigger auto-parametric resonance. Initially, membrane and clamped-clamped beam structures are preferred because they offer high modal frequencies, adjustable modal frequencies, and are easy to fabricate as MEMS resonators. The membrane structure, in particular, has proven effective under auto-parametric resonance conditions, facilitating the coupling of multiple modes due to its high modal density and symmetrical configuration [67]. Additionally, the design and dimensional constraints of square structure MEMS harvesters limit their frequency tuning flexibility. Conversely, the clamped-clamped beam structure, known for its nonlinear characteristics within MEMS resonators, allows for adjustments in the length-to-width ratio to achieve specific modal frequencies, though it tends to have a sparser modal frequency density. Given these characteristics, square membrane and clamped-clamped beam

structures are considered complementary in a MEMS energy harvester, combining high modal density with tunable modal frequencies crucial for the effective excitation of nonlinear modal coupling and frequency comb generation. To take advantages of both configurations, an innovative topology has been developed, merging the strengths of membrane flexibility with the structural benefits of clamped-clamped beams, thus enhancing the harvester's performance across a broader range of operational conditions.

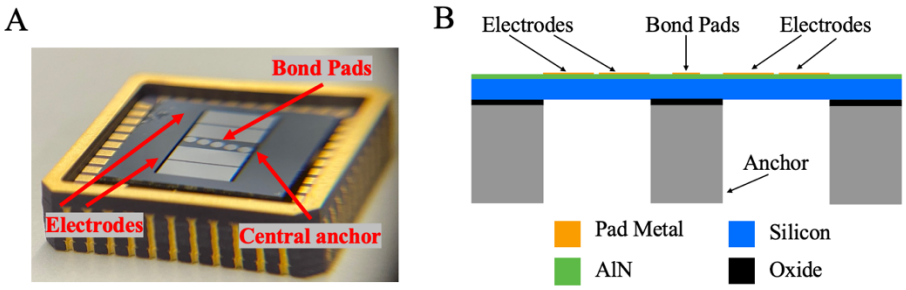

Figure 22. A: Photo of the packaged MEMS energy harvester. B: Cross-sectional view of fabricated FC harvester.

In this work, the harvester design comprises of a silicon micromachined inner plate attached to a central anchor pedestal and connected to an external outer frame. Figure 22. A shows the photo of the packaged MEMS chip. The harvester chip has dimensions of 11 mm × 11 mm, where the inner plate is separated from the outer frame by two 9 mm × 0.1 mm trenches on either side. A central rectangular post with dimensions 1.5 mm × 4.5 mm extends from the inner plate and serves as the anchor for the structure as a whole. A total of four electrodes covers the active area in the inner plate with two electrodes each situated on either side of the anchored region. The device stack comprises of a 3 μm AlN piezoelectric layer on a 25 μm single-crystal silicon device layer. The part not covered by electrodes and anchors has an additional 400 μm thick single-crystal silicon substrate layer to provide the proof mass component of the inertial energy harvesting device. Aluminum pad metallization is employed for the top electrode layer, metal interconnect and bondpads. Finite Element Analysis, shown in Figure 23. A-C, reveals the first three vibration modes of the MEMS harvester occur at approximately 261.3 Hz, 422.7 Hz, and 515.6 Hz. The first mode is characterized by torsional motion of the outer frame, while the third mode involves vertical translation of the outer frame coupled with bending of the inner plate. Notably, the frequency ratio between the first and third modes is approximately 1:2, indicating the potential for achieving internal resonance.

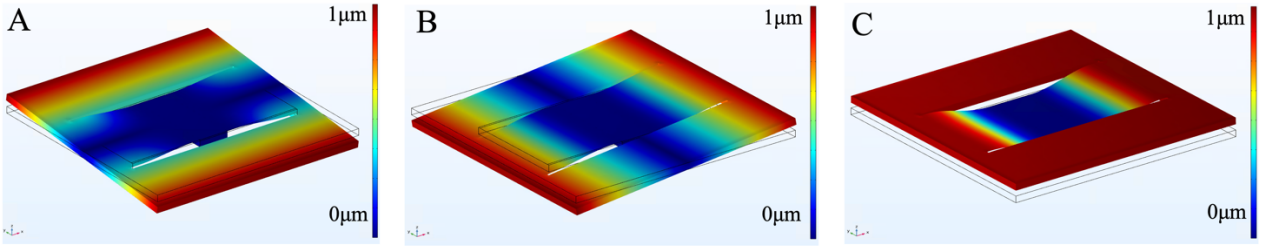

Figure 23. A-C: COMSOL simulated results of first three modes at 261.3 Hz, 422.7 Hz and 515.6 Hz respectively. The harvester is anchored by a central rectangular post from the bottom.

3.2.3 Experimental Characterization

The sample is mounted on top of a shaker (HBK, LDS V721), driven by a sinusoidal signal from a signal generator and power amplifier (HBK, LDS PA100E). A separate analog accelerometer is attached on the shaker desk closely to the sample as reference and acceleration indication. The analog accelerometer used is from Analog Device ADXL325EB, and acceleration readout can be derived based on $a = \frac{V_{peak-to-peak}}{2} \times sensitivity$ (g). Depending on choice of measurement equipment, the electrical signal can be read and downloaded from an oscilloscope (Keysight MSOS104A-MS) for fast Fourier transform, or to be analyzed by a lock-in amplifier (Zurich Instruments, HF2LI) for frequency response analysis in real time. The full experiment setup is shown in Figure 24 below.

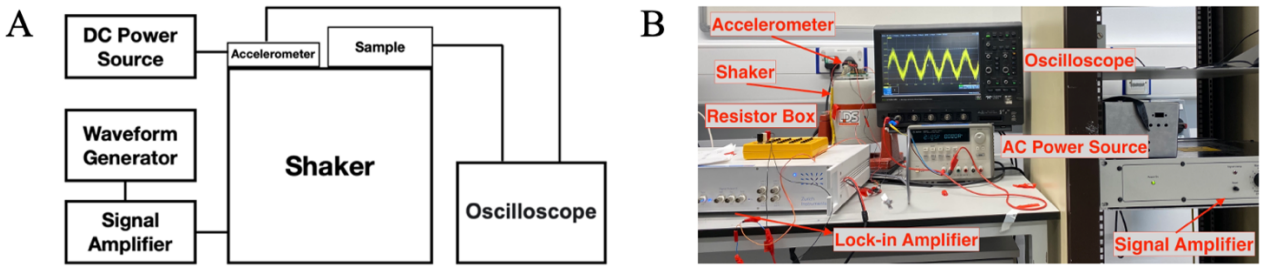

Figure 24. A: Block diagram of experimental setup for vibrational energy harvester. B: Experimental setup installed in the lab.

At first, the fabricated VEH chip was tested under an open-loop frequency sweep of the shaker excitation conducted at low acceleration levels (< 0.02 g). As shown in Figure 25, the measured response confirmed that the resonances of the first three mechanical modes of the representative device occur at 281 Hz, 396 Hz and 565 Hz respectively. Under the right driving conditions, 1:2 internal resonance is observed due to coupling between the first and third modes. The evolution of

frequency comb (FC) generation in the designed MEMS harvester is depicted in Figure 25. Four distinct phases can be observed, starting with linear resonant behavior at minimal acceleration as shown in Figure 25. A. As acceleration increases, the harvester undergoes Duffing hardening response until a critical base acceleration of 0.05 g is reached as depicted in Figure 25. B, where the system demonstrates nonlinear hardening behavior with increased bandwidth compared to the linear case. With further increase in the base acceleration, the harvester enters the internal resonance regime characterized by a sudden dip in forward frequency sweep results, as shown in Figure 25. C. The observed sudden dip indicates energy transfer into a coupled mode. Finally, upon exceeding the frequency comb threshold, as seen in Figure 25. D, the system response abruptly transitions to spontaneous oscillations, characteristic of FC behavior. This behavior is consistent with similar observations in other electrically driven resonator systems describing FC response [1-2].

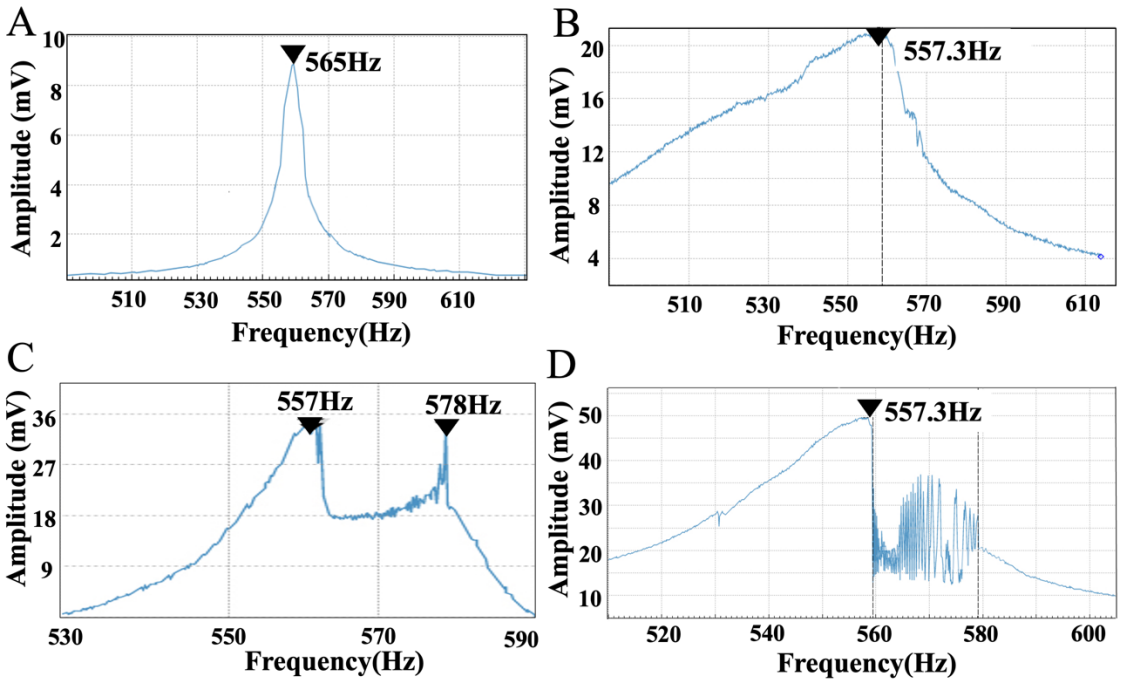

Figure 25. A: Frequency sweep around the comb mode under low acceleration shows a linear response. B: A frequency sweep under moderate acceleration levels shows evidence of Duffing nonlinearity. C: Increasing the driving acceleration until internal resonance occurs. D: Further increase of the driving levels results in the emergence of the frequency comb.

Aside from the driving level, a second determining factor in inducing frequency comb response is the choice of driving frequency. The frequency comb arises from signal mixing of three distinctive signals at f_{drive}, f_{comb}, and $f_{coupled}$, where f_{comb} and $f_{coupled}$ are frequencies of frequency comb mode and the coupled mode, which are recognized as the third mode and first mode in this design. The driving

signal is offset from the comb mode frequency by a detuning level $\delta_{detuning} = |f_{drive} - f_{comb}|$. As illustrated in Figure 26, the detuning factor must be sufficiently large to ensure the driving signal is distinct from both the comb mode and coupled mode signals; otherwise, the frequencies being too close may impede effective nonlinear mixing. However, the detuning level cannot be too large, as this would lead to a frequency mismatch that prevents efficient excitation of the coupled modes The appropriate range for the detuning factor is determined by the mechanical structure and the damping characteristics of the operating environment. From the experiment, an optimal range of frequencies for driving signal to trigger the nonlinear signal mixing for frequency comb response is observed and this is marked as the comb regime in Figure 26. B. The lower and higher frequency limits f_{low} and f_{high} for such a regime is proportional to the driving level or acceleration [61]. Under a base acceleration of 0.07g, the frequency comb regime is measured to be $1.3\ Hz \leq |\delta_{detuning}| \leq 21.2\ Hz$, and the driving signal within that frequency range could induce three-wave mixing, leading to the emergence of a frequency comb.

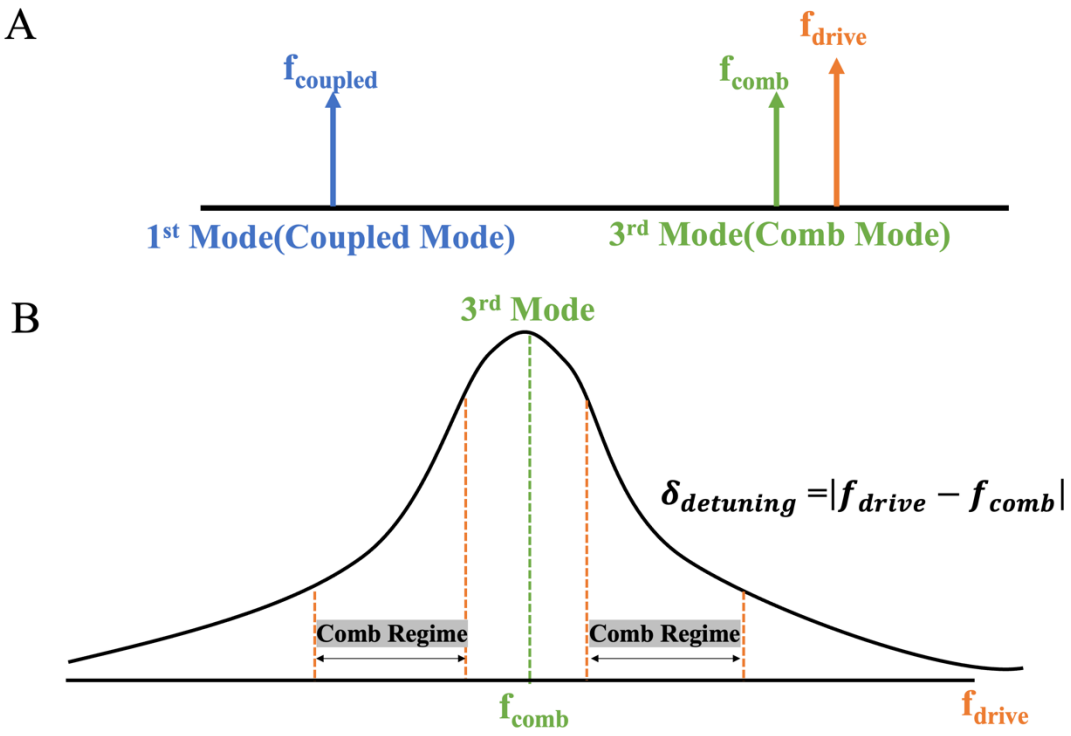

Figure 26. A: Intermodulation involving three distinct signals from the comb mode, coupled mode, and drive signal. B: Depiction of the comb regime and corresponding detuning level $\delta_{detuning}$.

From Figure 27. A, when directly driving and targeting the third mode as the comb mode with $\delta_{detuning} = 0$Hz, both the comb mode at 578.4 Hz and the coupled mode at 289.1 Hz are excited.

The harvester's electrical output was then recorded across its top and bottom electrodes. In the frequency domain, the electrical output shows a significant amplitude corresponding to the two modes. When slightly moving the driving signal off the 3rd mode (comb mode) with a 10 Hz detuning level and same driving acceleration of 0.07 g, the system response demonstrates emergence of a frequency comb spectrum at the driven mode, coupled mode and resulting harmonics. It is worth noting that the peak at 876.6 Hz is a higher-order harmonic, mirroring the peak at 289.1 Hz with respect to the central peak at 578.4 Hz in the frequency domain. These peaks correspond to triggered higher-order harmonics, indicating non-linear signal mixing between the drive and comb modes. The comb spacing between adjacent comb lines in the spectrum shown in Figure 27. B is equal to the detuning level of 10 Hz. The nominal value of the harvester electrical impedance is measured to be 400,000 Ω, and for energy harvesting experiments, a matched external load resistor is employed for power transfer. When driven with a single-tone signal in the frequency comb mode, a total output power of 14.74 μW is measured under 0.07 g acceleration, which is significantly improved compared to direct excitation case of 4.03 μW for the non-comb mode at the same acceleration level. For an elevated base acceleration of 0.39 g, the measured output power level was found to increase to 0.22 mW at a detuning level of 6Hz.

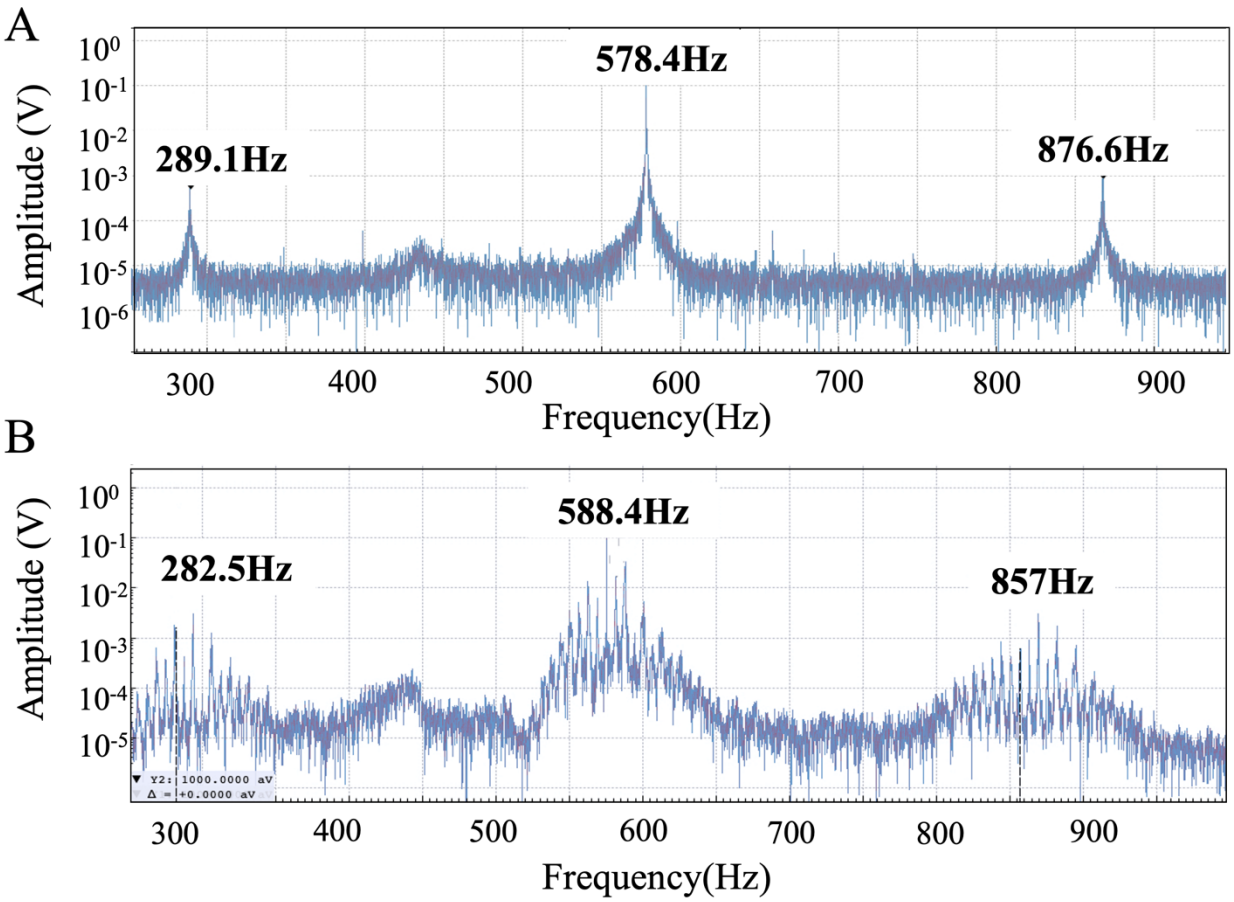

Figure 27. A: Spectrum indicating internal resonance and mode coupling when driving with a single tone signal at 578.4Hz. B: Spectrum characterizing frequency combs when driving with a single tone signal at 588.4Hz and 10Hz detuning level.

To further characterize the output power performance of the frequency comb harvester, the comb bandwidth is studied as a critical parameter. Experimental observations reveal that both the detuning factor and the driving level predominantly influence the comb spacing and the number of comb fingers, contributing to the overall comb width. This width is defined as the frequency range exhibiting a valid frequency comb on the frequency spectrum. A far-detuned vibration signal results in a weak mode coupling and requires a high driving acceleration threshold to induce frequency comb response. In return it yields large comb spacing but reduced comb density. On the other hand, a near-detuned signal requires a lower driving threshold, and it generates a comb with high density but narrow spacing. This situation presents a clear tradeoff between comb spacing and density. Achieving optimal comb bandwidth, therefore, requires a careful balance between these two aspects through careful adjustments in detuning and base acceleration levels

A further consideration is the assessment of the device's response when subjected to base vibrations that more closely resemble real-world environments, where vibration signals are inherently noisy and encompass a broad frequency range. In this research, the proposed VEH was tested with band-limited vibration noise to simulate a more real-world vibration environment. The shaker is driven by an electrical signal characteristic of band-limited noise and the electrical output of the harvester is then logged and displayed on an oscilloscope. As shown in Figure 28. A, a random noise signal was generated and filtered through a -20 dB passband filter between 300 Hz and 650 Hz. The measurements were repeated for several trials with the driving signals generated independently each time yielding consistent experimental results. The resulting response shows a broadband frequency comb response in contrast to single tone excited case. With multiple modes and harmonics engaged, the frequency comb spans most frequencies in the range between 100 Hz and 1.4 kHz. This result also has implications for other applications where frequency combs spanning multiple harmonics are of interest.

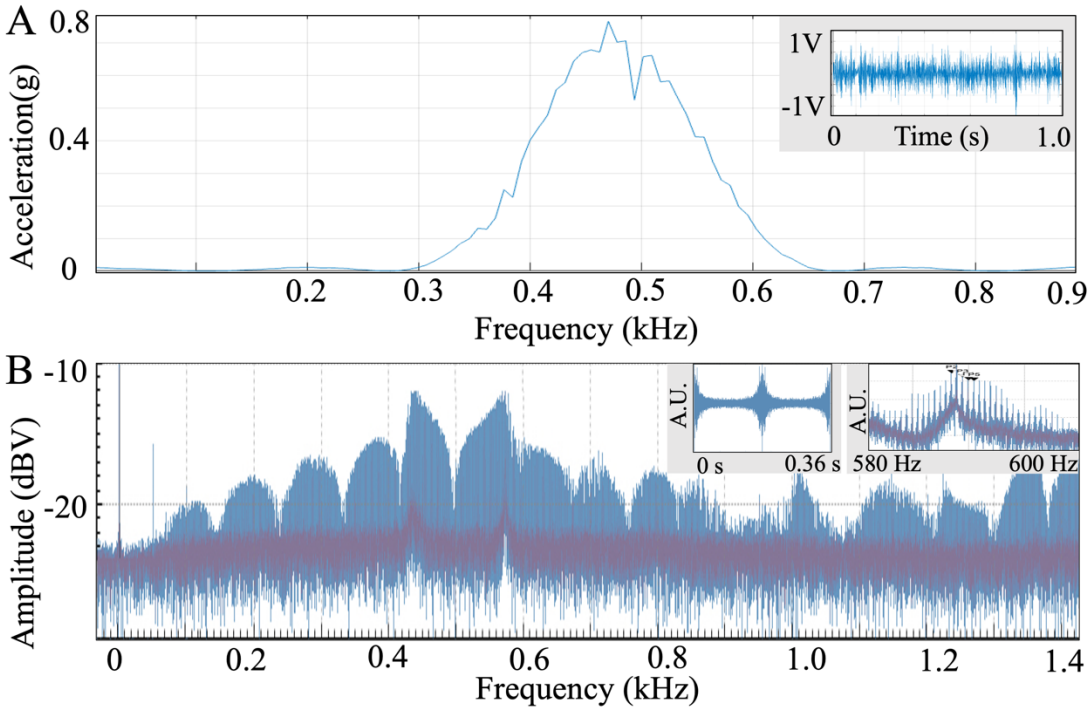

Figure 28. A: Band-limited noise spectrum (with inset showing the corresponding time-domain) of the electrical signal used to drive the shaker. B: Output spectrum of the frequency comb driven by noise with the response spanning multiple harmonics.

3.2.4 Conclusion

In conclusion, this study integrated the frequency comb concept, traditionally explored within the photonic field, into the domain of energy harvesting by developing a MEMS vibration energy harvester that exhibits frequency comb behavior under mechanical excitation. Such phenomena can enhance the harvested energy relative to vibration energy harvesters based on linear resonance. We measured an output power of 0.22 mW for a de-tuned sinusoidal excitation of 0.39 g. Significant improvements are also seen under driving conditions representative of practical environments where the ambient vibration can be noisy. The experiments validated the applicability of frequency comb concepts to energy harvesting and provided new insights into the behavior and characteristics of frequency comb phenomena under varying mechanical drive conditions. It was observed that base acceleration and frequency detuning critically affect the comb density and bandwidth, influencing the emergence and development of the frequency comb. Additionally, system damping could be effectively managed through methods such as vacuum packaging, which is anticipated to lower the activation threshold for frequency comb phenomena, thereby facilitating easier modulation of modal responses. Future work to develop detailed physical models of the underlying dynamics can enable improvements in performance including engineering the onset of frequency comb phenomena at reduced input acceleration thresholds and allowing for enhanced response bandwidth.

Chapter 4

Piezoelectric Micromachined Ultrasonic Transducers

4.1 State of the art: Micromachined Ultrasound Transducers

The conversion of kinetic energy from internal organ movements into sustainable power represents a potential avenue for energy conversion for medical implants. Simultaneously, the need for a safe, stable, and powerful energy source that can consistently deliver power—and potentially communication signals—to deeply implanted devices has led to the exploration of power and data telemetry through electromagnetic (EM) radiation. This technology is already employed in certain medical devices, such as cardiac pacemakers and neurostimulators, to establish a communication link between the implant and an external controller. However, the use of EM radiation is limited by the high impedance of body fat and human tissue, necessitating the maintenance of a low safety threshold for EM power to mitigate the risks of excessive heating and tissue damage. Furthermore, traditional EM receivers, including radiofrequency (RF) coils and antennas, occupy considerable space within medical implants. This spatial requirement obstructs the development of more compact devices and affects overall system integrity.

In recent years, ultrasound technology has attracted increasing attention for its superior biosafety, stability, and potential in power delivery and communication protocols for medical devices and challenging operational environments, such as deep-sea exploration and environments with hazardous chemicals [25]. Traditional ultrasound transducers, typically utilizing bulky piezoelectric materials like PZT and 1-3 piezo composites, are extensively used in biomedical imaging and non-destructive testing (NDT). Despite their high sensitivity in ultrasound transmission, these transducers are characterized by high power consumption and significant physical dimensions, making them unsuitable for integration into miniaturized implants for next-generation medical advancements.

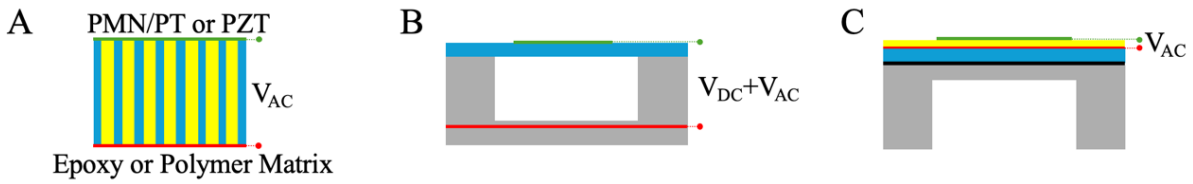

Figure 29. A: traditional composite PMN/PT or PZT bulky US transducer. B: capacitive micromachined ultrasonic transducer requiring a high DC bias voltage on top of AC drive signal. C: piezoelectric micromachined ultrasonic transducer requiring only AC driving signal on electrodes across piezoelectric layer.

The advent of microelectromechanical systems (MEMS) technology has facilitated the development of micromachined ultrasound transducers (MUTs), which are markedly smaller in both dimensions and power requirements. This advancement allows for the creation of high-density transducer arrays for diverse applications. MUTs primarily operate on the principle of flexural vibration of a thin membrane, generating and receiving acoustic pressure across various media. There are two primary categories of MUTs, based on their drive conditions: capacitive micromachined ultrasonic transducers (CMUTs) and piezoelectric micromachined ultrasonic transducers (PMUTs).

CMUTs consist of a minimal parallel plate capacitor arrangement, with one electrode fixed on a flexible, suspended membrane and another electrode fixed on a substrate. Applying a DC bias across these electrodes induces an electrostatic attraction, deforming the suspended membrane. Superimposing an alternating voltage on this DC bias modulates the electrostatic force, causing the membrane to vibrate and generate ultrasound at the modulation frequency. CMUTs, a relatively mature technology, have been extensively studied and applied in various fields, such as range finding, biomedical imaging, and vital signs monitoring [68-71]. Notably, pioneering works by Chen et al., Caronti et al., and Oralkan et al. have contributed to the development of high-frequency CMUTs, with operational frequencies exceeding 10MHz for biomedical imaging. These advancements not only meet but surpass the expectations set by conventional medical transducers, enhancing transducer bandwidth and thereby improving axial imaging resolution [72-74]. Additionally, researchers such as Lim et al., Zahorian et al., Wygant et al., Wang et al., and Yeh et al. have advanced the technology further by reducing the dimensions of CMUTs and integrating these transducers with small catheters for applications in intravascular imaging [75-79]. Despite their advantages, including superior signal and imaging resolution at frequencies above 1 MHz and the potential for integration with front-end electronic interfaces (e.g., CMUT-on-CMOS techniques), their application in wireless power transmission, data communication, and vital signs monitoring remains limited. One significant

limitation of CMUTs is the requirement for a high DC bias voltage (>100V), which presents substantial challenges for miniaturization and use in portable, battery-operated monitoring devices or implantable medical devices where biosafety and power consumption are critical considerations. Moreover, while CMUTs' capacitance changes more effectively at higher frequencies—where rapid membrane movements can induce a stronger and quicker change in electrical characteristics—the efficiency at lower frequencies is compromised. At these frequencies, ultrasound propagates with less attenuation, but the slower membrane movement results in less effective capacitance change. This efficiency drop necessitates either higher voltages or a larger silicon area, thus limiting the integration of CMUTs into compact and efficient biomedical devices [80]. PMUTs, on the other hand, offer a promising alternative that addresses these challenges. They facilitate the development of high-density transducer arrays that support efficient power and data transmission, as well as long-term monitoring with minimal power consumption, all without the need for high voltage bias. This positions PMUTs as an optimal choice for the next generation of medical devices and applications that require compactness, efficiency, and safety.

4.2 Piezoelectric Micromachined Ultrasonic Transducers

Piezoelectric micromachined ultrasonic transducers (PMUTs) share a structural similarity with capacitive micromachined ultrasonic transducers (CMUTs), possessing a thin suspended membrane that is located above a hollow cavity in the substrate. This membrane typically consists of electrodes on top of a piezoelectric layer and a structural layer. The piezoelectric effect is harnessed to convert electrical potential applied to the piezoelectric layer into internal lateral strain, resulting in membrane deformation. The flexural resonant frequency of a PMUT is influenced by a number of factors, which include, but are not limited to, mechanical stress, membrane shape, and boundary conditions. By driving the piezoelectric layer with an alternating current (AC) at the resonant frequency, the membrane undergoes maximum deflection vibration, thus generating ultrasound in the acoustic domain. PMUTs not only share the advantages of CMUTs, such as miniaturization and batch manufacturing capabilities for chip-scale arrays but also overcome a primary limitation of CMUTs by eliminating the need for a DC bias. Advances in thin piezoelectric film deposition technology have positioned PMUTs as a viable option for creating powerful, compact ultrasound transducers, drawing increased attention in recent years with significant research spanning multiple applications. Without the critical electrical drive requirements, such as the high DC bias voltage necessary for CMUTs, PMUTs present more opportunities for application in a broader range of promising industries.

Illustrative of their versatility, Sun et al. developed a 15 by 15 PMUTs array operating at a fundamental mode of 1 MHz [81]. Given the irregular spherical shape of the human eyeball, where the corneal position is slightly convex relative to the sclera, variations occur in the distances from the PMUT array to the cornea and sclera as the eyeball rotates. These distance changes lead to modifications in the time-of-flight (TOF) measurements, varying from 6 μs to 16 μs, allowing for the precise tracking of eyeball motion. The compact (2.5 mm by 2.5 mm) and lightweight (under 25 mg) PMUTs array was tested across multiple volunteers and successfully tracked eyeball rotation. Building on this technology, further research by Halbach et al. and Pala et al. underscores PMUTs' potential in developing high-density arrays for haptic and fingerprint sensing [82, 83]. These arrays, consisting of 64×64 and 12×12 elements, operate at fundamental mode resonant frequencies of 390 kHz and 109 kHz, respectively. Unlike CMUTs, which face efficiency challenges at sub-MHz frequencies, these PMUTs are designed for low-frequency operation, achieving high transmitting sensitivity (8.6 Pa/V and 79 Pa/V) and sufficient acoustic pressure to be perceived by human skin. Jiang et al. advanced this technology by developing a 65×42 PMUTs array with beamforming capabilities, crucial for high-contrast fingerprint image reconstruction [30]. Successfully commercialized when integrated with a CMOS interface, this innovation leverages the CMOS compatibility of AlN-PMUTs, demonstrating significant promise for next-generation application in consumer electronics market. These PMUTs research not only proves the efficacy of PMUTs in enhancing user interaction technologies but also sets a precedent for their application in more complex Internet of Things (IoT) systems, such as such as virtual reality (VR) and augmented reality (AR) environments.

Simultaneously, the field of medical diagnostics recognizes ultrasound technology as a powerful and safe tool, with innovative PMUT technology being explored to maximize ultrasound's potential in implantable medical devices (IMEs). Ding et al. developed a PMUTs chip comprising 6 channels, each with 23×26 PMUTs [84]. Utilizing four channels for transmitting and two for receiving, this array effectively employed a quadrature demodulation method to extract Doppler frequency shifts and measure real-time pulsatile flow velocities in a blood-mimicking vessel. Li et al. further demonstrated the capabilities of a high-density PMUTs array by employing a pair of 25×25 arrays at a fundamental mode frequency of 7.1 MHz for both Doppler flow measurements and 3D vascular imaging using Synthetic Aperture Focusing Techniques (SAFT) [85]. This and other concept validation research show PMUT's robust performance across various biomedical applications, where

its CMOS compatibility significantly enhances both power and spatial efficiency. For instance, Tillak et al. developed a CMOS-compatible PMUTs array, embedded directly with a frontend interface fabricated for Doppler ultrasound using standard 65nm 1P7M CMOS technology [86]. The entire chip, sized at 200×300 μm, consumes as little as 17.3 μW of power during operation—less than half the power required by comparable CMUTs research, which averages 39.4 μW. These innovations have led to the development of stable, continuous, and low-power Doppler flowmeters in biomedical contexts.

These studies have demonstrated the efficacy and capabilities of PMUTs in various applications, highlighting their low power consumption and reduced size compared to traditional ultrasonic transducers. Moreover, the custom structural design of PMUTs, facilitating operation across various modes and frequencies, addresses the traditional trade-offs between frequency, sensitivity, and bandwidth in ultrasound transducer design. Sun et al. and Shi et al. have exploited PMUTs' multifrequency capabilities by optimizing the length-to-width ratios of rectangular-shaped devices to induce an overlap between different flexural modes [35, 87]. This approach has expanded bandwidths significantly, achieving −6 dB bandwidths of 112% and 73.7% for applications in wireless power transfer and energy harvesting. The multifrequency capability of PMUTs has been tested across several demanding ultrasound applications, showing notable improvements. For instance, traditional ultrasound transducer designs often face a dilemma in balancing imaging resolution and penetration depth by adjusting operating frequencies. By operating PMUTs beyond their fundamental modes, it is possible to effectively address these performance trade-offs. Billen et al. designed a CMOS-compatible PMUT capable of operating from 7 to 20 MHz, enhancing multi-frequency imaging capabilities [88]. Although higher-order modes exhibit reduced imaging quality due to limited sensitivity, these PMUTs have successfully demonstrated visible ultrasound imaging capabilities. For example, a prototype driven at a fundamental mode of 6.6 MHz displayed distinct imaging of two nylon threads at approximately 6 mm depth, and also performed effectively at higher frequencies for more complex imaging tasks. Despite with reduced imaging quality towards higher-order mode due to limited sensitivity, the PMUTs still successfully exhibited visible ultrasound imaging capability on 2 nylon threads target at approximately 6 mm depth. Moreover, Wang et al. employed a multi-frequency PMUTs array for photoacoustic imaging, where the transducer’s bandwidth is crucial in capturing the broad and unpredictable acoustic signals emitted from the photoacoustic effect [89]. By integrating the broader bandwidth benefits of higher modes with the superior sensitivity of the fundamental mode, the developed PMUTs exhibit enhanced photoacoustic imaging performance.

Similarly, Wang et al. targeted the same multi-frequency PMUTs but utilized an unconventional method that does not require switching the drive signal's frequency [90]. Their PMUTs array, fabricated with strongly polarized ferroelectric material PZT, can switch between two driving modes at 5 MHz and 10 MHz under a single AC drive signal at 5 MHz. This innovative approach was tested for fingerprint imaging and showed an improved balance of lateral and axial resolution, combining the benefits from both low- and high-frequency ultrasound. This series of advancements underscores the potential of PMUTs to significantly enhance traditional and emerging ultrasound applications, paving the way for broader adoption and further technological development.

Continuing this line of research, we are exploring PMUTs' multifrequency capabilities not only by studying the mechanical structure of the membrane but also by enhancing their performance and electromechanical coupling efficiency with customized electrodes based on designated modes. These methods have been applied to a variety of traditional and innovative ultrasound applications, validating the efficiency of these customized PMUT arrays.

4.3 Numerical Analysis: Equivalent Circuit Method

The Piezoelectric Micromachined Ultrasound Transducer (PMUT) operates on the principle of generating or receiving ultrasound waves through the vibration of a piezoelectric plate. This vibration, facilitated by the piezoelectric effect, bridges the mechanical and electrical domains. Typically, PMUT designs feature a piezoelectric plate positioned atop a hollow cavity, clamped at its edges. In this section, a comprehensive numerical analysis is presented to model a circular PMUT's single- and multi-modal behavior, a cornerstone for optimizing device performance across electrical, mechanical, and acoustic domains [91, 92]:

$$D\nabla^4 w + \rho h \frac{\partial^2 w}{\partial t^2} = f \tag{36}$$

Here D represents the flexural rigidity, ρ is the mass density; h is the thickness of the plate; transverse displacement $w(r, \theta, \mathrm{t})$ is defined by polar coordinates r and θ across the surface of circular membrane; t is time; f is the external force per unit area. The Laplacian operator ∇^2 in polar coordinates is defined as:

$$\nabla^2 = \frac{\partial^2}{\partial r^2} + \frac{1}{r}\frac{\partial}{\partial r} + \frac{1}{r^2}\frac{\partial^2}{\partial \theta^2} \tag{37}$$

Differential operator ∇^4 and governing Equation (31) can be solved by using separation of variables for time and spatial coordinates respectively [93]. As a result, the governing equation of transverse displacement *W(r,θ)* has a general solution in the form of:

$$W(r,\theta) = AJ_m(\lambda_{m,n}r) + BI_m(\lambda_{m,n}r) \tag{38}$$

where J_m and I_m are Bessel functions of order m of the first kind and hyperbolic form respectively, and A and B are constants. λ is a mode shape and frequency dependent parameter referring to specific modes, which is denoted by m the number of nodal diameters, n the number of nodal circles and angular frequency $\omega_{m,n}$ of mode (m, n). λ is defined as:

$$\lambda^4 = \frac{\rho h {\omega_{m,n}}^2}{D} \tag{39}$$

For a circular PMUT design with radius a and clamped at its edges, the deflection can be further solved by the boundary conditions $W(a, \theta)=0$ and $(dW/dr)_{r=a}=0$. So that the equation (33) becomes:

$$W(r,\theta) = \left[J_m(\lambda r) - \frac{J_m(\lambda a)}{I_m(\lambda a)} I_m(\lambda r)\right](A_m \cos m\,\theta + B_m \sin m\,\theta),\ m = 0,1,2 \ldots \tag{40}$$

For simplicity, when only considering its symmetric modes for possibly maximal volumetric velocity and acoustic transmitting sensitivity, PMUT's number of nodal diameters m equals to zero ($m=0$). Thus equation (35) is simplified to

$$W(r,\theta) = J_0(\lambda_{0,n}r) - \frac{J_m(\lambda_{0,n}a)}{I_m(\lambda_{0,n}a)} I_m(\lambda_{0,n}r) \tag{41}$$

Where a is the radius of PMUT and r is the radial coordinate. Mode dependent parameter λ is defined normalized to PMUT radius as [94]:

$$\lambda_{0,n} = \frac{\gamma_{0,n}}{a} \tag{42}$$

For a circular PMUT clamped at its edges, the static deformation pattern and normalized mode shape across mode (0, n) from COMSOL simulation and harmonic approximation are compared in Figure 30 below:

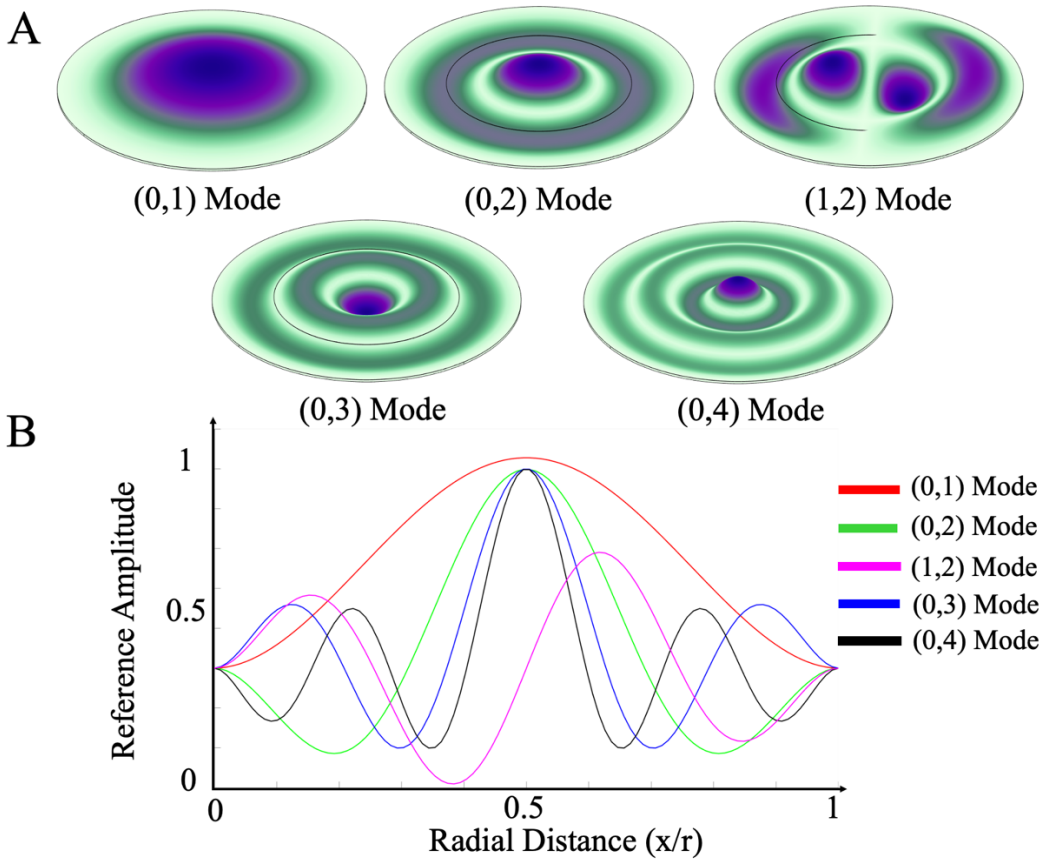

Figure 30. A: COMSOL simulated mode shape for (0,1), (0,2) and (0,3) modes. B: Deflection profile of numerical analysis results.

And by combing Equation (36) and (37), with converting angular frequency into frequency with relationship $\omega = 2\pi f$, the resonant frequency of mode (*0, n*) becomes

$$\omega_{0,n} = \frac{\gamma_{0,n}{}^2}{2\pi a^2}\sqrt{\frac{D}{\rho h}} \tag{43}$$

Where $\gamma_{0,n}$ are mode-specific constants related to the geometry and boundary conditions of the PMUT. are shown in Table 2 below.

Table 2. Mode-specific constants for first five modes of the circular PMUT clamped at edges.

Mode	$\gamma_{0,n}$
(0,1)	3.189
(0,2)	6.305
(1,2)	7.8
(0,3)	9.424
（0,4）	12.566

While plate theory studies PMUT's mode shape and resonant frequencies, there's a need to study and link PMUT's mechanical response to electrical and acoustic domains for actual applications. The Mason's equivalent method is designed to also address electrical and acoustic domains and simplify the modelling by translating parameters into circuit elements, thereby facilitating more intuitive calculations [95, 96]. This process involves the use of a 2-stage transformer concept that bridges the electrical, mechanical, and acoustic domains. As shown in Figure 32, the equivalent circuit is formed by several lumped elements, which represent PMUT and its operation's characteristics. The Rayleigh Ritz energy method is adopted to transform the PMUT response in each domain into equivalent electrical elements. The electrode design, focusing on shape and coverage, along with the transducer material's piezoelectric coupling coefficient, play a pivotal role in converting electrical energy into mechanical vibrations. Under electrical or acoustic drive, the electrodes surrounding the AlN layer link the mechanical strain across the piezoelectric material to the electrical domain. The top electrode is crucial for maximizing coupling efficiency. The mechanical strains covered by the electrode are given by

$$I_p = \int_{A_{\text{electrode}}} \left(\frac{d^2w(x)}{dx^2} + \frac{1}{x}\frac{dw(x)}{dx}\right) dA_{\text{electrode}} = 2\pi \int_{r_1}^{r_2} \left(\frac{d^2w(x)}{dx^2} + \frac{1}{x}\frac{dw(x)}{dx}\right) x\ dx \qquad (44)$$

Optimizing electrode design for different mode shapes is essential for achieving maximal electromechanical coupling efficiency, especially in multi-mode operations where different strain distributions across modes need to be considered. This involves balancing the trade-off between coupling efficiency and charge cancellation in areas covered by the electrode [97, 98]. Assuming a PMUT having a thin layer of AlN comparing to the thickness of structure layer ($h_{AlN} << h$), the radial σ_r and tangential σ_θ stresses across membrane can be derived from generation Equation (40) and (41) as

$$\sigma_r = -\frac{E}{1-v^2}\left(\frac{d^2w(r)}{dr^2} + v\frac{1}{r}\frac{dw(r)}{dr}\right)\frac{h}{2} \quad (45)$$

$$\sigma_\theta = -\frac{E}{1-v^2}\left(\frac{1}{r}\frac{dw(r)}{dr} + v\frac{d^2w(r)}{dr^2}\right)\frac{h}{2} \quad (46)$$

For instance, if only targeting the (0,1) mode, the PMUT's electrode should cover as much area as possible within same strain polarity, and extend to a critical radius where radial and tangential stresses sum to zero $\sigma_\theta + \sigma_r = 0$. This relationship is illustrated in Figure 31. B, which shows the critical electrode radius at a√2/2.

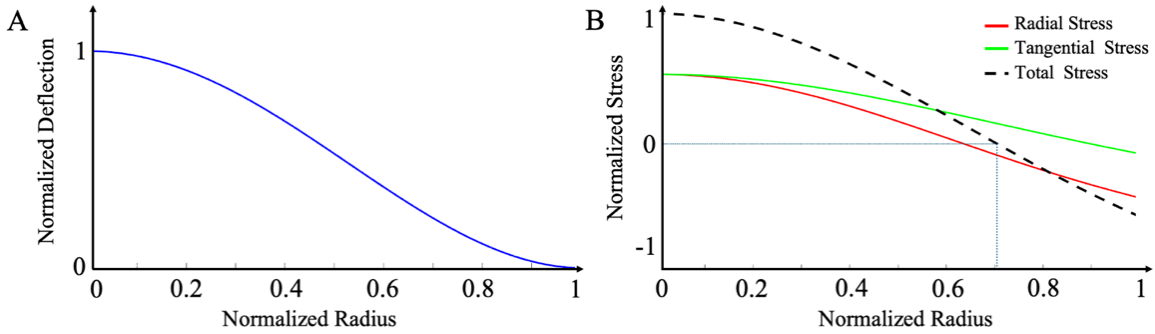

Figure 31. A: Normalized deflection profile of a circular PMUT at fundamental mode. B: Radial, tangential and total stress under fundamental mode. The electrode aims to match a critical radius at √2/2 when total stress equals flip the polarity.

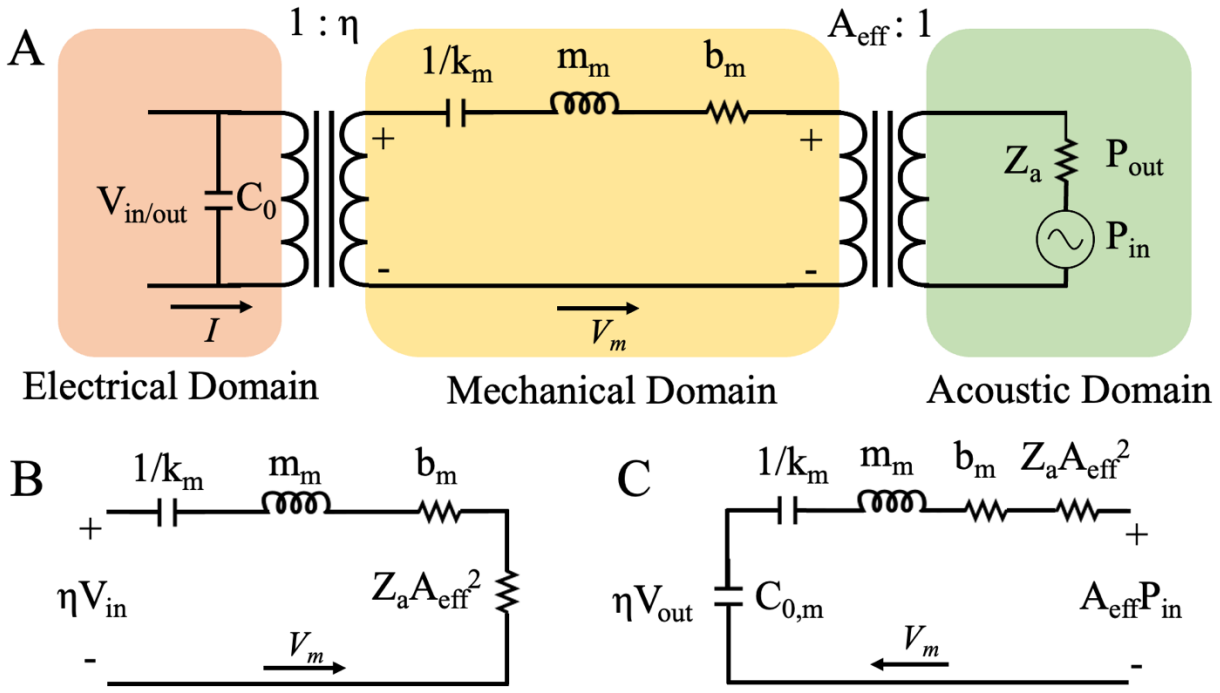

Figure 32. A: Mason's equivalent circuit diagram representation in the electrical, mechanical, and acoustic domains. B: Butterworth–Van dyke (BVD) equivalent circuit converted in mechanical domain only, when the PMUT is employed as transmitter. C: BVD equivalent circuit in electrical domain only, when the PMUT is employed as receiver. $C_{0,m}$ is modified static capacitance in mechanical domain.

To establish a connection between the electrical and mechanical responses of a PMUT, we define a transformer's turn ratio, η is defined as $\eta = \frac{F_e}{V}$ using electrical enthalpy method, and V is electrical potential across electrode and F_e is effective piezoelectric force. This force is then divided by the RLC circuit to determine the current.

$$\eta = e_{31,f} Z_p I_p = \frac{1}{2} e_{31,f} h_{Si} I_p \tag{47}$$

$e_{31,f}$ is 31-mode piezoelectric coefficient of AlN, and h_{Si} is the thickness of doped *Si* layer. The equivalent electrical components inductor m_m, capacitor k_m, and resistance b_m represent equivalent mechanical mass, stiffness and damping correspondingly. Equivalent mass m_m is derived as $m_m = \frac{1}{2}\left(\frac{\gamma_{o.n} J_0(\gamma_{o.n})}{2J_1(\gamma_{o.n})}\right)^2 \frac{\pi D}{a^2}$ and stiffness k_m is $\frac{{\gamma_{o.n}}^4}{2}\left(\frac{\gamma_{o.n} J_0(\gamma_{o.n})}{2J_1(\gamma_{o.n})}\right)^2 \frac{\pi D}{a^2}$. Most PMUTs operate in the MHz range, and the dimension of a single PMUT is generally large compared to the wavelength. Therefore, the mechanical damping b_m such as viscous damping and anchor is typically much smaller than the

radiation impedance Z_a of the PMUT in the acoustic domain, and can be neglected from the equivalent circuit calculation. We also introduce another transformer concept that relates the mechanical vibration of the PMUT to the acoustic response. Given the minimal physical dimension of the PMUT, the vibration of a single clamped transducer can be simplified as a moving piston. We define another turn ratio, A_{eff} (the effective piston area), to convert the vibration amplitude of the PMUT into acoustic output. The effective area can be calculated by integrating over the surface with the Bessel function and boundary conditions [47].

$$A_{eff} = \frac{F_{surface}}{P_{surface}} \tag{48}$$

For a circular membrane clamped at its edges, the effective area can be solved integrating over the surface with Bessel function $J_{0,n}$ and boundary conditions

$$A_{eff} = \iint W(r,\theta)dS = \int_0^a J_0(\lambda_{0,n}r) - \frac{J_m(\lambda_{0,n}a)}{I_m(\lambda_{0,n}a)} I_m(\lambda_{0,n}r)dr \approx 2\pi a^2 \frac{J_1(\gamma_{0,n})}{\gamma_{0,n}} \tag{49}$$

Selective effective area of symmetric modes are listed in Table 3 below.

Table 3. Effective area for first five symmetric modes of a circular PMUT.

Mode	$\mathbf{A_{eff}/A_{PMUT}}$
(0,1)	0.312
(0,2)	-0.163
(0,3)	0.073
(0,4)	-0.045

As expected, the effective areas for the higher-order radial modes progressively diminish due to counteractive effects generated by neighboring regions marked by nodal circles. These regions exhibit out-of-phase movements relative to each other, leading to a cancellation effect. Therefore, in subsequent experiments, it is preferred to combine modes with the same polarity of effective area for optimized dual-channel response. Beyond the effective area, we introduce the radiation impedance, Z_a, which facilitates the conversion of force and flow into ultrasound output in the acoustic domain. The radiation impedance is thus defined as the ratio of surface acoustic pressure to the surface velocity:

$$Z_a = \frac{P_{surfacae}}{v_a} = \frac{\iint p(r,0)dA}{v_a} = R_a + iX_a = \frac{\rho_m c_m}{\pi a^2}(r_a + ix_a) \quad (50)$$

Here, ρ_m and c_m are density and speed of sound in the medium. The radiation impedance consists of a resistive component R_a and a reactive component X_a, and r_a and x_a are dimensionless resistive and reactive terms, which can be extracted from FEM analysis or solved mathematically as

$$r_a = 1 - \frac{2J_1(2ka)}{2ka} \quad (51)$$

$$x_a = \frac{2K_1(2ka)}{2ka} \quad (52)$$

where J_1 is the first order Bessel function and K_1 is the first order Struve function [99]. Both r_a and x_a values can be determined by the multiply ka, the wave number k and radius a of PMUT.

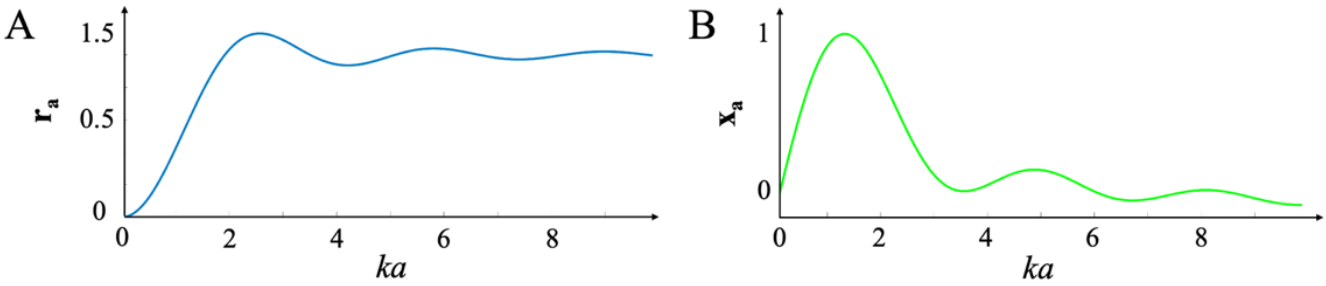

Figure 33. Dimensionless resistance r_a (A) and reactance x_a (B) components of the radiation impedance for the rigid piston mode.

Generally, ultrasonic transducers operate in the low ka << 1 regime, where the wavelength is significantly longer than the transducer size. The acoustic response of PMUTs can be approximated as behaving like a point source. Thus, the resistive and reactive components of the radiation acoustic impedance are analyzed using a piston vibrator approximation, with the results plotted in Figure 33. As a summary, the lumped parameters of first 4 symmetric modes for the equivalent circuit are listed in the table below.

Table 4. Equivalent circuit parameters obtained from exact solution for first 4 symmetric modes.

Mode	(0,1)	(0,2)	(0,3)	(0,4)
Resonant Frequency $f/f_{(0,1)}$	1	3.893	8.279	15.484
Shunt Capacitance C_0	$\varepsilon_0 \frac{A_e}{h_{AlN}}$	$\varepsilon_0 \frac{A_e}{h_{AlN}}$	$\varepsilon_0 \frac{A_e}{h_{AlN}}$	$\varepsilon_0 \frac{A_e}{h_{AlN}}$
Turn Ratio	$-0.98\pi e_{31,f} h_{Si} I_p$	$0.811\pi e_{31,f} h_{Si} I_p$	$0.79\pi e_{31,f} h_{Si} I_p$	$-2.33\pi e_{31,f} h_{Si} I_p$
Mass m_m	$0.2\pi a^2 I_0$	$0.65\pi a^2 I_0$	$1.29\pi a^2 I_0$	$2.28\pi a^2 I_0$
Stiffness $k_m = \frac{1}{C_m}$	$20.78 \frac{\pi D}{a^2}$	$1.03 \times 10^3 \frac{\pi D}{a^2}$	$1.02 \times 10^4 \frac{\pi D}{a^2}$	$5.7 \times 10^4 \frac{\pi D}{a^2}$
Effective Area Ratio A_{eff}	0.312	-0.163	0.073	-0.045
Radiation Impedance Z_a	$\frac{\rho_m c_m}{\pi a^2}(r_a + i x_a)$	$\frac{\rho_m c_m}{\pi a^2}(r_a + i x_a)$	$\frac{\rho_m c_m}{\pi a^2}(r_a + i x_a)$	$\frac{\rho_m c_m}{\pi a^2}(r_a + i x_a)$

When driving the PMUT for transmitting purpose at a single vibration mode, the surface output pressure is related the diaphragm vibration velocity v_m, which can further be solved from transformer's relation in equivalent circuit.

$$P_{out} = v_m Z_a A_{eff} = 2\pi f d_p Z_a A_{eff} = \frac{Z_a A_{eff} \eta}{j\omega m_m + {A_{eff}}^2 Z_a + \frac{1}{j\omega C_m}} V_{in} \tag{53}$$

Where transmitting sensitivity of PMUT at a single mode becomes:

$$\frac{Z_a A_{eff} \eta}{j\omega m_m + {A_{eff}}^2 Z_a + \frac{1}{j\omega C_m}} \quad (Pa/V) \tag{54}$$

Similarly, when driving the PMUT in receiving mode, the output voltage from PMUT at a single mode becomes

$$V_{out} = \frac{P_{in} A_{eff}}{\eta} \frac{\frac{1}{j\omega C_{0,m}}}{\frac{1}{j\omega C_{0,m}} + j\omega m_m + \frac{1}{j\omega C_m}} = \frac{P_{in} A_{eff}}{\eta} \frac{\frac{1}{j\omega \eta^2 C_0}}{\frac{1}{j\omega \eta^2 C_0} + j\omega m_m + \frac{1}{j\omega C_m}} \tag{55}$$

Where receiving sensitivity at a single mode becomes:

$$\frac{\eta A_{eff}}{1 - \omega^2 \eta^2 C_0 m_m + \frac{\eta^2 C_0}{C_m}} \quad (V/Pa) \tag{56}$$

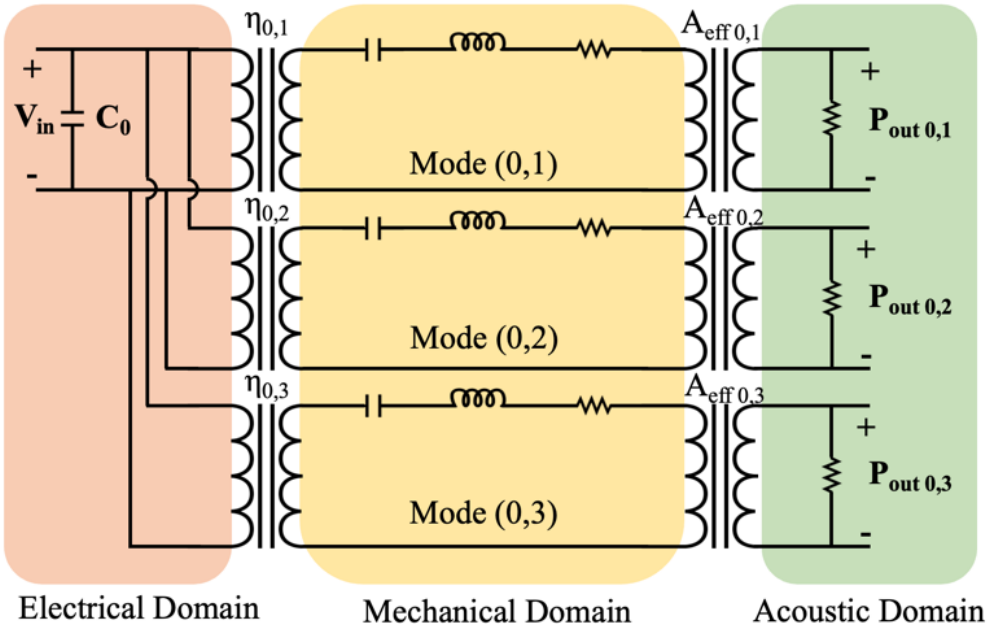

Figure 34. Equivalent circuit of three symmetric modes operating simultaneously.

Alternatively, the PMUT can be driven in more than one mode simultaneously, and a multi-channel drive scheme is adopted to transmit and receive ultrasound signals containing different frequencies using a pair of PMUTs. The drive signal contains multiple channels, each channel having its frequencies $\omega_{m,n}$, corresponding to resonant frequencies of PMUT across different modes.

$$V_{in} = \sum_{m,n} V_{m,n} \sin(\omega_{m,n} t) \tag{57}$$

For the case of our proposed circular PMUT, modes (0, 1), (0, 2) and (0, 3) are targeted, and the drive signal becomes:

$$V_{in} = V_{0,1} \sin(\omega_{0,1} t) + V_{0,2} \sin(\omega_{0,2} t) + V_{0,3} \sin(\omega_{0,3} t) \tag{58}$$

As illustrated in Figure 34, the Mason's method represents multi-channel operation with multiple parallel-connected circuits containing turn ratios and electrical components customized based on each mode. Each channel specifies a resonant mode (m, n), and when superimposing the acoustic response across multiple modes at a given channel, the PMUT has its acoustic signal intensity (Pa) at channel (m, n) as

$$\frac{\eta_{(m,n)} V_{m,n} \sin(\omega_{m,n} t)}{A_{eff(m,n)}} + V_{m,n} \sin(\omega_{m,n} t) \sum_{i,j} \frac{Z_{a(i,j)} A_{eff(i,j)} \eta_{i,j}}{j\omega_{m,n} m_{m(i,j)} + {A_{eff(i,j)}}^2 Z_{a(i,j)} + \frac{1}{j\omega_{i,n} C_{m(i,j)}}} \quad (59)$$

The numerical analysis elucidated the multi-mode operation of circular PMUTs. By integrating plate theory, Bessel functions, and Rayleigh-Ritz energy method into Mason's equivalent method, a comprehensive framework was established, highlighting the interplay between the electrical, mechanical, and acoustic domains of PMUTs. The derived equations provided pivotal insights into PMUT performance across various modes. Building on this foundation, the next phase will transition from theoretical constructs to practical device design in advancing the field of ultrasound transducers.

Chapter 5

Multi-channel Piezoelectric Micromachined Ultrasonic Transducers

In the field of Piezoelectric Micromachined Ultrasonic Transducers (PMUTs), researchers are particularly drawn to the technology for its potential for miniaturization, low power consumption, and capacity for integration into high-density arrays. These attributes are essential for developing compact and efficient devices across various applications. However, much research has focused on optimizing PMUTs for single, specific applications rather than their potential in combined uses. The unique advantages of ultrasound technology, particularly at varying frequencies, are well-suited for diverse applications. For instance, in the biomedical field of study, where there is an increasing demand for compact implants and low-power sensors, a multi-frequency ultrasound system could meet the intricate network requirements for efficient power delivery, data telemetry, as well as vital parameters monitoring [100-102]. The system's versatility is underpinned by the foundational understanding that ultrasound attenuation through biological tissues varies, following $A = A_0 e^{-\alpha x}$, with A_0 and A representing the ultrasound intensity before and after propagation through a medium over distance x, and α as the attenuation coefficient. Integrating these functions into a single application could significantly advance the dual-frequency operation of PMUTs. Despite this potential, the literature on the concurrent, diverse application of PMUTs remains limited. Efforts to employ traditional ultrasound transducers for multifrequency operations have been made, achieving simultaneous power transfer and backscatter communication [103]. Yet, these approaches often place demanding performance requirements on traditional transducers, especially in terms of bandwidth and sensitivity, and typically necessitate complex additional electrical circuits for frequency multiplexing. Addressing this gap, our study introduces and examines a multi-channel PMUT system, with electrodes tailored based on mode shape and strain distribution derived from numerical and finite

element analysis (FEA) [97, 104-107]. This design innovation enables the PMUT to operate across multiple modes simultaneously, maintaining balanced sensitivity [108, 109]. Furthermore, the mode-specific electrode customization also provides selective activation of these modes, allowing a single device to harness multiple resonant frequencies through dedicated channels. This feature is pivotal for a multi-resonant mode operation, setting the stage for a broad range of applications.

5.1 Device Design

To optimize the PMUT's capability operating in multiple modes simultaneously, this study investigates various design configurations and customized electrode setups to enhance multi-channel functionality. Two distinct PMUT arrays—one circular and one square— are designed and fabricated. The circular PMUT array features 7 identically dimensioned transducers, each operating at a fundamental frequency of approximately 100 kHz. On the other hand, the square PMUT array comprises 21 individual PMUTs with fundamental frequencies spanning from 50 kHz to 1.4 MHz to investigate and compare their performance under different dimension and operating frequency. It is worth mentioning that despite specific target specifications, variations in manufacturing processes, such as over-etching during substrate etching, can slightly alter the dimensions of the structures from one device to the next within the same chip and across the wafer(s). Both circular and square designs were realized on an Aluminum Nitride-on-Silicon-on-Insulator (AlN-on-SOI) fabrication platform. The fabrication process involved the deposition of an aluminum nitride (AlN) thin film on a doped silicon device layer. A cross-sectional view of the device is depicted in Figure 35. A and B. The 10 µm doped silicon layer serves as the bottom electrode, while the top electrode is composed of a metal layer, specifically 20 nm of Chromium (Cr) and 1000 nm of Aluminum (Al).

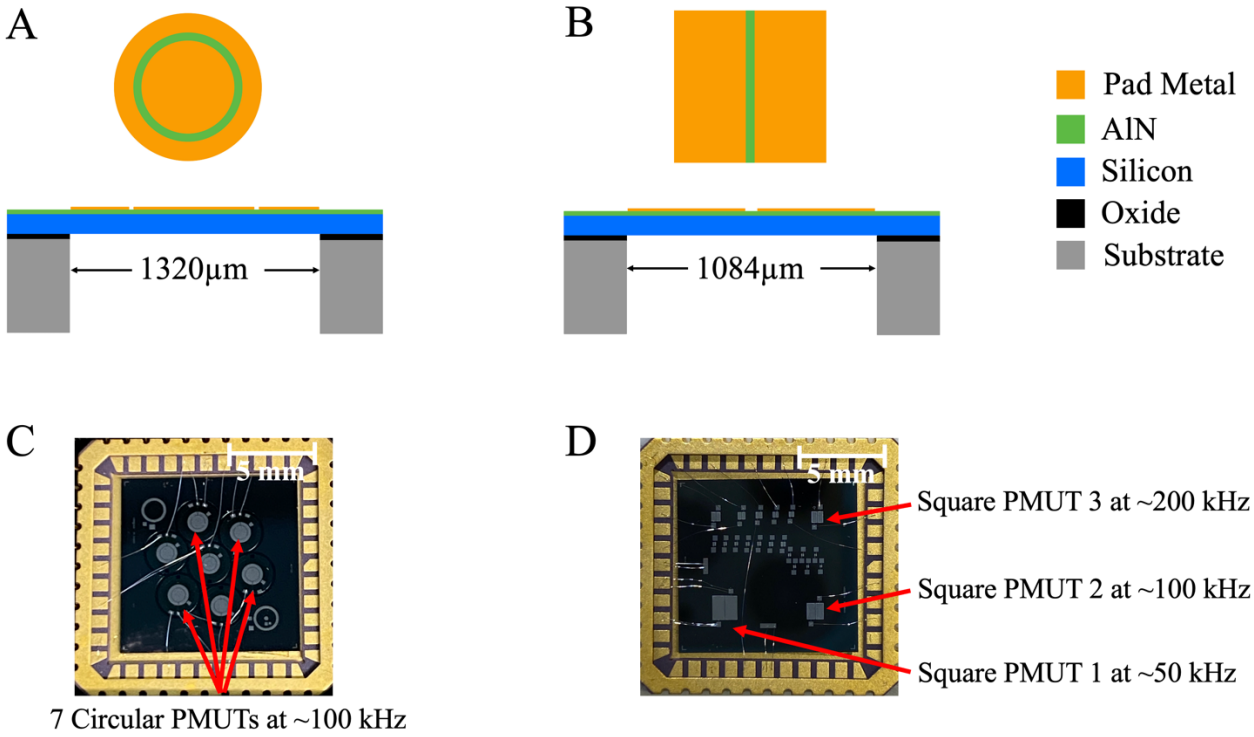

Figure 35. Top and cross-sectional views of circular (A) and square (B) PMUTs, alongside fabricated arrays of circular (C) and square (D) PMUTs.

In the experimental design, a circular PMUT is employed with fundamental (0,1) mode at approximately 100 kHz. Based on the insights gained from numerical analysis discussed in Section 4.3 and the requirements of the AlN-on-SOI structure, the circular PMUT was designed and fabricated with radius of 660 µm. To enable applications that employ higher operating frequencies, the (0,2) and (0,3) modes were incorporated into the design. As a result, a customized dual-electrode layout was developed considering the mode shape and strain distribution of the (0,1), (0,2), and (0,3) modes. Unlike standard circular PMUTs which normally have a single center electrode covering at least 2/3 of its surface area, our design strategically reduces the central electrode's coverage to 54.6% of the membrane. This reduction leaves more space for a distinctive electrode pattern that targets the deflection patterns along the borderline areas of the (0,2) and (0,3) modes, distinctly differing from the (0,1) mode. This annular ring electrode extends to the edge of the cavity and is separated from the central electrode by a 10 µm gap to minimize capacitive coupling. This dual-electrode design not only enhances the sensitivity for higher modes but also provides channel select functionality. This functionality allows for each electrode to be tuned for a response at a designated frequency channel, thereby enabling multi-frequency operation.

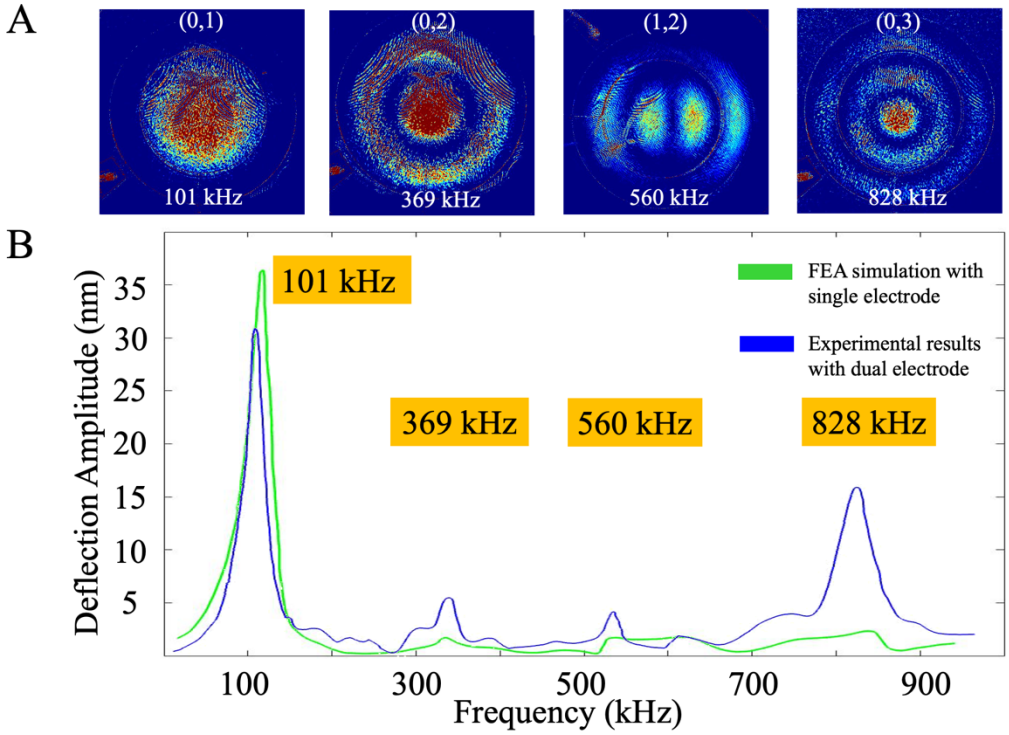

Figure 36. A: DHM recorded vibration profile of the circular PMUT. B: Frequency sweep of COMSOL simulations and experimental results for single and dual-electrode PMUTs, showing sensitivity balance improvement at 101 kHz and 828 kHz modes.

The frequency sweep characterization was conducted by electrically driving the PMUT at its central electrode over a range up to 1 MHz and selectively recording responses using a Digital Holographic Microscope (DHM). The results, presented in Figures 36, demonstrate the improved sensitivity achieved with this dual-electrode layout. In parallel, a square PMUT with dimensions of 1084 µm by 1084 µm is designed operating at a fundamental (1,1) mode at approximately 100 kHz as shown in Figure 35. D. The (1,2) mode is targeted for the square device due to its distinctive mode shape compared to the fundamental mode. To balance the sensitivity across modes, we proposed a customized dual-electrode design with each rectangular electrode 1064 µm by 527 µm and separated by 10 µm.

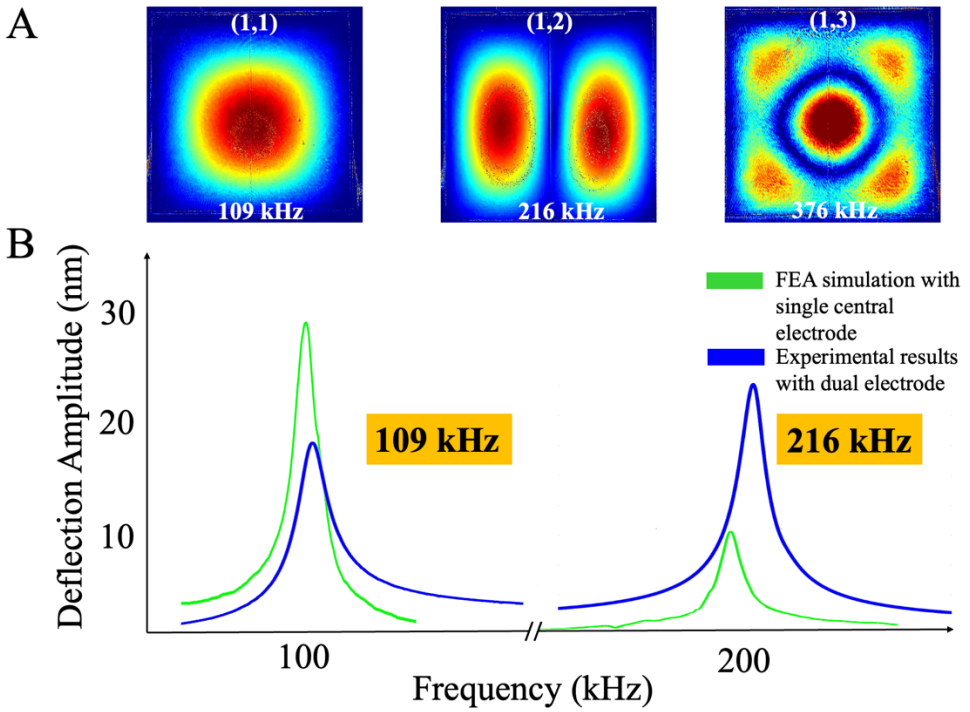

Figure 37. A: DHM recorded vibration profile of a square PMUT. B: Comparison of frequency response between COMSOL simulations for a single electrode design and experimental data from a fabricated PMUT with dual electrodes, illustrating the enhanced sensitivity achieved with the dual electrode configuration.

Within the square PMUTs array, 3 square PMUTs are designed with target fundamental mode frequencies at approximately 50 kHz, 100 kHz, and 200 kHz respectively. Figure 37 provides a comparison of the COMSOL simulated response of the 100 kHz-square PMUT with a standard circular electrode and the actual experimental frequency sweep results driving one side of splitting electrode pair. While there is a noted decrease in sensitivity at 109 kHz for the (1,1) mode, the split electrode configuration exhibits heightened sensitivity for the (1,2) mode. Typically, a single electrode design prioritizes the fundamental mode, often at the expense of higher mode sensitivity. However, the introduction of a dual electrode layout facilitates comparable driving and sensing response across both modes. This is exemplified by our circular and square PMUTs, which show a more balanced sensitivity profile due to the custom dual electrode structure. Thus, when the multi-channel PMUTs require simultaneous activation of multiple modes, the secondary or higher mode benefits from improved signal quality. To validate the efficacy and versatility of our design, experiments were conducted in two distinct environments: in ambient air and using a bio-mimetic

phantom, reflective of biomedical application scenarios. The outcomes affirm the PMUT's capacity for dual functionalities, showcasing efficiency in both power transfer and data communication.

5.2 Dual-Channel PMUTs Operation

In the experimental setup, a pair of PMUT arrays is housed within a custom-built jig, facilitating precise control over the inter-device distance in air. This configuration designates one PMUT as the transmitter (TX) and the other as the receiver (RX), with testing conducted to characterize the multi-channel responses. The TX is firstly driven in the (0,1) mode and the RX's electrical response is recorded from the inner electrodes. Figure 38 illustrates the open-circuit output voltage of the receiver as a function of separation distance under a 10 $V_{pk\text{-}to\text{-}pk}$ and 101 kHz AC drive. As the separation distance increases, the output voltage amplitude drops exponentially, and the output voltage then steadily reduces. This trend is similarly observed for the higher order modes, and therefore, the 15 mm separation distance is chosen for the experiments.

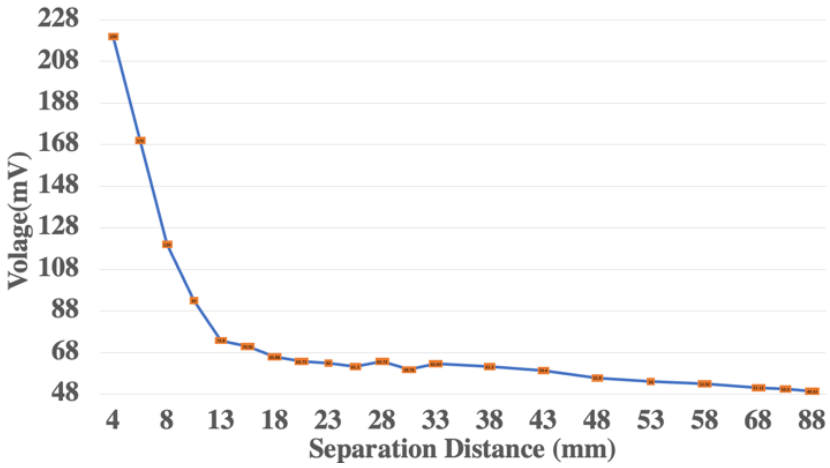

Figure 38. Open-circuit voltage recorded at the receiver at fundamental mod as a function of separation distance between the transmitter and receiver.

The fundamental principle of the multi-channel scheme is illustrated in Figure 39. Electric signals at different mode frequencies are combined using a signal mixer then used to drive a multi-channel PMUT. By employing a customized electrode design based on flexural responses of fundamental and selected higher modes, the electrical signal corresponding to each channel can be extracted from the designated electrode. For the circular PMUT, a combined driving signal is utilized by superimposing carrier signals at the (0,1) and (0,3) natural frequencies for a preliminary dual-channel operation. The

amplitude ratio of the electrical drive signal between these modes was found to be a crucial factor in balancing the quality of the signal and the sensitivity of each channel. Our initial numerical analysis, based on equation (8), predicted displacement sensitivities of 57.1 nm/V at center of PMUT for the (0,1) mode at 101 kHz and 23.2 nm/V at center of annular electrode for the (0,3) mode at 828 kHz when each mode is individually driven. The experimental outcomes showed values of 44 nm/V and 17.9 nm/V, respectively. This variation can be primarily attributed to an underestimation of actual mechanical damping in the numerical analysis model.

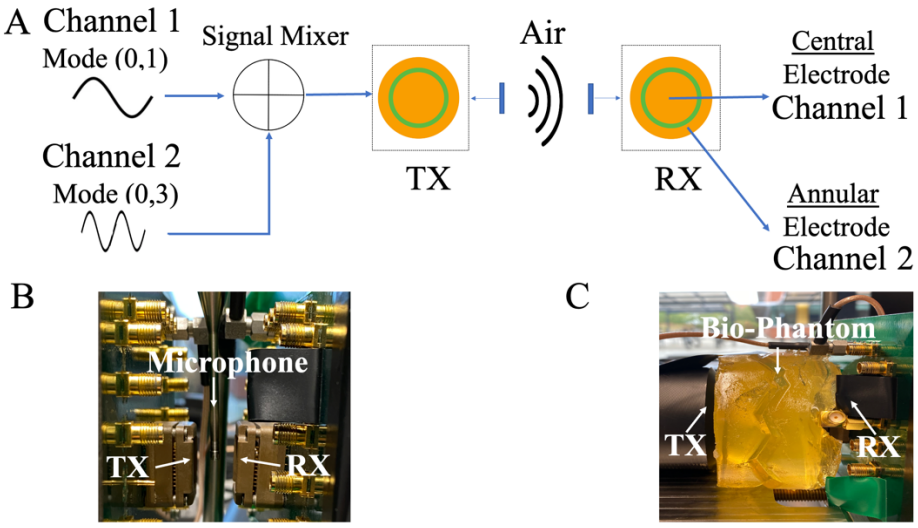

Figure 39. A: Illustration of dual-channel operation with TX and RX chips separated 1.5 cm in air. B: Experimental setup of a PMUT TX and a RX in air. B: A bio-mimicking phantom is inserted between the TX and RX chips.

By incorporating actual quality factor and system damping from experimental data, the revised Mason's method yielded improved predictions of 42.9 nm/V and 18.0 nm/V, aligning closely with experimental results with a reduced 1.7% error. This highlights the significance of accounting for mechanical damping and accurate acoustic radiation estimation. When the PMUT was driven with a combined signal with 1:1 drive amplitude ratio for (0,1) and (0,3) modes, predicted sensitivities were 36.1 nm/V and 16.3 nm/V for each mode. However, observed values were lower at 24.2 nm/V and 14.1 nm/V, likely due to electrical coupling and phase cancellation between closely positioned electrodes.

Besides, the mechanical interference on stress distribution from dominant modes might limit the PMUT performance when different modes overlap each other. Thus, in the later experiment, it's

crucial to balance drive amplitude to achieve optimal signal resolution on all channels. In the characterization, a combined signal of 10 V_{peak} with 1:1 drive ratio of (0,1) and (0,3) modes is firstly studied on the circular PMUT. The resulting waveform is illustrated in Figure 40. Since both targeted modes are symmetric, two points of interest were carefully selected to distinguish the vibration profiles based on their unique deflection characteristics. Specifically, the center of the center electrode (point A) was chosen to evaluate the flexural response of the fundamental (0,1) mode, while point B was selected to observe the vertical deflection amplitude of the (0,3) mode, which arises due to the unique stress distribution across the annular electrode. As depicted in Figure 40. A (right), the time-domain waveforms of each channel individually and in combination are represented with color coding: black for the composite drive signal, and green and red for the deflection responses at points X and Y, respectively. Our circular PMUT's dual-electrode layout is engineered to minimize interference between channels, isolating responses at points X and Y. Analysis reveals that while both modes demonstrate pronounced deflection at point X, the (0,1) mode exhibits a markedly dominant response. Conversely, at point Y, deflection is primarily indicative of the (0,3) mode, with reduced interference from the lower-frequency (0,1) mode.

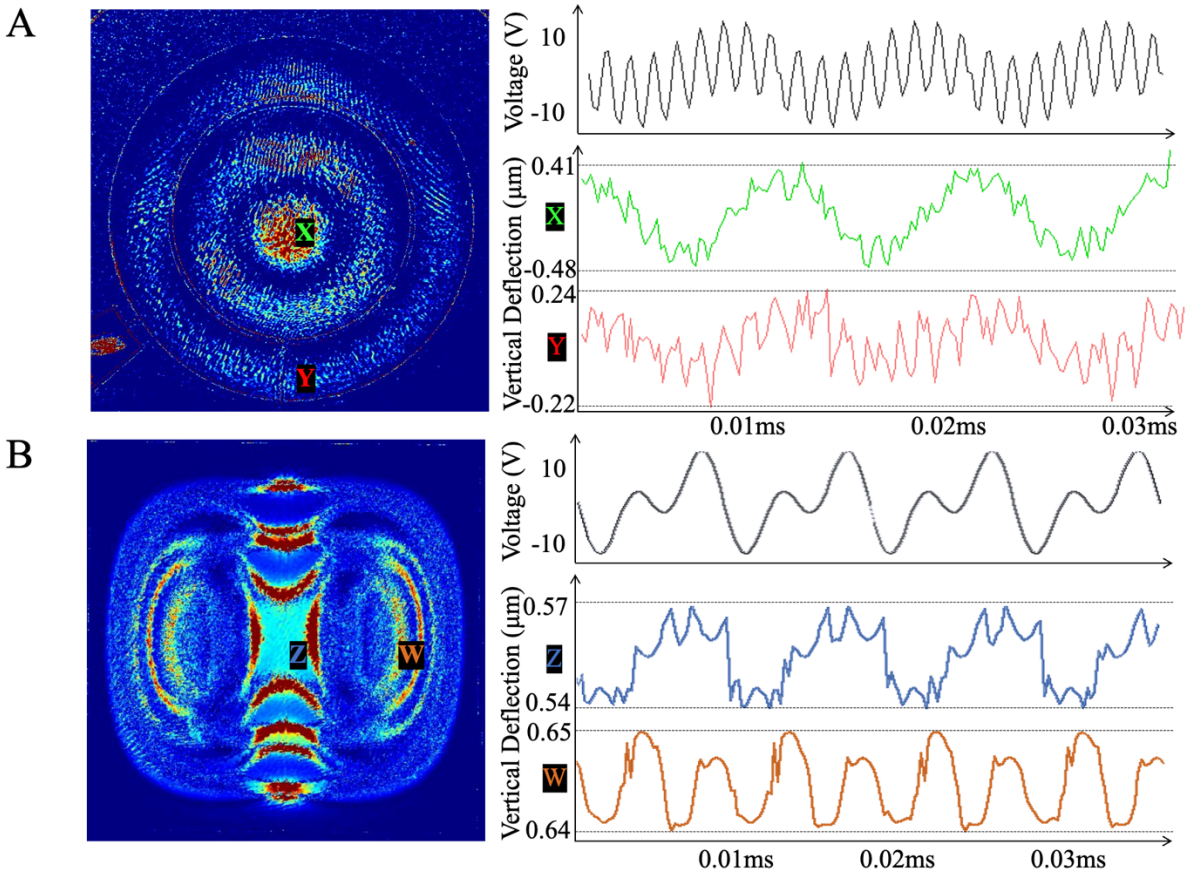

Figure 40. A: DHM recorded deflection profile of a circular PMUT TX in dual-channel operation (left). The summed drive signal (black), time-domain deflection responses at center X (green) and annular ring Y (red). B: DHM recorded deflection profile of a square PMUT TX in dual-channel operation (left). The summed drive signal (black), time-domain deflection responses at center Z (blue) and side W (orange).

For the square PMUT TX, we focused on the axisymmetric (1,1) mode at 109 kHz and the asymmetric (1,2) mode at 216 kHz. Figure 40. B presents the time-domain waveforms of each channel individually and in combination, marked by different colors where black represents the summed drive signal for the transmitting PMUT, and blue and orange depict the deflection profiles at the central and symmetric nodal locations at points Z and W, respectively. These deflection profiles, visualized using DHM, highlight the distinct vibrational responses at points Z and W, which were strategically chosen to exploit the unique deflection patterns inherent to each mode. Under a combined drive signal, the dual-channel PMUT displays two distinct flexural responses: one at the square membrane's center corresponding to the (1,1) mode, and another at the electrode centers symmetrically positioned, indicative of the (1,2) mode. Showing in Figure 40. B (right), at point Z, the center of the square

PMUT TX, the vibration was predominantly influenced by the (1,1) mode, with negligible high-frequency signal interference. In contrast, at point W, the vibration was dominated by the (1,2) mode, with minimal disruption from the fundamental mode. These observations underscore the capability of both circular and square PMUTs to transmit and receive acoustic signals across multiple channels simultaneously, offering significant insights into the behavior of multi-mode PMUTs when subjected to complex drive signals. This demonstrates the potential for simultaneous multi-mode excitation, enhancing the functional versatility of PMUT systems.

5.3 Acoustic Coupling and Remote Excitation

With the intention of designing more powerful ultrasound transducers, many researchers have developed high-density PMUT arrays to improve acoustic sound pressure level response, bandwidth, directivity, and transmission distance. However, as transducer density increases and inter-element pitch decreases, adjacent PMUTs often become undesirably coupled through electrical feedthrough and acoustic coupling of PMUT elements through the chip substrate and solid-air interface [110-112]. This phenomenon, known as cross-coupling or crosstalk, can degrade overall performance by increasing total ring-down time, reducing receiver resolution, and distorting ultrasound beams in transmitter configurations. Consequently, most existing research in the field focuses on mitigating undesirable crosstalk and inter-element coupling through structural modifications, such as inserting resonant cavities and grooves between transducers [113-115]. In contrast, this study utilizes the multi-channel PMUTs to analyze and investigate crosstalk in the electrical, mechanical, and acoustic domains. Based on these observations, innovative applications are explored that utilize cross-coupling, in contrast to previous research. This approach demonstrates the potential for remote filtering and remote excitation within a low-frequency PMUT array, validating the viability of harnessing cross-coupling for beneficial purposes.

5.3.1 Crosstalk Characterization

In the designed array, inter-element coupling arises from three primary sources: electrical coupling, acoustic coupling through air, and acoustic coupling through the Si substrate [115, 116]. To gain a comprehensive understanding and effectively control the cross-coupling in a high-density PMUT array, each coupling source is individually investigated.

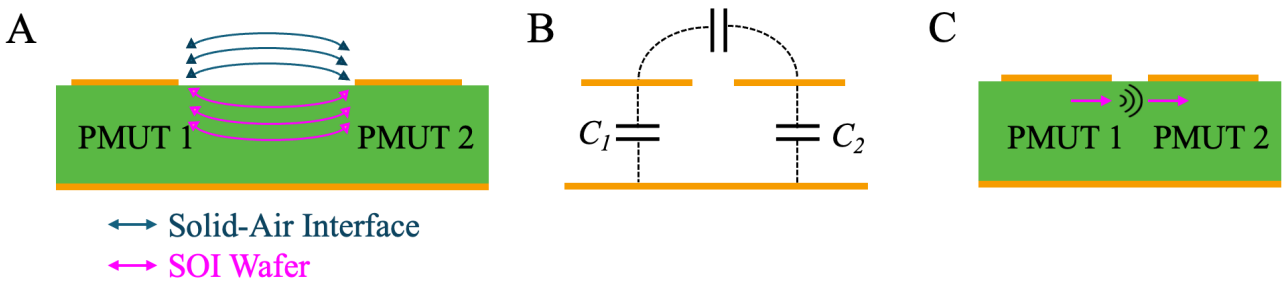

Figure 41. Sources of crosstalk between adjacent PMUTs. A: Acoustic crosstalk depicted as coupling between adjacent PMUTs across various media or interfaces. B: Electrical crosstalk shown through the interaction of electrodes from two neighboring PMUTs. C: Predominant acoustic crosstalk in PMUTs, primarily propagated through the SOI wafer.

Electrical coupling primarily stems from capacitive coupling between electrodes on adjacent PMUTs with minimal pitch [117, 118]. In this study, we adopted the circular PMUTs as illustrated previously in Figure 35. C. Although each PMUT is designed with identical dimensions, slight variations in resonant frequencies may occur among transducers on the same chip due to fabrication tolerances. To analyze the impact of electrical coupling on the overall coupling between PMUTs, we conducted an experiment where we drove a particular PMUT (referred to as PMUT 2) at various frequencies and monitored the electrical output from the electrodes of the adjacent PMUT (referred to as PMUT 1). In Figure 42, adjacent PMUT 1 and 2 exhibited fundamental modes at 97.98 kHz and 96.69 kHz, with 3 dB bandwidths of 1.04 kHz and 0.76 kHz respectively. Initially, we drove PMUT 2 at an off-resonant frequency (f_1) for both PMUT 1 and PMUT 2. We noticed a near-linear increase in the output voltage on PMUT 1 corresponding to the increase in voltage on PMUT 2. This observation confirmed the presence of electrical coupling through capacitive coupling, as the acoustic intensity from PMUT 2 is lower off-resonance thereby reducing the level of mechanical coupling. Next, we increased the driving frequency of PMUT 2 to match its resonant frequency (f_2). This change led to a substantial increase in the vibration amplitude and acoustic intensity of PMUT 2. Consequently, the voltage output on PMUT 1 exhibited an exponential increase, reaching 0.99 V when PMUT 2 was driven at 10 $V_{pk\text{-}to\text{-}pk}$. Comparing this outcome with the previous off-resonant frequency scenario (f_1), it became evident that acoustic coupling played a more substantial role in the overall coupling effect across transducers. Finally, we drove PMUT 2 at the resonant frequency (f_3) of PMUT1. In this case, the voltage output on PMUT1 increased but not as significantly as when driving PMUT2 at its

resonant frequency (f_2). This observation suggests that, despite the existence of capacitive coupling, its impact on overall cross-coupling effects during array operation is limited.

Our findings confirmed the existence of electrical coupling through capacitive feedthrough, but its impact on the overall cross-coupling is limited. Acoustic coupling proved to be a more significant factor, particularly when driving PMUT 2 at its own resonant frequency. By comparing the results across different driving frequencies, the relative contribution of capacitive and acoustic coupling to the overall cross-coupling during array operation can thus be deduced.

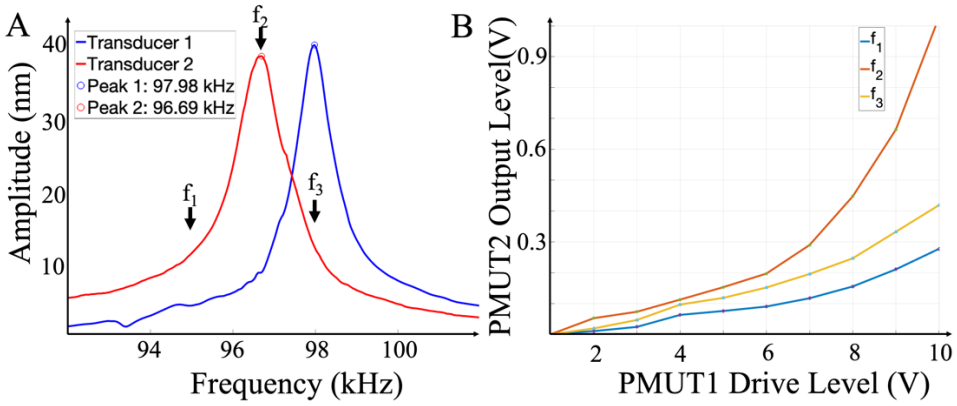

Figure 42. A: Frequency mismatch of two adjacent PMUTs under 3Vpk-to-pk drive. B: Electrical response from coupled PMUT 1 when increasing drive voltage on PMUT 2 under frequencies f_1, f_2 and f_3.

Concurrently, acoustic coupling through air and the Si substrate is investigated. Two adjacent PMUTs were selected for electrical driving at the same frequency, with comparable mechanical response amplitudes but with a calculated phase shift based on theoretical calculations. The mechanical and acoustic responses of one of the transducers was measured as impacted by the driving of the other PMUT. PMUT 1 and PMUT 2, from the electrical coupling test, were used for these tests. In contrast to the electrical coupling case, the drive signal was specified at a frequency of 97.3 kHz where the two PMUT frequency response curves intersect, ensuring both transducers had comparable amplitudes during operation. The phase shift is calculated based on the ultrasound wavelength and pitch between the two PMUTs to induce destructive interference on the response of the PMUT of interest. The material properties, wavelength, and phase delay were calculated and listed in Table 5. The distinct phase shifts for each medium enable the cross-coupling effects through air and the SOI wafer to be individually compared and understood.

Table 5. Calculated phase delay for vibration inhibition.

	Speed of Sound (m/s)	Wavelength (mm)	Phase Delay (°)
Air	340	3.54	34.39
SOI Wafer	8443	87.22	185.98

In the experiment, PMUT 1 is selected for monitoring its vibration and acoustic responses under a 2 $V_{pk\text{-}to\text{-}pk}$ drive with phase delay, while PMUT 2 is driven at different amplitudes ranging from 2 V to 20 $V_{pk\text{-}to\text{-}pk}$ to assess the inhibition effect on PMUT 1. As illustrated in Figure 43. A, when increasing the drive level of PMUT 2 from 2 V to 10 V and further to 20 V, the vibration amplitude on PMUT 1 decreased by 6% and 19.2% from the solid-air interface, respectively. On the other hand, when considering only the acoustic propagation through the SOI substrate, the PMUT 1 peak amplitude response is significantly reduced, having its peak amplitude less than 10 nm, when the adjacent PMUT 2 is driven under a 20 V signal. This finding suggests that acoustic coupling through the Si substrate dominates the overall crosstalk effect.

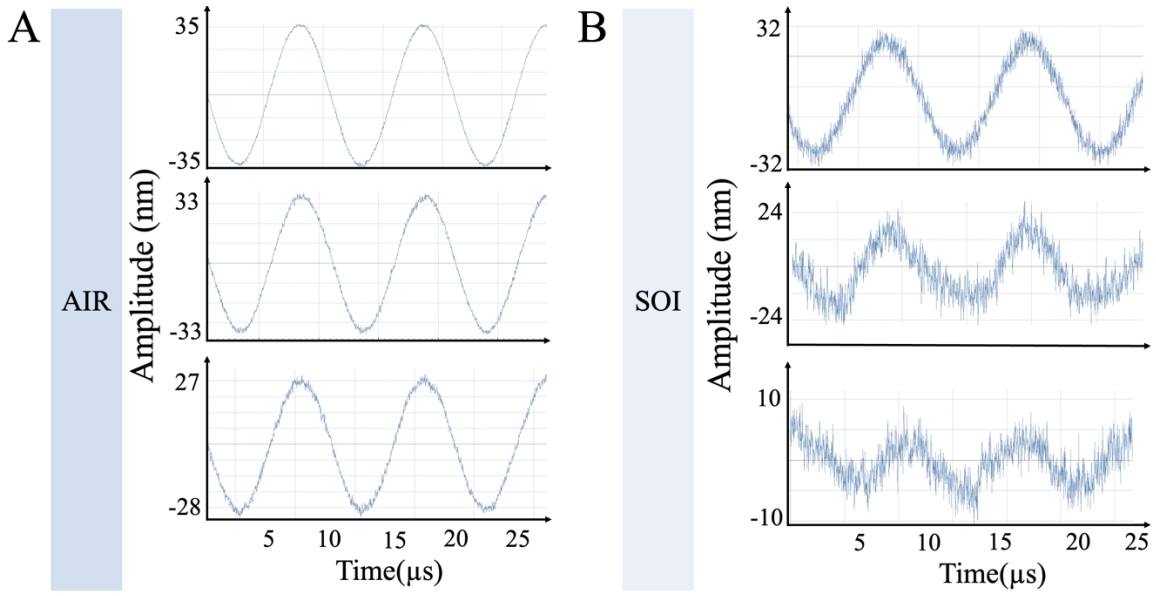

Figure 43. Comparative analysis of optically recorded deflection amplitudes on PMUT 1 with phased driving on PMUT 2. A: The deflection amplitude reduction correlates with acoustic coupling designed for propagation through a solid-air interface. B: The same phenomenon is observed when acoustic coupling is designed for propagation through an SOI wafer, demonstrating more pronounced coupling.

In both scenarios, the drive voltage ($V_{pk\text{-}to\text{-}pk)}$ on PMUT 2 increases incrementally from 2 V (top) to 10 V (middle), and finally to 20 V (bottom), illustrating the effect coupling levels on PMUT 1.

5.3.2 Remote Excitation

Building upon the identification and characterization of coupling sources summarized in the previous section, an exploratory study of potential applications is undertaken that leverage this coupling between PMUTs. Although crosstalk is often considered an undesirable effect in ultrasound imaging and other applications, the research presented here demonstrates how this effect may be leveraged to enable new and useful functionality. In this section, we analyze the behavior of higher modes across different frequencies and coupling levels, and discuss two practical applications derived from the observed coupling phenomena.

First, the acoustic coupling is utilized to excite a single PMUT with a complex signal comprising two frequencies by driving two PMUTs on the same chip operating at different modes. Such a dual-channel configuration is often of interest in applications where PMUTs are utilized as transducers for simultaneous acoustic power transfer and data telemetry or in acoustic data telemetry applications allowing for an increase in the number of channels for data transmission within a single device. Second, a PMUT is employed as an acoustically coupled filter to process such complex signals for on-chip filtering. The coupling level is quantified by comparing the optically recorded deflection amplitudes of an electrically driven PMUT and its adjacent acoustically coupled counterpart. Representative results are shown in Figure 44, where the vibration amplitudes and coupling levels are measured for a 10 $V_{pk\text{-}to\text{-}pk}$ drive. Coupling levels are found to be 16.3%, 9.2%, 6.8% for the (0,1), (0,2), and (0,3) modes, and less than 3% for the (1,2) mode. This observation supports the conclusion that acoustic crosstalk is more significant at lower operating frequencies [112].

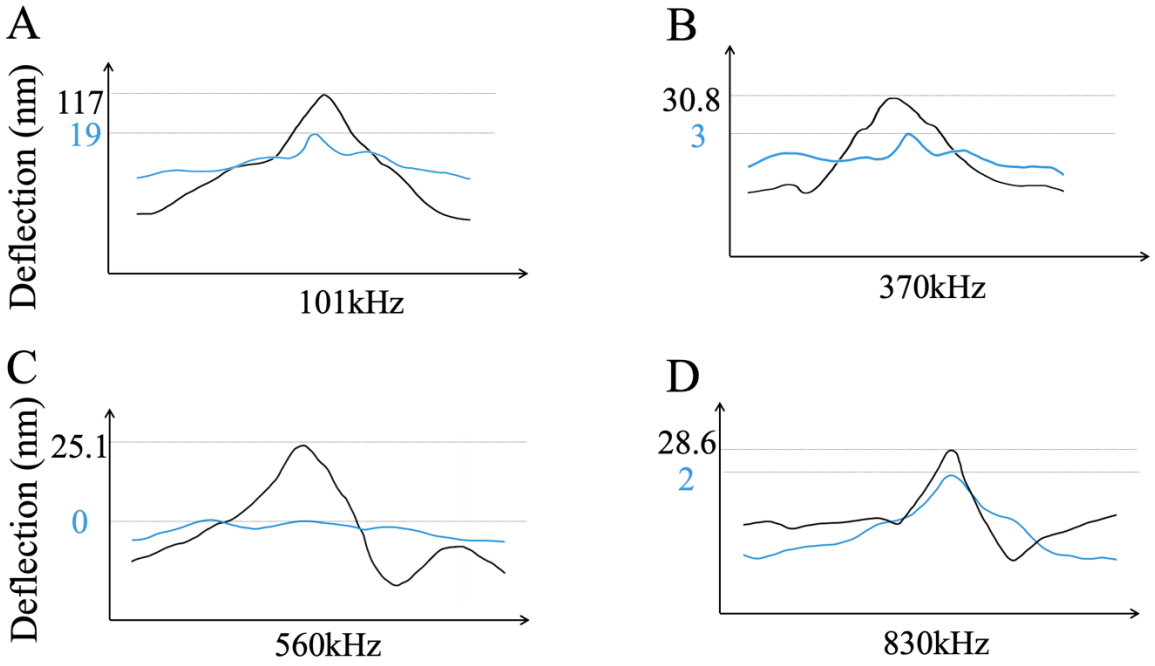

Figure 44. A-D: Measured frequency response and coupling level of direct-excited (black) and acoustically coupled (blue) PMUTs at (0,1), (0,2), (1,2) and (0,3) modes. Maximal deflection amplitude measured at center of PMUT using a DHM.

Based on the asymmetric coupling levels, an acoustically coupled PMUT was tested as a channel select filter. First, the central PMUT was driven in both (0,1) and (0,3) modes simultaneously with a hybrid signal combining both frequencies, and electrical signals from an adjacent PMUT were collected to verify the filtering effect. Since the deflection amplitude at the (0,3) mode is relatively weaker and its coupling level is less than half of the fundamental mode, the acoustically coupled PMUT exhibits a filtering effect, predominantly responding at the (0,1) mode. Figure 45. A and D show the deflection profile and electrical response of a PMUT filter coupled only through the acoustic domain, and predominantly reflecting only the fundamental (0,1) mode signal. In contrast, the vibration signals from a directly driven PMUT in Figure 44. C contain both frequencies at (0,1) and (0,3) modes.

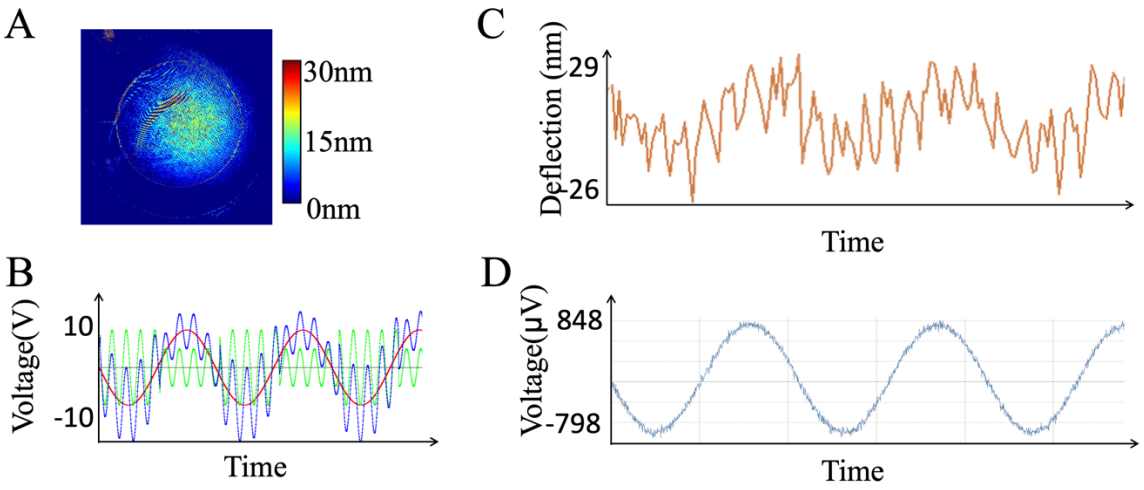

Figure 45. A: Deflection profile of the coupled PMUT. B: Waveform used to directly drive the actuated PMUT; Red channel 1 at 101 kHz; Green: channel 2 at 828 kHz; Blue: combined driving signal. C: Vibration amplitude of directly driven PMUT. D: Electric response of acoustically coupled PMUT shows the filtering effect with a signal at 101 kHz only.

In an alternative approach, the central PMUT can also be remotely excited into a hybrid dual-channel mode. In this experiment, all six outer PMUTs were electrically driven, and the central PMUT was remotely acoustically driven into a hybrid combination of the (0, 1) and (0, 2) modes as shown in Figure 46. A. Since the acoustic coupling is much weaker in the higher mode, only one annular PMUT is employed for exciting the (0,1) mode, while the remaining five PMUTs were driven concurrently in the (0,2) mode to compensate for the reduced coupling in this mode. The deflection profile from Figure 46. C-D displays a combined operating mode profile with the electrical signal extracted from the central PMUT exhibiting components at the two frequencies, with the amplitude in the (0,2) mode being significantly lower.

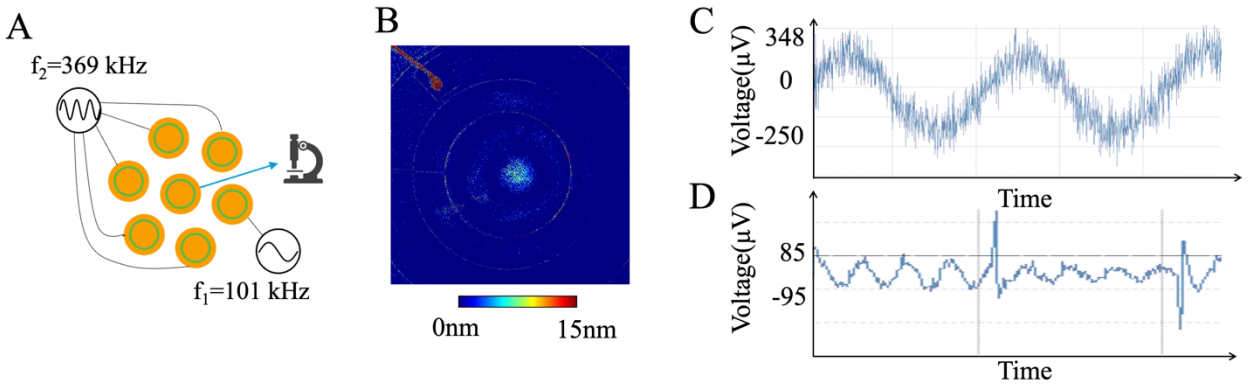

Figure 46. A: Experimental setup for inducing dual-mode operation in the central PMUT through remote excitation. B: Deflection profile of coupled secondary PMUT shows coupling of both (0,1) and (0,2) modes. C: Measured time-domain electrical response for the (0,1) mode. D: Measured time-domain electrical response for the (0,2) mode.

5.3.3 Conclusion

In this section, we explored the mechanisms of crosstalk in a PMUTs array and illustrated how these effects can be harnessed for beneficial outcomes, thereby expanding the functional scope of PMUT devices. A detailed investigation into cross-coupling effects within PMUTs has been carried out. Through comprehensive characterization of inter-element coupling, which includes both electrical and acoustic sources, it was determined that while electrical coupling through capacitive feedthrough is present, its impact on overall cross-coupling is limited. The dominant factor affecting the overall crosstalk effect is found to be acoustic coupling, particularly through the silicon substrate.

Exploiting asymmetric coupling levels across different modes, the study introduced two practical applications. The first application involved remotely exciting a single PMUT with a complex signal comprising two frequencies by driving two PMUTs on the same chip operating at different modes. The second application employed a PMUT as an acoustically coupled filter to process complex signals for on-chip filtering. These applications demonstrate the potential for utilizing acoustic cross-coupling in mode selection, filtering, and remote hybrid multi-mode excitation. This research shifts the traditional view of cross-coupling in PMUT arrays from a typically undesirable phenomenon to a utilizable feature in ultrasound technology. Future research could focus on further optimizing PMUT design to amplify these beneficial cross-coupling effects and exploring additional applications in high-density PMUT arrays.

5.4 Crosstalk and On-chip Filter

The previous section introduced and examined a novel multi-channel PMUT link [108, 109]. The PMUT can be configured to simultaneously operate in multiple resonant modes with specific channels assigned to each resonant mode thereby realizing multi-channel operation. Furthermore, drawing inspiration from MEMS resonator filter applications, yet with a distinct design, we now present an innovative on-chip filtering function integrated on the microfabricated chip [119]. This involves designing PMUTs of different dimensions on the same chip, each having fundamental frequencies corresponding to different carrier frequencies on the multi-channel PMUT. When functioning as on-chip resonators, these PMUTs demonstrate a passive filtering function, without any power supply or electric circuit support. As a result, this combination indicates a pathway to a potential dual-function operation when combined with a multi-channel PMUT.

5.4.1 Experimental Setup

In this study, we utilize the square PMUTs array designed to cover fundamental frequencies ranging from 50 kHz to 1.4 MHz. The primary objective is to employ PMUTs with varying dimensions and operational frequencies to match the fundamental mode frequency of high-frequency PMUTs with the higher-order mode frequency of low-frequency PMUTs within the same chip. It's worth mentioning the actual frequencies may vary due to fabrication tolerances and errors such as over-etching. We specifically focus on three square PMUTs targeted for fundamental mode frequencies at approximately 50 kHz, 100 kHz, and 200 kHz.

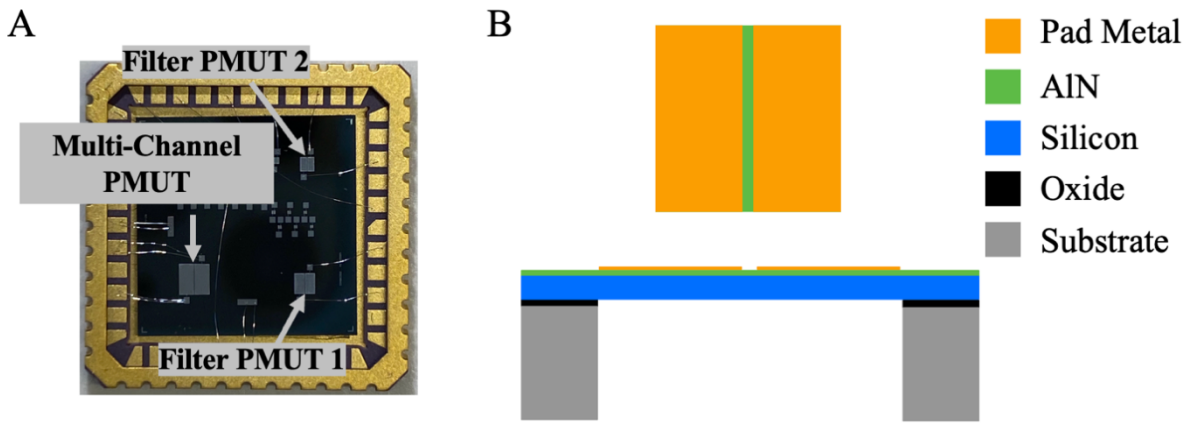

Figure 47. A: Fabricated array comprising multi-channel PMUT and filtering PMUT. B: Cross-sectional view of proposed PMUT design.

As illustrated in Figure 47, the array highlighted three designated PMUTs: multi-channel PMUT, filter PMUT 1, and filter PMUT 2. To enhance multi-channel operation, a dual-electrode layout is employed to leverage both symmetric and asymmetric modes effectively. The multi-channel PMUT, measuring 1578 µm by 1578 µm, is primarily designed to operate in the (1,1) mode at an intended frequency of 50 kHz. Recognizing that the sensitivity of the fundamental mode is typically more pronounced than that of higher-order modes, our dual-electrode layout is designed not only to support the fundamental mode shape—as common in traditional PMUT designs—but also to specifically enhance device sensitivity at higher order modes by aligning with the asymmetric (1,2) mode shape. Each electrode, measuring 1558 µm by 774 µm, is separated by a 10 µm gap. The fundamental and higher-order modes were recorded by electrically driving the PMUT and capturing its response using a digital holographic microscope (DHM). Figure 46 presents the sweep frequency responses and representative optical spectrums, obtained under a driving voltage amplitude of 10 V peak-to-peak. The multi-channel device exhibits resonant modes (1,1), (1,2), and (3,1) at 61.2, 116.5, and 200.8 kHz, respectively.

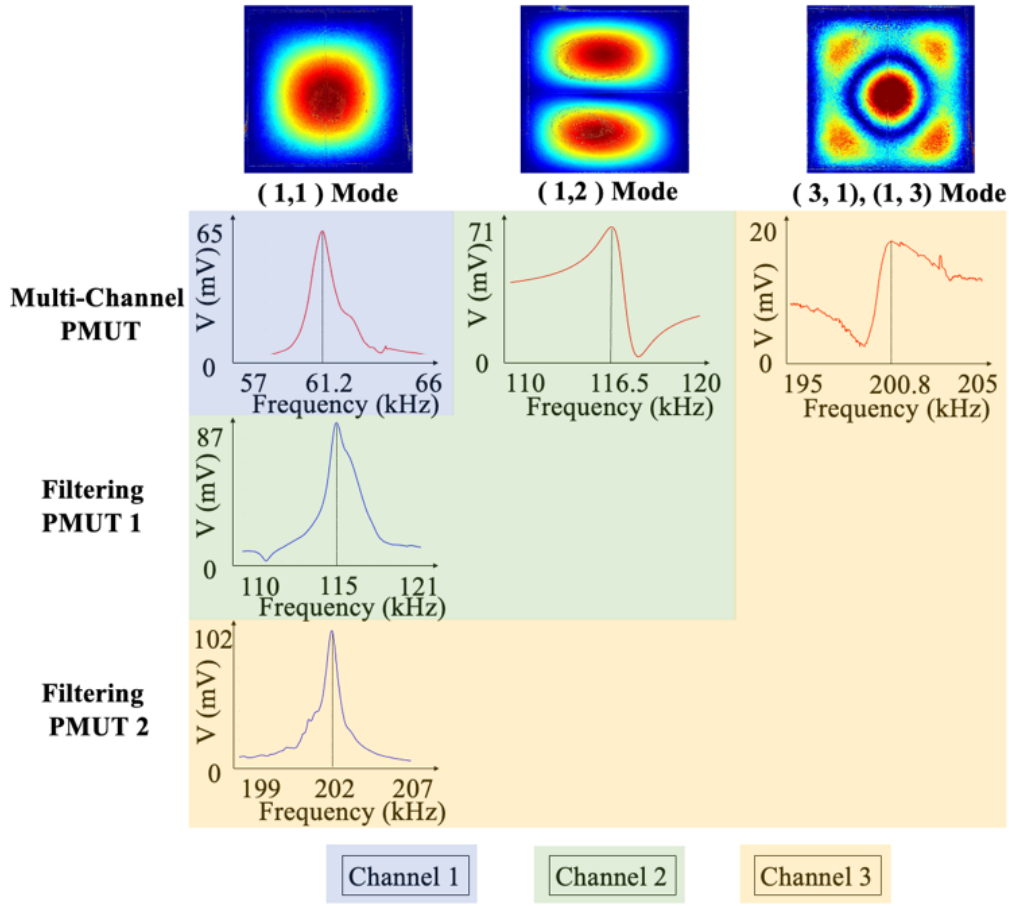

Figure 48. DHM recorded vibration profile and frequency sweep of multi-channel and filtering PMUT across fundamental and higher modes.

In the same array, filtering PMUTs with the same design are positioned next to the multi-channel PMUT. Each filtering PMUT has its fundamental (1,1) mode frequency matching one of the channel's carrier frequencies from the multi-channel PMUT, correspondingly. The frequency sweep results in Figure 48 confirm that the actual resonant frequencies of two filtering PMUTs have their resonant peaks at 115 kHz and 202 kHz, approximately matching the (1,2) and (3,1) modes of the transmitting multi-channel PMUT at 116.5 kHz and 200.8 kHz, respectively.

In the experimental setup, a pair of PMUT arrays is housed within a custom-built jig, facilitating precise control over the inter-device distance in an air medium. This configuration designates one PMUT as the transmitter (TX) and the other as the receiver (RX), with testing conducted to characterize the multi-channel responses. The fundamental principle of the multi-channel scheme is illustrated in Figure 49. Initially, signals at different mode frequencies are combined using a signal mixer with 0° phase difference and used to drive a multi-channel PMUT TX. Subsequently, a multi-

channel RX receives this signal and divides it into two components: one can be directly exported from one of its two electrodes, and the other is fed to an adjacent filtering PMUT to isolate the high-frequency channel.

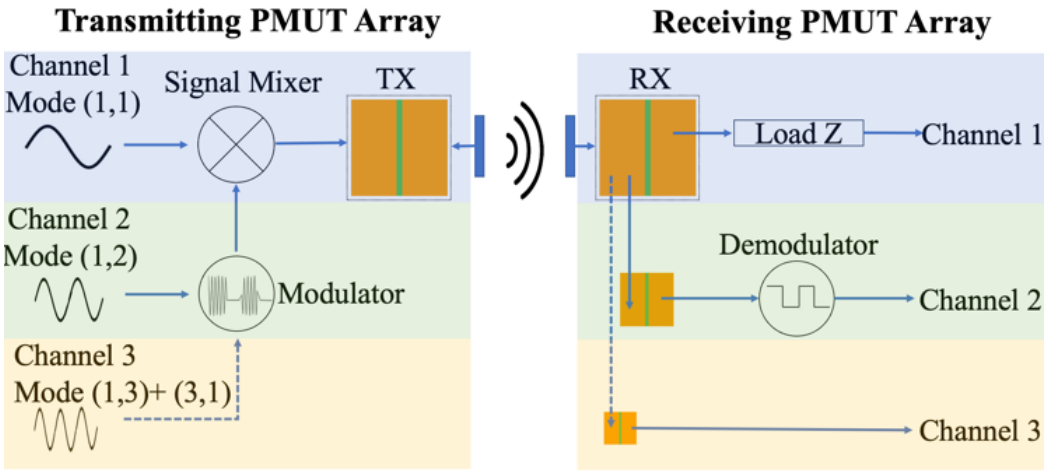

Figure 49. Illustration of multi-channel and filtering PMUT operation. In this study, channels 1 and 2 are focused and studied.

For the device under test, the signal strength on channel 3 or mode (1,3) is considerably weaker than the first two channels due to the reduced electromechanical coupling under the specified electrode configuration. This underscores the significance of electrode shaping and the interaction with structural design [107]. However, using the current asymmetric electrode design, the transduction efficiencies for the first two modes are similar. Therefore, this study targets the symmetric (1,1) mode and the asymmetric (1,2) mode. The waveforms for each channel, both individually and in combination, are depicted in Figure 50, represented in blue, red, and purple. The PMUT RX (spaced 1.5 cm away in air from the PMUT TX) successfully received the two-channel signal. The deflection profile is recorded using the DHM and shown in Figure 50. Points of interest were carefully selected to distinguish the vibration profiles based on their unique deflection characteristics. When driven with a combined signal, the dual-channel PMUT RX shows 3 distinctive flexural responses: one at the center of squared membrane and two at the center of electrode symmetrically, and these deflection patterns correspond to (1,1) and (1,2) modes, correspondingly. As a result, the PMUT RX proves its capabilities of transmitting and receiving acoustic signals for more than 1 channel or frequency at the same time.

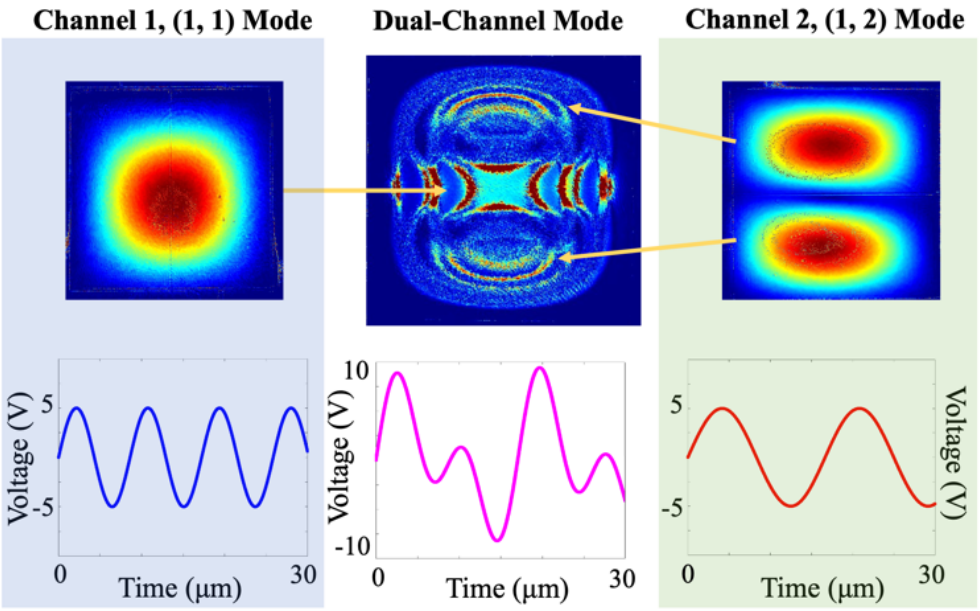

Figure 50. The DHM recorded vibration profile and waveform of drive signal. (Left): channel 1 at fundamental (1,1) mode. (Right): channel 2 at asymmetric (1,2) model. (Center): summed signal used for dual-channel mode.

In the output stage, the electrical signal, comprising two frequencies from the multi-channel PMUT RX, is exported from one of its two electrodes, and then fed to drive an adjacent filtering PMUT. This filtering PMUT, designed with a fundamental frequency aligning with the higher frequency channel, operates as an on-chip resonator and only responds to signals at its fundamental mode or high-frequency channel. This design realizes the on-chip filtering function without requiring an additional power source. Figure 51 illustrates the combined signal before (red) and after (green) passing through the filtering PMUT. It is evident that the low-frequency signal is significantly attenuated, leaving only the desired high-frequency signal at the output node of the filtering PMUT.

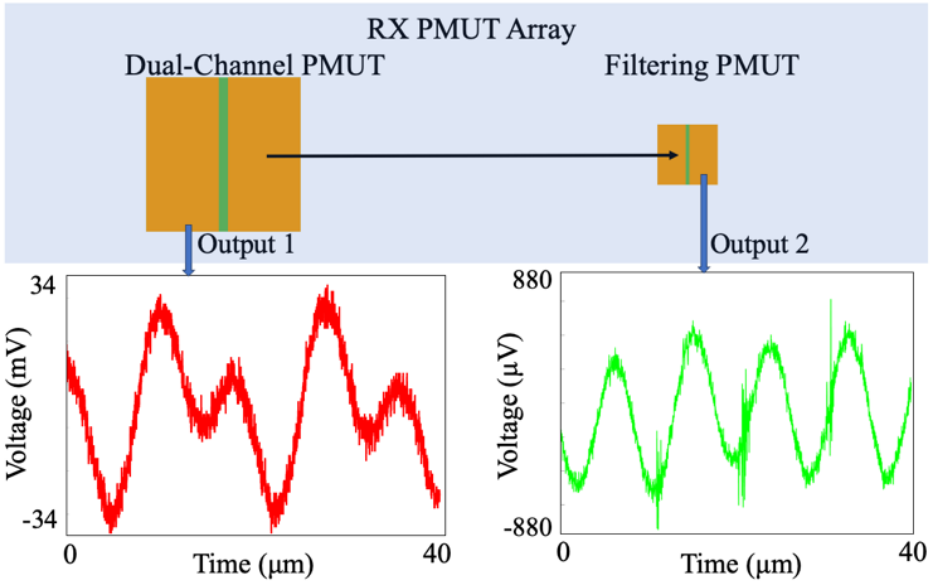

Figure 51. A schematic of the on-chip PMUT filtering operation, with one of the output electrodes on the multi-channel PMUT connected to the filtering PMUT. The bottom left plot (red) shows the output electrical signal before filtering, while the right plot (green) presents the output electrical signal after filtering.

5.4.2 Communication with On-Chip Filtering

The previous sections have underscored the potential of multi-modal excitation as a strategy to enhance their functionality. One of the significant advantages of these multi-modal PMUTs is their ability to simultaneously, and independently, control acoustic waves across different frequency ranges. To further explore this potential, the concept of simultaneous Wireless Power Transfer (WPT) and Communication (COM) is introduced within a dual-channel PMUT framework. This demonstration could pave the way for future applications that exploit the efficiency of low-frequency ultrasound for long-distance acoustic power transfer, while leveraging high-frequency ultrasound to boost data transfer rates in wireless communication scenarios [102]. In this experiment, we maintain the dual-channel operation at the (1,1) and (1,2) mode frequencies. However, unlike the previous case where both channels operate with a continuous sinusoidal wave, the higher-frequency channel is modulated as a carrier signal and encoded with a binary data stream. The (1,1) mode channel remains a continuous sinusoidal signal at 65 kHz for WPT application, while the (1,2) mode channel, serving as the COM channel, is encoded with a randomly generated 8-bit binary data through an Amplitude-Shift Keying (ASK) scheme, as depicted in Figure 51 (top). Consequently, the PMUT RX picks up

both channels simultaneously. For acoustic power transfer experiment, the PMUT impedance is measured to be 2300 Ω, and a matched external load resistor is connected to the output electrode of the receiving PMUT. The COM channel, on the other hand, is processed by an adjacent filtering PMUT, which is designed to reduce the low-frequency components and isolate the ASK-modulated signal for direct demodulation.

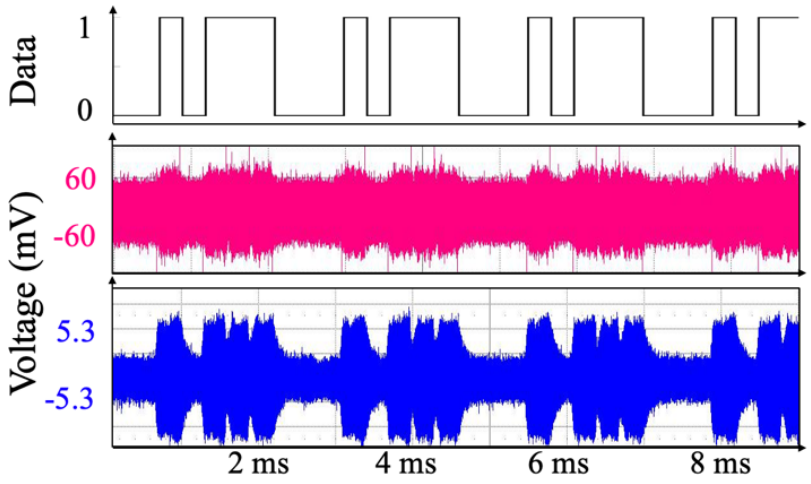

Figure 52. (Top): Randomly generated 8-bit binary data cycled for 3 times. (Middle): Electric signal from multi-channel PMUT RX. (Bottom): Electric signal after passing through the on-chip filtering PMUT.

During the experiment, the drive amplitude ratio between the two channels is observed significantly influencing the balance between the transferred power level and communication data. In this study, the drive amplitude ratio between the WPT and COM channels is set at 1:1.4 in order to optimize the data transfer fidelity. As shown in Figure 52 (middle), the multi-channel PMUT receives the dual-channel signal, and its output is directly exported to an external load for power transfer. It is noteworthy that the high-frequency COM channel is minimally observed amidst the strong fundamental mode signal. The low signal-to-noise ratio (SNR) and high bit-error rate (BER) make it impractical to extract a usable data stream if we were to perform demodulation directly on its raw output signal. However, after the signal passes through a customized on-chip filtering PMUT, as shown in Figure 52 (bottom), the electrical output yields a clear self-cycling 8-bit signal as transmitted. This allows for direct extraction and demodulation of the data. This method achieved a high data transfer rate of 4 kbps at a low bit error rate of 1.83×10^{-4}, while simultaneously delivering 1.22 μW to a matched load of value 2300 Ω. This experimental result underscores the potential of the dual-

channel PMUT design in enhancing the efficiency and functionality of wireless power transfer and communication systems.

5.4.3 Conclusion

In conclusion, this chapter has successfully validated an innovative design of multi-channel PMUTs with integrated on-chip passive filtering. This unique design capitalizes on the multi-frequency capabilities of PMUTs, enabling simultaneous wireless power transfer and data communication. The multi-channel operation is realized by driving PMUTs into multiple resonant modes, with each mode corresponding to a distinct channel. This dual-channel operation is facilitated by a meticulously designed dual-electrode layout, which balances the sensitivity between the fundamental and higher-order modes, thereby enhancing the overall performance of the system. Moreover, the integration of an on-chip passive filter, realized by an adjacent PMUT operating at the same frequency as the communication channel, allows the receiving PMUT array to isolate the high-frequency signal for direct demodulation, independent of any external power source. The experimental results provide robust validation of the feasibility and efficiency of this design, achieving a high data transfer rate and low bit error rate for data transfer, while simultaneously transferring power acoustically.

These findings not only broaden the application potential of PMUTs but also pave the way for future studies on multi-frequency PMUT arrays. While this study primarily focused on employing two modes with a dual-channel PMUT transmitter and receiver operation, future research could explore further modes to further enhance functionalities and channel capacity for wireless data and power telemetry.

5.5 Dual-Function Wireless Power Transfer and Data Telemetry

Building on insights from the previous section, the PMUT has demonstrated its potential for the simultaneous excitation of multiple modes This capability paves the way for simultaneous and independent manipulation of acoustic waves corresponding to the excitation of different mechanical modes. Thus, we further explore the multi-mode operation of PMUTs, aiming to establish both low- and high-frequency ultrasound links between individual PMUTs for applications in acoustic power transfer and data telemetry. The innovative dual-channel framework supports concurrent Wireless

Power Transfer (WPT) and Communication (COM), enhancing the potential for future applications. Low-frequency ultrasound ensures efficient power transfer over extended distances, while high-frequency ultrasound facilitates rapid data transfer rates, crucial for wireless communication. Such a configuration not only broadens data telemetry bandwidth but also maintains low error rates, ideal for complex communication tasks.

Specifically, intended applications include biomedical implants where an integrated PMUT array in a multi-channel setup is capable of providing deep-tissue power transfer through low-frequency channels, alongside high-frequency channels for data telemetry. In this study, we replicated the biomedical application environment and conducted experiments across bio-mimicking phantoms to validate the dual-functionality concept. Such capabilities enhance the efficacy and adaptability of biomedical devices, illustrating the transformative potential of multi-mode PMUT technology in medical applications.

5.5.1 Dual-Function Characterization

In our experimental design, while the dual-channel operation remained consistent, the higher-frequency channel underwent signal modulation. Instead of the standard continuous sinusoidal wave, it was encoded as a carrier signal with a randomly generated 8-bit binary data stream using the Amplitude-Shift Keying (ASK) scheme. This dual-function experiment is depicted in Figure 53.

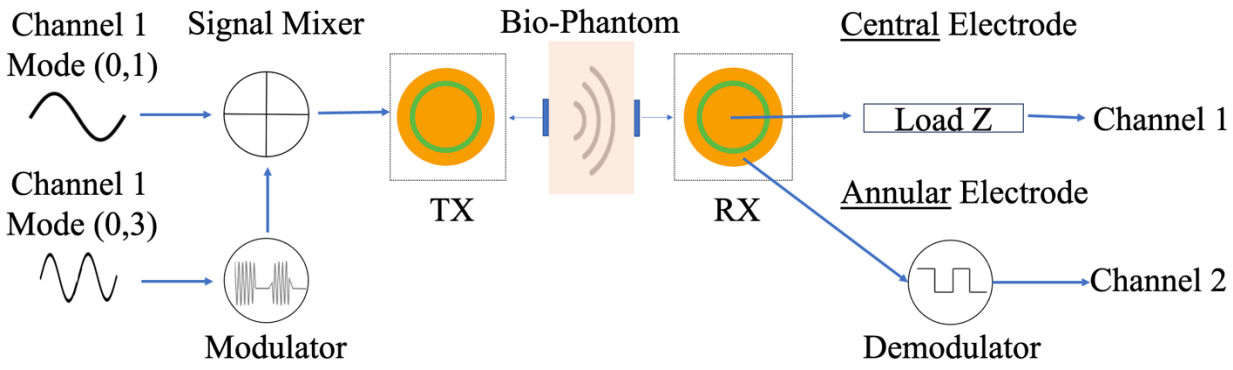

Figure 53. Illustration of dual-function operation of multi-channel PMUT with one channel specified for WPT and another for COM.

The PMUT RX, in its role, adeptly detects both channels. Initial validation of the dual-function experiment was conducted in air, followed by experiments with a bio-mimicking phantom targeting

biomedical contexts. The resultant electrical output bifurcates, each corresponding to a mode-customized electrode. Square PMUTs have been uniformly constructed to present an impedance of 2300 Ω across all electrodes, thereby providing flexibility in channel selection for hybrid applications. Improving upon the square design, the circular PMUT has a central electrode that is designed to ensure minimal interference from higher modes. It effectively directs the electrical signal to a matched impedance, which is fundamental for mitigating modal interference and precise characterization of power transmission (consistently measured at 3000 Ω). In a distinct operational capacity, the annular electrode is designed for the COM channel, which operates at higher frequencies. It is responsible for the transmission of the ASK-modulated carrier signal, which is subsequently prepared for demodulation using MATLAB, highlighting the electrode's role in facilitating signal processing.

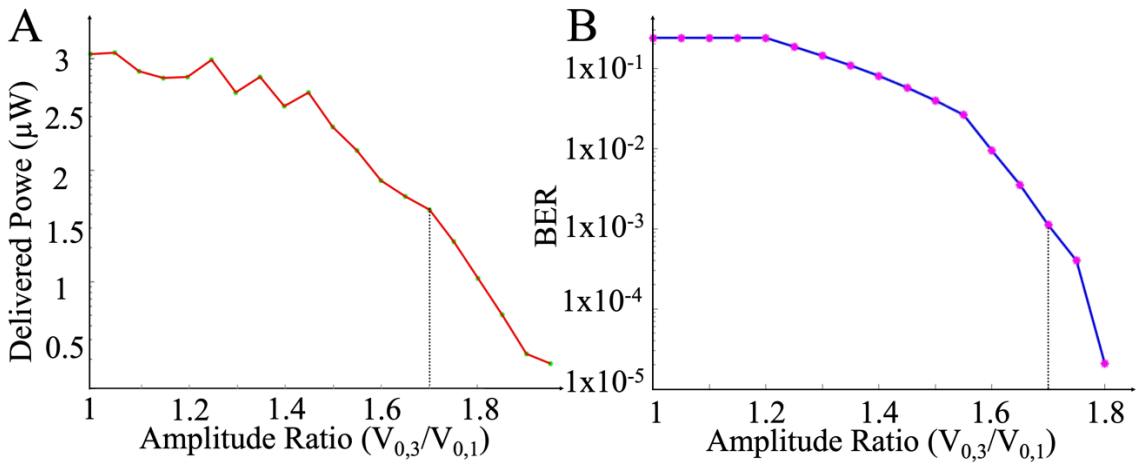

Figure 54. The impact of drive amplitude ratio between WPT and COM channel of the circular PMUT on A: power transfer efficiency and B: data transfer fidelity as quantified by BER while maintaining the drive level on WPT channel.

A critical facet of this dual-function application is the dual evaluation of power delivery and data quality. At a lower drive amplitude ratio between the WPT and COM channels, the RX delivers a commendable power output. However, this comes at the cost of the communication link's performance, with a high bit-error-rate (BER) and a low signal-to-noise rate (SNR), as the high-frequency carrier is overshadowed by the dominant fundamental mode signal. Adjusting the drive amplitude ratio thus emerges as a balancing act between power transmission efficiency and data quality enhancement. Figure 54 illustrates that when the drive amplitude ratio is set at 1:1 for COM and WPT channels of a circular PMUT, the higher-mode COM channel suffers from a high BER and low SNR. Despite the electrodes being optimized to balance the sensitivity of both transmission and

reception modes, the fundamental-mode WPT channel continues to generate a higher electrical amplitude at the receiver end due to the inherent sensitivity of the fundamental mode and the reduced ultrasound transmission attenuation at lower frequencies. To address this, increasing the drive ratio of the COM channel to the WPT channel ($V_{0,3}/V_{0,1}$) from 1:1 to 1.4:1 while maintaining a constant voltage level on the WPT channel, the transferred electrical power from the central electrode showed a gradual decline. Direct demodulation of the raw electrical signal from the annular electrode at this stage yields almost unrecognizable data without filtering. This trend persists until the drive amplitude reaches 1.5:1. Beyond this point, data quality from the COM channel, associated with the (0,3) mode, began to improve significantly. This enhancement in data quality correlates with an increase in the dominance of the (0,3) mode's mechanical and acoustic response, while the signal from the WPT channel declined linearly. A balanced operating point was set at a drive ratio of 1.7:1, the waveforms of individual channel before and after combination are shown in Figure 55 (top). Under this condition, the receiver PMUT, when separated by 1.5 cm in air from the TX, achieves a power transfer of 1.52 µW from its central electrode, and the COM channel achieves a BER of 9.7×10^{-4}.

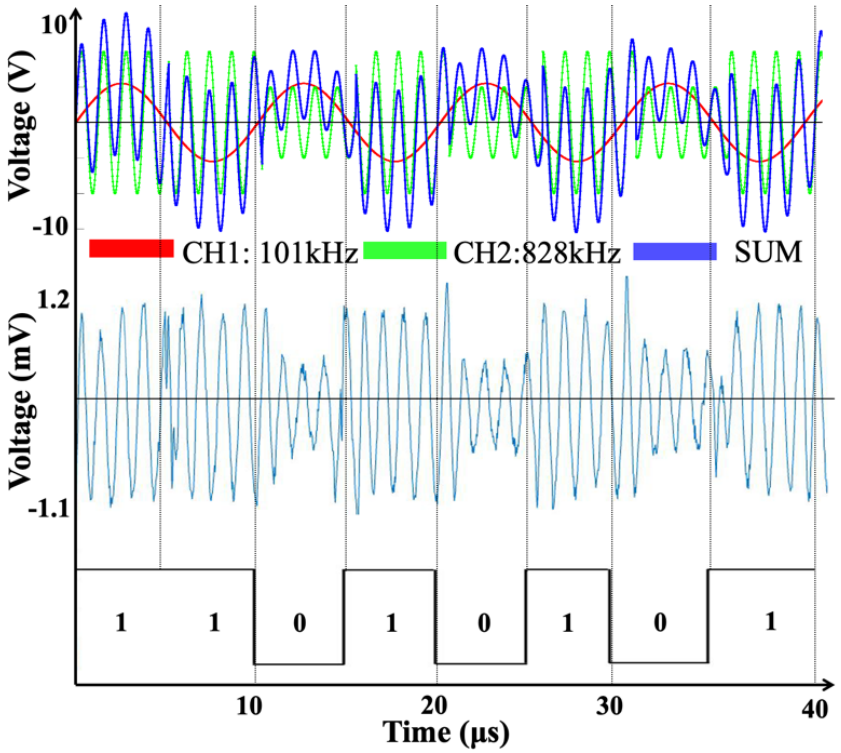

Figure 55. Top: driving signal (blue) with binary data encoded at channel 2 and 1.7:1 drive amplitude ratio between COM(CH2) and WPT(CH1) channel. Middle: open-circuit voltage output from the annular electrode. Bottom: demodulated binary signal using an asynchronous ASK demodulator with envelope detection scheme.

In the realm of communication applications, the carrier frequency plays a pivotal role. A higher carrier frequency allows for faster and direct modulation, which in turn enables a higher data rate. Nevertheless, designing electrodes for higher carrier frequency in COM channel tends to increase interference with WPT channel. For instance, the circular PMUT's COM channel utilizes a (0,3) mode at 828 kHz, facilitating a 50 kbps data rate. However, its electrode design, which overlaps with the fundamental (0,1) mode used for WPT channel, necessitates careful drive level adjustments to ensure both optimal data quality and power transfer. Conversely, the square PMUT operates its COM channel at a (1,2) mode of 216 kHz, resulting in a 10 kbps data rate, despite its lower BER of 1.9×10^{-4}, indicating higher data quality. This is attributed to the square PMUT's electrode design being specifically optimized for the 216 kHz mode, facilitating efficient transmission without the need for drive amplitude optimization between channels. In the design of dual-function PMUTs, the electrode design emerges as a critical factor—balancing the data rate with data quality. While the circular PMUT offers a faster data rate due to its higher frequency mode, the square PMUT, with its tailored electrode design, provides a more refined and accurate data transmission, as evidenced by its lower BER.

One promising application of the dual-function PMUT in WPT and COM is the establishment of an intrabody network [100]. This network would concurrently supply power and data to implants or sensors within the body. To emulate a genuine biomedical environment, we introduced a 17.2 mm-thick tissue-mimicking phantom between the TX and RX as previously shown in Figure 39. C. This phantom, composed of gelatine and water, was designed to mimic the acoustic properties of human tissue [120, 121]. The acoustic impedance of the phantom was determined by driving an ultrasound transducer in air and measuring the ultrasound intensity from a calibrated microphone (BRUEL & KJAER, Type 4138), both before and after the ultrasound wave penetrated the phantom. The acoustic power measured before and after the 17.2 mm phantom were 937.2 $\mu W/cm^2$ and 910.7 $\mu W/cm^2$, respectively. This corresponds to an attenuation of 0.069 dB/cm at 101 kHz or 0.68 dB/cm/MHz. For context, the actual attenuation coefficients of human fat and soft tissue are 0.63 dB/cm/MHz and 0.75 dB/cm/MHz, respectively[122]. This highlights the phantom's ability to closely replicate the acoustic properties of human tissue. While the frequency-dependent attenuation coefficient becomes more pronounced at higher frequencies, the sensitivity of the COM channel is significantly reduced when combined with the low-frequency WPT channel during dual-functional operation. As a result, a higher drive ratio between channels was required to compensate for the limited COM channel

resolution. The drive (V_{COM}/V_{WPT}) ratio was set to 3.5 for the circular PMUT and 1.9 for the square PMUT. Consequently, the circular PMUT achieved a power level of 411.3 nW and a data rate of 50 kbps with a BER of 1.7×10^{-2}. In contrast, the square PMUT received a power level of 202.4 nW and a data rate of 10 kbps with a BER at 8.1×10^{-4}.

5.5.2 Conclusion

In this chapter, the multi-channel operation of PMUTs was investigated using an integrated approach of numerical analysis combining with simulation, design, and experimental verification. Central to the findings is the intrinsic trade-off between power levels and the quality of communication data. The design of the PMUT electrodes, along with mode selection, impacts the reported performance.

The electrode design plays a pivotal role, facilitating the precise adjustment of the transmit/receive sensitivities across different modes. This aspect is crucial to the efficient operation of multi-channel PMUTs and becomes even more pronounced when coupled with mode selection. Experimental data shows that the choice of mode critically defines the signal resolution within each channel. For example, circular PMUTs with symmetric mode combinations feature strong mode shape overlaps, prioritizing signal quality at fundamental mode. On the other hand, when square-shaped PMUTs utilize a blend of symmetric and asymmetric modes, the resulting data quality in high-order asymmetric mode is notably sharp, evidenced by its low BER and high SNR. However, this increased signal resolution at high-order mode comes with a trade-off in the form of diminished signal intensity from fundamental symmetric mode. To maintain high-quality signals across different modes, adjustments in the drive amplitude ratio are necessary for balancing the overall performance in dual-mode operation. We seamlessly integrated the dual functionality of wireless power transfer (WPT) and communication (COM) into both circular and square PMUT prototypes. Preliminary tests, both in ambient air and using a tissue-mimicking phantom, validated their operational effectiveness. Adjustments in the drive amplitude ratio between the two channels allow for customized performance of WPT and COM according to specific application needs. This design approach has significant ramifications for future ultrasound transducer applications. With a single device now capable of accessing multiple frequency bands, this work opens the possibility of realizing multiple functions each optimized around a specific frequency band. This work illustrates this feasibility in the context of wireless power transfer and data telemetry. Importantly, this dual functionality has been

successfully emulated in a tissue-mimicking phantom, to establish initial feasibility in a biomedical application context.

This research not only highlights new capabilities of PMUTs, predominantly harnessing two modes for peak performance but also paves the way for further investigations. The direct comparison of mode combinations in the multi-channel performance of circular and square PMUTs reveals potential areas for future research, including the development of optimized mode combinations and electrode patterns that aim to achieve both high power and improved data quality without the need for adjustments. Future iterations could potentially encompass a broader array of modes spaced over a wider range of frequencies. When combined with enhanced electrode designs to stimulate multiple modes, an expansive exploration of the ultrasound spectrum is enabled, facilitating innovations in sensing and measurement applications as explored in this study.

5.6 Electrode Optimization

The previous section detailed the dual-mode operation of circular and square piezoelectric micromachined ultrasonic transducers (PMUTs) prototypes, which were meticulously engineered to support simultaneous activations under two distinct modes. This dual-channel design facilitates both wireless power transfer (WPT) and data telemetry. Experimental validations have demonstrated that while circular PMUT prototype exhibit faster data transmission capabilities due to the higher carrier frequency of the COM (0,3) mode, the quality of data transmission requires careful calibration of the drive amplitude ratio between the axisymmetric WPT (0,1) and the COM (0,3) modes. This attributes to the significant overlap in stress distribution when combining two axisymmetric modes (m=0 and n≠0) at the same time, which may lead to strong signal interference when combining to drive together. In contrast, square PMUTs, despite a reduced data rate attributed to the lower carrier frequency of the asymmetric COM (1,2) mode, provide superior data quality without the prerequisite of drive amplitude adjustments when combing with an axisymmetric (1,1) mode for WPT. This advantage is attributed to the distinct mechanical strain patterns that are generated by high-order asymmetric modes (m≠0 and n≠0), which feature multiple radial nodes and disparate mechanical strain distributions across various regions of the vibrating membrane. These distinctive strain patterns differ markedly from those generated by the axisymmetric modes, effectively reducing mode interference. Based on these observations, the performance of multi-channel PMUTs can be further improved

focusing on two primary objectives: increasing the carrier frequency to enhance data transmission speed and reducing intermodal interference to improve channel resolution. These goals are pursued through the development of innovative electrode designs that facilitate the excitation of higher-harmonic modes and the strategic selection of mode combinations that demonstrate minimal strain overlap.

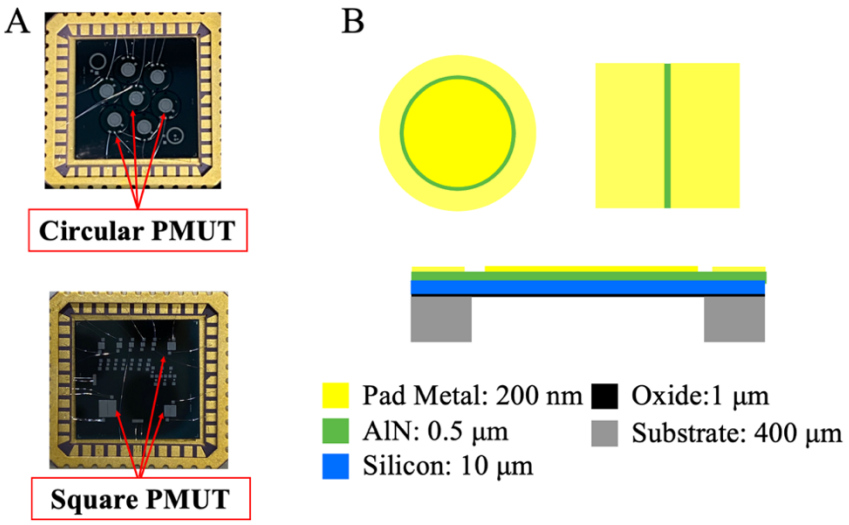

Figure 56. A: The circular and square dual-channel PMUT prototypes. B: The electrode layout of circular and square prototypes targeting axisymmetric and asymmetric modes.

5.6.1 Device Design

In Section 5.1, both circular and square PMUTs highlighted a significant benefit in employing both axisymmetric and asymmetric modes for multi-channel operation. This configuration effectively reduces strain distribution overlap, which is crucial for minimizing signal interference among channels. This section is devoted to the development of an optimized multi-channel PMUT array with two primary goals: minimizing inter-modal interference to enhance channel resolution and employing high-order resonant modes to boost operating frequencies and accelerate data transfer rates. For low-frequency Wireless Power Transfer (WPT), asymmetric modes have been selected, while high-order axisymmetric modes are utilized for Communication (COM) applications, reflecting their specific functional advantages.

Assuming the constant acoustic impedance and material properties of PMUTs, the transmitting sensitivity S_{TX} at a designated mode is derived in Section 4.3 and expressed by the Equation (54) as:

$$S_{TX} = \frac{Z_a A_{eff} \eta}{j\omega m_m + {A_{eff}}^2 Z_a + \frac{1}{j\omega C_m}} \tag{54}$$

Here, η, the turn ratio, is determined by electrode design, which directly affects sensitivity. Assuming the PMUT's electrode design is optimized based on the mechanical strain distribution specific to each mode, the normalized transmitting sensitivity of a circular PMUT with a cavity radius of 100 μm and consistent AlN-on-SOI structure are computed as 1, 6.84, and 17.52 for the (0,1), (0,2), and (0,3) axisymmetric modes respectively. Given their superior transmitting sensitivity, the higher-order axisymmetric (0,2) and (0,3) modes have been chosen for COM channels in this electrode-optimized PMUT design, which enhances signal resolution and supports faster data transmission due to higher carrier frequencies.

The electrode design adheres to a principle of covering as much area under the same mechanical stress polarity as possible to maximize electromechanical coupling efficiency, crucial for enhancing the performance of single-mode operations within a multi-mode scheme. This is supported by detailed numerical analysis, which resolves the general deflection functions (equations 10 and 13) under edge-clamped boundary conditions. As a result, the roots for the first three axisymmetric and two asymmetric modes have been determined, and their deflection profile are shown in Figure 57 with normalized radius. Their mechanical stress profiles, along with zero-crossing radial coordinates, are essential for guiding electrode optimization efforts and are listed in the following table:

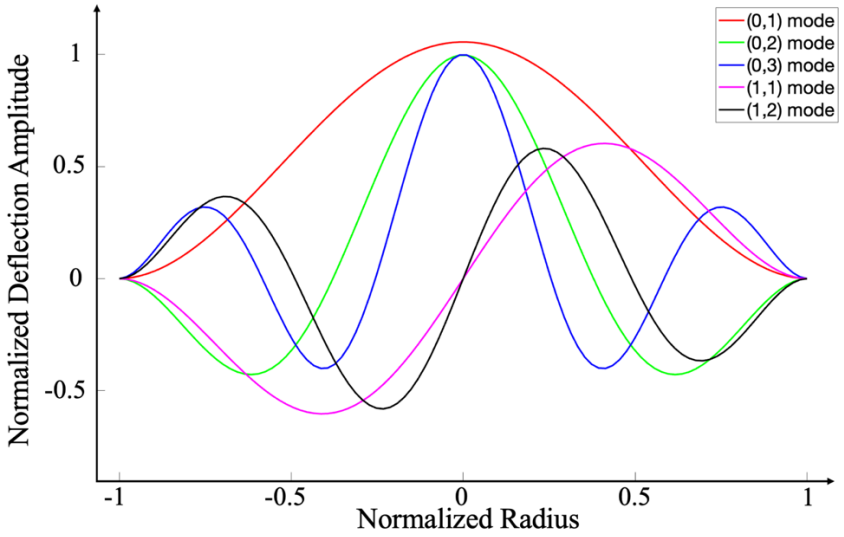

Figure 57: Normalized deflection profile of first 3 axisymmetric and 2 asymmetric modes.

The electrode design aims to efficiently cover areas within the same stress polarity as indicated by the stress nodal circle in the table, where r_0 represents the normalized radius of the stress nodal circle

for symmetric modes, at which location the mechanical stress flips the polarity. The normalized radius of stress nodal circles for first five modes are calculated in Table 6.

Table 6. Zero-crossing mechanical stress radius and resonant frequency ratio for first 3 axisymmetric and 2 asymmetric modes of circular PMUTs

mode	(0,1)	(1,1)	(0,2)	(1,2)	(0,3)
r_0	0.66	0.74	0.39 0.84	0.47 0.86	0.26 0.59 0.89
f/f_0	1	2.09	3.89	5.98	8.3

This strategic placement is critical for reducing inter-mode interference. Although the fundamental mode exhibits maximal deflection amplitude, its expansive deflection pattern frequently overlaps with those of other modes, resulting in significant intermodal interference under multi-mode operation. This overlap frequently results in significant intermodal interference during multi-mode operation. For instance, the previous circular PMUT prototype, which operated simultaneously in the fundamental (0,1) and higher-order axisymmetric (0,3) modes, experienced strong signal interference due to the overlapping mechanical responses at the center. Consequently, this necessitated adjustments in the drive amplitude ratios between the different modes and required a tradeoff between COM and WPT performance. Given these challenges, the current electrode optimization strategy excludes the fundamental mode operations despite their high sensitivity. Instead, this optimized design incorporates a combination of axisymmetric and asymmetric modes to reduce interference during multi-mode operation by minimizing the overlap of modal responses. Specifically, the asymmetric modes display peak deflections around the center at diametrically opposite points, whereas the higher-order axisymmetric modes, particularly (0,2) and (0,3), exhibit peak deflections both at the center and periphery of the circular PMUT. By employing uniformly distributed ring electrodes, strategically distanced from the central peak deflections of the asymmetric modes, this configuration is ideally suited for multi-channel operations with minimal modal response overlap. Furthermore, due to their higher operating frequencies—3.89 and 8.3 times that of the fundamental (0,1) mode—the axisymmetric mode such as (0,2) and (0,3) modes are selected for COM applications. Their uniform electrode layout is essential for facilitating high-speed

data communication. Conversely, the first asymmetric (1,1) mode, with its distinctive mode shape and unique deflection patterns, is ideally suited for WPT applications due to its minimal strain overlap and reduced mechanical interference with the axisymmetric modes. As a result, the chosen electrode pattern includes a pair of splitting electrodes E_1 for targeting the asymmetric (1,1) mode used for WPT, due to its distinctive mode shape and minimal overlap with the axisymmetric modes utilized in COM. Additionally, two annular ring electrodes E_2 and E_3 are designed to focus on the higher-order axisymmetric modes, thereby enhancing their functionality in COM applications. This tailored electrode pattern ensures that each mode operates with optimal efficiency and minimal interference under multi-channel operation, supporting the dual functionality of the PMUT in both WPT and COM applications.

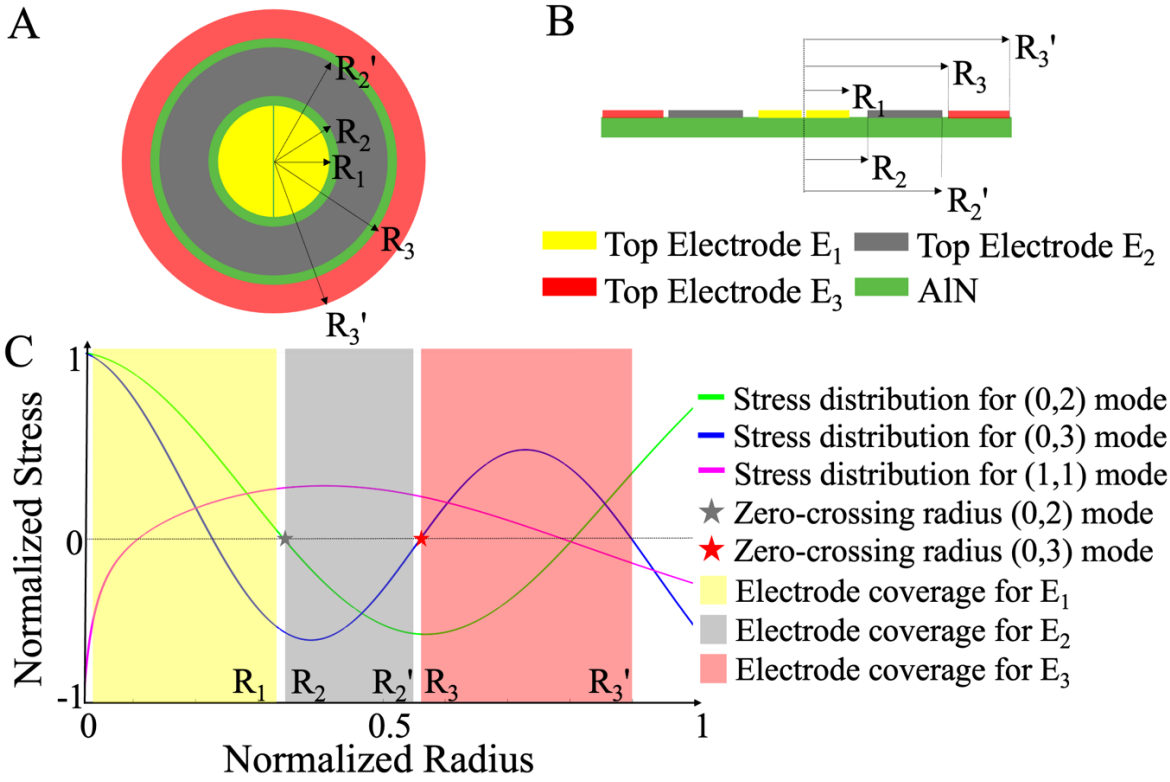

Figure 58. A: Top electrode pattern with splitting electrode E_1 (yellow), and two annular ring electrode E_2 (gray) and E_3 (red). B: Cross-section view of proposed electrode-optimized PMUT. C: Normalized stress distribution of two targeting axisymmetric modes and one asymmetric mode.

Shown in Figure 58. C, the radial stress are plotted of a circular membrane across normalized radius for 3 targeting modes. In this case, the zero-crossing radius are critical in balancing the channel sensitivity for these modes and also reducing the inter-mode interference when PMUT driven under

multiple modes simultaneously. The individual electrode dimension is firstly individually studied, then combined together to determine the optimal dimension for a sensitivity-balanced multi-mode PMUT.

In practical terms, the (0,3) mode, with its highest operating frequency and limited overlap with the asymmetric (1,1) mode, is prioritized for COM applications where high-quality data transmission is critical. The electrode pattern for this mode is designed to ensure minimal interference from lower-frequency modes. This is achieved by strategically positioning the annular electrode E_3 to cover the maximum stress area towards the edge of the PMUT, setting its inner radius precisely at a zero-crossing point of the stress distribution. Further electrode optimization focuses on the splitting electrode E_1 and the annular electrode E_2, which are optimized for operations involving the (1,1) and (0,2) modes, respectively. Aligning these electrodes within the positive stress regions of the (1,1) mode profile allows for connecting and driving E_1 and E_2 in parallel, significantly enhancing the sensitivity of the (1,1) mode. Alternatively, when targeting just the (0,2) mode, E_2 is driven individually. Its design includes positioning its inner radius at the zero-crossing radial location of its stress distribution, effectively reducing inter-mode interference and increasing its sensitivity. This flexibility in electrode configuration enhances the PMUT's ability to select and switch specific channels or operating frequencies effectively, providing robust multi-channel operation capabilities that adapt to the needs of different application. The finalized PMUT and electrode dimensions are determined through this comprehensive analysis. The PMUT features a radius of 280 μm and includes a central splitting electrode E_1 with a radius of 109 μm. The annular electrode E_2 spans from 110 μm to 155 μm, and the annular electrode E_3 extends from 165 μm to 252 μm. Fabrication of the PMUTs utilized a consistent Aluminum Nitride (AlN) on Silicon-on-Insulator (SOI) platform, with each device featuring a 0.5 μm-thick AlN layer atop a 10 μm-thick SOI wafer. The fabricated PMUTs are shown in Figure 59 below. The fabricated devices then undergo frequency response testing to validate the performance improvements.

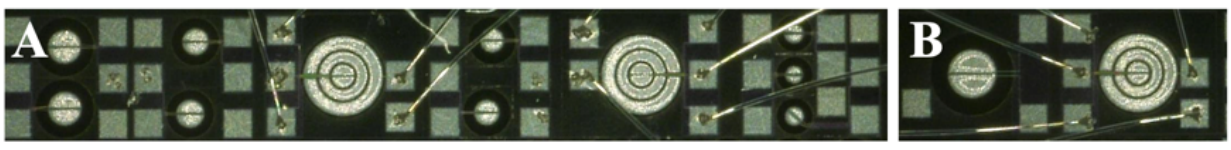

Figure 59. Optical image of optimized multi-channel PMUT A: TX; and B: RX.

5.6.2 Device Characterization

In the experiment, Digital Holographic Microscopy (DHM) was utilized to record the vibration responses and resonant frequencies of the optimized PMUTs, capturing the first five modes at 464 kHz, 950 kHz, 1.78 MHz, 2.31 MHz, and 4.28 MHz. Subsequently, the deflection sensitivity of both the traditional single-electrode PMUT and this section's optimized multi-channel PMUT were studied and compared. The traditional single-electrode PMUT, having identical dimensions and structure, was analyzed using COMSOL by driving its central circular electrode with a 4 V_{pk} AC signal, and the deflection sensitivity of its first five modes was recorded. The results of these analyses are displayed in Figure 58. The optimized multi-channel PMUTs were characterized by applying a 4 V_{pk} signal to specific electrodes. The axisymmetric modes (0,1), (0,2), and (0,3) were driven using annular ring electrode E_3, while the asymmetric modes (1,1) and (1,2) were driven using central splitting electrode E_1.

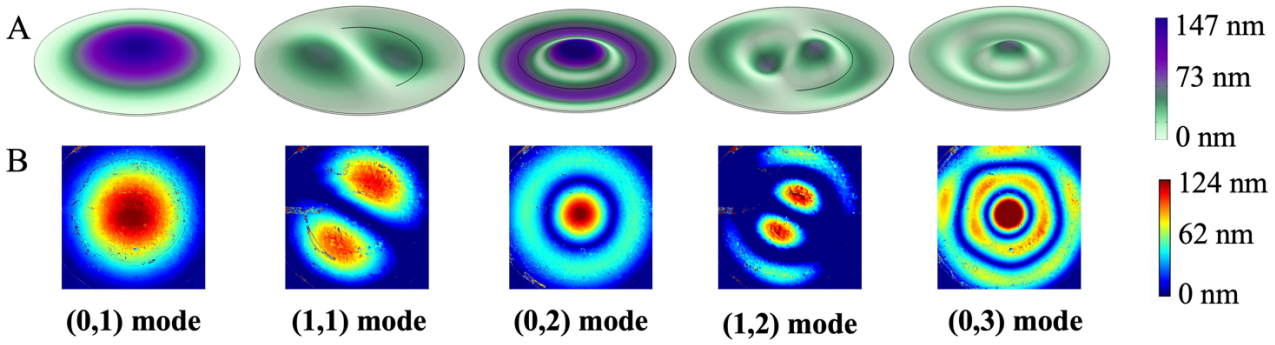

Figure 60. A: COMSOL simulated mode profile of a traditional single-electrode PMUT. B: Experimentally measured vibration profiles of an electrode optimized multi-channel PMUT for first 5 modes from 464 kHz to 4.3 MHz.

Figure 60 shows that despite a reduced driving sensitivity at the fundamental mode—attributable to the electrode optimization compromising electromechanical efficiency—the electrode optimized multi-channel PMUT exhibited superior driving sensitivity across all higher-order resonant modes. Notably, the asymmetric modes (1,1) and (1,2) demonstrated 28.2 nm/V and 20.7 nm/V deflection sensitivity, corresponding to 57.8% and 42.4% increase compared to the dual-channel PMUT prototype and 71.7% and 56.5% compared to traditional single electrode PMUT from FEA simulation and experimental characterization. Meanwhile the axisymmetric (0,3) mode showed a 46.4% increasing comparing to dual-channel PMUT prototype from 17.9 nm/V to 26.2 nm/V. These findings

underscore the effectiveness of electrode optimization in enhancing the PMUT's mechanical sensitivity for higher modes, setting the stage for further investigations into its acoustic performance in actual transmitting-receiving applications. Each mode exhibits distinct relative movements determined by its corresponding vibration profile, which is illustrated as effective area in the equivalent circuit method from numerical analysis in section A. The actual acoustic performance of the multi-channel PMUT still requires further investigation in real environments. For example, asymmetric modes naturally yield lower transmitting output when used to drive a PMUT as a transmitter due to their opposite movement relative to the center of the circle, resulting in a significant acoustic pressure offset. To verify the improvement of electrode optimization on the actual performance of the PMUT in multi-channel operation, we defined a figure of merit to evaluate the PMUT's sensitivity-bandwidth (SBW) product:

$$SBW = S_{Max} \times BW_F \tag{60}$$

where S_{Max} represents the transmitting-receiving sensitivity in V/V at the resonant peak of each mode, and BW_F is the -6dB fractional bandwidth for the designated mode ($BW_F = \frac{BW_{-6DB}}{f_o}$). The SBW for the first five modes from the previous dual-channel PMUT prototype and the optimized multi-channel PMUT are measured and summarized in the table below. Specifically, improvements in the (1,1) and (0,3) modes' transmitting-receiving sensitivity, and the balance between them, realize the design goal and prove the effectiveness of electrode optimization for simultaneous multi-mode operation in specified applications.

Table 7. SBW comparison between dual-channel PMUT prototype and electrode optimized PMUT

SBW (dB)	(0,1)	(1,1)	(0,2)	(1,2)	(0,3)
Dual-Channel Prototype	-73.3	-119.9	-88.7	-120.3	-85.6
Optimized Electrode PMUT	-87.8	-95.5	-79.1	-101.4	-70.3

5.6.3 Wireless Power Transfer and Data Telemetry

The Wireless Power Transfer (WPT) and Communication (COM) dual-channel applications were tested on the optimized multi-channel PMUTs, using the (1,1) mode for WPT and the (0,3) mode for COM. A pair of PMUTs—one as a transmitter and the other as a receiver—were positioned across the same 17.2 mm-thick bio-mimicking phantom. This phantom, composed of gelatine and water, was designed to mimic the acoustic properties of human tissue. The transmitter was driven with a summed signal from the splitting electrodes. As shown in Figure 61. B, the transmitter was driven by a summed signal, combining a continuous 10V sinusoidal AC signal for the WPT channel at the (1,1) mode frequency and a 10 V Amplitude Shift Keying (ASK)-modulated signal for the COM channel at the (0,3) mode frequency. On the receiving end, the inner splitting electrode of the receiver PMUT was targeted to pick up the WPT signal, while the annular ring electrode was used to capture the COM signal. The responses from each channel were recorded with an oscilloscope and are depicted in Figure 61. C and D.

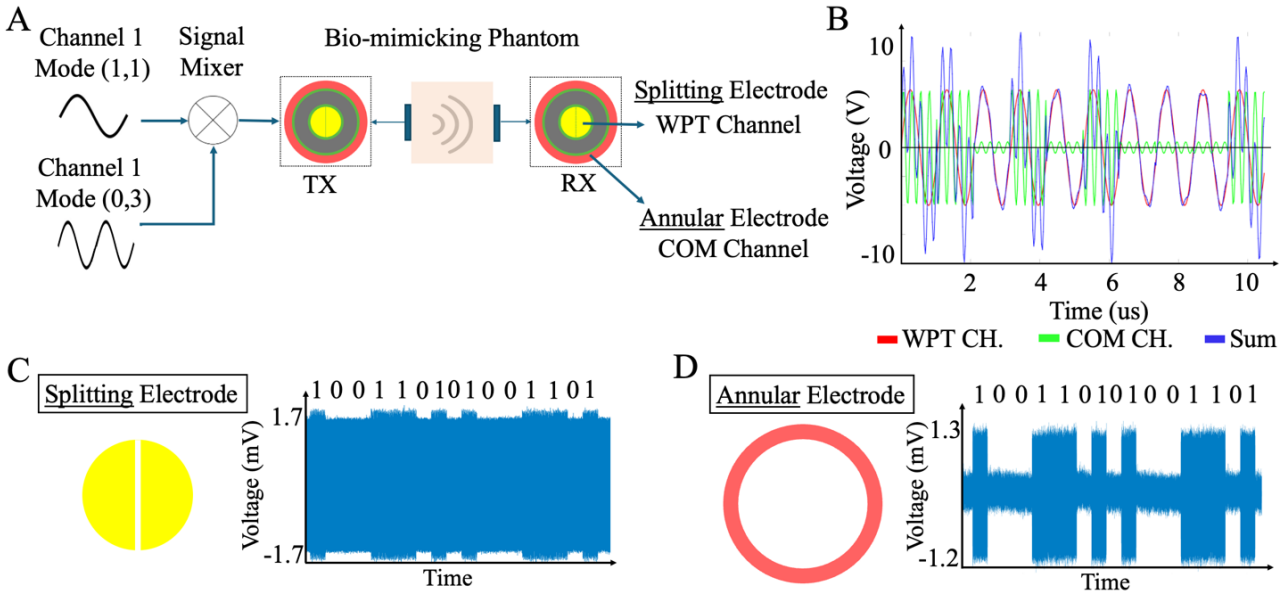

Figure 61. A: Experimental Setup for dual-function WPT and COM experiments on optimized multi-channel PMUT utilizing asymmetric (1,1) mode for WPT and axisymmetric (0,3) mode for COM. B: A summed signal to drive the PMUT TX with 1:1 amplitude ratio between WPT and COM channels. C: Electrical response from splitting electrode reflecting a dominant response from (1,1) mode WPT channel. D: Electrical response from annular electrode showing sharp ASK-modulated response from (0,3) mode COM channel.

Because of the higher carrier frequency, the data transfer rate significantly increased from 50 kbps to 945 kbps comparing to previous multi-channel PMUT prototype with COM channel frequency at 828 kHz. By integrating both axisymmetric and asymmetric modes, the new electrode layout reduced overlapping areas of mechanical stress compared to the original multi-channel PMUT design. This enhancement led to improved data quality with reduced Signal-to-Noise Ratio (SNR) on the COM channel, even without adjusting the drive amplitude ratio between the WPT and COM channels. The previous dual-channel PMUT prototype was driven and tested with an amplitude ratio ($V_{COM}/V_{WPT=}3.5$) between COM and WPT channel. As a result, the Bit Error Rate (BER) decreased from 1.7×10^{-2} to 8.8×10^{-3}, when driving the two channels at a 1:1 amplitude ratio for this electrode optimized PMUT. For WPT, the static capacitance was measured at 1.8 pF for either side of electrode E_1. The tailored electrode design, based on the asymmetric mode deflection profile, resulted in a reduced electrode area and static capacitance, thereby enhancing the PMUT's receiving sensitivity and leading to a higher output voltage. Consequently, while the COM channel exhibited a faster transfer rate and improved data quality, the received electric power from the WPT channel at the asymmetric (1,1) mode reached 504.3 nW, marking a 22.7% increase compared to the previously designed multi-channel PMUT prototype.

5.6.4 Conclusion

This section demonstrates the effectiveness of multi-channel PMUTs through innovative electrode designs that facilitate the concurrent operation of multiple modes. The optimized PMUT design integrates both axisymmetric and asymmetric modes, specifically tailored for wireless power transfer and communication applications. The strategic electrode design, characterized by distinct separation of ring and splitting electrodes, effectively minimizes mechanical stress overlap and intermodal interference, a critical factor in multi-channel operation. This approach not only preserves the integrity of data transmission and power delivery but also optimizes the acoustic performance of each mode. The experimental validation confirms improvements in data rate, data quality, and power levels, outperforming previous dual-channel PMUT prototype. Furthermore, the dual-functionality of the optimized PMUT array is tested within a biomedical application framework using a biomimicking phantom, which simulates the operational environment of biomedical implants. In this setup, a low-frequency carrier supports wireless power transfer, while high-frequency channels enable acoustic communication.

In conclusion, this section highlights the significant role of electrode optimization in enhancing the performance of multi-channel PMUTs. Drawing on insights from previous prototypes, the electrode optimization strategy incorporates the selection of specific mode combinations and the designing customized electrode patterns to effectively minimize interference among modes during operation. This optimization facilitates simultaneous multi-mode operations, enabling the multi-channel PMUT to surpass traditional limitations associated with fixed-frequency ultrasonic devices that often necessitate a compromise between operating frequency and application specificity. The capacity to operate across multiple frequencies without significant interference not only extends the practical applicability of multi-channel PMUTs but also enhances their adaptability for more sophisticated ultrasonic systems across a broader range of applications. Future research will aim to refine these electrode configurations further and explore new combinations of operational modes to expand the operational bandwidth and adaptability of PMUT arrays in complex applications. This advancement contributes to the field by broadening the utility and functionality of ultrasonic devices, thereby paving the way for their application in areas where traditional ultrasonic solutions have fallen short.

5.7 Conclusion

In this chapter, we describe the design and characterization of a multi-channel PMUT operation scheme that simultaneously drives and senses multiple resonant modes. The first-generation prototypes, featuring both circular and square geometries with customized electrodes, were validated. These prototypes targeted combinations of a fundamental mode and a higher-order axisymmetric or asymmetric mode, respectively. Initial characterizations confirmed good agreement with predictions from the equivalent circuit models used in our numerical analysis.

Building on this multi-mode PMUT scheme, a multi-channel ultrasound link was successfully established between a pair of PMUT chips, demonstrating potential innovations and applications that leverage both low- and high-frequency ultrasound simultaneously. For example, the dual-functionality of wireless power transfer (WPT) and data telemetry was achieved by exploiting the low attenuation properties of low-frequency ultrasound for power delivery and the high communication rate capabilities of high-frequency ultrasound for data transmission. Testing across a biomimicking phantom, the circular PMUT demonstrated a power output of 411.3 nW and a data rate

of 50 kbps with a Bit Error Rate (BER) of 1.7×10^{-2}. Conversely, the square PMUT recorded a power output of 202.4 nW and a data rate of 10 kbps with a BER of 8.1×10^{-4}.

Further analysis of the first-generation multi-channel PMUTs highlighted the significant impact of inter-modal interference on performance, affecting signal quality across each channel. It was observed that different mode combinations directly influenced the isolation and suppression of shared modal responses in deflection and strain distribution when operating two or more modes simultaneously. This insight led to the design of an electrode-optimized multi-channel PMUT. By focusing on higher-order axisymmetric and asymmetric modes and studying the strain distribution and mode responses through numerical and analytical models, the new design abandoned the commonly utilized fundamental mode. The optimized multi-channel PMUT significantly enhanced signal quality and reduced intermodal interference through calibrated electrode patterns and mode selection. Subsequent tests on the same dual-function WPT and data telemetry applications showed considerable improvements: the data transfer rate increased significantly from 50 kbps to 945 kbps compared to the first-generation prototype, and the BER reduced from 1.7×10^{-2} to 8.8×10^{-3}. Moreover, in the WPT channel, the received power at the asymmetric (1,1) mode reached 504.3 nW, marking a 22.7% increase over the previous design.

Chapter 6

Multi-frequency PMUT Array

6.1 Device Design

In the previous chapter, we investigated the potential of driving Piezoelectric Micromachined Ultrasound Transducers (PMUTs) beyond their fundamental modes to establish simultaneous multi-channel links. In this section, we further this exploration by investigating a high-density array comprising various PMUT designs, which operate at diverse frequencies. This approach utilizes wider ultrasound spectrum and aims to maximize the operational frequency limits within current microfabrication capabilities. Leveraging advanced microfabrication technology, we have developed a high-density PMUT array featuring three distinct circular designs. This includes configurations known as PMUT 1, PMUT 2, and PMUT 3, with respective radii of 150 μm, 224 μm, and 98.5 μm. Due to the constraints imposed by fabrication tolerances and electrode deposition, each PMUT is equipped with a single central electrode, covering 69.6% of the area. The PMUT chip was manufactured using the same Aluminum Nitride (AlN) on Silicon-on-Insulator (SOI) platform, with an identical structural configuration—a 0.5 μm-thick AlN layer situated atop a 10 μm-thick SOI wafer. PMUT 1 (shaded in yellow) features seven channels, each channel comprising 19 PMUTs connected in parallel. PMUT 2 (shaded in green) is similarly structured, with seven channels of 28 PMUTs each. PMUT 3 (shaded in red), slightly differing, includes six channels with 41 PMUTs each. The layout of the fabricated chip is depicted in Figure 62 below.

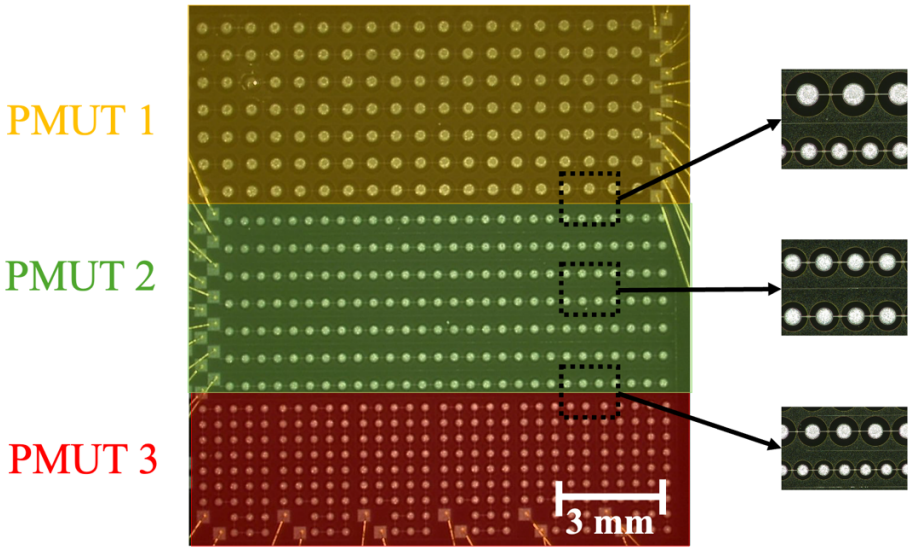

Figure 62. Fabricated multi-frequency PMUTs array with different dimension as PMUT 1 (yellow), PMUT 2 (green), and PMUT 3(red).

Using a lock-in amplifier, we conducted a frequency response analysis by electrically driving one selected array of PMUTs with a 1 V_{pk} AC signal across an estimated frequency range and measuring the electrical output from another array of the same design. The frequency sweep results for PMUTs 1, 2, and 3 identified their fundamental resonant frequencies at 1.5 MHz, 2.7 MHz, and 3.2 MHz in air. To better simulate the application environment typical of most pulse-echo ultrasound testing, which often occurs in a medium with acoustic properties similar to human tissue, the multi-frequency PMUTs were coated with 2 µm of parylene C for testing in a liquid environment. The coated PMUT chip was mounted on a customized PCB submerged in Fluorinert FC-70, an engineered liquid chosen for its acoustic impedance roughly equivalent to that of human tissue (~1.5 MRayls). For the liquid environment testing, a pair of PMUTs was separated by 15 cm to assess their frequency response. One PMUT served as the transmitter, driven with an AC signal across the estimated frequency range, while the other functioned as the receiver, capturing its electrical output. The results of this frequency sweep under liquid conditions are recorded at 750 kHz, 1.35 MHz and 1.8MHz shown in Figure 63, with estimated 40% reductions in the resonant frequencies of PMUT 1, 2, and 3 due to the additional damping effect of the liquid. Notably, it is important to highlight that even with the same design specifications, variations in manufacturing processes such as over-etching during substrate etching can slightly alter the dimensions of the structures, thus shifting the frequency response from one chip to another. As shown in the frequency sweep tests that there often exists more than one resonant peak, corresponding to the resonant frequencies of both the transmitting and receiving PMUTs, as

illustrated in Figure 63. In the context of miniaturized structures like the proposed multi-frequency PMUTs, such variability in frequency response is particularly pronounced. However, the shifts due to fabrication deviations generally remain within the -3dB bandwidth, thus that their overall impact on PMUT performance is relatively limited.

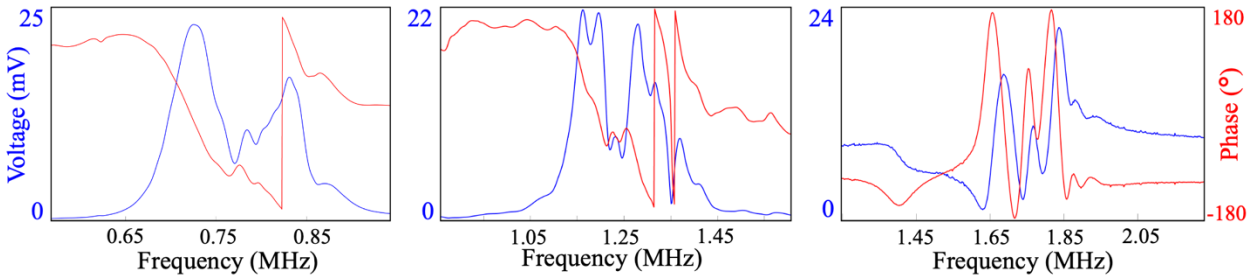

Figure 63. Frequency response of PMUT 1(left), PMUT 2(middle), and PMUT 3(right) arrays coated and immersed in engineered liquid FC-70.

6.2 Concurrent Pulse-Echo and Through-Transmission Ultrasound Tracking

In the previous chapter, the potential of micromachined ultrasound transducers for wireless power and data transmission within biomedical applications was investigated. Specifically, PMUTs have demonstrated their optimal power, miniaturization, and adaptability to complex ultrasound application environments. In the field of ultrasound, two methodologies are commonly employed: the through-transmission and pulse-echo methods. The through-transmission method involves ultrasound waves traveling through a sample to measure the impact of the sample's physical properties on acoustic properties like sound speed and frequency. Commonly applied in non-destructive testing, flowmeters, and temperature tracking, this method has seen significant advancements through PMUTs leveraging MEMS technology to improve accuracy and performance. For instance, Gao et al. successfully implemented a ScAlN PMUT array that accurately measures liquid flow velocity by utilizing transit-time techniques derived from pulse echo methods. This setup achieved a measurement sensitivity of 82 ns/(m/s) and a signal-to-noise ratio (SNR) greater than 15 dB, capable of handling flow measurements from 2 to 300 L/h in channels as narrow as 4 mm in diameter [123]. In contrast, the pulse-echo method analyzes echo signal's time-of-flight (ToF), amplitude and frequency to determine the physical properties of samples, crucial for applications such as sonar, biomedical imaging, and IoT devices like eye trackers and range finders. Utilizing ToF data from

ultrasound echoes, researchers can accurately gauge changes in the diameter of an artery model under varying vital parameters. Zhou et al. utilized a 23 by 26 PMUT array to monitor blood pressure variations, while Wu et al. employed a hexagonal PMUT array to assess the stiffness of a radial artery [124, 125]. Similarly, Sun et al. developed a 15 by 15 PMUT array at 1 MHz to observe eye movement based on ToF variations from different angles of eye model rotation [81]. Despite their extensive application, traditional ultrasound systems typically utilize only one measurement method at a time. For example, in pulse-echo detection, energy penetrating the sample is often ignored, and in through-transmission testing, echoed signals from various media interfaces are overlooked. With the rising demands of next-generation technologies, such as the IoT and implantable biomedical devices, there is a pressing need to explore the integration of both measurement methods to enable multi-functional sensing during operation. This approach, however, faces challenges, particularly the interference between reflected and transmitted waves when attempting to measure both simultaneously. For example, the pulse-echo method, which relies on constant sound speed to measure time-of-flight for target location, conflicts with the through-transmission method that measures variations in sound speed due to changes in temperature or flow velocity.

To overcome these challenges, we have utilized the flexibility of MEMS and microfabrication technologies to develop a multi-frequency Piezoelectric Micromachined Ultrasonic Transducer (PMUT) array. This array is capable of transmitting and receiving multiple frequencies simultaneously, enabling us to concurrently track reflected and transmitted ultrasound signals. The fundamental operation scheme features a pair of multi-frequency PMUT arrays: one operates as the transmitter (TX), capable of both emitting and detecting ultrasound waves at distinct frequencies, and the other serves as the receiver (RX). The TX generates multiple ultrasound pulses at frequencies f_1, f_2 and f_3 as depicted in Figure 64. Depending on the specific measurement objectives, some ultrasound waves reflect back to the TX as echo signals upon encountering boundaries between media with differing acoustic impedances, while others continue travelling through the media, despite with some attenuation, to be detected by the RX on the other side. This innovative approach, which does not rely solely on a fixed-frequency signal, leverages both reflected and transmitted signals. By using multi-frequency signals and analyzing the relative phase differences, frequency, and amplitude of these ultrasound pulses, we can mitigate the common interference and measure two distinct physical variables in one go.

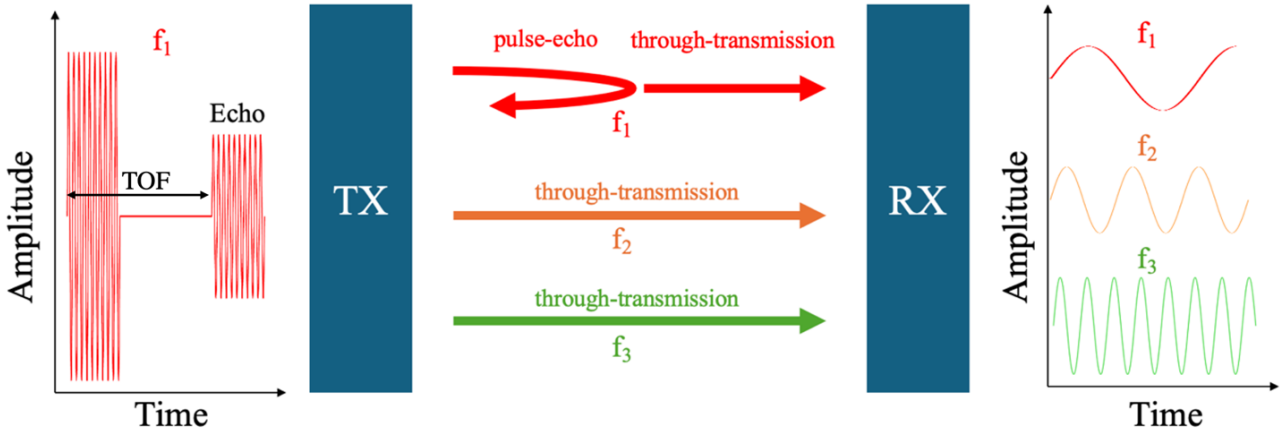

Figure 64. Working principle of the multi-frequency PMUTs array in simultaneous tracking pulse-echo and through-transmission ultrasound signals.

6.2.1 Multi-Frequency Blood Vessel Motion and Temperature Measurement

As discussed in the previous chapter, a significant challenge in using both pulse-echo and through-transmission methods simultaneously to capture dual physical variables is the interference that arises from multiple measurement variables affecting common acoustic properties. For example, ultrasound imaging and clamp-on flowmeters depend on recording the time-of-flight of echoed and transmitted ultrasound signals, respectively. Variations in the acoustic impedance of imaging tissues and flow speed in individual tests can alter the sound velocity and the time-of-flight. Traditional ultrasound transducers operating at a fixed frequency are unable to distinguish the actual variables causing changes in time-of-flight when conducting both measurements concurrently. To resolve this issue, we implemented the proposed multi-frequency PMUTs array that utilizes pulse-echo and through-transmission methods to simultaneously track two target variables. The core operational principle is based on tracking the relative phase shift between two parallel ultrasound waves at distinct frequencies, allowing for the isolation and neutralization of interference from two measurement variables. This approach enables the PMUTs to exploit both echoed and transmitted acoustic energy from a single measurement setup.

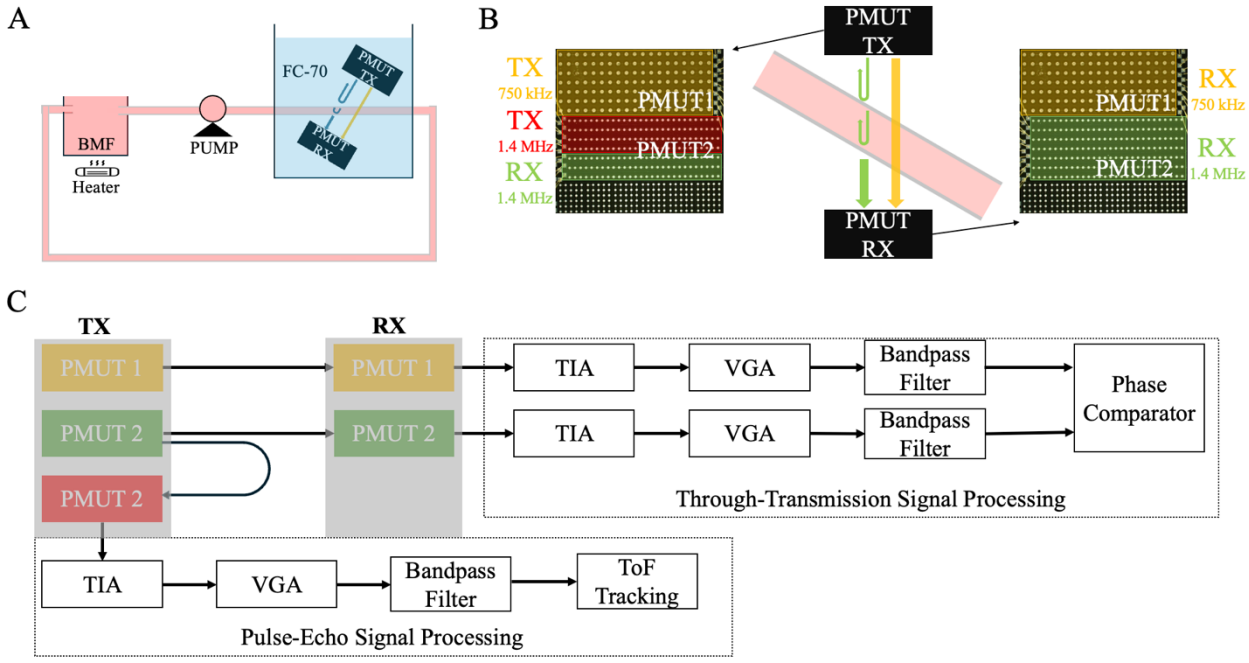

Figure 65. A: Experimental setup of temperature monitoring and blood vessel expansion tracking B: PMUT TX and RX arrangements for Pulse-Echo and Through-Transmission methods. C: Signal processing workflow for relative phase shift tracking and time-of-flight measurement.

In this section, our experimental setup involves monitoring the expansion motion of a blood vessel model and the temperature of a blood-mimicking fluid using pulse-echo and through-transmission techniques. As depicted in Figure 65. A, the approach comprises two PMUT arrays positioned on opposite sides of a polymer tube, which mimics the physical properties of a blood vessel. This model vessel has an outer diameter of 6.5 mm and a wall thickness of 0.75 mm, with the PMUT pairs mounted at a 60-degree angle to one another. The tube is filled with a blood-mimicking fluid (BMF), which consists of a suspension of Sephadex particles in a 42% glycerol and 58% water mixture, at a concentration of 1.5 g/L of water [126, 127]. And BMF is circulated by a centrifugal pump simulating an adult heartbeat with a cycle of 0.6 seconds at 1 Hz, thus inducing rhythmic expansion of the vessel walls. The temperature of the BMF is regulated via an external heater and continuously monitored by a reference thermometer to ensure experimental consistency. Our setup employs a pair of multi-frequency PMUT chips, with one serving as a transmitter (TX) and the other as a receiver (RX), each containing two PMUT arrays PMUT 1 and PMUT 2 operating at frequencies of 750 kHz and 1.4 MHz. This configuration facilitates the simultaneous monitoring of both vessel motion and fluid temperature. During operation, the TX emits consecutive ultrasound pulses at these two frequencies from PMUT 1 and 2. As depicted in Figure 65. B, all seven rows of PMUT 1 are utilized for

transmission. PMUT 2 employs four channels for transmission (highlighted in red) and three for echo detection (highlighted in green). On the RX side, all PMUTs are exclusively employed for receiving these pulses. Both the TX and RX PMUT chips are mounted on custom-PCBs equipped with signal processing modules, detailed in Figure 65. C. The acquired signals are initially amplified using a transimpedance amplifier (TIA), followed by a voltage gain amplifier (VGA), and subsequently filtered through a Biquad bandpass filter using AD8054 before signal analysis. This setup ensures that signals from each pulse-echo and through-transmission methods are optimally processed individually without interference. Initially, rhythmic expansion of the vessel walls is captured solely through pulse-echo methods using the 1.4 MHz signals. Due to the acoustic impedance differences between the FC-70 liquid and the silicone tube, ultrasound waves reflect from the liquid-tube interface twice (lower and upper walls) then return to the TX. When the pump activates, an increase in BMF pressure expands the tube, allowing measurement of minimal changes in diameter based on the time interval between the first and second echoes, calculated as follows:

$$D_{tube} = \frac{C_{BMF}(t_2 - t_1)}{2} \tag{61}$$

Here, D_{tube} represents the diameter of the silicone tube, t_1 and t_2 are the time-of-flights (ToF) between transmitting and receiving of the first and second echoes, respectively, and c_{BMF} is the speed of sound in the BMF. What sets this study apart is our utilization of the residual ultrasound energy for a secondary measurement. After ultrasound waves at both frequencies pass through the silicone tube, with some energy reflected back to the TX, the remainder continues to the RX on the opposite side. Unlike traditional methods that operate at a single fixed frequency, our RX captures the transmitted pulses at both 750 kHz and 1.4 MHz. Temperature variations in the propagating medium induce a change in wavelength, resulting in a relative phase shift between two ultrasound signals. These phase shifts are directly proportional to the changes in wavelength and serve as a metric for determining the temperature of the medium. This relationship is mathematically expressed as:

$$D_{tube} = \left(n_1 + \frac{\theta_1}{2\pi}\right)\lambda_1 = (n_2 + \frac{\theta_2}{2\pi})\lambda_2 \tag{62}$$

$$\Delta C = \Delta\lambda_1 f_1 = \Delta\lambda_2 f_2 \tag{63}$$

Here, n_1 *and* n_2 denote the number of cycles it takes for two ultrasound signals to travel from the transmitter to the receiver, f and λ represent the frequency and wavelength of two signals emitted by

the PMUT TX, and θ is the relative phase shift in radians of the signal received by the PMUT receiver RX. As the temperature fluctuates, the speed of sound changes ΔC, which shifts the relative phase difference between the two signals $|\theta_1 - \theta_2|$. By analyzing these relative phase shifts at both frequencies, we can accurately monitor the temperature of the blood-mimicking fluid (BMF) using the through-transmission method. Importantly, vessel motion also induces phase shifts at both ultrasound frequencies. By systematically comparing these shifts, we effectively neutralize the impact of vessel motion, thus isolating the temperature measurements from the through-transmission data.

6.2.2 Results and Discussion

Figure 66. B and C showcases the results from analyzing the blood vessel's motion using pulse-echo methods. When the pump is inactive, both the blood-mimicking fluid and the vessel model remain static, allowing PMUT 2 to record two closely situated peaks for each upper and lower wall in the time-domain signal. These peaks shown in Figure 66. C, with round-way travel times of 1.62 µs and 1.92 µs respectively, indicate the ultrasound travel times between the inner and outer surfaces of the vessel wall. Utilizing the speed of sound in silicone at 940 m/s, the estimated wall thicknesses are calculated to be 0.76 mm and 0.9 mm, closely approximating the actual thickness of the silicone tube specified at 0.75 mm [128]. Upon activation of the pump, a noticeable expansion of the vessel's inner diameter occurs. When the pump operates at a frequency of 1 Hz, mimicking the blood flow rate in arteries, the increase in BMF pressure causes the thin silicone walls to expand. Consequently, the time of flight between the two interior surfaces of the upper and lower walls increases, resulting in a change in diameter from 5.1 mm to 5.6 mm, as calculated using the BMF's speed of sound at 1550 m/s.

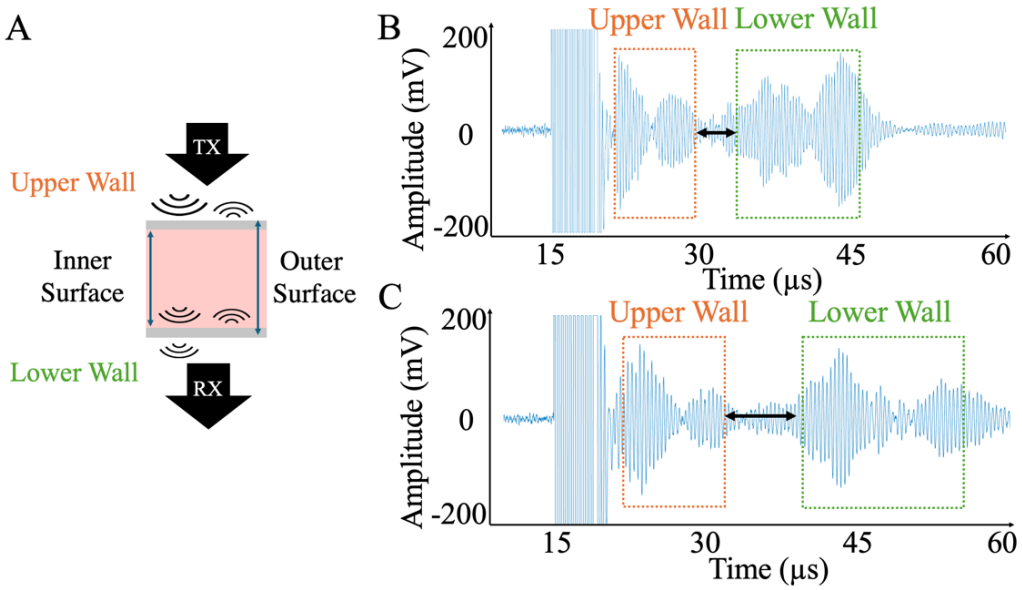

Figure 66. A: The working principle of transmitting and echo measurements of upper and lower walls on the silicone tube. B: Recorded echo response of upper and lower walls when the pump is kept off and BMF static. C: Recorded echo response of upper and lower walls when the pump is turned on and BMF expanded the tube walls.

Concurrently, an external heater incrementally raises the BMF's temperature from 35 °C to 45 °C. Initial temperature measurements are conducted with the BMF and vessel model static (pump deactivated) to validate the measuring concept and assess accuracy using the relative phase method. Figure 66 displays the transmitted US signals at frequencies of 750 kHz and 1.4 MHz, captured by the PMUT receiver (RX) on the opposite side and recorded with an oscilloscope. A distinct peak (marked by the green line) in the 750 kHz signal serves as a reference point for calculating the relative phase shift at 1.4 MHz in relation to this reference. The relative phase difference, as illustrated in Figures 67. A and B, varies with temperature changes, enabling continuous temperature monitoring of the BMF. The Figure 67. C presents a linear correlation between the actual temperature, confirmed by a reference thermometer, and the relative phase difference. The data points are fitted using a piecewise linear method, revealing a sensitivity of 9.7° per degree Celsius within the temperature range of 35°C to 45°C.

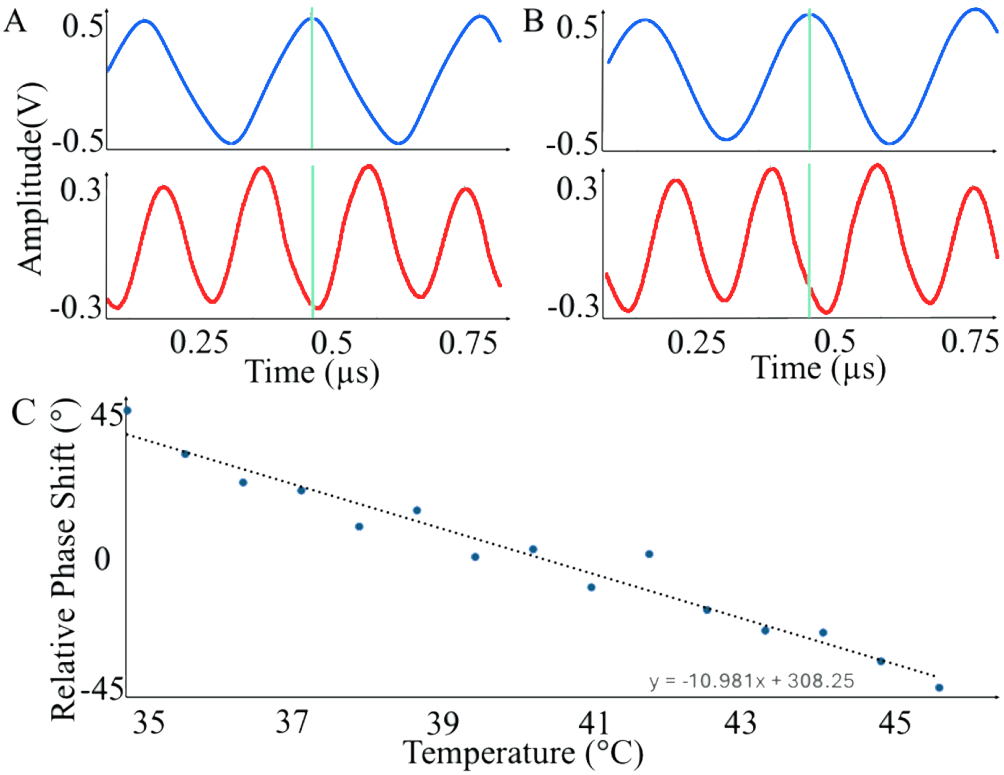

Figure 67. The relative phase shift measured between PMUT 1(blue) and PMUT2 (red), with a peak at signal from PMUT 1 marked in green line as reference mark to track the relative phase shift of two measurements A and B. C: The linear correlation between relative phase shift and temperature of BMF.

During dual-function tests with the fluid being circulated periodically by the pump at 1 Hz, theoretical considerations suggest that the slight expansion of the blood vessel model's diameter introduce additional travel distance and cause a relative phase shift for both US signals. However, empirical observations indicate that the change in relative phase due to vessel expansion is almost negligible for temperature tracking (results indicated by small changes in degrees for 750 kHz and 1.4 MHz signals). This negligible effect is attributed to the minimal expansion amplitude of the vessel's diameter relative to the wavelength of the two US waves. Therefore, the overall impact of diameter expansion on phase drift is minor compared to the changes in relative phase resulting from variations in the medium's temperature. This finding is further validated through the linear correlation observed between the actual temperature and the relative phase shift from simultaneous dual-function measurements. Even when the pump is activated at a 1 Hz frequency, the relationship between temperature and relative phase shift remains stable and linear, underscoring the minimal impact of the vessel's expansion on the measurements. This stability highlights the efficacy of the multi-

frequency PMUTs array in simultaneously tracking both pulse-echo and through-transmission US signals, enabling reliable measurements of two distinct physical properties—vessel movement and fluid temperature changes—in this study.

6.3 Multi-Frequency PMUTs for Photoacoustic Imaging

Ultrasound imaging is recognized as a well-established technology and celebrated for its safety, versatility, and capacity for real-time analysis. In the biomedical domain, photoacoustic imaging (PAI) has emerged as a significant advancement since its first observation in the 1880s [129, 130]. PAI uniquely combines laser excitation and ultrasonic detection to provide detailed images that reveal functional and molecular information, such as tissue oxygenation and hemoglobin concentration. This capability is invaluable for applications like tumor detection, vascular imaging, and studying metabolic processes in tissues.

PAI achieves this by directing a brief laser pulse at a target, which absorbs the energy and momentarily converts it into heat. This rapid thermal and contraction expansion then generates an acoustic wave captured by ultrasound transducers. Unlike conventional ultrasound, PAI offers enhanced contrast by exploiting the optical absorption properties of tissues, making it particularly effective in scenarios where traditional methods fall short. Lin et al. developed a photoacoustic computed tomography, which has successfully imaged angiographic structures up to 4 cm deep, achieving visualization of vasculature with a resolution down to 400 μm in apparent vascular diameter [131]. Similarly, Matsumoto et al. introduced a PAI system equipped with a hemispherical probe array specifically designed for breast cancer examinations, enabling the visualization of tumor-associated angiogenesis and depicting relative oxygen saturation through pseudocolors [132]. Despite its advanced capabilities, the implementation of PAI often relies on bulky ceramic-based ultrasonic transducers. The increasing demand for compact and efficient biomedical devices is driving further innovation in PAI systems and ultrasonic transducers. In response to this, piezoelectric micromachined ultrasonic transducers (PMUTs) emerges as a promising alternative. With their small size and the ability to form high-density arrays, PMUTs are ideally suited to meet the high-resolution requirements of advanced PAI applications.

The image quality in photoacoustic imaging is primarily determined by two factors: lateral resolution and axial resolution. Lateral resolution depends on the intensity of the detected ultrasonic signal, whereas axial resolution is linked to the bandwidth of the acoustic detector, measured by the full width at half maximum (FWHM) of the photoacoustic signal. Current efforts in transducer development are challenged by the need to balance bandwidth and sensitivity, which typically involves trade-offs that can limit the overall performance of the imaging system. Some research has explored using higher modes of PMUTs to extend the total bandwidth of transducer arrays, but the significantly lower receiving sensitivity at higher modes often limits the resolution of imaging results [89, 133].

This chapter explores the use of our multi-frequency based PMUT array designed to capture photoacoustic signals with high fidelity. These arrays feature PMUTs designed with AlN and varying dimensions and operational frequencies, expanding the bandwidth without sacrificing sensitivity and simultaneously maintaining an improved imaging resolution. Despite AlN-based PMUTs exhibiting lower ultrasound transmission sensitivity due to their relatively lower piezoelectric coefficients compared to traditional composite transducers or those using Lead Zirconate Titanate (PZT), their enhanced receiving sensitivity makes them particularly suitable for such application. The lower dielectric constant of AlN reduces the capacitive load, thereby enhancing bandwidth and sensitivity in receiving ultrasound signals. Furthermore, the superior elastic compliance of AlN enables more effective deformation under acoustic pressures, enhancing its responsiveness to ultrasound waves and increasing its efficacy as a receiver. Most importantly, it has been observed that targets of different colors exhibit distinct heat absorption capabilities; when exposed to a laser of constant wavelength and energy, they produce varying acoustic responses in amplitude and frequency. These subtle variations are detectable by our multi-channel PMUT array, which compares the amplitude ratios across three distinctive arrays, enabling two-dimensional color photoacoustic imaging. By deploying PMUTs across a spectrum of frequencies, we have optimized imaging efficiency and quality for diverse scenarios, thereby enhancing the device's utility in various imaging applications beyond the capabilities of traditional ultrasound transducers.

6.3.1 Device Design and Frequency Response

In photoacoustic imaging (PAI) experiments, our process begins with a pulsed laser, specifically a Nd:YAG laser (CNI Optics, DPS-532-B) operating at a wavelength of 532 nm. The laser is configured to generate pulses at a repetition frequency of 10 Hz, each lasting 10 nanoseconds and delivering peak energy of 7.5 mJ. When directed at the target, this pulsed energy is absorbed, leading to thermal expansion and the subsequent generation of broadband acoustic waves through the photoacoustic effect. The ultrasound transducer is a central component in PAI systems; its center frequency, bandwidth, and sensitivity are critical for determining spatial resolution and imaging depth. The photoacoustic signals, inherently unpredictable, vary based on the target's size, geometry, color, and material, influencing the frequency, bandwidth, and intensity of the emitted acoustic signals [134, 135]. Unlike traditional ultrasound imaging where transducers both emit and receive pulses, in PAI the transducer's role is exclusively to receive. This requires the transducer to be highly sensitive to capture a wide range of acoustic signals, enabling the detection of minimal yet critical acoustic responses essential for producing high-quality images. Transducers operating at higher frequencies provide better spatial resolution for smaller targets, though they are challenged by lower signal-to-noise ratios and reduced imaging depth due to greater acoustic attenuation. On the other hand, transducers at lower frequencies offer deeper penetration, making them more effective for imaging larger targets, thus balancing the system's overall capabilities.

These acoustic properties necessitate the strategic use of multi-frequency PMUTs for PAI. Multi-frequency PMUTs are instrumental in balancing the requirements for both high spatial resolution and deep imaging penetration. This balance is achieved by employing transducers capable of operating across a broad spectrum of frequencies, thus enabling the system to adaptively respond to varying target characteristics. To address these requirements, a PMUT array comprising three circular PMUTs with varying radii—150 μm, 224 μm, and 98.5 μm—was designed and fabricated. These PMUTs are engineered to have fundamental resonant frequencies of 1.5 MHz, 2.5 MHz, and 3 MHz in air, respectively. The entire array is then coated with a 2 μm layer of parylene C for under-liquid testing. When fully immersed under engineered fluid Fluorinert FC-70, the resonant frequencies were recorded at 760 kHz, 1.07 MHz, and 1.4 MHz, respectively, demonstrating a shift due to additional loading in liquid environments. The liquid loading also results in bandwidth expansion for the PMUTs.

6.3.2 Experimental Setup

The experimental setup consists of two primary components: the laser scanning control and the PA signal processing modules. The workflow is demonstrated in Figure 68 below. Initially, the laser passes through a focusing lens to narrow its beam diameter to 0.1 mm, after which it is steered by a 2-axis galvanometer (Thorlabs, GCM102/M) across a bio-mimicking phantom embedded with pencil leads to simulate imaging targets. The bio-mimicking phantoms made of PDMS with thick of 1.3 cm have several pencil lead targets with different properties in dimension, geometry, colors etc. to restore different PAI scenarios. The x- and y-axis scanner of galvanometer are controlled by two synchronized function generators (Agilent 3600A)) with micro stepping signals, enabling scanning over an area of 1.5 cm by 1.5 cm with a minimal step size of 0.05 mm.

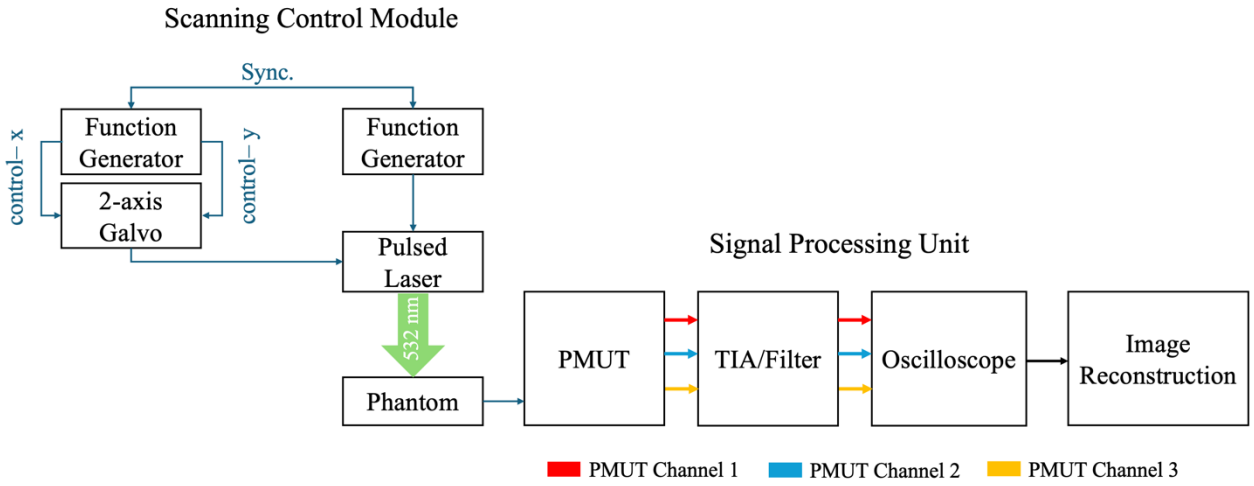

Figure 68. Workflow of photoacoustic imaging measurements with Galvo control module and signal processing unit.

On the receiving end, the photoacoustic signals collected by the PMUTs are first processed by a custom-built PCB, featuring a 2-stage amplifier and a bandpass filter. These signals are then captured by either an oscilloscope or a data acquisition (DAQ) card for image reconstruction. The electric output of three channels of the PMUT array—indicated by red, blue, and yellow—are measured as electric charge across the piezoelectric layer and initially amplified by a transimpedance amplifier (TIA) using ADA 4817 and converted into electrical potential. This is followed by a passive high-pass filter that eliminates low-frequency noise. Subsequently, a variable gain amplifier enhances the voltage level to a readable range, and a Biquad bandpass filter employing AD8054 minimizes further

noise interference. Finally, the preprocessed signals are averaged eight times by the oscilloscope and exported for detailed image reconstruction. A picture of experimental setup is shown in Figure 69.

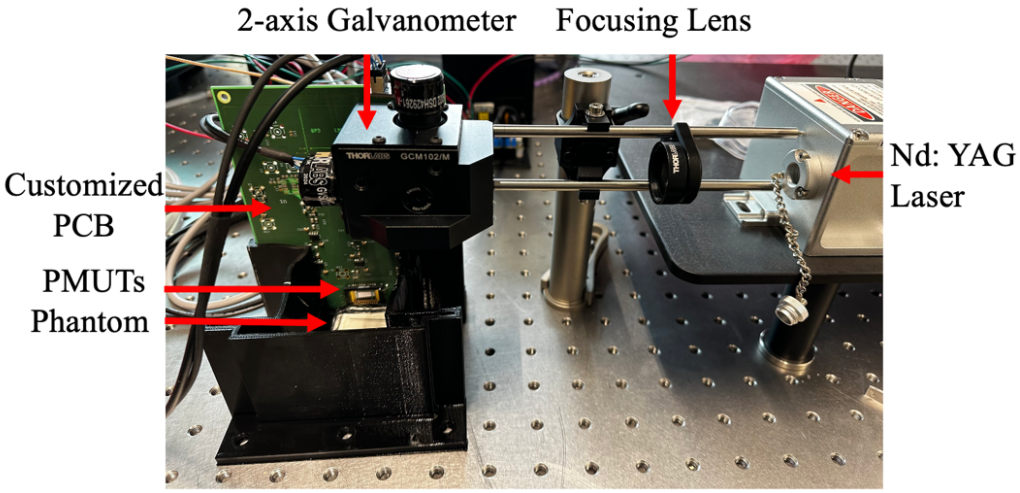

Figure 69. Experiment setup for photoacoustic imaging with multi-frequency PMUTs array.

6.3.3 Photoacoustic Imaging

In photoacoustic imaging (PAI) experiments, the initial photoacoustic response was characterized using a phantom embedded with a 0.5 mm-thick pencil lead as the imaging target. The setup utilized a laser tuned to emit pulses of 6 mJ peak energy with a 10 ns duration at a 10 Hz repetition rate. The photoacoustic signals were captured from three PMUT channels and their responses in both time and frequency domains are illustrated in Figure 70.

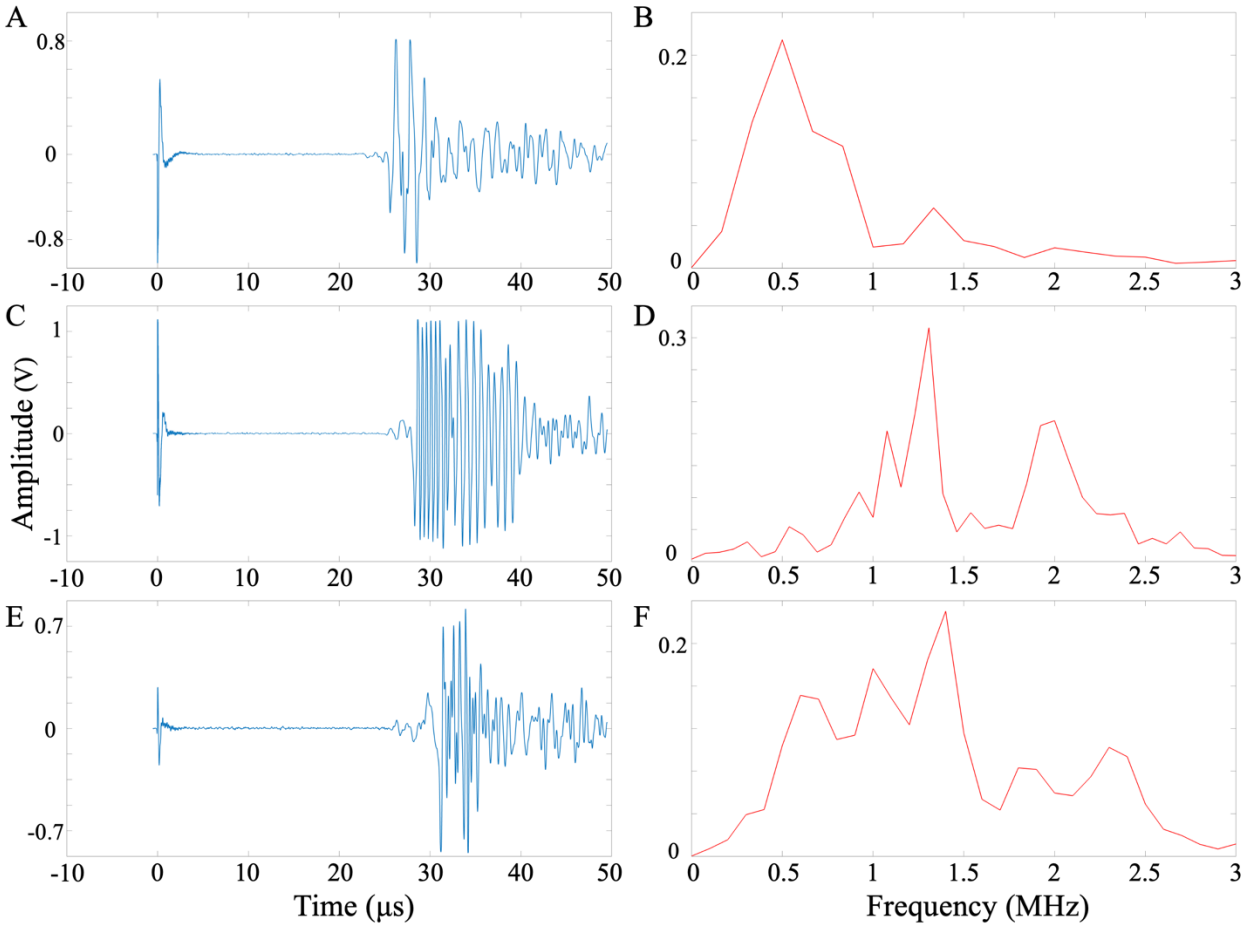

Figure 70. A, C, and E: PA signal recorded from PMUT 1, 2 and 3 in time domain. B, D, and F: Corresponding signal recorded in frequency domain.

The initial peak observed in the time-domain traces is attributable to the electrical coupling from the q-switching signal of the laser, which triggers each pulse. Following the absorption of laser energy, the target undergoes thermal expansion, generating vibrations that propagate through the surrounding medium and are detected by the PMUT array. The resulting photoacoustic signals display significant oscillations at high amplitudes, and the time delay between the laser firing and signal detection correlates with the acoustic signal's time of flight from the target to the PMUT array, moving through the engineered liquid FC-70 at corresponding sound velocity. This PA signal is inherently broadband, as evidenced by the distinct central frequencies of PMUT 1, 2, and 3, ranging from 760 kHz to 1.4 MHz, capturing different portions of the PA signal spectrum as shown in the frequency responses of Figure 70. B, D, and F.

Subsequent experiments commenced with imaging targets consisting of three thin pencil leads of varying diameters: 0.3 mm, 0.5 mm, and 0.7 mm. This configuration was chosen to assess the resolution and contrast differences across various PMUT settings. Initially, the laser was steered to precisely target each pencil lead, and the photoacoustic signals were then captured and analyzed through our multi-channel PMUT array in both time and frequency domains. As depicted in Figure 71. B, the static frequency-domain analysis from PMUT 1 revealed that the largest lead (0.7 mm) produced the highest amplitude around 0.5 MHz. A notable shift in the central frequency of the photoacoustic response was observed as the dimensions of the imaging targets varied, with the smallest lead (0.3 mm) showing a central frequency exceeding 1.5 MHz. This aligns with theoretical predictions that the characteristic PA signal frequency is inversely proportional to the axial dimension of the imaging target.

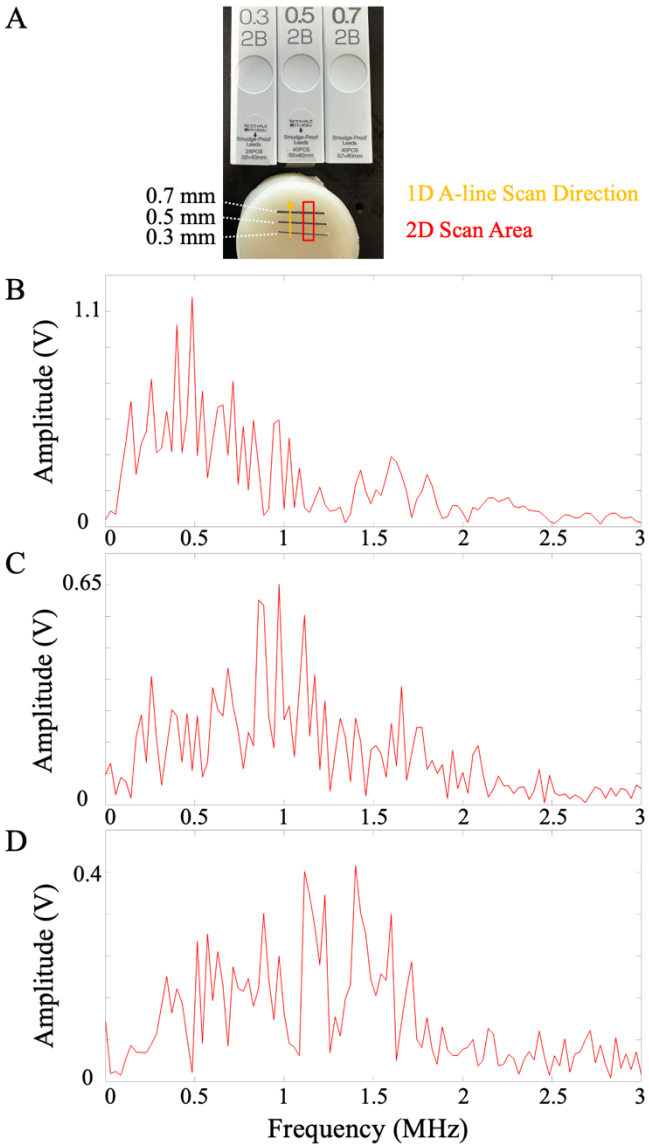

Figure 71. A: Prepared phantom with pencil leads as imaging target at varying dimensions. Yellow arrow indicates the 1D A-line scan direction, and red box marks the 2D scan area. B-D: The frequency response of PA signal from imaging target at diameter of 0.7, 0.5 and 0.3 mm, highlighting the shift in central frequency associated with the reducing dimension of the target. The plotted results are recorded from PMUT 1.

Subsequent 1D A-line scan was conducted across the phantom by moving the laser beam through the three pencil leads, following the path indicated by the yellow arrow in Figure 71. A. Photoacoustic signals from the three distinct PMUT channels were recorded and processed using a delay-and-sum algorithm. The results, illustrated in Figure 72, revealed three peaks corresponding to the photoacoustic responses of the pencil leads, where each peak's bandwidth correlated with the respective lead's diameter. PMUT 1, characterized by the lowest resonant frequency, effectively

captured the profile of the thickest lead (0.7 mm) but demonstrated limited resolution for thinner targets. Conversely, PMUTs 2 and 3, which operate at higher resonant frequencies, achieved sharper responses from the thinnest lead (0.3 mm), though the signal intensity for thicker leads was significantly reduced. The pattern from dynamic scanning measurement once again confirms the theoretical expectations that an imaging target's size influences the frequency response of the emitted photoacoustic signal.

Leveraging the diverse resonant frequencies of the multi-frequency PMUT array, the setup captures a broad range of photoacoustic responses with high fidelity. By integrating signals from all three channels, the PMUTs array yields three distinct peaks corresponding to the three pencil leads and bandwidth of each peak specifies the thickness of each pencil lead, as depicted in Figure 72. D. Following this, a 2D laser scanning was undertaken, navigating the laser across a rectangular grid outlined in red in Figure 71. A. The laser covers the grid in 10 and 200 steps along the x- and y-axes, respectively, with each step indexed for precise image reconstruction. Using the combined signals from all three PMUT channels, the 2D image distinctly displayed all three imaging targets with progressively increasing diameters. This result underscores the enhanced resolution achievable by integrating low- and high-frequency PMUT channels in PAI applications.

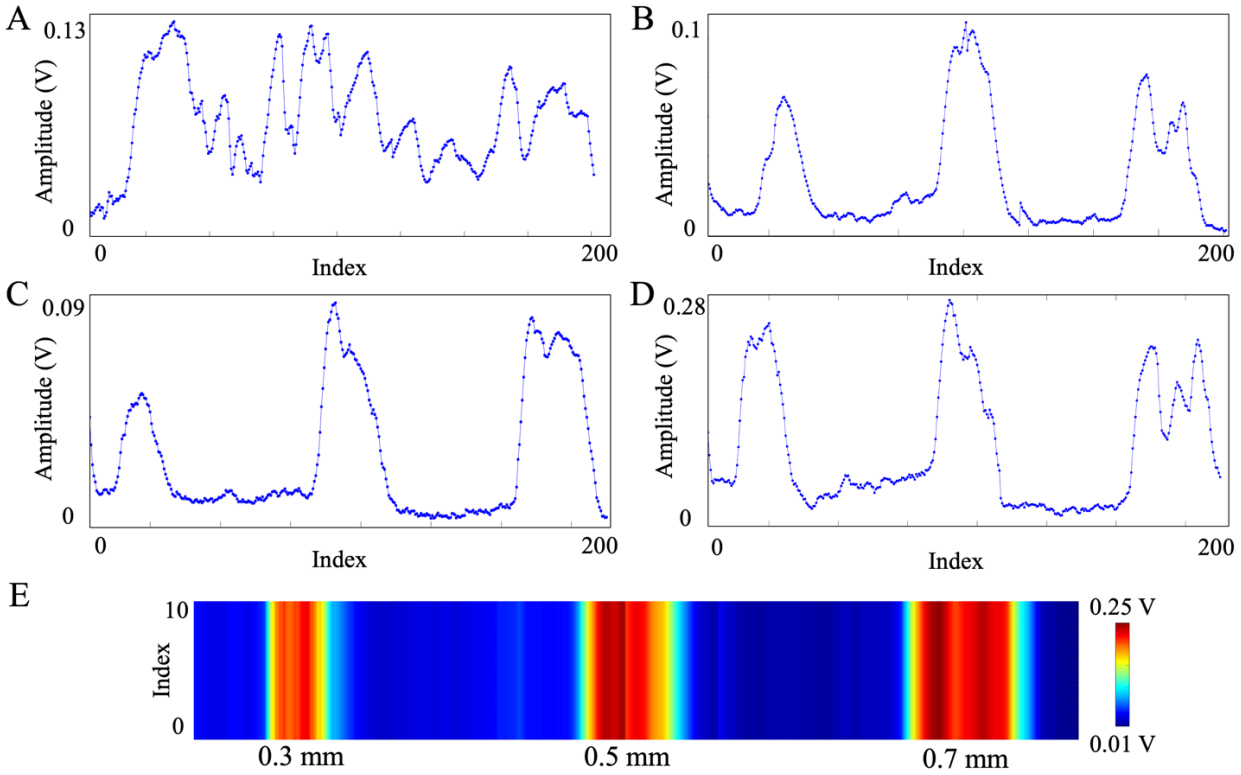

Figure 72. A-C: The 1D A-line scanned PA results using PMUT 1, 2, and 3 respectively. D: The 1D scanned PA results using all PMUTs. E: 2D scanned image processed and reconstructed using all channels from multi-frequency PMUTs array.

6.4 Conclusion

In Chapter 5, we investigated the multi-frequency operation of PMUT by combining multiple resonant modes within a single device to establish a multi-channel frequency link between paired PMUT chips. This method effectively harnesses both low- and high-frequency ultrasound, using a single PMUT to transmit and sense multiple modes simultaneously. However, a notable challenge with this approach is the reduced transmitting and receiving sensitivity caused by intermodal interference, which may limit its applicability in scenarios requiring high-sensitivity ultrasound transduction. To address this limitation, this chapter introduces an alternative strategy: designing a high-density PMUT array that features transducers with varied designs and operational frequencies to achieve multi-frequency operation while maintaining sensitivity. This concept was demonstrated by designing and fabricating an array composed of transducers operating at 750 kHz, 1.2 MHz, and 1.7 MHz, all immersed in a liquid environment.

This design effectively addressed the challenge of simultaneously tracking transmitted and reflected ultrasound signals, enabling a single ultrasound transducer within the PMUT array to perform both through-transmission and pulse-echo measurements. An experimental setup was then devised to measure both the motion of a blood vessel model and the temperature of a circulating blood-mimicking fluid. Testing results revealed a sensitivity of 9.7° per degree Celsius within a temperature range of 35°C to 45°C and successfully captured the expansion and contraction of the blood vessel model. Building on this, the multi-frequency PMUT array was further evaluated in a photoacoustic imaging experiment. The results confirmed a correlation between the dimensions and geometry of the imaging target and the frequency distribution of the emitted ultrasound signal. This enabled the multi-frequency PMUT array to capture photoacoustic signals from an imaging phantom containing targets of varying dimensions. Through image reconstruction algorithms, the array demonstrated improved imaging resolution on objects of different sizes compared to a fixed-frequency PMUT array. This chapter underscores the multi-frequency capabilities of PMUT arrays fabricated using advanced micromachining techniques while preserving the optimal sensitivity of the transducers.

Chapter 7

Conclusion

In this dissertation, various energy conversion approaches utilizing MEMS technology have been explored, ranging from self-sustaining internal vibrations to external ultrasound energy sources. The results demonstrated enhanced efficiency and performance attributable to the optimized micromachined transducer design.

For energy harvesting from internal vibrations, traditional harvester prototypes such as clamped-clamped beam and cantilever systems were evaluated found to have certain limitations. Particularly, these prototypes are limited by their narrow operational bandwidth, which proves insufficient for applications requiring a broad and diverse frequency spectrum, such as those found in biomedical environment. The concept of a phononic frequency comb was therefore investigated to address this limitation in the context of vibration energy harvesting. The proposed design involved engineered mode coupling with excitation of multiple resonant modes under a single excitation drive. A particular example of a microfabricated frequency comb energy harvester optimized for both fundamental and higher mode frequencies with high mode density is demonstrated. Experimental validation confirmed the efficacy of the frequency comb phenomena via a single frequency excitation signal and nonlinear mode coupling. When driven by a noisy and broadband vibration source, mimicking more practical settings, the frequency comb harvester exhibited a notable increase in power output compared to conventional harvesters, which lose efficiency due to limitations in operational bandwidth.

The thesis also explores ultrasound energy transmission using micromachined transducers. A common challenge with conventional ultrasonic transducers is the trade-off between operating frequency and acoustic energy loss due to attenuation. Lower frequencies typically enhance deep tissue penetration and signal fidelity, while higher frequencies are essential for high-resolution imaging and rapid data telemetry. However, traditional ultrasound transducers are typically bound to operate at a fixed frequency, prioritizing either low or high-frequency applications based on specific

requirements. Leveraging the flexibility enabled by microfabrication technologies, we explored an approach by designing a piezoelectric micromachined ultrasonic transducer (PMUT) array capable of operating beyond the fundamental mode to facilitate both low- and high-frequency functions from a single device. By customizing electrode patterning based on mode shape and strain distribution for specific modes, a multi-channel ultrasound link was successfully established between paired PMUT chips across a bio-mimicking phantom. This setup allowed for simultaneous power transfer at low frequencies and fast data telemetry at high frequencies, enhancing the system's overall efficacy without compromising power or data transfer capabilities. Based on insights gained from the initial squared and circular multi-channel PMUT prototypes, our research delved deeper into fundamental electromechanical and acoustic principles. The equivalent circuit model was employed to analyze the mechanical and acoustic behaviors of each PMUT prototype at fundamental and higher harmonic modes. Additionally, this model facilitated the integration of a multi-operation scheme to evaluate the impact of mode combination and electrode patterning on balancing the signal quality of individual modes while reducing inter-modal interference. We experimented with various mode combinations and developed an optimized multi-channel PMUT that integrates distinctive axisymmetric and asymmetric modes to minimize intermodal interference. Such optimization not only improves power transfer efficiency and data transmission rates but also facilitates the establishment of more than two channels between PMUT arrays, paving the way for more sophisticated and versatile applications. In parallel, we explored another solution of designing a high-density, multi-frequency PMUT array with varied dimensions and operating frequencies to assess the benefits of combining multiple operational frequencies within a single device. A key advantage of this design is its ability to simultaneously implement two major ultrasound measurement principles—pulse-echo and through-transmission—within a single device. For instance, our experimental setup included a simulated blood vessel model, allowing the multi-frequency array to concurrently monitor blood temperature and vessel contractions using two differently dimensioned PMUTs within the same array. The multi-frequency PMUT array is explored in the context of photoacoustic imaging experiments with the benefit of operating over an enhanced frequency range. The inherently broadband photoacoustic signals, when analyzed using the arrays' diverse operating frequencies, provided insights into how the dimensions of imaging targets affect the frequencies of emitted photoacoustic signals. By integrating three differently designed PMUTs on a single multi-frequency array, we captured a wider range of photoacoustic signals, substantially broadening the overall bandwidth and enhancing imaging resolution.

7.1 Future Works

7.1.1 Frequency Comb Energy Harvester

While preliminary characterization has yielded promising results in applying a comb mechanism within a piezoelectric energy harvester, some challenges remain. One of challenge is reducing the operating frequency to below 100 Hz, a range critical for capturing energy from internal organ and muscle movements. The effective implementation of a frequency comb mechanism relies on auto-parametric resonance, necessitating the harvester to possess multiple resonant modes with modal frequencies in integer or near-integer ratios. During the microfabrication process, several factors such as over-etching and electrode deposition can affect the structural integrity and frequency response of the final device. Even minor structural alterations can significantly shift the resonant frequency, particularly towards higher-harmonic modes. Therefore, future designs must account for these fabrication and environmental factors, exploring various structural combinations to develop a low-frequency energy harvester based on the frequency comb mechanism. Additionally, insights from studying the relationship between drive amplitude threshold and frequency detuning provide essential guidance for designing next-generation frequency comb harvesters. A notable observation is the influence of system damping on the drive amplitude threshold necessary to excite the frequency comb. Future devices could benefit from vacuum packaging, which reduces mechanical damping, allowing for lower drive thresholds and broader bandwidths. This enhancement is expected to further improve the energy conversion efficiency of the harvesters.

On the other hand, the simple impedance matching technique was used in evaluating the power output from the proposed energy harvester. Given the electromechanical coupling between the mechanical and electrical domains, backward coupling from the electrical domain can modulate the performance of a vibrational energy harvester. Several attempts have been made to develop customized electrical interfaces to tune the resonant frequency and power output of piezoelectric energy harvesters [12, 136-138]. Thus, there is considerable room for improvement in the current frequency comb energy harvester concept through customized power management in the electrical domain. To address this challenge, we have initiated an ongoing collaboration with Delft University of Technology to integrate the SSHC power management interface with piezoelectric MEMS energy conversion device.

7.1.2 Multi-Channel PMUT

Building on insights from first-generation circular and square multi-channel PMUT prototype, this work has evaluated an electrode-optimized multi-channel PMUT, highlighting the critical importance of mode combination and electrode patterns on overall multi-channel operation. While existing designs have focused on combining two modes or operating two channels simultaneously, there is significant potential for advancing this technology by incorporating multiple modes simultaneously and devising diverse electrode configurations to isolate signal responses from each channel, thereby enhancing signal quality.

Future work could explore the integration of programmable multi-gate Doppler measurement capabilities, which would broaden the utility of multi-channel PMUTs in dynamic clinical applications. In this context, a gate refers to a specific, adjustable depth or region along the ultrasound beam path where measurements are taken. A multi-gate system can simultaneously capture data from multiple depths, allowing for comprehensive flow or motion measurements without needing to move the probe. For instance, a programmable multi-gate Doppler platform designed for real-time, high-frequency Doppler applications enhances the assessment of blood flow dynamics and other motion-sensitive metrics [139]. By adapting similar Doppler measurement techniques, future PMUT-based sensors could address broader diagnostic applications in vascular imaging or tissue monitoring.

Additionally, research on multi-frequency PMUT arrays has shown that optimized designs can achieve high spatial resolution and depth penetration, which are critical for applications requiring precise signal measurements, such as Doppler flow monitoring [140]. These advancements underscore the importance of electrode configurations and impedance matching to improve signal integrity and sensor sensitivity in multi-channel PMUT applications. For example, PMN-PT-based ultrasound sensors exhibit enhanced acoustic sensitivity in multi-channel configurations when coupled with tailored impedance circuits, suggesting potential improvements in signal-to-noise ratios and operational stability[141].

From an application perspective, future research could focus on developing a comprehensive testing environment that supports a range of clinical and non-clinical applications for integrated multi-channel PMUT systems. This would involve real-time Doppler applications and novel measurement techniques that utilize frequency-shifting modes to expand the functional capabilities of PMUTs

beyond traditional ultrasound imaging. Such advancements would not only increase the accuracy of flow and motion measurements but also open pathways for more sophisticated uses, such as continuous, real-time monitoring in wearable medical devices or implantable systems. Expanding on the foundations laid by dual-mode PMUTs, these multi-channel designs hold promise for diverse applications across biomedical imaging and diagnostics, with the potential to revolutionize ultrasound-based monitoring and broaden the scope of PMUT technology in clinical diagnostics.

7.1.3 Multi-Frequency PMUT Array

In this study, the multi-frequency PMUT array was evaluated for its application in photoacoustic imaging. With its broad frequency spectrum and comparable sensitivity across the spectrum, the array has demonstrated the capability to produce high-resolution images of targets with varying dimensions. This initial design incorporated three transducer designs, with a peak frequency below 3 MHz in air, which is at the lower end of the spectrum typically used in biomedical ultrasound applications. This highlights significant potential for future developments to design a high-density array that spans a wider frequency range. Additionally, it was observed that the geometric configuration of the transducers, including their positioning and density within the array, plays an important role in overall device performance. An in-depth theoretical analysis of transducer density and inter-element pitch could help understand optimal configurations for maximizing receiving sensitivity in photoacoustic applications. From an application perspective, there is growing interest in developing compact and wearable ultrasound systems for continuous, long-term monitoring of patients' biomarkers [124, 142, 143]. While recent research has shown promise by integrating PMUT arrays onto wearable and flexible substrates for ultrasound testing, few studies have extended this technology to include photoacoustic characterization. Considering the advantages of low power consumption and miniaturization, future research could beneficially explore multi-channel PMUT arrays. This would involve integrating traditional ultrasound imaging with photoacoustic imaging to create a dual-mode imaging system, which would combine the strengths of both techniques to provide more comprehensive diagnostic results. A schematic of the proposed future design, which adopts a dual-mode ultrasound and photoacoustic system using a multi-channel PMUT array, is illustrated in Figure 73 below.

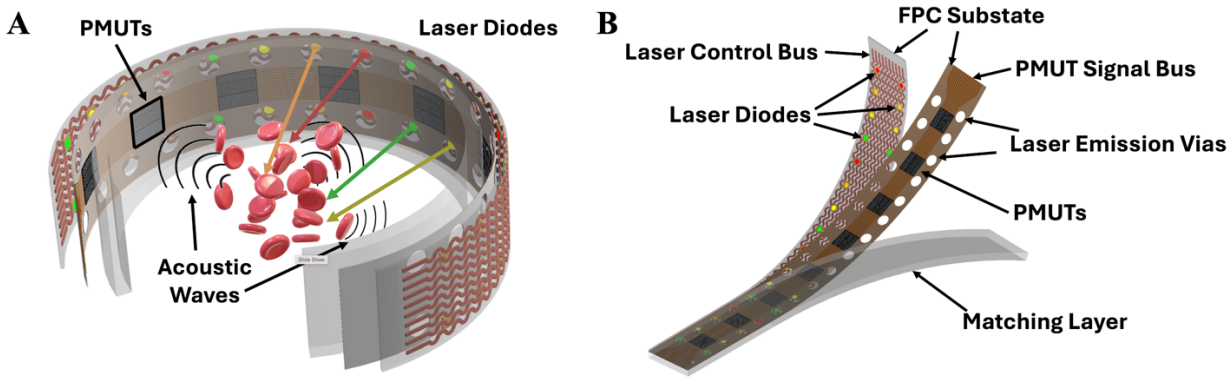

Figure 73. A: Schematic of the proposed dual-mode ultrasound and photoacoustic system featuring a multi-channel PMUT array and laser diode array. B: Layered structure stacked on a flexible substrate, designed for wearable applications to enable continuous monitoring of a patient's biomarkers.

Despite the minimal size and low power needs of PMUT arrays, their integration into photoacoustic systems is currently limited by the use of bulky, high-energy lasers. Initiatives to replace these lasers with pulsed laser diodes or laser emitting diode arrays are encouraging, as they could substantially decrease the system's size and increase its portability [144-146]. Future research worth exploring the integration of miniaturized PMUT arrays with laser diode arrays to develop a compact, wearable system. This innovation has the potential to transform the application of PMUT arrays in clinical settings, enabling the continuous monitoring of localized organs or tissues.

Appendix A

Contribution of the Author

Articles in International Peer Reviewed Journals

T. Zhang, A. Seshia. "A MEMS Frequency Comb Energy Harvester", Journal of Microelectromechanical Systems. 10.1109/JMEMS.2023.3316436

T. Zhang, A. Seshia. "Multi-Channel PMUT in WPT and Data Telemetry," IEEE Sensors Journal, Under review.

T. Zhang, A. Seshia. "Neural Network-Enhanced Color Photoacoustic Imaging using Multi-Channel PMUTs," IEEE Sensors Journal, In preparation.

Proceedings in International Conferences

T. Zhang, A. Seshia. "Acoustic Coupling and Remote Excitation in an Array of Multi-Mode Piezoelectric Micromachined Ultrasonic Transducers", 2023 Joint Conference of the European Frequency and Time Forum and IEEE International Frequency Control Symposium (EFTF/IFCS).

T. Zhang, A. Seshia. "Multi-Mode Piezoelectric Micromachined Transducers for Multi-Channel Acoustic Power Transfer and Data Telemetry." 2023 22nd International Conference on Solid-State Sensors, Actuators and Microsystems (Transducers).

T. Zhang, H. Raheem, A. Seshia. "Multi-Channel Piezoelectric Micromachined Transducers Using On-chip Passive Filtering." 2023 IEEE Symposium (IUS) Ultrasonics.

T. Zhang, A. Seshia. “Electrode Optimization for Multi-Channel Piezoelectric Micromachined Ultrasonic Transducers”, 2024 European Frequency and Time Forum (EFTF).

T. Zhang, Z. Hou, and A. Seshia. “Concurrent Pulse-Echo and Through-Transmission Ultrasound Tracking with Multi-Frequency PMUTs,” 2024 IEEE Ultrasonics, Ferroelectrics, and Frequency Control Joint Symposium (UFFC-JS).

References

1. Bhunia, S., S. Majerus, and M. Sawan, *Implantable biomedical microsystems: design principles and applications*. 2015: Elsevier.
2. Boisseau, S., G. Despesse, and B.A. Seddik, *Electrostatic conversion for vibration energy harvesting.* Small-Scale Energy Harvesting, 2012. **5**.
3. Ali, F., et al., *Piezoelectric energy harvesters for biomedical applications.* Nano Energy, 2019. **57**: p. 879-902.
4. Liu, H., et al., *A comprehensive review on piezoelectric energy harvesting technology: Materials, mechanisms, and applications.* Applied Physics Reviews, 2018. **5**(4): p. 041306.
5. Dagdeviren, C., et al., *Conformal piezoelectric energy harvesting and storage from motions of the heart, lung, and diaphragm.* Proceedings of the National Academy of Sciences, 2014. **111**(5): p. 1927-1932.
6. Li, N., et al., *Direct powering a real cardiac pacemaker by natural energy of a heartbeat.* Acs Nano, 2019. **13**(3): p. 2822-2830.
7. Dong, L., et al., *Flexible porous piezoelectric cantilever on a pacemaker lead for compact energy harvesting.* Advanced Materials Technologies, 2019. **4**(1): p. 1800148.
8. Deterre, M., et al., *Micro blood pressure energy harvester for intracardiac pacemaker.* Journal of Microelectromechanical Systems, 2013. **23**(3): p. 651-660.
9. Almouahed, S., C. Hamitouche, and E. Stindel. *Self-powered device for tibiofemoral force measurement in knee implant*. in *2016 2nd International Conference on Advanced Technologies for Signal and Image Processing (ATSIP)*. 2016. IEEE.
10. Safaei, M., R.I. Ponder, and S.R. Anton. *Detection of compartmental forces and location of contact areas with piezoelectric transducers in total knee arthroplasty*. in *Active and Passive Smart Structures and Integrated Systems XII*. 2018. International Society for Optics and Photonics.
11. Zhang, H., et al., *A flexible and implantable piezoelectric generator harvesting energy from the pulsation of ascending aorta: in vitro and in vivo studies.* Nano Energy, 2015. **12**: p. 296-304.

12. Guyomar, D., et al., *Toward energy harvesting using active materials and conversion improvement by nonlinear processing.* IEEE transactions on ultrasonics, ferroelectrics, and frequency control, 2005. **52**(4): p. 584-595.
13. Ansari, M. and M.A. Karami, *A sub-cc nonlinear piezoelectric energy harvester for powering leadless pacemakers.* Journal of intelligent material systems and structures, 2018. **29**(3): p. 438-445.
14. Jackson, N., et al. *Ultra-low frequency PiezoMEMS energy harvester for a leadless pacemaker*. in *2018 IEEE Micro Electro Mechanical Systems (MEMS)*. 2018. IEEE.
15. Ansari, M. and M.A. Karami, *Experimental investigation of fan-folded piezoelectric energy harvesters for powering pacemakers.* Smart Materials and Structures, 2017. **26**(6): p. 065001.
16. Hajati, A. and S.-G. Kim, *Ultra-wide bandwidth piezoelectric energy harvesting.* Applied Physics Letters, 2011. **99**(8): p. 083105.
17. Kaajakari, V., et al., *Nonlinear limits for single-crystal silicon microresonators.* Journal of Microelectromechanical systems, 2004. **13**(5): p. 715-724.
18. Xu, R., H. Akay, and S.-G. Kim, *Buckled MEMS beams for energy harvesting from low frequency vibrations.* Research, 2019. **2019**.
19. Daqaq, M.F., et al., *On the role of nonlinearities in vibratory energy harvesting: a critical review and discussion.* Applied Mechanics Reviews, 2014. **66**(4).
20. Kumar, P., M.M. Inamdar, and D.N. Pawaskar, *Characterisation of the internal resonances of a clamped-clamped beam MEMS resonator.* Microsystem Technologies, 2020: p. 1-17.
21. Jia, Y., et al. *Autoparametric resonance in a piezoelectric MEMS vibration energy harvester*. in *2018 IEEE Micro Electro Mechanical Systems (MEMS)*. 2018. IEEE.
22. Jia, Y., S. Du, and A.A. Seshia, *Twenty-eight orders of parametric resonance in a microelectromechanical device for multi-band vibration energy harvesting.* Scientific reports, 2016. **6**(1): p. 1-8.
23. Haeberlin, A., et al., *The first batteryless, solar-powered cardiac pacemaker.* Heart rhythm, 2015. **12**(6): p. 1317-1323.
24. Haeberlin, A., et al., *Successful pacing using a batteryless sunlight-powered pacemaker.* Europace, 2014. **16**(10): p. 1534-1539.
25. Nelson, B.D., et al., *Wireless technologies for implantable devices.* Sensors, 2020. **20**(16): p. 4604.
26. Denisov, A. and E. Yeatman. *Ultrasonic vs. inductive power delivery for miniature biomedical implants*. in *2010 International Conference on Body Sensor Networks*. 2010. IEEE.

27. Auricchio, A., et al., *First-in-man implantation of leadless ultrasound-based cardiac stimulation pacing system: novel endocardial left ventricular resynchronization therapy in heart failure patients.* Europace, 2013. **15**(8): p. 1191-1197.
28. Barbruni, G.L., et al., *Miniaturised Wireless Power Transfer Systems for Neurostimulation: A Review.* IEEE Transactions on Biomedical Circuits and Systems, 2020.
29. Seo, D., et al., *Model validation of untethered, ultrasonic neural dust motes for cortical recording.* Journal of neuroscience methods, 2015. **244**: p. 114-122.
30. Jiang, X., et al., *Ultrasonic fingerprint sensor with transmit beamforming based on a PMUT array bonded to CMOS circuitry.* IEEE transactions on ultrasonics, ferroelectrics, and frequency control, 2017. **64**(9): p. 1401-1408.
31. Smyth, K. and S.-G. Kim, *Experiment and simulation validated analytical equivalent circuit model for piezoelectric micromachined ultrasonic transducers.* IEEE transactions on ultrasonics, ferroelectrics, and frequency control, 2015. **62**(4): p. 744-765.
32. Wang, Q., et al., *Design, fabrication, and characterization of scandium aluminum nitride-based piezoelectric micromachined ultrasonic transducers.* Journal of microelectromechanical systems, 2017. **26**(5): p. 1132-1139.
33. Lu, Y., A. Heidari, and D.A. Horsley, *A high fill-factor annular array of high frequency piezoelectric micromachined ultrasonic transducers.* Journal of Microelectromechanical Systems, 2014. **24**(4): p. 904-913.
34. Lu, Y., et al. *Broadband piezoelectric micromachined ultrasonic transducers based on dual resonance modes*. in *2015 28th IEEE International Conference on Micro Electro Mechanical Systems (MEMS)*. 2015. IEEE.
35. Shi, Q., T. Wang, and C. Lee, *MEMS based broadband piezoelectric ultrasonic energy harvester (PUEH) for enabling self-powered implantable biomedical devices.* Scientific reports, 2016. **6**(1): p. 1-10.
36. Du, S., et al., *A fully integrated split-electrode SSHC rectifier for piezoelectric energy harvesting.* IEEE Journal of Solid-State Circuits, 2019. **54**(6): p. 1733-1743.
37. Kim, S.G., S. Priya, and I. Kanno, *Piezoelectric MEMS for energy harvesting.* MRS bulletin, 2012. **37**(11): p. 1039-1050.
38. Priya, S., et al., *A review on piezoelectric energy harvesting: materials, methods, and circuits.* Energy Harvesting and Systems, 2019. **4**(1): p. 3-39.

39. Kim, S.-B., et al., *Comparison of MEMS PZT cantilevers based on $ d_ {31} $ and $ d_ {33} $ modes for vibration energy harvesting.* Journal of microelectromechanical systems, 2012. **22**(1): p. 26-33.
40. Du, S., et al., *A nail-size piezoelectric energy harvesting system integrating a MEMS transducer and a CMOS SSHI circuit.* IEEE Sensors Journal, 2019. **20**(1): p. 277-285.
41. Du Toit, N.E., *Modeling and design of a MEMS piezoelectric vibration energy harvester*. 2005, Massachusetts Institute of Technology.
42. Liu, W., et al., *A simplified lumped model for the optimization of post-buckled beam architecture wideband generator.* Journal of Sound and Vibration, 2017. **409**: p. 165-179.
43. Kim, M., *Materials and device design for MEMS piezoelectric mechanical vibration energy harvesters*. 2012, Massachusetts Institute of Technology.
44. Hagood, N.W., W.H. Chung, and A. Von Flotow, *Modelling of piezoelectric actuator dynamics for active structural control.* Journal of intelligent material systems and structures, 1990. **1**(3): p. 327-354.
45. Thomson, W., *Theory of vibration with applications*. 2018: CrC Press.
46. Dutoit, N.E., B.L. Wardle, and S.-G. Kim, *Design considerations for MEMS-scale piezoelectric mechanical vibration energy harvesters.* Integrated ferroelectrics, 2005. **71**(1): p. 121-160.
47. Garrett, S.L., *Understanding Acoustics: An Experimentalist's View of Sound and Vibration*. 2020: Springer Nature.
48. Pop, F., et al., *Enabling real-time monitoring of intrabody networks through the acoustic discovery architecture.* IEEE Transactions on Ultrasonics, Ferroelectrics, and Frequency Control, 2020. **67**(11): p. 2336-2344.
49. Butikov, E.I., *Parametric resonance in a linear oscillator at square-wave modulation.* European journal of physics, 2004. **26**(1): p. 157.
50. Krylov, N.M. and N.N. Bogoliubov, *Introduction to Non-Linear Mechanics.(AM-11), Volume 11*. 2016: Princeton University Press.
51. Lee, Y., *A study of parametric excitation applied to a MEMS tuning fork gyroscope*. 2007: University of Missouri-Columbia.
52. Nayfeh, A.H., D.T. Mook, and P. Holmes, *Nonlinear oscillations.* 1980.
53. Kippenberg, T.J., R. Holzwarth, and S.A. Diddams, *Microresonator-based optical frequency combs.* science, 2011. **332**(6029): p. 555-559.
54. Ganesan, A., C. Do, and A. Seshia, *Phononic frequency comb via intrinsic three-wave mixing.* Physical review letters, 2017. **118**(3): p. 033903.

55. Sun, J., et al., *Generation and evolution of phononic frequency combs via coherent energy transfer between mechanical modes.* Physical Review Applied, 2023. **19**(1): p. 014031.
56. Bu, L., E. Arroyo, and A.A. Seshia. *Frequency combs: a new mechanism for mems vibration energy harvesters*. in *2021 21st International Conference on Solid-State Sensors, Actuators and Microsystems (Transducers)*. 2021. IEEE.
57. Ganesan, A. and A. Seshia, *Resonance tracking in a micromechanical device using phononic frequency combs.* Scientific reports, 2019. **9**(1): p. 9452.
58. Ganesan, A. and A.A. Seshia, *Tracking the resonant frequency of a micromechanical resonator using phononic frequency combs.* arXiv preprint arXiv:1710.07058, 2017.
59. Bu, L., E. Arroyo, and A.A. Seshia, *Frequency combs: a new mechanism for mems vibration energy harvesters.*
60. Qi, Z., et al., *Existence conditions for phononic frequency combs.* Applied Physics Letters, 2020. **117**(18).
61. Ganesan, A., *Phononic frequency combs*. 2018, University of Cambridge.
62. Qi, Z., et al., *Existence conditions for phononic frequency combs.* Applied Physics Letters, 2020. **117**(18): p. 183503.
63. Cao, L., et al., *Phononic frequency combs through nonlinear resonances.* Physical review letters, 2014. **112**(7): p. 075505.
64. Park, M. and A. Ansari, *Formation, evolution, and tuning of frequency combs in microelectromechanical resonators.* Journal of Microelectromechanical Systems, 2019. **28**(3): p. 429-431.
65. Nayfeh, A.H. and D.T. Mook, *Nonlinear oscillations*. 2008: John Wiley & Sons.
66. Nayfeh, A.H. and P.F. Pai, *Linear and nonlinear structural mechanics*. 2008: John Wiley & Sons.
67. Bartilson, D.T., J. Jang, and A.W. Smyth, *Symmetry properties of natural frequency and mode shape sensitivities in symmetric structures.* Mechanical Systems and Signal Processing, 2020. **143**: p. 106797.
68. Joseph, J., B. Ma, and B. Khuri-Yakub, *Applications of capacitive micromachined ultrasonic transducers: A comprehensive review.* IEEE Transactions on Ultrasonics, Ferroelectrics, and Frequency Control, 2021. **69**(2): p. 456-467.
69. Mills, D.M. *Medical imaging with capacitive micromachined ultrasound transducer (cMUT) arrays*. in *IEEE Ultrasonics Symposium, 2004*. 2004. IEEE.
70. Haider, S.T., et al., *A review of the recent applications of aluminum nitride-based piezoelectric devices.* Ieee Access, 2023.

71. Jin, X. and B. Khuri-Yakub, *Surface micromachined capacitive ultrasonic transducers.* IEEE transactions on ultrasonics, ferroelectrics, and frequency control, 1998. **45**(3): p. 678-690.
72. Chen, K., et al., *Ultrasonic imaging transceiver design for CMUT: A three-level 30-Vpp pulse-shaping pulser with improved efficiency and a noise-optimized receiver.* IEEE Journal of Solid-State Circuits, 2013. **48**(11): p. 2734-2745.
73. Oralkan, O., et al., *Capacitive micromachined ultrasonic transducers: Next-generation arrays for acoustic imaging?* IEEE transactions on ultrasonics, ferroelectrics, and frequency control, 2002. **49**(11): p. 1596-1610.
74. Caronti, A., et al., *Capacitive micromachined ultrasonic transducer (CMUT) arrays for medical imaging.* Microelectronics Journal, 2006. **37**(8): p. 770-777.
75. Lim, J., et al., *Towards a reduced-wire interface for CMUT-based intravascular ultrasound imaging systems.* IEEE transactions on biomedical circuits and systems, 2016. **11**(2): p. 400-410.
76. Zahorian, J., et al., *Monolithic CMUT-on-CMOS integration for intravascular ultrasound applications.* IEEE transactions on ultrasonics, ferroelectrics, and frequency control, 2011. **58**(12): p. 2659-2667.
77. Wang, J., et al., *Capacitive micromachined ultrasound transducers for intravascular ultrasound imaging.* Microsystems & Nanoengineering, 2020. **6**(1): p. 73.
78. Yeh, D.T., et al., *3-D ultrasound imaging using a forward-looking CMUT ring array for intravascular/intracardiac applications.* IEEE transactions on ultrasonics, ferroelectrics, and frequency control, 2006. **53**(6): p. 1202-1211.
79. Wygant, I.O., et al., *Integration of 2D CMUT arrays with front-end electronics for volumetric ultrasound imaging.* IEEE transactions on ultrasonics, ferroelectrics, and frequency control, 2008. **55**(2): p. 327-342.
80. Thacker, M.B., A. Emadi, and D.A. Buchanan, *Design, development, and characterization of a low frequency CMUT-based anemometer.* IEEE Access, 2021. **9**: p. 127735-127741.
81. Sun, S., et al., *Eye-tracking monitoring based on PMUT arrays.* Journal of Microelectromechanical Systems, 2021. **31**(1): p. 45-53.
82. Halbach, A., et al. *Display compatible PMUT array for mid-air haptic feedback*. in *2019 20th International Conference on Solid-State Sensors, Actuators and Microsystems & Eurosensors XXXIII (TRANSDUCERS & EUROSENSORS XXXIII)*. 2019. IEEE.
83. Pala, S., et al. *Ultrasond-induced haptic sensations via PMUTS*. in *2021 IEEE 34th International Conference on Micro Electro Mechanical Systems (MEMS)*. 2021. IEEE.

84. Ding, H., et al., *A pulsed wave Doppler ultrasound blood flowmeter by PMUTs.* Journal of Microelectromechanical Systems, 2021. **30**(5): p. 680-682.
85. Li, J., et al. *Three-dimensional vascular reconstruction and Doppler flow measurement using PMUTs*. in *2022 IEEE International Ultrasonics Symposium (IUS)*. 2022. IEEE.
86. Tillak, J. and J. Yoo. *A 23μW digitally controlled pMUT interface circuit for Doppler ultrasound Imaging*. in *2015 IEEE International Symposium on Circuits and Systems (ISCAS)*. 2015. IEEE.
87. Sun, C., et al., *Investigation of broadband characteristics of multi-frequency piezoelectric micromachined ultrasonic transducer (MF-pMUT).* IEEE sensors journal, 2018. **19**(3): p. 860-867.
88. Billen, M., et al. *Multi-frequency imaging with a CMOS compatible scandium doped aluminum nitride pMUT array*. in *2021 IEEE 34th International Conference on Micro Electro Mechanical Systems (MEMS)*. 2021. IEEE.
89. Wang, Y., et al. *Photoacoustic dual-mode microsensor based on PMUT technology*. in *2022 IEEE International Symposium on Circuits and Systems (ISCAS)*. 2022. IEEE.
90. Wang, T. and C. Lee. *Electrically switchable multi-frequency piezoelectric micromachined ultrasonic transducer (pMUT)*. in *2016 IEEE 29th International Conference on Micro Electro Mechanical Systems (MEMS)*. 2016. IEEE.
91. Dym, C.L. and I.H. Shames, *Solid mechanics*. 1973: Springer.
92. Rao, S.S., *Vibration of continuous systems*. 2019: John Wiley & Sons.
93. Morse, P.M. and K.U. Ingard, *Theoretical acoustics*. 1986: Princeton university press.
94. Wang, C.Y. and C. Wang, *Structural vibration: exact solutions for strings, membranes, beams, and plates*. 2013: CRC Press.
95. Smyth, K.M., *Piezoelectric micro-machined ultrasonic transducers for medical imaging*. 2017, Massachusetts Institute of Technology.
96. Mason, W.P., *Electromechanical transducers and wave filters.* (No Title), 1948.
97. Smyth, K., et al., *Analytic solution for N-electrode actuated piezoelectric disk with application to piezoelectric micromachined ultrasonic transducers.* IEEE transactions on ultrasonics, ferroelectrics, and frequency control, 2013. **60**(8): p. 1756-1767.
98. Wu, L., et al., *Dual-frequency piezoelectric micromachined ultrasonic transducers.* Applied Physics Letters, 2019. **115**(2).
99. Pala, S. and L. Lin, *An improved lumped element model for circular-shape pMUTs.* IEEE Open Journal of Ultrasonics, Ferroelectrics, and Frequency Control, 2022. **2**: p. 83-95.
100. Pop, F.V., et al. *Novel pmut-based acoustic duplexer for underwater and intrabody communication*. in *2018 IEEE International Ultrasonics Symposium (IUS)*. 2018. IEEE.

101. Herrera, B., et al. *AlN PMUT-based ultrasonic power transfer links for implantable electronics*. in *2019 20th International Conference on Solid-State Sensors, Actuators and Microsystems & Eurosensors XXXIII (TRANSDUCERS & EUROSENSORS XXXIII)*. 2019. IEEE.

102. Pop, F., B. Herrera, and M. Rinaldi, *Lithium Niobate Piezoelectric Micromachined Ultrasonic Transducers for high data-rate intrabody communication.* Nature communications, 2022. **13**(1): p. 1782.

103. Allam, A., K. Sabra, and A. Erturk, *Piezoelectric transducer design for simultaneous ultrasonic power transfer and backscatter communication.* Smart Materials and Structures, 2022. **31**(9): p. 095003.

104. Mansoori, A., et al., *Electrode Design Based on Strain Mode Shapes for Configurable PMUTs.* IEEE Open Journal of Ultrasonics, Ferroelectrics, and Frequency Control, 2023.

105. Ganesan, A. and A. Seshia. *A Proposal for Absolute Inertial Imaging using Two Mechanical Modes*. in *2018 IEEE International Frequency Control Symposium (IFCS)*. 2018. IEEE.

106. Zhang, H., et al., *A low-noise high-order mode-localized MEMS accelerometer.* Journal of Microelectromechanical Systems, 2021. **30**(2): p. 178-180.

107. Puder, J.M., et al., *Rapid harmonic analysis of piezoelectric mems resonators.* IEEE Transactions on Ultrasonics, Ferroelectrics, and Frequency Control, 2018. **65**(6): p. 979-990.

108. Zhang, T. and A. Seshia. *Multi-mode piezoelectric micromachined tranducers for multi-channel acoustic power transfer and data telemetry*. in *2023 22st International Conference on Solid-State Sensors, Actuators and Microsystems (Transducers)*. 2023. Kyoto, Japan.

109. Zhang, T. and A. Seshia. *Acoustic Coupling and Remote Excitation in an Array of Multi-Mode Piezoelectric Micromachined Ultrasonic Transducers*. in *2023 Joint Conference of the European Frequency and Time Forum and IEEE International Frequency Control Symposium (EFTF/IFCS)*. 2023. Toyama, Japan.

110. Jin, X., et al., *Characterization of one-dimensional capacitive micromachined ultrasonic immersion transducer arrays.* ieee transactions on ultrasonics, ferroelectrics, and frequency control, 2001. **48**(3): p. 750-760.

111. Wang, H., et al., *Development of dual-frequency PMUT arrays based on thin ceramic PZT for endoscopic photoacoustic imaging.* Journal of Microelectromechanical Systems, 2021. **30**(5): p. 770-782.

112. Zhao, Y., et al., *Coupling Effects of Crosstalk and Parasitic Loss on Capacitive Micromachined Ultrasonic Transducers.* IEEE Sensors Journal, 2022. **22**(4): p. 3281-3297.

113.Xu, T., et al., *Array design of piezoelectric micromachined ultrasonic transducers with low-crosstalk and high-emission performance.* IEEE transactions on ultrasonics, ferroelectrics, and frequency control, 2019. **67**(4): p. 789-800.

114. Yang, Y., et al., *An ultra-high element density pMUT array with low crosstalk for 3-D medical imaging.* Sensors, 2013. **13**(8): p. 9624-9634.

115. Liu, L., et al., *A dual-frequency piezoelectric micromachined ultrasound transducer array with low inter-element coupling effects.* Journal of Micromechanics and Microengineering, 2021. **31**(4): p. 045005.

116. Liu, Z., et al., *Fabrication and characterization of row-column addressed pMUT array with monocrystalline PZT thin film toward creating ultrasonic imager.* Sensors and Actuators A: Physical, 2022. **342**: p. 113666.

117. Lee, J.-Y. and A.A. Seshia, *Parasitic feedthrough cancellation techniques for enhanced electrical characterization of electrostatic microresonators.* Sensors and Actuators A: Physical, 2009. **156**(1): p. 36-42.

118. Raskin, J.-P., et al., *Substrate crosstalk reduction using SOI technology.* IEEE Transactions on Electron Devices, 1997. **44**(12): p. 2252-2261.

119. Gao, A., et al., *AlN MEMS filters with extremely high bandwidth widening capability.* Microsystems & Nanoengineering, 2020. **6**(1): p. 74.

120. Chen, P., et al., *Acoustic characterization of tissue-mimicking materials for ultrasound perfusion imaging research.* Ultrasound in Medicine & Biology, 2022. **48**(1): p. 124-142.

121. Farrer, A.I., et al., *Characterization and evaluation of tissue-mimicking gelatin phantoms for use with MRgFUS.* Journal of therapeutic ultrasound, 2015. **3**: p. 1-11.

122. Shankar, H., P.S. Pagel, and D.S. Warner, *Potential adverse ultrasound-related biological effects: a critical review.* The Journal of the American Society of Anesthesiologists, 2011. **115**(5): p. 1109-1124.

123. Gao, Y., et al., *A miniaturized transit-time ultrasonic flowmeter based on ScAlN piezoelectric micromachined ultrasonic transducers for small-diameter applications.* Microsystems & Nanoengineering, 2023. **9**(1): p. 49.

124. Zhou, J., et al., *Continuous and Non-Invasive Monitoring of Blood Pressure Based on Wearable Piezoelectric Micromachined Ultrasonic Transducers Array.* Journal of Microelectromechanical Systems, 2023.

125. Wu, S., et al., *Aluminum nitride piezoelectric micromachined ultrasound transducer arrays for non-invasive monitoring of radial artery stiffness.* Micromachines, 2023. **14**(3): p. 539.

126. McDicken, W., *A versatile test-object for the calibration of ultrasonic Doppler flow instruments.* Ultrasound in medicine & biology, 1986. **12**(3): p. 245-249.
127. Oglat, A.A., et al., *A review of suspension-scattered particles used in blood-mimicking fluid for Doppler ultrasound imaging.* Journal of medical ultrasound, 2018. **26**(2): p. 68-76.
128. Genovés, V., et al., *Variation in the viscoelastic properties of polydimethylsiloxane (PDMS) with the temperature at ultrasonic frequencies.* Polymer Testing, 2023. **124**: p. 108067.
129. Bell, A.G., *The production of sound by radiant energy.* Science, 1881(48): p. 242-253.
130. Bell, A.G., *On the production and reproduction of sound by light.* American journal of science, 1880. **3**(118): p. 305-324.
131. Lin, L., et al., *High-speed three-dimensional photoacoustic computed tomography for preclinical research and clinical translation.* Nature communications, 2021. **12**(1): p. 882.
132. Matsumoto, Y., et al., *Visualising peripheral arterioles and venules through high-resolution and large-area photoacoustic imaging.* Scientific reports, 2018. **8**(1): p. 14930.
133. Cai, J., et al., *Beyond fundamental resonance mode: high-order multi-band ALN PMUT for in vivo photoacoustic imaging.* Microsystems & nanoengineering, 2022. **8**(1): p. 116.
134. Chandramoorthi, S., et al., *Wideband photoacoustic imaging in vivo with complementary frequency conventional ultrasound transducers.* Frontiers in Physics, 2022. **10**: p. 954537.
135. Wang, L., *Photoacoustic imaging and spectroscopy*. 2017: CRC press.
136. Yu, H., et al., *A vibration-based MEMS piezoelectric energy harvester and power conditioning circuit.* Sensors, 2014. **14**(2): p. 3323-3341.
137. Ibrahim, S.W. and W.G. Ali, *A review on frequency tuning methods for piezoelectric energy harvesting systems.* Journal of renewable and sustainable energy, 2012. **4**(6).
138. Cheng, Y., N. Wu, and Q. Wang, *An efficient piezoelectric energy harvester with frequency self-tuning.* Journal of Sound and Vibration, 2017. **396**: p. 69-82.
139. Qiu, W., et al. *A programmable ultrasound platform for multi-gate Doppler measurement*. in *2014 IEEE International Ultrasonics Symposium*. 2014. IEEE.
140. Gao, H., et al. *Design of polymer-based PMUT array for multi-frequency ultrasound imaging*. in *2019 IEEE International Ultrasonics Symposium (IUS)*. 2019. IEEE.
141. Chun, S., et al. *Acoustic Measurement of Ultrasound Sensors in a Water Bath*. in *Fluids Engineering Division Summer Meeting*. 2020. American Society of Mechanical Engineers.
142. Jeong, Y., et al., *Fully flexible PMUT based on polymer materials and stress compensation by adaptive frequency driving.* Journal of Microelectromechanical Systems, 2020. **30**(1): p. 137-143.

143. Savoia, A.S., et al. *A feasibility study of a PMUT-based wearable sensor for the automatic monitoring of carotid artery parameters*. in *2021 IEEE International Ultrasonics Symposium (IUS)*. 2021. IEEE.

144. Zhong, H., et al., *Review of low-cost photoacoustic sensing and imaging based on laser diode and light-emitting diode.* Sensors, 2018. **18**(7): p. 2264.

145. Allen, T.J. and P.C. Beard, *Pulsed near-infrared laser diode excitation system for biomedical photoacoustic imaging.* Optics letters, 2006. **31**(23): p. 3462-3464.

146. Kolkman, R.G., W. Steenbergen, and T.G. van Leeuwen, *In vivo photoacoustic imaging of blood vessels with a pulsed laser diode.* Lasers in medical science, 2006. **21**: p. 134-139.